UNIVERSITÀ
DEGLI STUDI
DI TRIESTE

UNIVERSITÀ DEGLI STUDI DI TRIESTE

XXXVI CICLO DEL DOTTORATO DI RICERCA IN

SCIENZE DELLA TERRA, FLUIDODINAMICA E MATEMATICA.
INTERAZIONI E METODICHE

Reconstructing the dynamics of the West Antarctic Ice Sheet since the last glacial (MIS2) by studying the sector from the Glomar Challenger inner continental shelf to the slope and rise area (East Ross Sea, Antarctica): a multidisciplinary approach

Settore scientifico-disciplinare: **GEO/02**

DOTTORANDO / A
ANDREA GENIRAM

COORDINATORE
PROF. STEFANO MASET

SUPERVISORE DI TESI
PROF. ESTER COLIZZA

CO-SUPERVISORE DI TESI
PROF. ROMANA MELIS

ANNO ACCADEMICO 2022/2023

Alla mia famiglia

Table of contents

Abstract

The Ross Sea is one of the key sectors to reconstruct the evolution of the Antarctic Ice Sheet. Several ice streams from both the West and East Antarctic Ice Sheets advanced and retreated many times on the continental shelf, reaching the shelf margin (e.g. Anderson et al., 2019). Ice streams crossed basins and troughs with different characteristics and morphologies, which led to different behaviours during both advances and retreats (Livingstone et al., 2012; Danielson & Bart, 2023). These differences allow the division of the Ross Sea in the Western and the Eastern part. The former is characterised by deep narrow troughs separated by high relief banks, while the latter is characterised by wide shallow basins divided by low relief ridges (e.g. Halberstadt et al., 2016). The Western Ross Sea is also characterised by consolidated sediments (Cooper et al., 1991; Anderson & Bartek, 1992), while the Eastern Ross Sea is filled with unconsolidated Plio-Pleistocene sediments (e.g. Alonso et al., 1992).

Studying past glacial cycles is crucial to understand the evolution of the ice sheet related to climate changes. One of the more studied phases in the Ross Sea area is the Last Glacial Maximum (e.g. Anderson et al., 2014, 2019; Halberstadt et al., 2016; Prothro et al., 2020; Danielson & Bart, 2023). Although the Ross Sea has the largest amount of data of any region in Antarctica (e.g., Anderson et al., 2019), there are still uncertainties about the evolution of this area, particularly the timing of events. This is due to the extensive use of organic matter for radiocarbon ages, as it is difficult to find well-preserved carbonate material (Anderson et al., 2014).

During the last glacial advance, the ice sheet reached the continental margin in the Eastern Ross Sea (e.g. Mosola & Anderson, 2006; Bart & Cone, 2012; Halberstadt et al., 2016), while it was in the outer shelf in the Western Ross Sea (e.g. Prothro et al., 2020). While the Western Ross Sea has been widely studied, the Eastern Ross Sea is still affected by lacks and uncertainties, in particular on the duration of the grounding event and timing of the retreat. Previous studies suggested the ice sheet retreated during or even before the LGM (e.g. Licht & Andrews, 2002; Mosola & Anderson, 2006; Bart & Cone, 2012), while more recent studies suggested that the retreat took place after the LGM (e.g. Bart et al., 2018; Danielson & Bart, 2023).

Adding more data will help to better constrain timing and mechanisms of ice sheet retreat since the Last Glacial Maximum. The objective of this PhD thesis is to add more data to try to better constrain

the history of the Glomar Challenger Basin and the slope and rise area from the Last Glacial Maximum to the present.

The study area considered in this work is located in the Eastern Ross Sea and takes into account the Glomar Challenger Basin, on the continental shelf and the slope and rise area at the mouth of the basin itself.

Glomar Challenger Basin is located at the border with the Western Ross Sea, separated from it by the Ross Bank in the innermost part, but it joins with the Pennell Trough near the continental margin. The slope and rise area in front of the basin are located on the eastern side of the Hillary Canyon, one of the main sediment drainages of the continental shelf.

The aim of this work is to reconstruct the sedimentary dynamics in the Glomar Challenger Basin and the slope and rise area during the late Quaternary.

This work has been conducted in the frame of two projects:

- STREAM (Late Quaternary evolution of the ocean - ice sheet interactions: the record from the Ross Sea continental margin (Antarctica)); 2019-2021
- ANTIPODE (Onset of Antarctic Ice Sheet vulnerability to ocean conditions). 2020-2023

STREAM was a joint project between Italy and the Rep. of Korea developed from 2019 to 2021. The principal investigators, E. Colizza for Italy and B.-K. Khim for Korea, focused the project on the sedimentary material collected in the slope and rise in the Hillary Canyon area, at the mouth of the Glomar Challenger. Several gravity cores and box cores have been studied using a multidisciplinary approach. Geophysical data have been used as well. Studying timing and mechanisms of advance and retreat of the ice sheet in the continental margin area during late Quaternary was the aim of this project, also allowing to reconstruct environmental changes during the studied time frame.

ANTIPODE was a PNRA project led by F. Colleoni (OGS – Italy). It was based on a combination of modelling with geological, geophysical and oceanographic data. The aim was to reconstruct the evolution of the ice sheet in the Ross Sea during different geological periods. In order to fulfil this achievement, reconstruction of morphological and geometrical variations have been performed and interactions of the ice sheet with water masses have been studied and modelled.

The PhD thesis considered a transect of gravity cores and box cores collected during several PNRA expeditions (Programma Nazionale di Ricerca in Antartide): the XI expedition (1995-1996), XIV expedition (1998-1999) and the XXIX expedition (2013-2014). Several sub-bottom profiles (SBPs), a sparker profile (SPK) and single channel seismic lines also acquired during the XIV and XXXII (2016-2017) PNRA expeditions were considered. Sedimentary material had already been partly analysed as part of three-year theses (Calligaris, 2003; Torricella, 2016; Valle, 2016), but data were revised, sampled re-analysed and integrated also using new methodologies and increasing the stratigraphic resolution in the framework of this thesis. Geophysical data have been used to provide the Glomar Challenger Basin geomorphological context and in particular in the site where the gravity cores have been collected, also providing useful information about sedimentary dynamics. A multidisciplinary approach has been adopted on sediment cores and box cores. In particular, in addition to the magnetic susceptibility measured on board when the cores were collected, X rays were combined with the visual description and have been used to count clasts >2 mm using the method proposed by Grobe (1987). Analyses have been divided into physical analysis, chemical and geochemical analysis and microscopy analysis. Physical analysis consisted in magnetic susceptibility, compressive strength, water content and grain size analysis, aiming to identify textural differences. Elemental analysis via core scanner x-ray fluorescence (XRF cs) was used to identify compositional differences of the sediments. Geochemical analyses have been used to identify variations in paleo-productivity (organic matter) and sea ice coverage (biomarkers). Sand and foraminifera analysis via microscope have been carried out in order to identify compositional and biological content. A series of radiocarbon ages measured on organic matter were already available: four for the innermost gravity core on the shelf and thirteen for the box cores and the core on the slope and rise. An amount of 23 new radiocarbon ages were planned for the gravity cores on the shelf, but unfortunately the chosen samples were not analysed for reasons beyond my control. A total of 17 radiocarbon ages (4 for the Glomar Challenger Basin and 13 for the slope and rise area) obtained from organic matter were used.

Physical and microscopy analysis have been conducted at the Department of Mathematics, Informatics and Geosciences (University of Trieste), while chemical and geochemical analyses have been mainly conducted at the Institute of Polar Sciences – CNR of Bologna.

The results allowed to identify 4 sedimentary facies and 2 sub-facies in the gravity cores collected in the Glomar Challenger Basin:

1) the stiff diamicton identified in the sub bottom profiles under an unconformity and recovered in the cores collected in the inner continental shelf. It is characterised by a uniform trend of the measured parameters and interpreted as a subglacial environmental deposition. This facies is marked by a distinct unconformity in the SBPs. One AIOM radiocarbon age dates this facies in an inner shelf core (GC12) as pre-LGM (34,3 cal kyr);

2) the soft diamicton characterised by parameters similar to those of facies 1, and it is interpreted as a subglacial deposit. It was recovered in all the cores above the stiff diamict and above the unconformity identified in the SBPs. Radiocarbon age (AIOM) obtained from core GC12 is 35,1 cal kyr (pre-LGM);

3) the glaciomarine diamicton characterised by a higher amount of clasts and by the presence of laminated intervals. It was recovered in the cores collected in the inner and middle shelf and interpreted as a sub-ice shelf facies. The radiocarbon age performed at the at the top of this facies in an inner continental shelf core (GC12) suggests an age around the beginning of the LGM (26,3 cal kyr);

4) this facies is divided in two sub-facies 4a) a silt with a very low content of sand and clasts, a higher content of organic carbon and characterised by the presence of agglutinated foraminifera. This sub-facies has been identified at the top of the cores collected in the inner continental shelf and the biomarker characteristics allow to interpret this sub facies as seasonal open marine conditions, 4b) sandy silt with a high content of sand and clasts, presence of agglutinated foraminifera and biomarkers, leading to interpret it as a seasonal open marine facies. It was recovered in the cores collected in the middle and outer shelf.

Regarding the slope and rise area, three facies were identified:

1) a clayey silt facies characterised by laminations and interpreted as a deposit formed during the glacial period. Radiocarbon ages (AIOM) range from 27,1 kyr to 23,3 cal kyr BP. It represents the basal unit of the two deepest box cores and the interval considered of the gravity core;

2) a massive sandy silt facies with clasts interpreted as glacigenic material deposited during the deglacial phase when the ice sheet was grounded near the continental shelf edge and started to retreat between 20,8 to 13,6 cal kyr BP. It represents the major part of the BC3 and it represents the intermediate facies in the other box cores and in the gravity core;

3) a sandy silt facies with high content of clasts dropped by icebergs, interpreted as a seasonal open marine paleoenvironment, Holocene in age (from 11,4 cal kyr BP to the present). It was recovered at the top of each box core/gravity core.

Ha et al. (2022) identified three facies in the gravity cores collected in the same sites of the box cores studied for this thesis. Adding more data (XRF cs data, organic matter and biomarkers) and increasing the stratigraphic resolution allowed to identify and better characterise three sedimentary facies, slightly modifying their intervals. Using these data, the interpretation of grain size data considered by Gales et al. (2021) was improved too.

The results obtained by present study allow to highlight the ice sheet evolution from the LGM to the present: in particular during the LGM, when the ice sheet advanced across the continental shelf and reached the shelf margin, stiff and soft diamicton were deposited on the shelf in a subglacial environment. Meanwhile, the presence of a perennial sea ice cover, leads to deposit the laminated facies identified in the slope and rise. When the ice sheet retreated from this position, glacigenic material was deposited in the slope and rise area. During the glacial retreat, a sub ice shelf facies was deposited on the continental shelf when the ice sheet decoupled from the sea floor. Seasonal open marine conditions were established in the Holocene in the slope and rise area, first, and then on the shelf, as confirmed by the presence of biomarkers, with icebergs dropping sand and clasts on the slope. The outer shelf was affected by currents that winnowed fine sediments. A silt with sparse IRD facies was deposited in the inner/middle shelf.

The sequence of the facies in the GCB was not identified in all the cores. This may be correlated with erosive events related to the advance of the ice sheet or paleo-ice streams or because of rapid retreats (e.g. Mosola & Anderson, 2006; Halberstadt et al., 2016). Considering the only dated core on the shelf, radiocarbon ages may suggest a hiatus between facies 3 and 4. Radiocarbon ages on the shelf were obtained from one core, suggesting ages older than the LGM (26,5 - 19,0 kyr BP from Clark et al., 2009). The presence of reworked organic matter must be considered, as suggested by (Andrews et al., 1999; Domack et al., 1999). The advance of the ice sheet is associated with mixing of sediments characterised by different ages.

The results of the paleoenvironmental dynamics of the GCB here described will be supported in the future by radiometric analyses essential to place these events in a corrected temporal context.

List of Figures

Supplementary

List of Tables

Supplementary

List of Abbreviations

9-OHD = 9-octylheptadec-8-ene

AABW = Antarctic Bottom Water

AASW = Antarctic Surface Water

ACC = Antarctic Circumpolar Current

ADW = Antarctic Deep Water

AIOM = Acid Insoluble Organic Matter

AIS = Antarctic Ice Sheet

Al = Aluminium

AMS = Accelerator Mass Spectrometry

ASC = Antarctic Slope Current

Avg = average

AWI = Alfred Wegener Institute

Ba = Barium

BC = Box core

BioSi = Biogenic Silica

BP = Before Present

Br = Bromine

C = Carbon

Ca = Calcium

CA = Cape Adare

$CaCO_3$ = Calcium Carbonate

Cal = Calibrated

CB = Crary Bank

CC = Cape Colbeck

CDW = Circumpolar Deep Water

CNR = National Research Council

Cps = counts per second

cs = continental shelf

CS = Compressive Strength

DCM = Dichloromethane

DCM:MET = Methacryloyloxyethyl Trimellitic acid)

DSDP = Deep Sea Drilling Project

DT = Drygalski trough

EAIS = East Antarctic Ice Sheet

ENSO = El Niño Southern Oscillation

ERS = Eastern Ross Sea

ERSF = Eastern Ross Sea Fan

Fe = Iron

GC = Gravity Core

GCB = Glomar Challenger Basin

Gx = Geochron

GZ = Grounding Zone

GZW = Grounding Zone Wedge

H_2O_2 = Hydrogen Peroxide

HBI = Highly Branched Isoprenoid

HC = Hillary Canyon

HCl = Hydrochloric Acid

HSSW = High Salinity Shelf Water

IB = Iselin Bank

IBCSO = International Bathymetric Chart of the Southern Ocean

IODP = Integrated Ocean Drilling Program

IP_{25} = Ice Proxy with 25 Carbon atoms

$IPSO_{25}$ = Ice Proxy for Southern Ocean with 25 Carbon atoms

IRD = Ice Rafted Debris

IS = Internal Standard

ISMAR = Institute of Marine Sciences

ISP = Institute of Polar Sciences

ISW = Ice Shelf Water

JT = JOIDES Trough

K = Potassium

KOH = Methanolic Potassium Hydroxide

Kyr = Kiloyears

LAB = Little America Basin

LCO = Local Contamination Offset

LGM = Last Glacial Maximum

LSSW = Low Salinity Shelf Water

MB = Mawson Bank

MBL = Marie Byrd Land

MCDW = Modified Circumpolar Deep Water

Md = Median diameter

MIGe = Department of Mathematics, Informatics and Geosciences

MIS = Marine Isotope Stage

Mn = Manganese

MNA = National Museum of Antarctica

MRE = Marine Reservoir Effect

MS = Magnetic Susceptibility

MSGL = Mega Scale Glacial Lineation

MSW = Modified Shelf Water

MWP-1A = Meltwater Pulse 1A

Myr = Million years

Mz = Mean diameter

N = Nitrogen

NOSAMS = National OCean Sciences Accelerator Mass Spectrometry

OGS = National Institute of Oceanography and Applied Geophysics

OS = NOSAMS

Pa = Peak area

PB = Pennell Bank

PNRA = National Antarctic Research Program

Poz = Poznan

PT = Pennell Trough

Rb = Rubidium

RB = Ross Bank

RIS = Ross Ice Shelf

RS = Ross slope

RSU = Ross Sea Unconformity

SAM = Southern Annular Mode

SBP = Sub Bottom Profile

SCSL = Single Channel Seismic Lines

St. dev. = Standard deviation

SDLS = Seismic Data Library System

Si = Silica

SI = International System

Sk = Skewness

Sort = Sorting

SPK = Sparker Profile

sr = slope and rise

Sr = Strontium

SST = Sea Surface Temperature

SW = Shelf Water

TAM = Transantarctic Mountains

Ti = Titanium

TN = Total Nitrogen

TOC = Total Organic Carbon

UniTS = University of Trieste

VL = Victoria Land

W% = Water content

WAIS = West Antarctic Ice Sheet

WARS = West Antarctic Rift System

WD = Whales Deep Basin

WRS = Western Ross Sea

XRF cs = X-Ray Fluorescence core scanner

Zr = Zirconium

1. Introduction

The Ross Sea (Antarctica) is a key sector to study the evolution of the ice sheet because it was influenced by both West and East Antarctic Ice Sheets (Anderson et al., 2014 and references therein). They are divided in several ice streams that had a different behaviour during the ice advances and retreats because of the different characteristics of basins and troughs in the Ross Sea (Danielson & Bart, 2023). Focusing on the last deglaciation, several studies have been conducted (e.g. Anderson et al., 2014; Halberstadt et al., 2016; Bart et al., 2018; Anderson et al., 2019; Prothro et al., 2020; Danielson & Bart, 2023). Even though, there are still uncertainties, in particular about timing of events because of the lack of carbonate material and the consequent large use of organic matter to obtain ages (Anderson et al., 2014).

One of the sectors of the Ross Sea affected by greatest uncertainties is the Glomar Challenger Basin, in the Eastern Ross Sea. Several Authors suppose this area has been occupied by ice grounded near the shelf break (e.g. Mosola & Anderson, 2006; Halberstadt et al., 2016), but there are still questions about the duration of the grounding event and timing of retreat. Several studies have been conducted obtaining radiocarbon ages from both organic matter and carbonate material, suggesting an early retreat (e.g. Licht & Andrews, 2002; Mosola & Anderson, 2006; Bart & Cone, 2012). More recent studies suggested an after-LGM retreat (e.g. Bart et al., 2018; Danielson & Bart, 2023). Adding more data will help to better constrain timing and mechanisms of events.

The aim of this work is to reconstruct the sedimentary dynamics of the Glomar Challenger Basin (Eastern Ross Sea, Antarctica) and the slope and rise area in front of this basin during the last glacial (MIS2). A transect of gravity cores and box cores has been obtained during several PNRA (Programma Nazionale di Ricerca in Antartide) expeditions. A multidisciplinary approach has been adopted applying physical (grain size, magnetic susceptibility, compressive strength, water content), chemical (elemental analysis), geochemical (organic matter, biomarkers) and micropaleontological analyses (sand content and foraminifera).

This research has been conducted in the frame of two projects:

- STREAM (Late Quaternary evolution of the ocean - ice sheet interactions: the record from the Ross Sea continental margin (Antarctica)); 2019-2021
- ANTIPODE (Onset of Antarctic Ice Sheet vulnerability to ocean conditions). 2020-2023

STREAM was a joint project between Italy and South Korea, active in the period 2019-2021, led by professor Colizza Ester (University of Trieste - Italy) and professor Khim Boo-Keun (Pusan University - Rep. of Korea). The purpose of this project was to study timing and mechanisms of advances and retreats of the ice sheet in the Ross Sea and related environmental changes during late Quaternary. To obtain this, a multidisciplinary approach using sediment cores and geophysical data, collected on the Ross Sea slope and rise area, was adopted.

ANTIPODE was a PNRA project based on a combination of geological, geophysical and oceanographic data and modelling. The aim was to reconstruct how changes in morphology and geometry of the Ross Sea and interactions with water masses have influenced the evolution of the ice sheet during different geological periods. The principal investigator was Dr. Colleoni Florence (OGS - Italy).

2. Antarctica

Antarctica (fig. 1) is a unique continent. It is located in the southernmost position of the globe and is surrounded by waters of the Southern Ocean, with no direct connection with other land masses, allowing the circulation of the clockwise Antarctic Circumpolar Current (ACC) all around Antarctica driven by the westerly winds. About 98% of its surface is covered by the largest ice sheet on Earth, the so-called Antarctic Ice Sheet (AIS). The continent, and so the ice sheet, are divided in two parts: East Antarctica (and East Antarctic Ice Sheet, EAIS) and West Antarctica (and West Antarctic Ice Sheet, WAIS) with the border represented by the Transantarctic Mountains (TAM), one of the longest mountain range in the world (about 3500 km). East Antarctica is a continental shield, while West Antarctica is characterised by a complex morphology and it is formed by an archipelago. Other peculiar features are the Peninsula Antarctica, which extends toward South America, and the Ross Sea and the Weddell Sea, the two largest embayment which are the main drainage areas of the continent.

The Antarctic Ice Sheet is the largest ice sheet on Earth, with a surface of about 14 million km^2 and a volume of 30 million km^3. TAM divides the ice sheet in two (Anderson, 1999): EAIS and WAIS. Like the two parts of the continent, these two parts of the ice sheet show distinctive features. The EAIS

is dome shaped with a flat centre and steep borders and is mainly grounded above the sea level. The WAIS shows a smooth profile and is mainly grounded below sea level; therefore, it is called marine-based ice sheet. The WAIS is also characterised by the two largest ice shelves of the continent: the Ross Ice Shelf (RIS) in the Ross Sea, and the Ronne-Filchner Ice Shelf in the Weddell Sea. Continental margins of Antarctica show the presence of other smaller ice shelves.

The climate of Antarctica is extreme, with very low levels of precipitation, very cold temperatures, and powerful winds (katabatic winds), making data collection difficult.

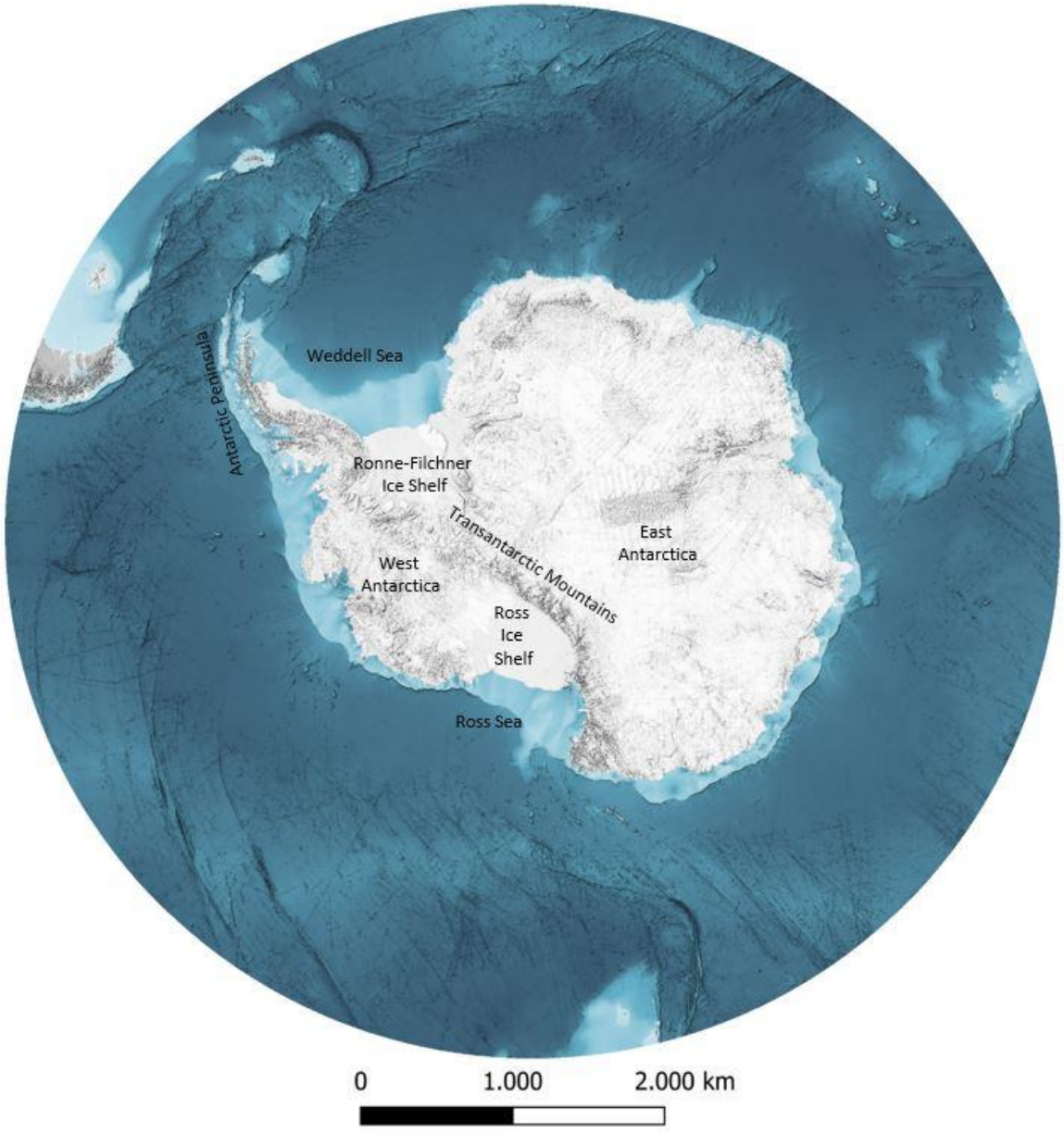

Figure 1 Map of Antarctica (from IBCSO version 2, Dorschel et a., 2022).

3. Ross Sea

Continental margins of Antarctica have been extensively studied, in order to reconstruct the climatic history of this continent. The Ross Sea, in particular, is the most studied area of Antarctica, owing to the largest amount of sediment cores, drilling cores, and geophysical data, with the goal of reconstructing the geological evolution of this area and its glacial history since the formation of the ice sheet and its first interaction with the marine environment.

The Ross Sea (fig. 2) is one of the two great embayments of Antarctica. The western boundary is formed by Cape Adare (CA), which is located in the Victoria Land (VL), and by the Transantarctic Mountains (TAM). The eastern boundary is represented by Cape Colbeck (CC), which is located in the Marie Byrd Land (MBL). The Ross Sea is Antarctica's largest drainage (e.g. Halberstadt et al., 2016; Prothro et al., 2018; Anderson et al., 2019), draining roughly 25% of the AIS. Part of the Ross Sea is covered by the Ross Ice Shelf (RIS), with an area of about 400.000 km^2 (Prothro et al., 2018). Both WAIS and EAIS drains in the Ross Sea (Halberstadt et al., 2016 and references therein). The limit that divides the floating ice from the grounded ice sheet, called grounding line, is currently located in the innermost part of the Ross Sea, hundreds of kilometres from the continental shelf break (Bentley et al., 2014; Anderson et al., 2014).

The Ross Sea can be divided in two sectors: the Western Ross Sea (WRS) and the Eastern Ross Sea (ERS). WRS is bounded by Cape Adare and the TAM on the western edge and by the Ross Bank and the Iselin Bank on the eastern side. The ERS is bounded by the Ross bank and Marie Byrd Land (MBL). These two areas are characterised by different morphologies and geology. The WRS is characterised by a complex morphology, with deep narrow troughs surrounded by high relief banks (fig. 2) (e.g Halberstadt et al., 2016), and with a seafloor characterised by consolidated sediment (Cooper et al., 1991; Anderson & Bartek, 1992). Three main troughs, Drygalski (DT), JOIDES (JT) and Pennell (PT), from west to east, converge toward the ice shelf in front of the Ross Island. The ERS is characterised by three wide basins: Glomar Challenger (GCB), Whales Deep (WD) and Little America Basin (LAB), which are separated by low relief ridges (fig. 2) (e.g. Halberstadt et al., 2016).

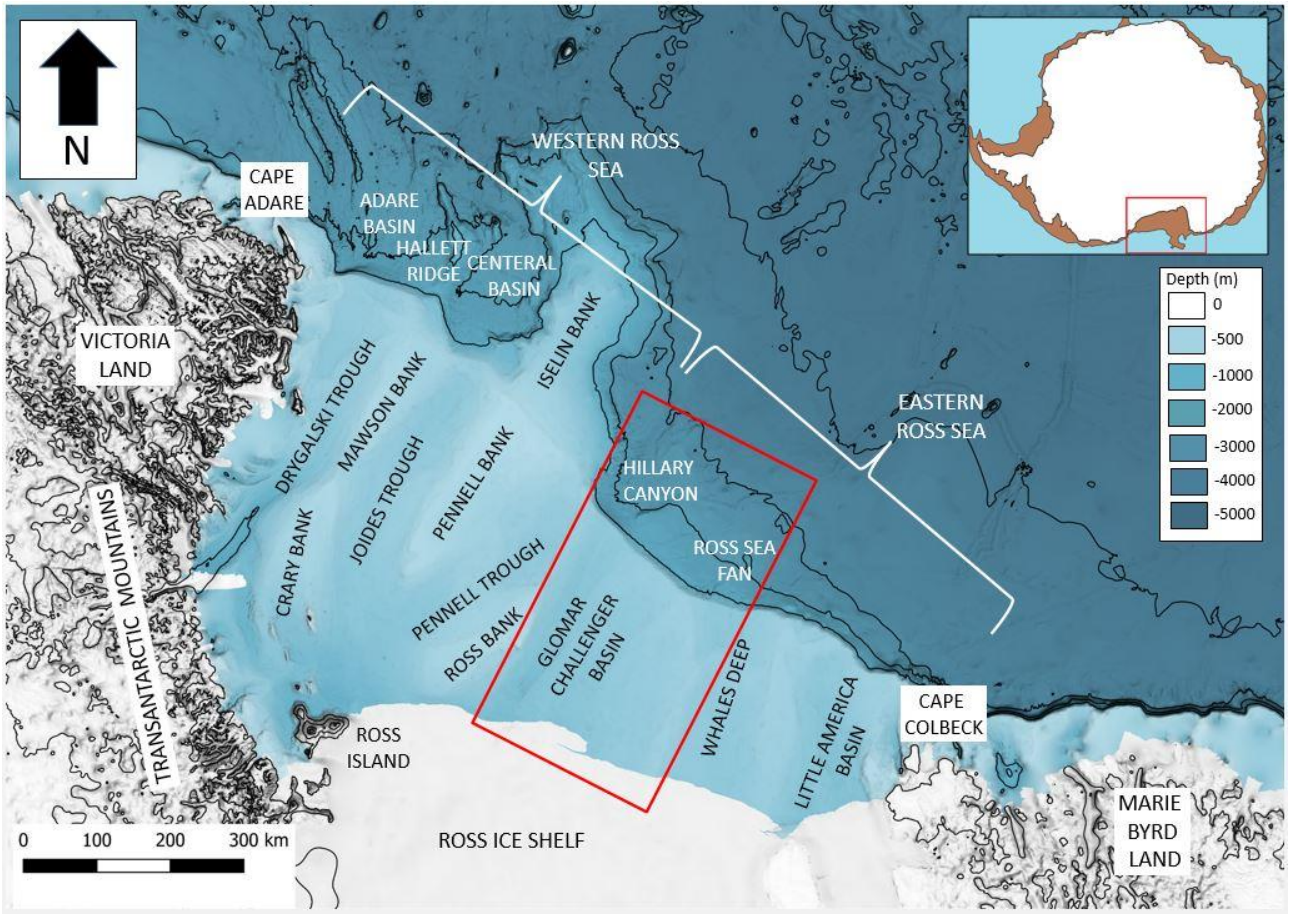

Figure 2 Ross Sea bathymetric map (modified from Dorschel et al., 2022). The red rectangle highlights the study area.

3.1 Geological history

The Ross Sea has deeply changed during its geological history. An extensional phase formed the West Antarctic Rift System (WARS) during Mesozoic and Cenozoic (e.g. Granot & Dyment, 2018 and references therein). This process led to the formation of four N-S oriented tectonic basins (Davey et al., 1982; Brancolini et al., 1995; Davey & Brancolini, 1995). The Victoria Land Basin, the Northern Basin and the Central Trough have been formed in the Western Ross Sea (WRS). The Eastern Basin, which is a single rift basin with isolated highs (Cooper et al., 1991; Halberstadt et al., 2016) has been formed in the ERS. The extensional tectonic history of this area formed the foundation for the seven bathymetric troughs that characterises the Ross Sea (Lawver et al 1991). These troughs have been modelled by ice streams during several glacial cycles (Cooper et al., 1991; Anderson et al., 1991).

The onset of the glaciation of Antarctica had been established around 34 million years (Myr) before present, during the Eocene - Oligocene transitions, but the AIS was mainly terrestrial at that time

(Escutia et al., 2019), while first interaction with marine environments happened around 32,8 Myr in the WRS (Galeotti et al., 2016). During late Oligocene - Early Miocene, the ERS was characterised by isolated ice caps, confirmed by geophysical data that highlighted the presence of glacial valleys along the flanks of morphological highs (De Santis et al., 1995, 1999; Bartek et al., 1996; Sorlien et al., 2007) and by the presence of till and proximal glacio-marine sediments recovered at DSDP drilling sites (Barrett, 1975; Hayes & Frakes, 1975; Anderson, 1999). Drilling sites studies (e.g. Kulhanek et al., 2019; Levy et al., 2019) suggest a glacial expansion, with Levy et al. (2019) suggesting that it may have taken place around 24,5 - 24 Myr. As reported by Anderson et al. (2019), during Miocene, several glacial advances and retreats happened and have been identified using geophysical data studying glacial unconformities (Ross Sea unconformities - RSUs) (e.g. Anderson & Bartek, 1992; Brancolini et al., 1995; De Santis et al., 1995; Bartek et al., 1996) and successions of sediments from till to glacio-marine units (Anderson & Bartek, 1992; De Santis et al., 1995; Anderson 1999; Bart, 2003). This series of advances and retreats modified the continental shelf profile. The modern continental shelf of the Ross Sea is characterised by a landward-dipping profile formed because sediment eroded on the inner shelf have been deposited on the outer shelf during episodes of ice sheet expansion, and because of glacial isostasy (Anderson, 1999). This morphology was acquired when glacial processes started to control its evolution during Miocene (Bartek et al., 1992; De Santis et al., 1999; Decesari et al., 2007). Before that, tectonic subsidence was the main control factor that led to a first seaward-dipping profile (De Santis et al., 1995). Then, a higher number of glacial advances and retreats have been recorded during the Plio-Pleistocene (Anderson et al., 2019 and references therein; King et al., 2022). The last glacial expansion was recorded in both hemispheres during the Last Glacial Maximum (LGM), a time frame fixed at 26,5 - 19 thousand years (kyr) by Clark et al. (2009). The presence of grounding wedges (GZWs) at the shelf break in the ERS and the presence of mega-scale glacial lineations (MSGLs) along all the Glomar Challenger Basin and the Little America Basin, and in the middle-outer shelf of the Whales Deep, confirmed that the WAIS reached the continental margin in the ERS (Shipp et al., 1999; Mosola & Anderson, 2006; Halberstadt et al., 2016). GZWs are ice-marginal feature wedge shaped that represents periods of grounded ice stability (Halberstadt et al., 2016), while MSGLs are linear subglacial features generated by streaming ice (King et al., 2009). The presence of gullies, incisions that may have been formed by sediment-dense meltwater (e.g. Anderson, 1999) or by slope failures (Gales et al., 2012, Gales et al., 2021), on the ERS continental margin is a proof as well (Mosola & Anderson, 2006; Gales et al., 2021).

In the geological past, the WRS outer shelf was not completely occupied by a grounded ice sheet, as suggested by some radiocarbon ages >20 kyr recorded in glaciomarine sediments from the outer shelf of WRS (Licht et al., 1996). The grounding line was located north of Coulman Island in the Drygalski Trough (Domack et al., 1999; Licht et al., 1999; Shipp et al., 1999; Bart et al., 2000; McKay et al., 2008; Anderson et al., 2014; Halberstadt et al., 2016; Prothro et al., 2020), while it was located in the middle-outer shelf of the JOIDES and Pennell Troughs (Shipp et al., 1999; Halberstadt et al., 2016; Prothro et al., 2020). This reconstruction has been also confirmed by the biogenic carbonate, LGM in age (Taviani et al. 1993; Frank et al., 2014; Melis & Salvi, 2020), located along the outer shelf. Gullies are not present at the mouth of the Pennell Trough, confirming that the ice sheet did not reach the shelf edge (Gales et al., 2021).

Several works focused on the last glaciation (Anderson et al., 2019 and references therein) studying sediment cores and seafloor morphologies like GZWs and MSGLs to reconstruct the position of the grounding line during LGM, and timing and mechanisms of the retreat (e.g. Shipp et al., 1999; Licht & Andrews, 2002; Mosola & Anderson, 2006; Bart & Cone, 2012; Bart & Owolana, 2012; Greenwood et al., 2012, 2018; Anderson et al., 2014, 2019; Halberstadt et al., 2016; Lee et al., 2017; McGlannan et al., 2017; Bart et al., 2018; Simkins et al., 2018; Prothro et al., 2018, 2020; Danielson & Bart, 2023). Different models have been proposed to represent the retreat of the ice sheet after the LGM (Halberstadt et al., 2016). Conway et al. (1999) proposed the “swinging gate” model based on the presence of a linear grounding line and little influence of sea floor characteristics, which led to an earlier retreat in the WRS than in the ERS (e.g. McKay et al. 2008; Hall et al., 2013). On the contrary, a model based on an earlier retreat in the ERS has been proposed by Ackert (2008), the “saloon door model”, which implies the formation of an embayment in the ERS. Halberstadt et al. (2016), studying seafloor geomorphology, proposed a “marine based model”, which implies a different behaviour of each trough and basin. They agree with the formation of an embayment and an early retreat in the ERS (Glomar Challenger Basin, Whales Deep), favoured by unconsolidated Plio-Pleistocene sediment. This destabilised the WRS, but it experienced a delayed retreat with banks that acted as pinning points, an also supported the presence of an ice shelf (Anderson et al., 2014; Simkins et al., 2016; Yokoyama et al., 2016) confirmed by the presence of retreating morphological features on the banks (Halberstadt et al., 2016; Lee et al., 2017; Simkins et al., 2017; Greenwood et al., 2018). Older sediments characterising the WRS, but also the Little America Basin and a localised area of the Glomar Challenger, are more resistant to erosion and deformation and are responsible for reduced velocities (Halbestadt et al., 2016 and references therein). All these differences between

the ERS and WRS explain different dimensions of ice-marginal features and different extensions of subglacial features (Anderson et al., 2019). Small and closely spaced GZWs, iceberg furrows and short fields of MSGLs indicate a gradual retreat with several pauses that allowed the formation of these features (Halberstadt et al., 2016). The ERS is characterised by several large scale composite GZWs and extensive linear features, which represents periods of stabilisation alternated by extensive episodes of retreat (Halberstadt et al., 2016). These physiographic differences controlled deglaciation (Anderson et al., 2019) that had been completed in the ERS before the grounded ice left the inner continental shelf of the WRS (Halberstadt et al., 2016).

A very recent work by Danielson & Bart (2023) suggests that the retreat of the grounding line after the LGM proceeded in an unstable and staggered manner from one depression to the next with very different timing. In this regard, the timing of the retreat is still much debated due to the poor reliability of the dates generally performed on the organic matter (see for discussion Anderson et al., 2014). The first phase of the grounding line retreat is reported in the DT from about 16,5 cal kyr BP (Prothro et al., 2020; Anderson et al., 2014), which is followed by the subsequent opening of the PT (ca. 15 cal kyr BP) and subsequently the JT (ca. 13 cal kyr BP) (Prothro et al., 2020). The last troughs to break free from the grounding line were the LAB and GCB middle shelf from about 8 cal kyr BP (see fig. 5 in Danielson & Bart, 2023).

3.2 Oceanography

Another important component of Ross Sea (and global) dynamics are the oceanographic settings. Intrusion of warm water masses on the shelf can influence the sea ice and the ice shelf and the production of cold water masses (Smith et al., 2012). Several water masses have been identified in the Ross Sea considering temperature, salinity and density (Orsi & Wiederwohl, 2009 and references therein; Budillon et al., 2011 and references therein). Orsi & Wiederwohl (2009) distinguished between slope and shelf water masses considering a water depth of 700 m as boundary. The upper layer is represented by a single water mass called Antarctic Surface Water (AASW). The middle layer is represented by Circumpolar Deep Water (CDW) on the slope and by Modified Circumpolar Deep Water (MCDW) on the shelf. Antarctic Bottom Water (AABW) represents the bottom layer outside

the shelf, while on the shelf water mass settings are more articulated, represented by several water masses: Shelf Water (SW), Modified Shelf Water (MSW), Ice Shelf Water (ISW), High Salinity Shelf Water (HSSW) and Low Salinity Shelf Water (LSSW). AASW is formed by fresher water and subjected to seasonal heating/cooling and formation/melting of sea ice (Orsi & Wiederwohl, 2009; Budillon et al., 2011). When AASW interacts with the subsurface layer, Low Salinity Shelf Water (LSSW) is formed (Budillon et al., 2011 and references therein).

CDW occupies the largest volume in the Southern Ocean (Worthington, 1981). It is carried around Antarctica by the ACC (Orsi & Wiederwohl, 2009) and along the slope by the Antarctic Slope Current (ASC) (Ainley & Jacobs, 1981; Whitworth et al., 1998). CDW can intrude on the shelf through the Hillary Canyon when the ASC is deviated northward by the Iselin Bank (Conte et al., 2021) or in the Central Basin (Dinniman et al., 2011). Intrusion of CDW can be regulated by the extension of the ice sheet (King et al., 2022). CDW can also intrude on the shelf in the Central Basin (WRS) CDW is important because its mixing with shelf water leads to the formation of MCDW that brings heat, salt and nutrients onto the shelf (Budillon et al., 2011 and references therein). AABW is formed when the outflow of CDW mixes with the HSSW (Budillon et al., 2011; Castagno et al., 2019). The outflow is located in both the WRS (Drygalski and JOIDES Troughs) and the ERS (Glomar Challenger Basin) (Smith et al., 2012 and references therein). On the shelf, a water mass with the same characteristics of AABW is called MSW (Budillon et al., 2011). HSSW is related to sea ice formation and brines are produced (Castagno et al., 2019). HSSW can also flow below the ice shelf, interacting with meltwater, and then it flows along the Glomar Challenger Basin in the form of ISW (Budillon et al., 2011 and references therein). The coldest portion of the bottom shelf layer is the so-called SW (Orsi & Wiederwohl, 2009). A scheme of water masses is presented in figure 3.

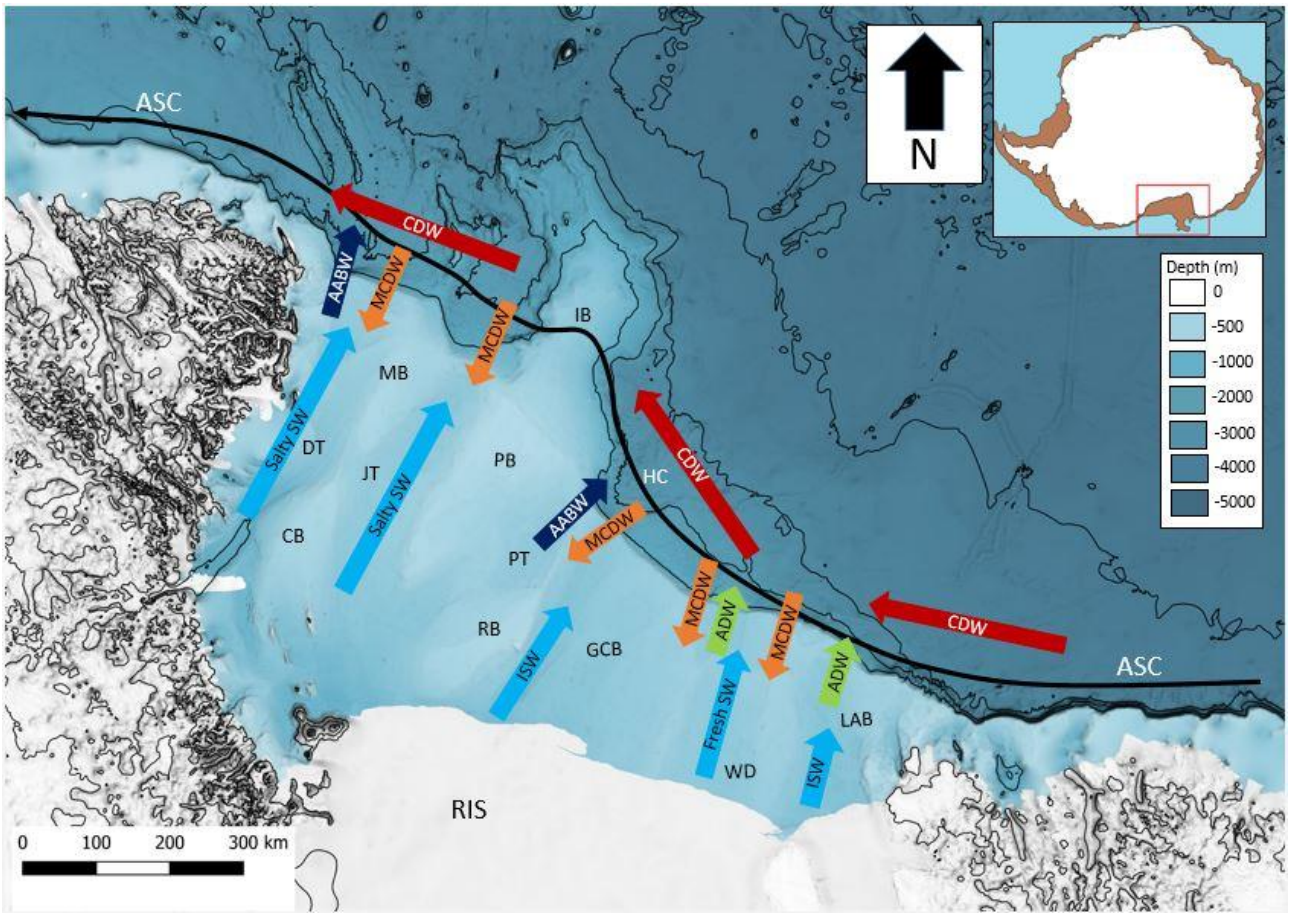

Figure 3 Ross Sea water masses (modified from Smith et al., 2012). Ross Sea bathymetric map modified from Dorschel et al. (2022). AABW = Antarctic Bottom Water, ADW = Antarctic Deep Water, ASC = Antarctic Slope Current, CDW = Circumpolar Deep Water, MCDW = Modified Circumpolar Deep Water, ISW = Ice Shelf Water, SW = Shelf Water; RIS = Ross Ice Shelf; DT = Drygalski trough, JT = JOIDES Trough, PT = Pennell Trough, GCB = Glomar Challenger Basin, WD = Whales Deep, LAB = Little America Basin; CB = Crary Bank, MB = Mawson Bank, PB = Pennell Bank, IB = Iselin Bank, RB = Ross Bank; HC = Hillary Canyon.

3.3 Sea ice

Sea ice is a fundamental component for the southern hemisphere and for the global climate regulating exchange between ocean and atmosphere, influencing albedo and primary productivity (for instance Pezza et al., 2012 and references therein; Tesi et al., 2020). Formation/melting of sea ice and changes in its extent are responsible for changes of both oceanic and atmospheric circulations and sea ice behaviour is regulated by atmospheric forcing (Pezza et al., 2012 and references therein). Several authors studied the relationship between sea ice variation and climate variability (Pezza et al., 2012 and references therein). In particular, Pezza et al. (2012) studied how sea ice is affected by the Southern Annular Mode (SAM), which is a decadal/secular variation of the position of westerly winds that move southward (positive phase) or northward (negative phase)

(e.g. King et al., 2023). Pezza et al. (2012) have highlighted a positive correlation between SAM and sea ice extent in particular when SAM works in synergy with La Niña, the cold phase of El Niño Southern Oscillation (ENSO), which is a variation in the sea surface temperature (SST) in the Central-East equatorial sector of the Pacific Ocean (e.g. Yang et al., 2018). SAM variations can also affect sea ice and ice shelves helping CDW to intrude on the continental shelf (Rignot et al., 2019).

Several biological proxies have been used to study sea ice (Belt, 2018 and references therein). An interesting group of lipids, the Highly Branched Isoprenoids (HBIs), known to be produced by few genres of diatoms (Belt, 2018 and references therein) has drawn the attention. HBIs are characterised by different numbers of carbon (C) atoms and have been retrieved in different environments around the world (Rowland & Robson, 1990). A mono-unsaturated HBI has been named IP_{25} (Ice Proxy with 25 carbon atoms) (Belt et al., 2007) is produced by diatoms that lives within sea ice (Brown et al., 2014) and it is related to past presence of sea ice in the Arctic (Belt & Müller, 2013) has not ever been retrieved in Antarctica. On the contrary, another HBI with 25 atoms of C and characterised by an additional double bond (HBI diene II) has been recorded in Antarctica. This di-unsaturated HBI, identified by Nichols et al. (1988, 1989, 1993), has been proposed as an Antarctic sea ice proxy later on by Massé et al. (2011), and in particular as a proxy for landfast sea ice by Belt et al. (2016). Belt et al. (2016) suggested for him the name $IPSO_{25}$: Ice Proxy for Southern Ocean with 25 C atoms, proposing *Berkeleya adeliensis*, a sympagic diatom (Medlin, 1990) as a possible source. The absence of this biomarker is related to both perennial ice cover and absence of seasonal sea ice. Belt & Müller (2013 and references therein) combining IP_{25} and phytoplankton biomarkers, identified different situations based on the presence/absence of these molecules. Lamping et al. (2021) proposed a similar graphic scheme with the distribution of $IPSO_{25}$ and phytoplankton biomarkers.

Sterols are a class of biomarkers that have frequently been coupled with HBIs (e.g. Vorrath et al., 2020 and references therein; Harning et al., 2023 and references therein). This lipid group is found in all eukaryotic species and reflects open water conditions (Volkman, 1986; Müller et al, 2011; Belt & Müller, 2013). It is difficult to determine the source because they can be produced not only by pelagic phytoplankton but also by other organisms (Harning et al., 2023 and references therein). Brassicasterol, for example, is related with, but not limited to, pelagic phytoplankton (Navarro-Rodriguez et al., 2013) and has been employed by Müller et al. (2011) and Belt and Müller (2013) to distinguish between perennial to seasonal ice cover and ice free conditions (fig. 4).

Three main environments can be distinguished in fig. 4: perennial ice cover, seasonal sea ice and ice free conditions. Perennial ice cover environment is characterised by a reduced sedimentation rate that increases toward the calving line, where sedimentation is related to ice rafting and biogenic productivity, and currents play an important role as well (e.g. Smith et al., 2019). Mezgec et al. (2017) reported two main types of sea ice: pack ice, influenced by winds and currents, and coastal sea ice or land fast ice. Land fast ice can also form attached to ice shelves (Fraser et al., 2012 and references therein). The persistence of fast ice is associated with katabatic wind and the formation of polynyas, ice free areas, where sea ice is produced and drifted away (e.g. Mezgec et al., 2017). The abundance/prolonged presence of sea ice influences exchanges between ocean and atmosphere, which can influence sea ice dynamics (e.g. Pezza et al., 2012).

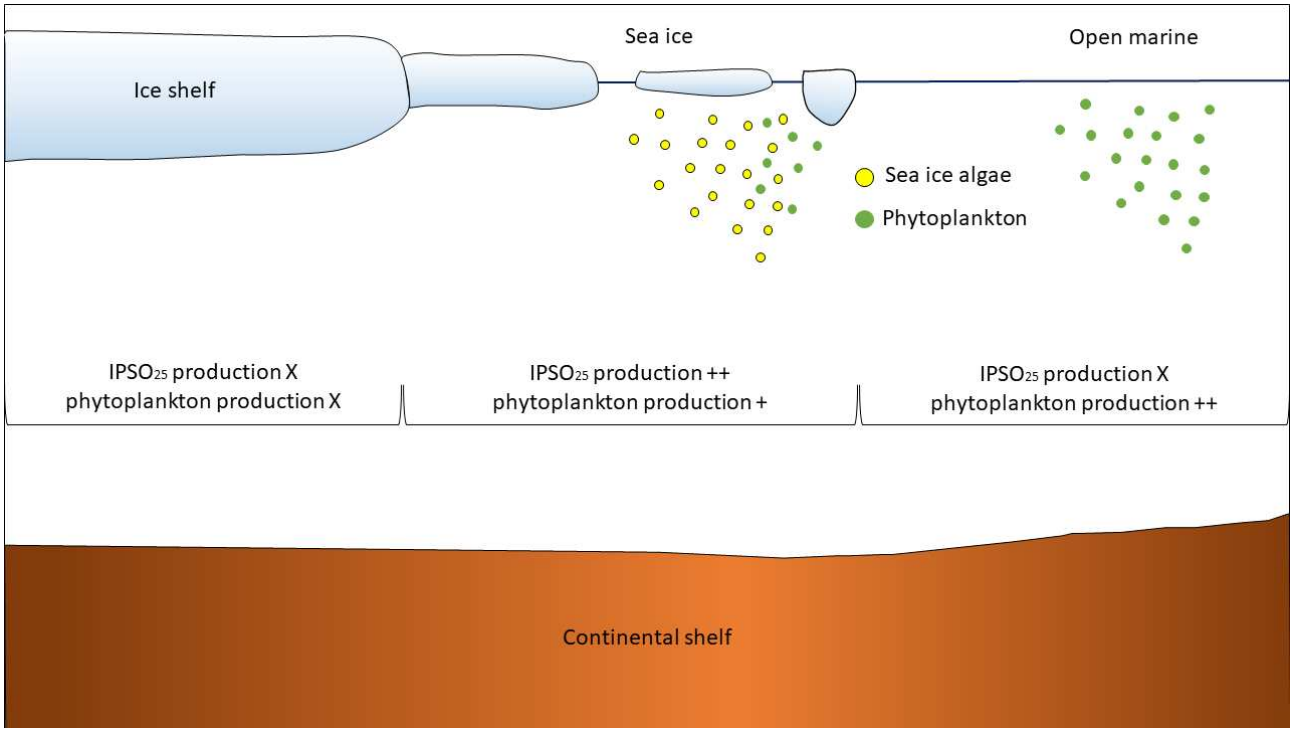

Figure 4 $IPSO_{25}$ and phytoplankton production; modified from Müller et al. (2011) and Lamping et al. (2021). X = no production, + = production, ++ = strong production.

3.4 Sedimentary facies

Several studies have been conducted studying sediments retrieved on the continental margin of Antarctica (e.g. Anderson et al., 1980, 1984; Anderson, 1999; Domack et al., 1999; McGlannan et al., 2017; Prothro et al., 2018, Smith et al., 2019).

Anderson et al. (1980) studied sediments of Antarctica, distinguishing between glacial and glaciomarine sediments. Basal till is an homogeneous over compacted deposit related to grounded ice. Glaciomarine sediments have been distinguished in “compound glaciomarine”, a stratified silt mode sediment with unsorted Ice Rafted Debris (IRDs) and “residual glaciomarine”, a coarser sediment with fine component winnowed by currents. Deposition of both glaciomarine sediments are related to floating ice.

Then, studying Ross Sea sediment, Anderson et al. (1984) identified three types of sediments on the continental shelf. Compound glaciomarine unit (from Anderson et al., 1980), characterised by a muddy matrix with high IRD (>20%) and low biogenic component (<10%). Terrigenous material (silty clay and clayey silt) with low biogenic component (<10%) and low IRDs (<10%). Siliceous mud (10-30% siliceous biogenic component) and ooze (>30% siliceous biogenic component), generally laminated with low IRDs (>10%).

Domack et al. (1999) described four different facies, representing the transition from a subglacial environment to an open marine environment, and reporting the presence of the “granulated facies”, characterised by sediment pellets, deposited in the grounding zone proximal environment.

Anderson (1999) reported two different types of till: an over compacted “lodgement till” and a soft “deformation till”, distinguishing them using the shear strength.

More recently, McGlannan et al. (2017), studying a transect of sediment cores collected in the Whales Deep Basin, identified 4 main units that represent a succession from grounding zone proximal (grey diamicton) to open marine (characterised by an increasing coarse fraction from the middle toward the outer continental shelf), passing through sub ice shelf (proximal, characterised by pellets, and distal, characterised by a sparse coarse fraction) environment and ice shelf break (light grey diamicton collected only in the outer continental shelf).

Prothro et al. (2018), studying sediment cores (physical, geotechnical and biogenic properties) identified six main facies present in the Ross Sea, formed by different processes and/or in different environments, from subglacial to open marine (fig. 5):

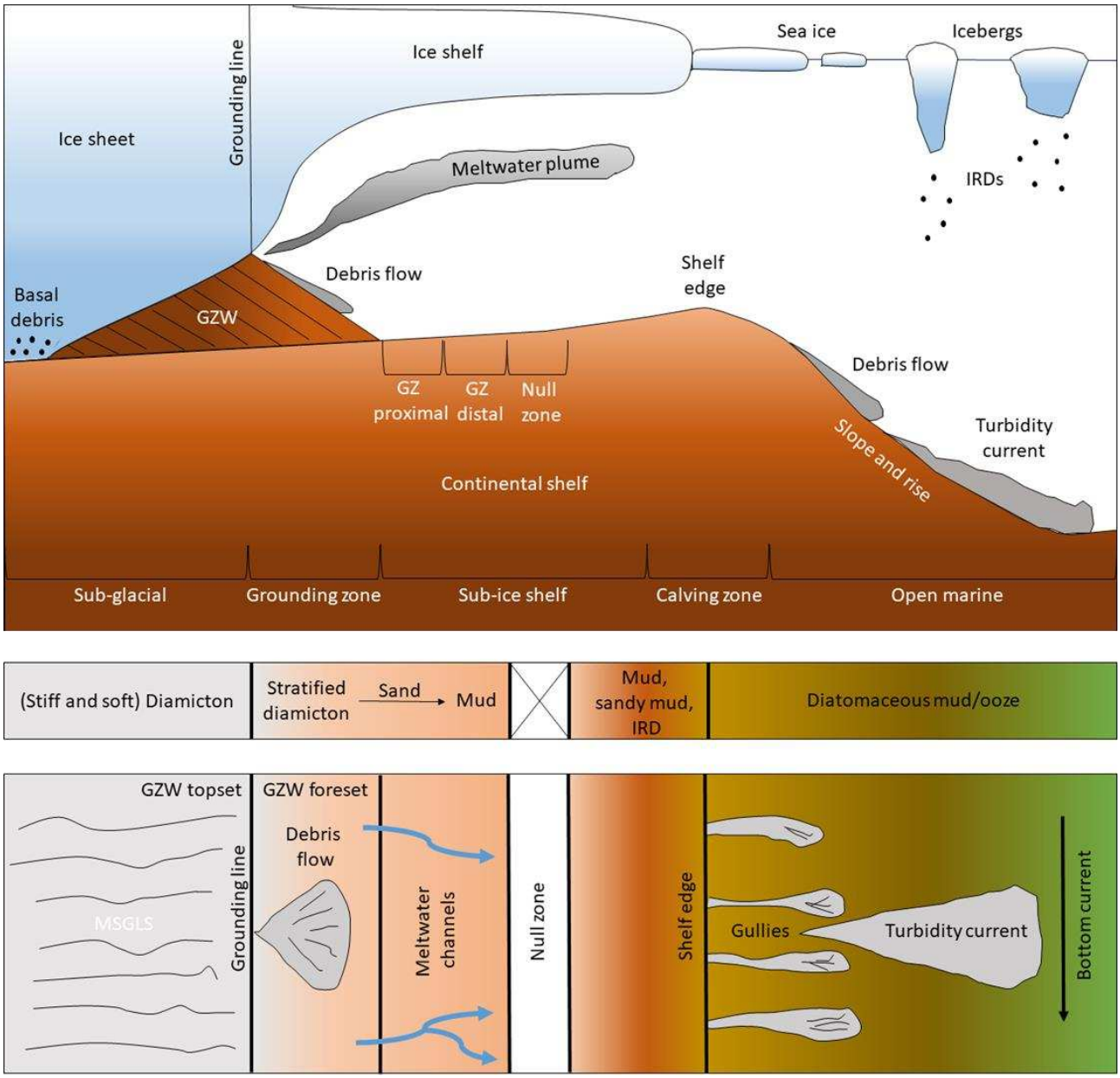

Figure 5 Scheme of glacial environment (modified from Prothro et al. (2018), Smith et al. (2019) and Gales et al., (2021)). GZ = Grounding zone, GZW = Grounding zone wedge, IRD = Ice rafted debris.

Facies 1: Starting from subglacial environment (MSGLs and top of GZWs), till is a homogeneous (considering both texture and mineralogy) deposit with low water content, absent or reworked foraminifera, recovered in subglacial environments.

Facies 2 and 3: Two different deposits have been identified in the grounding zone proximal environment: debris flow deposit and basal debris melt out. The former is a heterogeneous (but downcore homogeneous sometimes) deposit with both reworked and well preserved foraminifera. The latter is characterised by sediment pellets and well preserved calcareous foraminifera.

Facies 4: Meltwater deposits, associated to meltwater channels, are made of well sorted fine sediments. It does not represent a specific environment, the presence of agglutinated and calcareous foraminifera confirm this statement (Prothro et al., 2020).

Facies 5: Open marine facies is ubiquitous on the seafloor and is represented by diatomaceous sandy silt and agglutinated foraminifera are also present.

Facies 6: The continental shelf edge and top of the bank are characterised by coarse reworked sediments or "residual glaciomarine" sediments.

Smith et al. (2019) recently presented an idealised sedimentary sequence related to a retreating ice shelf, from the subglacial to the open marine conditions, where several proxies are used to differentiate these paleoenvironments (fig. 5). Among them, the biotic indexes like the diatom concentration, the foraminiferal assemblages and the TOC content are very useful to recognize the depositional sequences.

Despite the fact that biogenic calcareous sediments are relatively rare in the Antarctic shelves, sediments with carbonate-rich intervals have been recovered in the north-western part of the Ross Sea continental shelf. (e.g. Frank et al., 2014; Melis & Salvi, 2020 and references therein). These biogenic carbonates are mainly related to the maximum expansion of the ice shelves in the Ross Sea, from MIS3 up to the LGM, when the glacial expansion limited the siliciclastic influx to the outer shelf. These intervals have been mainly recovered in the WRS, where the ice sheet did not reach the western continental shelf edge during the LGM.

4. Study area

The study area of this PhD project comprises the Glomar Challenger Basin, from the Margin of the RIS to the continental shelf break, and the slope and rise area East of the Hillary Canyon at the mouth of the Glomar Challenger Basin (fig. 2).

4.1 Glomar Challenger Basin

The Glomar Challenger Basin is one of the seven bathymetric troughs/basins of the Ross Sea. It is located between the Ross Bank and the Whales Deep Basin and, at the head of the Hillary Canyon,

it joins the Pennell Trough. Seafloor is characterised by several features. They have been previously described (Halberstadt et al., 2016 and reference therein) following the scheme proposed by Benn & Evans (2010): subglacial, ice-marginal and proglacial features. Following this order, several groups of linear features with different orientation have been identified along the trough. In the inner part of the shelf, drumlinoids have been identified where the crystalline bedrock is close to the surface. Several GZWs are also present. Mosola & Anderson (2006) reported the presence of GZWs on both sides of the Glomar Challenger Basin. Then, Bart & Cone (2012) described them as large GZWs that occupy the full width of the trough. Two are located at the shelf edge (Halberstadt et al., 2016) and two composite GZWs are present in the inner-middle shelf (Bart & Cone, 2012). More recently, Danielson & Bart (2023) mapped GZWs in the Ross Sea, identifying 5 GZWs in the Glomar Challenger Basin, 2 large features in the outer and middle shelf and 3 small ones in the inner shelf (see table 1 from Danielson & Bart, 2023) Gullies, which are proglacial features are present at the shelf edge (Anderson, 1999; Mosola & Anderson, 2006; Gales et al., 2021).

Sediment cores collected in the ERS (Licht & Andrews, 2002; Mosola & Anderson, 2006; Bart & Cone, 2012; McGlannan et al., 2017; Prothro et al., 2018) mainly recovered diamicton and thin intervals of glaciomarine sediments at the top of the cores. WRS sediment cores are characterised by the presence of a thick interval of diatomaceous mud at the top of the core, while in ERS it usually is very thin or absent (Prothro et al., 2018). This difference may have been caused by the sea-ice cover in the ERS and the consecutive reduced productivity (Anderson et al., 2019 and reference therein).

The glaciological history of this part of the Ross Sea, in particular since the LGM, is still debated. Several studies have been conducted. The scientific community agree regarding the position of the ice sheet at the shelf edge during the last glacial expansion (Shipp et al., 1999; Mosola & Anderson, 2006; Anderson et al., 2014, 2019; Halberstadt et al., 2016; Lowry et al., 2020). Several authors proposed an early retreat of the ice sheet (Licht & Andrews, 2002; Mosola & Anderson, 2006; Bart & Cone, 2012; Anderson et al., 2014; Halberstadt et al. 2016). Halberstadt et al. (2016) suggested that the deglaciation started with the formation of an embayment in the Whales Deep. Studying geomorphological features, Halberstadt et al. (2016) have highlighted that linear features in the ERS are characterised by different orientations, due to different flow directions. From these results, Halberstadt et al. (2016) proposed two different retreat models to explain these differences. The “dynamic flow-switching model” is based on a change from westward to eastward flow direction, followed by a trough-parallel retreat. The “embayment scenario” is based on an initial trough-

parallel retreat, during the formation of an embayment in the Whales Deep, followed by a cross ridges retreat from the Glomar Challenger basin and the Little America Basin toward the Whales Deep. According to Halbestadt et al (2016) the second scenario agrees with the early retreat in the ERS, but timing of events is still debated. Licht & Andrews (2002), considering three carbonate radiocarbon ages, suggested that the grounded ice reached the continental shelf edge after 13,8 ^{14}C kyr (depth 63-66 cm), but the other carbonate ages are not in stratigraphic order: 16,6 ^{14}C kyr at 20-22 cm and 20,8 ^{14}C kyr at 2-4 cm. According to Licht & Andrews (2002), this is due to reworking by the advancing ice sheet, but Mosola & Anderson (2006) proposed a different scenario with reworking operated by icebergs, suggesting an early retreat from the ERS, even considering the presence of reworked old carbon. Bart & Cone (2012), using carbonate ages obtained from foraminifera recovered from inner-middle shelf GZWs and even considering the possible presence of reworked specimens in their samples, proposed an early retreating ice sheet located in the inner-middle shelf around 27,5 ^{14}C kyr BP. Anderson et al. (2014) resumed radiocarbon ages obtained in the Ross Sea, proposing a reconstruction of the late Quaternary history based on both marine and terrestrial information. Majority of ages have been obtained using Acid Insoluble Organic (AIO) fraction, and considering the scarcity of well preserved carbonate material and different reliability of ages due to the possibility of reworked material included in the analysed samples, reconstruct timing of events is tough, in particular in the ERS (Anderson et al., 2014 and references therein). Then, Bart et al. (2018), using foraminifera recovered in the Whales Deep, suggested that the retreat of the grounding line started around 14,7 cal kyr BP. Considering this age for the retreat from the WD and the retreat model proposed by Halberstadt et al. (2016) and excluding pre-LGM retreat suggested by Bart & Cone (2012), Danielson & Bart (2023) considered 8,7 cal kyr BP (from deglacial sediments; Bart & Cone, 2012) as the age of the beginning of retreat in the GCB.

4.2 Slope and rise area

The slope and rise area of the ERS is characterised by the presence of a trough mouth fan, named Eastern Ross Sea Fan (ERSF), which has been formed at the mouth of the Glomar Challenger Basin and the Whales Deep (Alonso et al., 1992). It has been formed during several glacial cycles when the ice sheet reached the shelf break (King et al., 2022 and references therein). The shelf break and the upper slope are characterised by the presence of gullies at the mouth of the Glomar Challenger

Basin where the grounded ice was located during its maximum expansion (Anderson, 1999; Mosola & Anderson, 2006; Gales et al., 2021). This network of incisions has been recently studied by Gales et al. (2021). They highlight the control exercised by glacial advance. They have identified several straight narrow incisions that become wider and longer toward East where the slope is gentler and their number decreases. They also highlighted the presence of paleo-gullies, which indicate that these processes occurred for prolonged timeframes. According to Gales et al. (2021) and references therein, changes in the slope gradient and sediment transported by meltwater are responsible for changes in gullies morphologies. Moving westward, at the mouth of the Pennell Trough, gullies and paleo-gullies are not present (Gales et al., 2021).

The mouth of the conjunction between the Glomar Challenger Basin and the Pennell Trough is characterised by a deep narrow incision (length 180km): the Hillary Canyon. This feature is very important because it acts as a sediment drainage (Gales et al. (2021) and it also allows the inflow of CDW and the outflow of dense shelf water Conte et al. (2021).

Sediments recovered along the slope can be divided in two: glaciomarine sediments and gravity flow deposits (Anderson, 1999). More recently studying drilling cores from IODP Expedition 374 (McKay et al., 2019), King et al. (2022) described different facies related to bottom currents, turbidity currents, IRD deposition and gravity flows; they have reconstructed the evolution of the slope, identifying a stronger and more frequent glacial influence on this area from late to early Pleistocene. Then, Ha et al. (2022) studying gravity cores collected in the slope rise area east of Hillary Canyon identified three units related to glacial, deglacial and interglacial phases.

5. The dataset

The dataset used for this work is composed of geophysical (sub bottom profiles, a sparker profile and single channel seismic lines) and sedimentological data (gravity cores and box cores).

5.1 Geophysical dataset

A total of 11 sub bottom profiles (tab. 1) were acquired during the XIV PNRA expedition (project "2a.1.4 – Recent climatic cycles in marine sediments of the Ross Sea") in the Glomar Challenger area. During the same expedition, a sparker profile was also acquired in the outermost portion of the continental shelf.

SBP SPK	**Latitude**	**Longitude**	**Water depth (m)**	**Latitude**	**Longitude**	**Water depth (m)**
	Profile starting point			**Profile ending point**		
SBP 11	77°30.34' S	177°51.97' W	715	77°37.60' S	178°01.02' E	765
SBP 12	77°36.98' S	178°01.99' W	763	77°13.01' S	179°44.84' E	751
SBP 13	77°12.88' S	179°44.42' E	760	76°54.98' S	179°25.97' W	699
SBP 14	76°52.93' S	179°25.26' E	698	76°25.33' S	178°45.42' W	669
SBP 15	76°23.85' S	178°49.26' W	653	76°02.92' S	178°55.76' W	650
SBP 16	76°02.20' S	177°54.79' W	654	75°54.38' S	177°45.37' W	640
SBP 17	75°51.17' S	177°40.03' W	637	75°39.98' S	177°09.94' W	608
SBP 18	75°41.38' S	177°12.65' W	617	75°53.33' S	177°45.98' W	639
SBP 19	75°53.82' S	177°40.49' W	644	75°55.66' S	177°46.69' W	643
SBP 20	75°55.13' S	177°47.61' W	639	75°404.28'S	177°10.67' W	610

SBP 21	75°40.25' S	177°10.62' W	612	74°41.18' S	173°23.92' W	2353
SPK 3	75°40.25' S	177°10.62' W	612	75°05.04' S	176°00.09' W	1540

Table 1 Starting and ending profile coordinates of the sub bottom profiles (SBP) and the sparker profile.

During the XXXII PNRA expedition (2016/2017), a series of single channel seismic lines (SCSL) were acquired in the frame of the project Eurofleets ANTSSS (Antarctic Ice Sheet Stability from continental Slope process investigation). These lines are available in the Antarctic Seismic Data Library System (SDLS; https://sdls.ogs.trieste.it/cache/index.jsp).

SCSL	**Latitude**	**Longitude**	**Latitude**	**Longitude**
	starting point		**ending point**	
IT17RS304	74°2809,00 S	172°4334,15 W	74°3611,22 S	173°0845,14 W
IT17RS304A	74°3437,78 S	173°0520,17 W	75°0746,47 S	173°3321,81 W
IT17RS306	75°0720,07 S	173°3157,48 W	75°1858,89 S	175°5537,99 W

Table 2 Ending and starting point coordinates of the single channel seismic lines (SCSL) acquired on the continental slope and rise.

5.2 Sediment dataset

The dataset (tab. 3) considered consists of 10 gravity cores and 3 box cores collected in the Glomar Challenger Basin and the slope-rise area near the Hillary Canyon during three PNRA (Progetto Nazionale di Ricerca in Antartide) expeditions (fig. 6). Six gravity cores and 3 box cores were opened and used for both direct and indirect analyses, while four gravity cores remain closed and were only utilised for indirect analysis. In particular, during the XI expedition (1995-1996), conducted in the frame of the project "2a.7 – Clastic sedimentation (II part)" and the XIV expedition (1998-1999), conducted in the frame of the project "2a.1.4 – Recent climatic cycles in marine sediments of the Ross Sea", nine gravity cores on the continental shelf of the Ross Sea, in the Glomar Challenger Basin have been collected. Five of these gravity cores, ANTA96-c04, ANTA99-GC12, ANTA99-GC14, ANTA99-GC17 and ANTA99-GC18, were studied in detail for this PhD project. Other four gravity

cores, ANTA99-GC13, ANTA99-GC15, ANTA99-GC16 and ANTA99-GC19, remain closed. The core ANTA99-c20 was collected on the slope and rise area. Moreover, three box cores (RS14-BC1, RS14-BC2 and RS14-BC3) collected on the continental slope and rise area, east to the Hillary canyon, in the frame of the project "2013/AN2.01 - ROSSLOPE II (Past and present sedimentary dynamic in the Ross Sea: a multidisciplinary approach to study the continental slope) during the XXIX (2013-2014) PNRA expedition were considered.

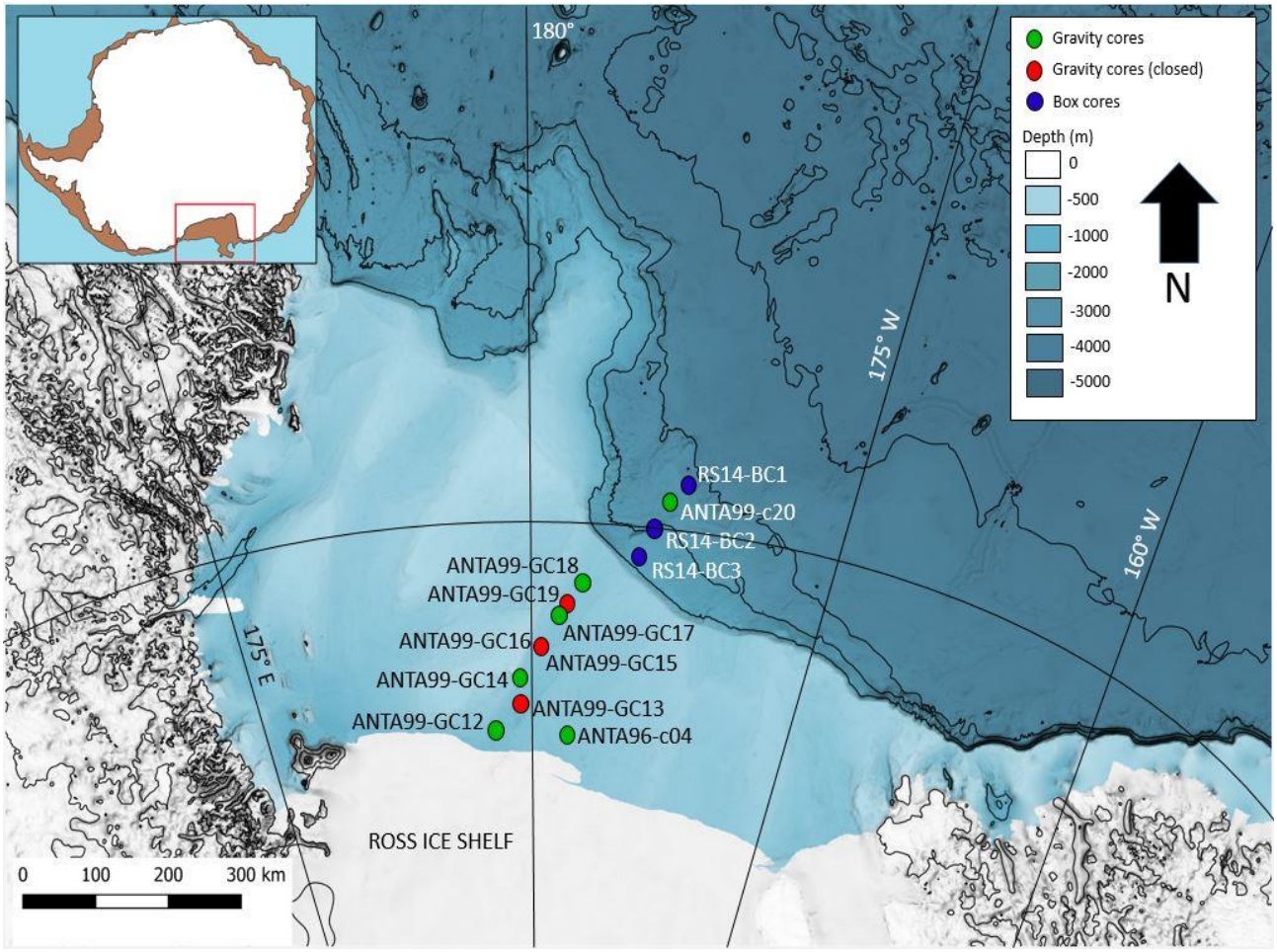

Figure 6 Location of gravity cores and box cores used for this thesis. Bathymetric map modified from Dorschel et al. (2022).

Cores (ANTA) Box cores (RS)	Latitude	Longitude	Water depth (m)	Length (cm)
ANTA96-c04	77°37.94' S	177°25.06' W	657	197
ANTA99-GC12	77°33.70' S	178°01.02' E	765	290
ANTA99-GC13	77°13.01' S	179°44.84' E	751	329

ANTA99-GC14	76°54.98’ S	179°25.97’ E	669	325
ANTA99-GC15	76°25.34’ S	178°45.03’ W	669	185
ANTA99-GC16	76°24.68’ S	178°47.62’ W	659	84
ANTA99-GC17	76°03.01’ S	177°55.41’ W	650	342
ANTA99-GC18	75°39.98’ S	177°09.94’ W	608	169
ANTA99-GC19	75°55.67’ S	177°46.70’ W	643	117
RS14-BC3	75°20.41’ S	174°36.43’ W	1214	39
RS14-BC2	75°00.58’ S	173°55.21’ W	1742	35
ANTA99-c20	74°41.18’ S	173°23.92’ W	2353	202
RS14-BC1	74°30.54’ S	172°53.04’ W	2382	42

Table 3 Location of the sediment cores, water depth and length for each core is reported.

6. Methods

Geophysical data was used in order to provide a geomorphological overview and improve the interpretation of the cores, aiming to correlate limits of sedimentological facies with seismic interfaces and to determine sedimentological dynamics.

Sub bottom profiles acquired using a sub bottom profiler 3,5 kHz, and the sparker 500J profile acquired in the Glomar Challenger were scanned and digitised at the University of Genova.

The SCSL profiles in the slope and rise area were acquired by two 210 cu.inGI guns and a 10 m solid state streamer with 10 channels, during the XXXII expedition. See Gales et al. (2021) for details.

Regarding the analyses on **sedimentary material**, a combination of sedimentological, chemical, geochemical and micropaleontological proxies (tab. 4) was measured, aiming to reconstruct the sedimentary dynamics of the Glomar Challenger Basin and correspondent slope and rise area during late Quaternary.

The cores ANTA96-c04, ANTA99-GC12, GC14 and GC17 and all the box cores RS14 were opened, described, partly sampled and analysed in the frame of previous unpublished theses (Calligaris, 2003; Torricella, 2016; Valle, 2016), while some analyses were carried out as part of the PNRA ROSSLOPE project on the ANTA99-c20 core.

The previous analyses concern the physical aspect (radiographies, magnetic susceptibility, water content and some grain size analysis) and some geochemical aspects (organic matter analysis). Radiocarbon ages were obtained using 4 samples from the core ANTA99-GC12 (tab. 5) and a total of 13 samples from the three RS14 box cores (tab. 5) and core ANTA99-c20 (tab. 5). Some RS14 box core data were published in Ha et al. (2022). Some grain size data of RS14-BC3 were considered in Gales et al. (2021).

This series of analyses was used to plan the new analyses carried out as part of this work. Several new analyses were conducted by introducing new proxies and using new instruments (e.g. Malvern Mastersizer Hydro2000S). In addition, study levels were added in all cores to increase the stratigraphic resolution. All results were then unified and used for the overall interpretation of the data.

The table 4 summarises the analyses performed on the gravity cores and box cores and available data considered for this thesis.

Below are reported details about analyses performed on sediment dataset. Tables with results of these analyses are reported in the supplementary.

Name	MS	Rx	Opening/ description	W%	CS	Grain size	Clasts counting	XRF	Organic matter	Biomarkers	Forams	Sand	14C (AIOM)	References
c04	x	x	x	x	x	x	x	x	x	x	x	x		Calligaris, 2003
GC12	x	x	x	x	x	x	x	x	x	x	x	x	x	Calligaris, 2003
GC13	x	x					x							
GC14	x	x	x	x	x	x	x	x	x	x	x	x		Calligaris, 2003
GC15	x	x					x							
GC16	x													
GC17	x	x	x	x	x	x	x	x	x	x	x	x		Calligaris, 2003
GC18	x	x	x	x	x	x	x	x	x	x	x	x		
GC19	x	x					x							
BC3	x	x	x	x		x	x	x	x	x			x	Valle, 2016; Ha et al., 2022
BC2	x	x	x	x		x	x	x	x	x			x	Valle, 2016; Ha et al., 2022
c20	x	x	x	x		x	x	x	x				x	
BC1	x	x	x	x		x	x	x	x	x			x	Torricella, 2016; Ha et al., 2022

Table 4 Analyses performed on the cores. Green represents analyses considered and/or performed during previous thesis/works; Yellow is for analyses performed during this thesis. Blue represents analyses performed both during this thesis and previous works (increasing of the stratigraphic resolution); Grey represents analysis not performed on these cores.

6.1 Opening, description and sampling strategy

Gravity cores and box cores previously studied (Calligaris, 2003; Torricella, 2016; Valle, 2016) were redescribed and sampled, in order to increase the stratigraphic resolution.

In the framework of this PhD thesis, core ANTA99-GC18 was opened, halved and described at the sedimentological laboratory of the Department of Mathematics, Informatics and Geosciences (Trieste). The Munsell colour chart was used to describe the colour of sediments. One half has been used to collect samples for analysis, while the other one has been stored in the MNA-Trieste section Sorting Center and used only for indirect analysis (elemental analysis). The previously collected samples were implemented in such a way as to have a sampling step every centimetre from the top of each core to the contact between muddy sediments with sparse clasts and more dense and compacted sediments. The interval of more dense sediments in the ANTA99-GC18 gravity core was sampled at an interval of approximately 10 centimetres, while in the other gravity cores was sampled with intervals of 20-50 centimetres.

All cores, except for ANTA99-GC16, were x-rayed. Radiographic images were described and clasts >2 mm were counted every centimetre on the radiographic images using the method proposed by Grobe (1987). Then, data was elaborated using the mobile average (interval of 5 cm).

6.2 Physical analyses

6.2.1 Magnetic susceptibility (MS)

Magnetic susceptibility of the cores was measured aboard the ship using a Bartington MS2C. MS of the box cores was measured at the CNR of Bologna, using the same instrument. MS of both cores and box cores was measured every 2 cm. Results are expressed in SI (International System). This parameter depends on the presence of coarse material and ferromagnetic minerals, normally present in terrigenous sediments (Stoner et al., 1996).

Average values were calculated after removing values at the top and the bottom of each core section because measurement is affected by air. Peaks related to the presence of clasts were removed before calculating the average value as well.

6.2.2 Compression strength (CS)

Compression strength was measured using a pocket penetrometer, equipped with a tip, with a diameter of 2 cm. Smaller tips have been used for some intervals. CS of the cores collected in the Glomar Challenger Basin was measured with a variable interval of 10 cm to 30 cm. Results are expressed in Kg/cm^2. This measure is used to determine the penetration resistance of the sediment. CS for cores c04, GC12, GC14 and GC17 was previously measured by Calligaris (2003).

6.2.3 Water content (W%)

Previous analyses of water content were conducted around every 10 cm for the gravity cores (Calligaris, 2003) and every centimetres for the box cores (Torricella, 2016; Valle, 2016). Water content data of core c20 come from Colizza E. (personal communication).

Core ANTA99-GC18 was sampled every 5 cm from the top to the limit between muddy sediments with sparse clasts sediments and more dense and compacted sediments. From this boundary to the bottom of the core, samples were collected around every 10 cm. The samples were weighed both wet and after drying in an oven at 50°C for 24 hours to determine the % water content according to the following formula

$$w\% = \frac{\left(mass\ of\ humid\ sediments\ (g)\ -\ mass\ of\ dry\ sediments\ (g)\right) * 100}{mass\ of\ humid\ sediments\ (g)}$$

6.2.4 Grain size analysis

Subsamples of shelf cores were collected every 5 cm from the top of the core to the interface between muddy sediments and more homogeneous and dense ones, and every 20-30 cm in the lower part of the cores. Grain size analyses were performed every cm on the box cores and every cm on core 20c for the first 10 cm and then every 8 cm in the upper 55 cm. The preparation of the samples followed the protocol of the sedimentological laboratory of the MIGe - Department of Mathematics, Informatics and Geosciences (Trieste). Sediments were prepared, treating them with 20 ml of distilled water and 20 ml of hydrogen peroxide (H_2O_2). Then, an electric water bath was used to heat the samples at 50°C for 24 hours. After that, each sample was wet sieved to separate the fraction >1 mm.

The analyses of the fraction <1 mm was carried out using a "Malvern Mastersizer Hydro2000S" at the sedimentological laboratory of the Department of Mathematics, Informatics and Geosciences (MIGe, University of Trieste). The fraction >1 mm was dry sieved to obtain two subfractions: 1-2 mm and >2 mm. Grains of both fractions were counted and both groups was separately weighted.

To determine content of sand, silt and clay, the classification by Friedman & Sanders (1978) was used. Folk & Ward (1957) was used for statistical parameters, such as mean grain size (Mz), sorting (Sort) and skewness (Sk). The median (Md) is also indicated.

6.3 Chemical and geochemical analyses

6.3.1 X-Ray Fluorescence (XRF) core scanner

XRF core scanner is a non-invasive methodology used to study major elements composition of sediments. Variations in element concentration and elemental ratios can be used as indicators of different paleoenvironments, paleoceanographic settings and paleoproductivity conditions (e.g. Jimenez-Espejo et al., 2020 and references therein; López-Quirós et al., 2021 and references therein). The analysis was performed with a XRF Avaatech scanner at the CNR-ISMAR (Bologna) and a generator setting of 10/30/50 kV allowing the measurements of 31 elements. 1-centimetre interval resolution was used, except where cores presented fractures or large surficial clasts. Elements concentration was measured in counts per second (cps). XRF analysis performed on box core BC1 and core c20 was conducted at the Alfred Wegener Institute (AWI; Germany) with the same instrument.

Cores on the shelf and cores on the slope and rise area were studied as two different datasets. Considering the most used elements in Antarctica, such as aluminium (Al), titanium (Ti), silica (Si), potassium (K), iron (Fe), barium (Ba), bromine (Br), calcium (Ca), strontium (Sr), zirconium (Zr) and rubidium (Rb) (e.g. Presti et al., 2011; Jimenez-Espejo et al., 2020; López-Quirós et al., 2021; Hillenbrand et al., 2021), a Pearson's correlation was used among these elements, performed with PAST 4.12b (Hammer et al., 2001). Correlations were performed considering each core/box core separately. Then, a new Pearson's correlation was performed considering all the continental shelf gravity cores together. Manganese (Mn) was not used for correlation because of the presence of negative values, in the lower part of the cores in particular. Positive values in the upper part of the

cores were considered, because it is used as a redox proxy even though its use is limited by the high reactivity of Mn (Canfield et al., 1993). Several authors (e.g. Jaccard et al., 2016; Wu et al., 2018; Jimenez-Espejo et al., 2020; López-Quirós et al., 2021) used Mn as an indicator of bottom water oxygenation. Al, Si, K, Ti and Fe are detrital proxies (e.g. Rodrigo-Gámiz et al., 2014; Rothwell & Croudace, 2015). Biogenic Ba is known to be a paleoproductivity proxy (Hillenbrand et al., 2021 and references therein), but Ba can also have a detrital origin (Hillenbrand et al., 2021). Br has been used as an indicator of organic matter and as a paleoproductivity proxy (e.g. Ziegler et al., 2008; Evangelinos et al., 2020; López-Quirós et al., 2021; Hillenbrand et al., 2021). Ca and Sr are related to both biogenic and detritic carbonates. Zr and Rb provide grain size information (Dypvik & Harris, 2001). Zr is related to coarse grain size (Pettijohn, 1941), while Rb is related to K-rich minerals of the fine fraction (Dypvik & Harris, 2001). Zr normalised to Rb (Zr/Rb) is a proxy for grain size variation along the cores. Other elements were normalised to Ti. Ti has been previously used for normalisation because of its nature of proxy for lithogenic fraction (e.g. Presti et al., 2011 and references therein; Jimenez-Espejo et al., 2020 and references therein). Variation of the provenance of terrigenous material produces variation of K normalised to Ti reflecting glacial/interglacial oscillations (e.g. Bertram et al., 2018; López-Quirós et al., 2021).

6.3.2 Organic matter

Total Organic Carbon (TOC) and Total Nitrogen (TN) have been measured for both the cores and the box cores. Calcium carbonate ($CaCO_3$) and Biogenic silica (BioSi) have been also measured in the sediments collected on the slope and rise area. All these analyses were performed at the CNR of Bologna. Additional samples were measured for TOC at the MIGe (UniTS) for the radiocarbon analyses. In order to eliminate the inorganic carbon, ~30-35mg of dry sediments was put in silver capsules and acidified with HCl 1,5 N. The C/N ratio has been calculated as:

$$C/N = \frac{(TOC/Molar\ mass\ of\ C)}{(TN/Molar\ mass\ of\ N)}$$

Organic matter is used as a paleo-productivity index, while the ratio C/N is used to identify between marine and terrestrial origin of organic matter (Stein, 1991).

6.3.3 Biomarkers

Samples preparation and analyses were carried out at the CNR-ISP (Bologna), following their protocol based on methodology proposed by Belt et al. (2012, 2019). Eight samples of gravity core ANTA99-GC18 have been first used as test samples to verify the presence of a sufficient concentration of HBIs and sterols. Then, other samples from the upper part of the shelf cores and box cores were prepared using an interval of 5 cm. Biomarkers were analysed every centimetre in the upper part of the core ANTA99-GC18.

The preparation for biomarkers analysis requires several passages in order to extract HBIs and sterols. Because of the sparse organic matter in our samples,~2 gr of dry sediments was used. During the first step, 50µL of two internal standard (IS) solutions were added to quantify both HBIs (polar fraction) and sterols (non-polar fraction). For HBIs, 9-octylheptadec-8-ene (9-OHD) was used. 5α-androstan-3β-ol was used for sterols. Methanolic potassium hydroxide (KOH) (5%, MeOH/H2O 9:1) was added for lipoid saponification. Unsaponifiable lipids, like HBIs and sterols, were extracted using hexane. Next, the vials were manually agitated and oven heated at 70 °C for 1 hour. Then, biomarkers were extracted using hexane and centrifuging the vials. Hexane was recovered using Pasteur pipettes and placed in vials on a heating plate at 50°C under a gentle stream of N_2. Dry extracts were re-dissolved in hexane (0,5 mL). The solution was transferred into chromatographic columns and eluted with hexane in order to recover the polar fraction and then with DCM:MET (Methacryloyloxy ethyl trimellitic acid) 1:1 for elution for the non-polar fraction. Solvents were removed again (heating plate at 50°C under a gentle stream of N_2). After that, 500µL of hexane for polar fraction samples and 500µL of DCM for non-polar fraction samples were added in each vial. In order to obtain more concentrated samples for analysis of HBIs, hexane was removed one last time, before adding 30 µl of hexane.

Samples were analysed using a system formed by a gas chromatograph Agilent 7820A GC System and a mass spectrometer Agilent 5977B MSD. This system allows to separate each phase of the samples analysing them in a specific moment in time. Then, knowing their masses (e.g. Belt et al., 2012), HBIs and sterols were detected and data was manually checked to be sure that each peak was correctly identified, and to remove misinterpreted peaks, obtaining qualitative data (peak areas (Pa)), converted into quantitative data using the following formulas (e.g. Belt et al., 2012; Smik, 2016):

$$HBIs\ (\mu g/g\ of\ dry\ sediment) = \frac{((Pa\ of\ HBIs/Pa\ of\ IS) * Response\ Factor)}{mass\ of\ dry\ sediment\ (g)} * mass\ of\ IS\ (\mu g)$$

$$Sterols\ (\mu g/g\ of\ \ dry\ sediment) = \frac{((Pa\ of\ sterols/Pa\ of\ IS) * Response\ Factor)}{mass\ of\ dry\ sediment\ (g)} * mass\ of\ IS\ (\mu g)$$

Biomarkers, in particular $IPSO_{25}$ and sterols (22-dehydrocholesterol, cholesterol and brassicasterol), were studied to identify changes in the ice cover.

6.4 Microscopy analyses

6.4.1 Sand fraction

Sand fraction of the shelf cores was analysed under a stereomicroscope in order to describe the presence of inorganic and biogenic content (foraminifera, radiolarian, sponge spicule and diatoms). Samples were prepared via wet sieving (>63 µm). Samples for studying foraminifera were collected with an interval of 10 centimetres in the upper part of the cores and around 20-30 cm in the lower part of the cores.

6.4.2 Foraminifera

Foraminifera, where present in the sample of cores collected on the shelf, were distinguished between planktonic and benthic, calcareous and agglutinated, counted and identified at species (or genus) level. Violanti (1996), Igarashi et al. (2001), Murray & Pudsey (2004), Majewski (2005, 2013) and Majewski et al. (2018) were used to recognise the species. The % of fragmentation was calculated as the number of damaged tests in respect to the total number (pristine and damaged tests).

6.5 Chronology

The chronology is based on four samples from gravity core ANTA99-GC12 (tab. 5), 10 samples from RS14 box cores (tab. 5), and 3 samples from the core ANTA99-c20 (tab. 5). All the radiocarbon ages were obtained by Accelerator Mass Spectrometry (AMS) on the Acid Insoluble Organic Matter (AIOM). Eleven (RS14 box cores and one of core c20) radiocarbon ages were obtained using the facilities of the Poznan Radiocarbon Laboratory, Adam Mickiewicz University of Poznan (Poland), two radiocarbon ages of the core c20 were obtained at the NOSAMS of the Woods Hole Oceanographic institution (Massachusetts, USA) and four (GC12) at the Geochron Laboratory (Massachusetts, USA).

Considering that the radiocarbon chronologies using the AIOM fraction from bulk sediments are often compromised by contamination from reworked ancient organic carbon derived from glacial erosion and/or from the reworking of unconsolidated sediments (e.g. Andrews et al., 1999; Melis et al., 2021), the AIOM dates were corrected by the AIOM age of the well-preserved box-core or core-top sediments.

The down-core AIOM dates of the three box-cores located along the slope, were corrected by the AIOM age of their preserved box-core-top, while the c20 core was corrected using the AIOM age of the core-top sediments of the BC1 box-core. Having no other data available for the inner part of the GCB, to correct the dates of the GC12 core, the AIOM top age of two trigger cores located a short distance apart (respectively NBP 95-1 TC16 and TC18, see Domack et al., 1999) were used.

The age difference between the AIOM ^{14}C age of the box-core and core-top sediment, along with the marine reservoir effect (MRE), were assumed as representatives of the local contamination with older organic matter in this area, and hereafter it is referred to as “local contamination offset” (LCO; see the discussion in Hillenbrand et al., 2009). Before calibrating the ^{14}C dates, the LCO obtained for this area was subtracted from the AIOM ^{14}C down-core ages (LCO-corrected ages), assuming that LCO did not change over the late Quaternary (see Hall et al., 2010). An MRE of 1,1 ± 0,12 kyr ^{14}C suggested by Hall et al. (2010) for the Ross Sea area carbonate samples was used.

The calibration of the radiocarbon dates was based on the Marine20 calibration curve by means of CALIB 8.2 software at 95% confidence ranges (Stuiver & Reimer, 1993). A regional marine offset (delta R) from the global MRE of 0,609 ± 0,137 kyr, for the Holocene dates and 1,069 ± 0,137 kyr for the pre-Holocene dates was used in agreement with Heaton et al. (2023).

Uncorrected and calibrated ^{14}C data are summarised in Tables 5. All the ages reported in the following text represent the calibrated ages unless otherwise specified.

Radiocarbon ages obtained at the top of the three RS14 box cores were used by Ha et al. (2022) in order to calibrate radiocarbon ages of their cores. In the frame of this work, those ages were re-calibrated.

Name	Depth (cm)	Carbon source	Conventional age (yr BP)	Error (yr)	LCO	LCO corrected age (yr BP)	Median probability Cal age (yr BP)	Lower cal range (yr BP)	Upper cal range (yr BP)	Laboratory code
ANTA99-GC12	0-1	AIOM	6560	60	3325	3235	2141	1732	2553	GX-30570
ANTA99-GC12	35-36	AIOM	27400	140	3325	24075	26371	25916	26884	GX-30571
ANTA99-GC12	202-203	AIOM	35950	210	3325	32625	35148	34567	35721	GX-30572
ANTA99-GC12	212-213	AIOM	35100	210	3325	31775	34345	33840	34880	GX-35100
RS14-BC3	0-1	AIOM	3448	32	2348	0	0			Poz-79268
RS14-BC3	4-5	AIOM	6670	40	2348	4322	3476	3092	3863	Poz-79269
RS14-BC3	12-13	AIOM	21419	115	2348	19071	20822	20353	21348	Poz#2-82563
RS14-BC3	24-25	AIOM	27500	369	2348	25152	27433	26581	28296	Poz-79271
RS14-BC2	0-1	AIOM	4275	34	0	0	0			Poz#2-79261
RS14-BC2	4-5	AIOM	14601	69	3175	11426	11383	10912	11874	Poz#2-78995
RS14-BC2	20-21	AIOM	28035	237	3175	24860	27167	26533	27686	Poz-79265
ANTA99-c20	0-1	AIOM	9520	40	4006	5514	5010	4615	5392	OS-102622
ANTA99-c20	22-23	AIOM	21580	141	4006	17574	19038	18596	19536	Poz-82573
ANTA99-c20	36-37	AIOM	25300	100	4006	21294	23385	22966	23768	OS-102624
RS14-BC1	0-1	AIOM	5106	34	0	0	0			Poz#2-79258
RS14-BC1	8-9	AIOM	17325	83	4006	13319	13608	13223	14026	Poz#2-79259
RS14-BC1	16-17	AIOM	25897	181	4006	21891	24049	23491	24656	Poz#2-79260

Table 5 Uncorrected and calibrated (cal) radiocarbon ages of the cores GC12 and c20 and RS14 box cores. Radiocarbon ages at the top of the three box cores were used by Ha et al. (2022) but were recalibrated for this thesis. GX = Geochron, Poz = Poznan, OS = NOSAMS.

Further dating on twenty-three new levels of the continental shelf cores was planned as part of this thesis but, unfortunately, these samples were not analysed for reasons unrelated to the conduct of this thesis.

7. Results

In this chapter, the results are described separately for the two investigated sectors: 1) Glomar Challenger Basin and 2) Slope and rise area. The geophysical data has been used to provide a geomorphological context of each core site on the continental shelf and the slope and rise area. The sediment parameters are grouped by type of analysis: description and radiographies, physical properties (magnetic susceptibility, compressive strength, water content, grain size), chemical and geochemical analyses (elemental analyses, organic matter, biomarkers) and microscopy analyses (sand characterisation via optical microscope, foraminifera assemblage). More details on the results are given for each core in the Supplementary.

7.1 Glomar Challenger Basin – Geomorphological context

Sub-bottom profiles and sparker profile are used to provide a geomorphological overview of the Glomar Challenger along the transect where the cores have been collected (figs. 7-8-9).

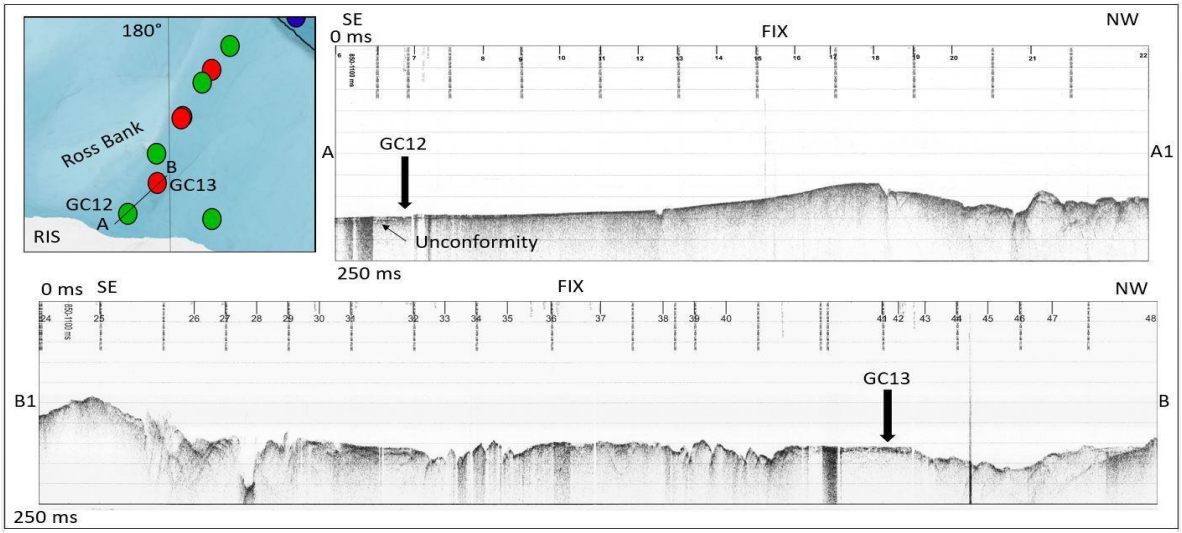

Figure 7 a) Glomar Challenger bathymetric map (zoom of fig. 6) with the position of the gravity cores and the two sub bottom profiles; b) SBP_11 and SBP_12 (FIX from 6 to 22); c) SBP_12 and SBP_13 (FIX from 24 to 48). 250 ms is the total vertical length of each SBP (25 ms between two horizontal lines).

The SBP dataset highlighted that the inner continental shelf is characterised by an acoustically transparent substrate under an erosional surface, draped by a thin layer of sediments.

Sub bottom profiles 12 and 13 (figs. 7b and 7c), recorded in the inner shelf, crossed an area characterised by an irregular seafloor, which is also covered by a thin layer of sediments.

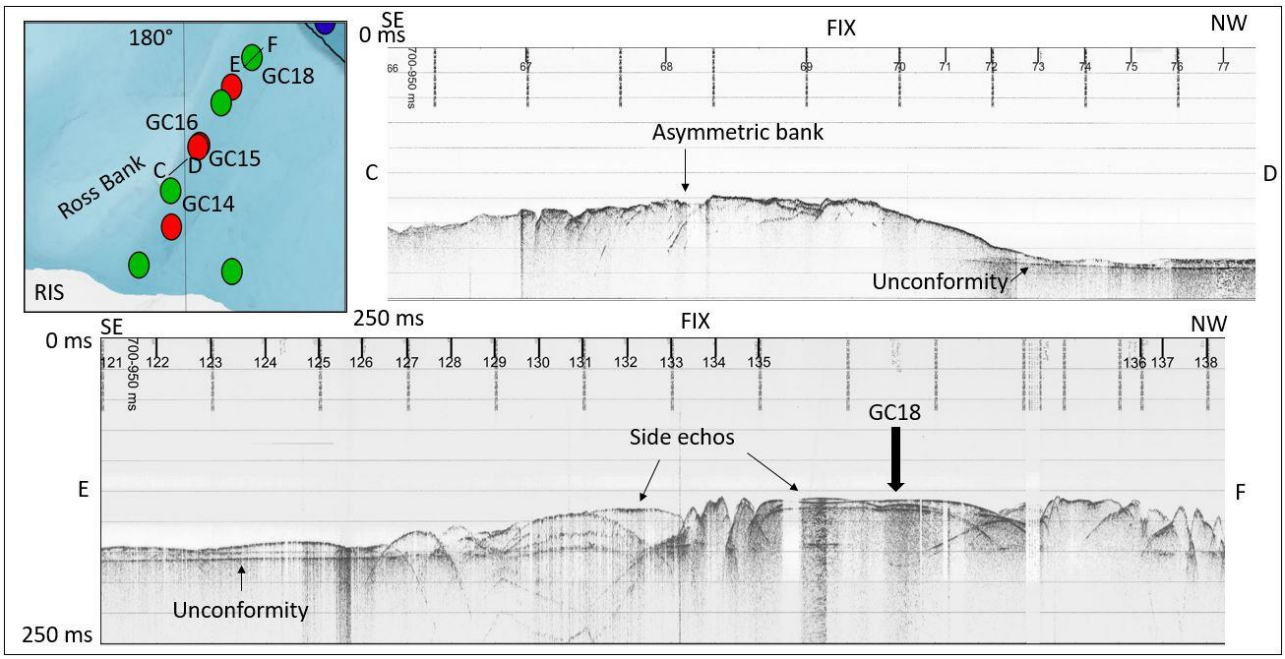

Figure 8 a) Glomar Challenger bathymetric map (zoom of fig. 6) with the position of the gravity cores and the two sub bottom profiles; b) SBP_14 (FIX from 66 to 77); c) SBP_17/18 (FIX from 121 to 138). 250 ms is the total vertical length of each SBP (25 ms between two horizontal lines).

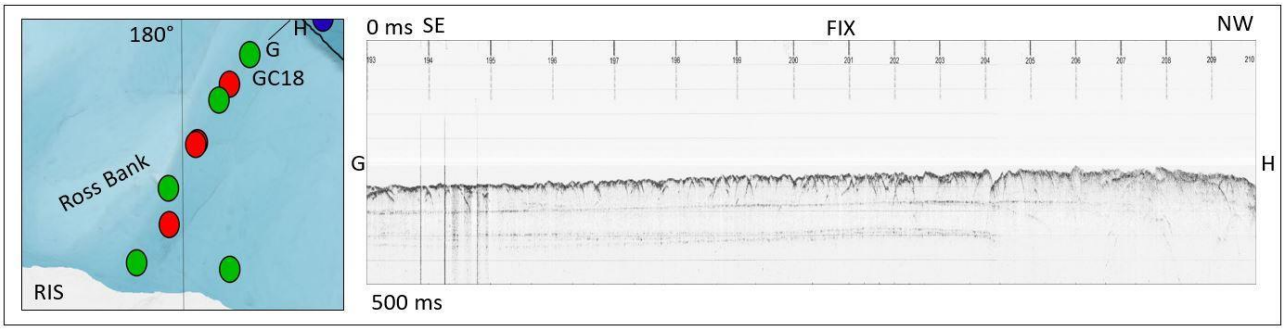

Figure 9 Bathymetric map of the Glomar Challenger Basin with the location of the gravity core (zoom of fig. 6) and the section of the sparker profile SPK3 (FIX from 193 to 210). Total vertical length is 500 ms.

A morphological bank, asymmetric with a seaward step, can be recognised in the middle shelf (fig. 8b). Its gentler flank has an irregular surface, while the step is flat. Sub bottom profiles acquired in the middle and in the outer shelf highlights the presence of deposits, characterised by a variable height, along the Glomar Challenger Basin (fig. 8b). Over the core sites the seafloor appears flat (fig.

8 between FIX 135 and 136). However, this is an artefact that originated when the ship stopped to collect the gravity cores. Toward the shelf edge, the seafloor is characterised by an irregular hummocky seafloor. It is visible in both the sparker profile (fig. 9) and the sub bottom profile.

7.2 Slope and rise area – Geomorphological context

The single channel seismic lines (fig. 10) highlighted that the slope and rise can be divided in three sectors: upper, middle and lower slope.

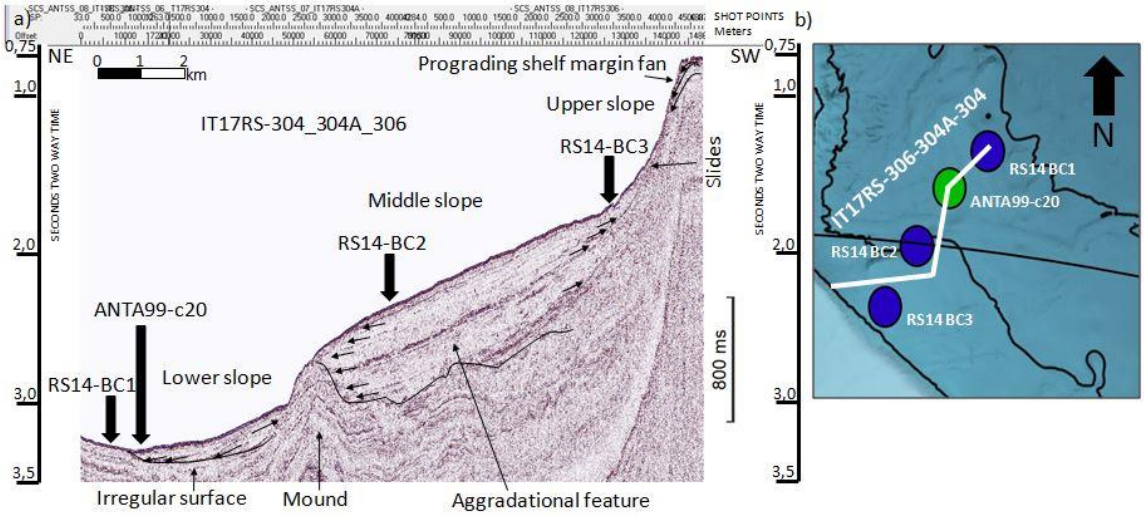

Figure 10 a) Profile of the slope and rise area (single channel seismic lines IT17RS304, IT17RS304A and IT17RS306 available in the Antarctic Seismic Data Library System (SDLS) https://sdls.ogs.trieste.it/cache/index.jsp, b) IBCSO version 2 bathymetric map (Dorschel et al., 2022) with the position of the seismic lines and box cores/gravity core collected in the slope and rise area(zoom of fig. 6).

The upper slope is characterised by a steep profile, characterised by a dip around 3,5 degrees (Gales et al., 2021). The seismic profile shows inclined foreset beds truncated by erosional surfaces and horizontal topset beds, previously described by Gales et al. (2021), and interpreted as part of a prograding margin fan at the shelf edge, cut by recent and paleo-gullies and slide scars. The box core BC3 was collected in the lower part of the upper slope, in correspondence of one of the slide scars. The middle slope is less steep, with a dip lower than 3 degrees (Gales et al., 2021), and it is characterised by a mounded seafloor. Seismic reflectors below the seafloor in the middle slope are discontinuous, subparallel, show an aggradational trend and are truncated seaward by the seafloor. They onlap the inclined foreset beds of the upper slope. The box core BC2 was collected in the middle slope. The lower slope, where the gravity core c20, were collected, is characterised by

discontinuous reflectors, slightly inclined seaward downlapping on an irregular surface with high amplitude. The lower slope area, where the box core BC1 was collected, is characterised by subparallel discontinuous reflectors inclined landward.

7.3 Glomar Challenger Basin – Sediments parameters

In this chapter, results obtained from gravity cores are presented as follows: description and radiography, physical analysis, chemical and geochemical analysis and microscopy analysis. The more detailed description of each parameter with figures and tables is reported in the supplementary 1.

7.3.1 Cores description and radiography

The nine gravity cores (figs. S1, S7, S13, S15, S21, S23, S25, S31, S37) collected along the Glomar Challenger Basin are mainly composed of massive sediments with a sandy silt matrix and millimetric to pluri-centimetric clasts. The upper 10 to 35 cm of cores c04, GC12 and GC14 are characterised by highly hydrated silt, while sand content increases in the other cores located toward the shelf edge. The clasts count performed following the method of Grobe (1987) highlighted a reduced presence of clasts >2 mm in the upper part of each core (tabs. S1, S9, S18, S20, S29, S32, S41, S50, figs. S1, S7, S13, S15, S21, S23, S25, S31, S37).

7.3.2 Physical analyses - Magnetic susceptibility, Compression strength, Water content and Grain size

The trends of the physical parameters (supplementary 1) show similar variations in the lower part of each core, while the main differences are reported in the upper part, distinguishing two different situations in the inner and the outer shelf. The magnetic susceptibility (MS) (tabs. S10, S19, S21, S30, S31, S33, S42, S51, figs. S8, S13, S16, S21, S23, S26, S37) is variable from core to core, showing a wide range of values between 300 and $900*10^{-6}$ SI, with even higher peaks caused by massive clasts and/or clasts concentration. MS shows a constant trend in some cores, while it shows an increasing up core trend in others, before decreasing in the upper part of each core, with values between 110 and $350*10^{-6}$ SI. Compressive strength measure (CS) (tabs. S2, S11, S22, S34, S43, figs. S2, S8, S16,

S26, S32) shows an up core decreasing trend from values higher than 3,0 kg/cm^2 at the bottom of the cores, and higher than 4,0 kg/cm^2 at the bottom of core GC12 (tab. S11, fig. S8), to 0,0 kg/cm^2 at the top cores. Water content (w%) (tabs. S3, S12, S23, S35, S44, figs. S2, S8, S16, S26, S32) shows higher values at the top of the cores collected in the inner continental shelf, reaching values higher than 50%. The cores collected in the outer shelf show more fluctuating values in the upper part of the core.

The grain size analysis (tabs. S4, S13, S24, S36, S45, figs. S2, S8, S16, S26, S32) highlights that the main sedimentary component of all studied cores is silt with values ranging between 44,6 and 90%. The cores collected in the inner shelf show higher silt values than the outer shelf cores. The sand content is characterised by an opposite trend, with the highest content in the cores collected in the outer shelf reaching a sand content of over 44% and average values between 23 and 25%.

The cores collected in the inner shelf are characterised by average (avg) values lower than 20% and a very low content (<5%) in the upper part of the cores c04 (tab. S4, fig. S2) and GC14 (tab. S24, fig. S16), while sand is almost absent in the upper part of core GC12 (tab. S13, fig. S8). Mean diameter (Mz) varies between coarse and fine silt, with average values in the range of medium silt. The only exception is core GC17 (tab. S36, fig. S26) with values between 5,0 and 6,0 ϕ (medium silt). Sediments are mainly very poorly sorted. The cores collected in the inner shelf show poorly sorted sediments in the upper part, but also the outermost core (GC18) (tab. S45, fig. S32) shows levels of poorly sorted sediments. Regarding the skewness (Sk), the distribution curves are mainly symmetric with more asymmetric intervals in the innermost cores. Median diameter (Md) decreases from the bottom toward the top of the cores collected in the inner shelf, while is more constant in the outer shelf. Core GC18 (tab. S45, fig. S32) is characterised by an increase of Md in the upper 20 cm. The primary mode of the cores (tabs. S4, S13, S24, S36, S45, figs. S3, S9, S17, S27, S33) is coarser in the lower part of the cores (4,0 – 5,0 ϕ) with unimodal distribution curves. Moving up the core, the distribution curves show an enrichment in coarse silt and sand, reaching a bimodal distribution with a primary mode of 6,5 – 7,5 ϕ in the inner shelf and a mainly unimodal distribution (5,0 – 7,0 ϕ) in the outer shelf. The upper part of the inner shelf cores is characterised by a unimodal distribution with a primary mode of 6,5 – 7,5 ϕ, characterised by a reduced sandy fraction. The upper part of the outer shelf cores is characterised by bimodal distribution curves with a coarse primary mode between 3,5 and 4,5 ϕ in core GC17 (fig. S27) and between 2,0 and 2,5 ϕ in core GC18 (fig. S33).

7.3.3 Chemical and Geochemical analyses – Elemental analyses, Organic matter and Biomarkers

The elemental analyses highlighted diverse correlations among the considered elements: Al, Si, K, Ti, Fe and Rb are well correlated among them suggesting a lithogenic origin of these elements (tab. 6 and tabs. S5, S14, S25, S37, S46 in the supplementary 1 for each core). Rb shows a moderate/good correlation with Sr, Ba and Zr, likely suggesting a biogenic origin of these elements. Br shows a low to moderate correlation only with Sr, Rb, Zr and Ba. Ca shows no correlation with the other elements.

Shelf	Al_cps	Si_cps	K_cps	Ca_cps	Ti_cps	Fe_cps	Br_cps	Rb_cps	Sr_cps	Zr_cps	Ba50_cps
Al_cps		2,28E-302	8,95E-267	1,62E-18	4,34E-143	7,00E-207	0,039901	9,65E-95	8,16E-72	3,83E-60	1,10E-88
Si_cps	**0,84846**		0	0,004427	1,70E-289	0	4,74E-06	2,55E-182	1,82E-77	4,31E-82	1,05E-138
K_cps	**0,82114**	**0,93827**		0,02689	0	0	4,38E-23	2,46E-305	1,59E-77	5,84E-109	1,25E-154
Ca_cps	0,26185	0,08622	-0,06710		0,001521	0,002838	2,09E-28	0,056089	4,96E-54	0,003137	5,87E-07
Ti_cps	**0,67071**	**0,83915**	**0,93080**	-0,09601		0	1,95E-49	0	7,02E-85	9,37E-121	3,67E-124
Fe_cps	**0,76167**	**0,87331**	**0,92679**	0,090407	**0,90235**		1,07E-26	5,98E-243	2,92E-84	2,28E-76	5,44E-139
Br_cps	-0,06231	0,13822	0,29368	-0,32629	0,42697	0,31625		7,49E-87	1,55E-15	1,01E-32	5,05E-37
Rb_cps	*0,56997*	**0,73082**	**0,85052**	-0,05793	**0,86550**	**0,79979**	*0,54950*		9,77E-126	1,03E-184	9,56E-213
Sr_cps	*0,50606*	*0,52313*	*0,52331*	0,44499	*0,54415*	*0,54245*	0,23849	**0,63867**		7,20E-249	7,61E-209
Zr_cps	0,46741	*0,53642*	**0,60358**	0,089479	**0,62871**	*0,51990*	0,35008	**0,73403**	**0,80535**		2,56E-196
Ba50_cps	*0,55438*	**0,66298**	**0,69000**	0,15075	**0,63556**	**0,66349**	0,37192	**0,76841**	**0,76395**	**0,74895**	

Table 6 Pearson elements correlation of the gravity cores collected on the continental shelf (GCB). Bold and underlined values represent moderate to strong correlation. Underlined values in italics represent low correlation.

Lithogenic elements are characterised by a similar trend along the cores. Ti (cps), used to represent lithogenic elements, is variable along the cores, but it shows lower values near the top, except in GC12 where it shows higher values. Zr/Rb, useful for the grain size definition, is characterised by constant trends along the cores, but it decreases in the upper part of the cores collected in the inner continental shelf (c04, GC12, GC14) (figs. S4, S10, S18), while it increases in the cores collected in the outer shelf (GC17, GC18) (figs. S28, S34). Elemental ratio of the elements shows more constant trends in the lower part of the cores, where sediments are more homogeneous. More evident variations are mainly concentrated in the upper part of the cores, where the other parameters changes and sediments are mainly characterised by silt (inner shelf) or sand (outer shelf). Mn/Ti, linked to the bottom water oxygenation, presents peaks in the upper part of each inner shelf core (figs. S4, S10, S18). GC17 doesn't have a clear peak of Mn/Ti (fig. S28) while this peak is present at the very top of core GC18 (fig. S34).

Despite the majority of analyses focused mainly on the upper part, the organic matter analyses highlighted differences between the upper 10 to 30 cm of each core and the lower part, but also

between inner shelf and outer shelf cores. The total organic carbon (TOC) (tabs. S6, S15, S26, S38, S47, figs. S5, S11, S15, S29, S35) is characterised by values ranging from 0,15% to 0,65%. The lower part of each core shows lower values and a more constant trend, with peaks concentrated in the upper part of the core and in the interval between 191 and 199 cm of core GC12 (tab. S15, fig. S11) and mainly formed by silt sediments. The upper 15 cm of core GC18 (tab. S47, fig. S35) are characterised by a higher content of sand and lower values of TOC. The ratio C/N (tabs. S7, S16, S27, S39, S48, figs. S5, S11, S15, S29, S35) is characterised by lower values in the upper part of the core and slightly lower values in the inner shelf cores. The biomarkers (HBI diene II and sterols) (tabs. S6, S15, S26, S38, S47, figs. S5, S11, S15, S29, S35) are characterised by a trend similar to that of TOC, increasing in the upper part of the studied cores, while both decrease in the upper 15 cm of core GC18, where the sand content increases. The exceptions are represented by core c04 (tab. S6, fig. S5), characterised by a peak of HBI at the very top of the core, and by core GC17 (tab. S38, fig. S29), characterised by lower values of HBI in the upper 15 cm than between 20 and 25 cm.

7.3.4 Microscopy analyses – Sand and Foraminifera

The sand is mainly formed by angular to sub-rounded quartz grains, rounded feldspar, micas and other femic minerals. Lithic fragments are present along the cores, but are less abundant in silt intervals of cores c04, GC12 and GC14. The biogenic component is sparse and consists mainly of siliceous organisms. Siliceous component is represented by radiolarians, sponge spicules and diatoms. Foraminifera (tabs. S8, S17, S28, S40, S49) are mainly represented by agglutinated foraminifera and subordinately calcareous foraminifera which were recovered along core GC18 (tab. S49), in particular. A total of 23 genera, representing 34 different species, were recognized. The most common species of foraminifera are: *Miliammina earlandi, Portatrochammina antarctica, Globocassidulina subglobosa* and *Trifarina earlandi*. Few tests of planktonic foraminifera, pertaining to *N. pachyderma*, were recovered. The foraminifer fragmentation rate varies between 20 and 100%, but ranges between 40 and 50% in the majority of samples.

7.4 Glomar Challenger Basin – Sedimentary facies

The sedimentary facies identified in the gravity cores are described in this chapter considering the complete dataset: texture and physical parameters, element composition, organic matter,

biomarkers and microscopy analyses. Four facies have been identified. Two sub-facies are identified in facies 4.

Facies 1cs: Stiff diamicton

The sediment is a very dark grey massive silty sand with a constant sand, silt, clay content down core. Abundant millimetric to pluri-centimetric clasts are present. The grain size distribution is unimodal with the primary mode in the order of coarse silt/sand. The magnetic susceptibility and element ratio here considered (see chapter 7.3 and supplementary 1) have a constant trend down core. The homogeneity of this facies is also highlighted by high correlation between the elements representative of the lithogenic fraction (Ti, Si, K, Fe, Zr, Rb) and the low variability of their trends. The main diagnostic feature is a compressive strength higher than the other facies: the average CS is 3,2 kg/cm^2 but the highest value was measured in the core GC12 (4,4 kg/cm^2).

Facies 2cs: Soft diamicton

This facies shows characteristics similar to those of facies 1cs, but the colour passes from grey to brownish grey, the compressive strength is higher at the base of the facies and tends to decrease upward. The MS is high but less constant than in the facies 1cs. Core GC14 presents an interval of iso-oriented clasts. This interval may be the result of deformation, but this feature is not always clear (Prothro et al., 2018 and references therein).

Facies 2cs has been identified in all the cores of the continental shelf, with thicknesses varying from 74 cm (GC15) to 312 cm (GC17).

Facies 3cs: Glaciomarine diamicton

The colour of this facies varies from dark olive grey/ olive grey to dark greyish brown. High magnetic susceptibility, sand-rich levels and high-density intervals characterise this facies. In cores GC13 and GC15, sub centimetric to centimetric horizontal laminae are evident. Compressive strength is low while water content is higher than those recorded in the previous two facies. Grain size distribution curves are characterised by a silty primary mode, with a bi-modal distribution in cores c04 and GC12 and a unimodal distribution in the core GC14. A pellets interval is present in the core GC12.

Lithogenic elements show a slight increasing trend and Mn/Ti ratio shows a peak in the upper part of the facies near the contact with the upper one, leading to interpret it, with some caution, as the signal for the end of the glacial phase and the reoxygenation of bottom waters (e.g. Jimenez-Espejo et al., 2020 and ref. therein). Foraminifera are almost absent and mainly broken suggesting that they were transported by post-depositional processes.

Facies 3cs has been identified in the cores collected in the inner and middle shelf, above the facies 2cs. Considering magnetic susceptibility, clasts counting and the presence of laminations, this facies is supposed to be present also in the core GC13 and GC15. The thickness varies from 34 cm (GC13) cm to 127 cm (GC12).

Facies 4cs

Two sub-facies were identified in this facies.

-Sub-facies 4cs-a: Silt

This sub-facies is characterised by a silty olive to olive green sediment with a high water content, relatively low MS and very low compressive strength. In the cores c04 and GC12 collected close to the RIS, sand and clasts are sparse, while their presence increases in the core GC14. The decrease in grain size is also highlighted by the decrease of Zr/Rb and the lithogenic elements, but with higher or constant values of Si/Ti. This is probably related with the reduced clasts presence and the increase of siliceous material. Agglutinated foraminifera are present and mainly represented by *Miliammina earlandi* (tabs. S7, S15, S25, S36 and S44).

This sub-facies has been identified at the top of the cores collected in the inner-middle Glomar Challenger continental shelf (c04, GC12, GC13 and GC14) with thickness ranging between 13 and 39 cm and it cannot be distinguished in the sub-bottom profiles because of its reduced thickness. The thickness found is coherent with the values found by Prothro et al. (2018) in the Eastern Ross Sea (0-100 cm).

-Sub-facies 4cs-b: Sandy silt with silty sand intervals

This sub-facies is characterised by sandy silt/silty sand with the presence of IRD. The sand content is high with an average of 28,1%, the value of 50,9% in the GC18. Grain size analysis has highlighted an average bimodal distribution (fig. 11). Magnetic susceptibility is higher than those of the facies

4cs-a, due to the presence of coarser material, also evidenced by the higher values of Zr/Rb. Water content is lower than facies 4cs for the same reason. This sub-facies shares similar features with facies 4cs-a: an increase of TOC, presence of HBI diene II and sterols, higher values of Br/Ti and Ba/Ti, and the presence of agglutinated foraminifera. TOC is high where the sand content is lower at the top of the core GC17 and between 25 and 14 cm in the core GC18. Biomarkers show a similar trend. Sub-facies 4cs-b has been identified at the top of the cores collected in the middle/outer shelf: GC15, GC17, GC18 and GC19 with thickness from 23 to 44 cm and lies above facies 2cs in cores GC17, GC18 and GC19 and above facies 3cs in core GC15. Similarly to sub-facies 4cs-a, its reduced thickness does not allow distinguishing this facies from the facies 2cs in the sub-bottom profiles.

7.5 Slope and rise area – Sediments parameters

The results obtained analysing the box cores and the core collected in the slope and rise area are presented here. The results are reported dividing physical analysis from chemical and geochemical ones. A more detailed description of each parameter with figures and tables is reported in the supplementary 2.

7.5.1 Cores description and radiography

Box core BC3 (fig. S38) is formed by grey to greyish brown sandy silt and even silty sand in the upper 4 cm. Box cores BC2 (fig. S43) and BC1 (fig. S48) and the gravity core c20 (fig. S53) are characterised by light brown to brown sediments with intervals of laminated clayey silt. In these intervals, clasts are sparse or absent (tab. The upper part of the cores is made of sandy silt with a higher content of clasts (tabs. S52, S59, S66, S73).

7.5.2 Physical analyses - Magnetic susceptibility, Compression strength, Water content and Grain size

The physical parameters vary moving from the upper toward the lower slope. Magnetic susceptibility (tabs. S53, S60, S67, S74, figs. S39, S44, S49, S54) is more constant near the upper

slope (BC3) (tab. S53, fig. S39) with values between 280 and 330*10^{-6} SI. On the contrary, BC2 (tab. S60, fig. S44) in the middle slope is characterised by an increasing up core trend, reaching 818 *10^{-6} SI at the top of the core. MS of BC1 (tab. S67, fig. S49) is higher from the bottom to 28 cm and in the upper 10 cm. Core c20 (tab. S74, fig. S54) is characterised by values higher than 1000*10^{-6} SI from the bottom to 179 cm and between 29 and 21 cm, and lower values in the rest of the core. Water content is characterised by a constant trend in BC3 (20-30%) (tab. S54, fig. S39). Water content of BC2 (tab. S61, fig. S44) is characterised by a decreasing trend from higher than 40% to about 30%. BC1 increases up core from 29% to 50% (tab. S68, fig. S49). Water content of c20 is higher from the bottom to 35 cm and in the upper 15% (tab. S75, fig. S54).

Grain size analysis of core c20 (tab. S76, fig. S54) was performed only in the upper 55 cm, in order to make a comparison with the three box cores. Silt is the main sedimentary component (tabs. S55, S62, S69, S76, figs. S39, S44, S49, S54), ranging between 36,4 and 87,4%. Sand content decreases moving downslope from the BC3 (tab. S55, fig. S39) toward BC1 (tab. S69, fig. S49). It reaches 60,7% in BC3 (min 8,3%) (tab. S55, fig. S39), while maximum sand content ranges between 14 and 31% in the other box cores/gravity core, and in some intervals, sand is <1%. Clay content is more abundant in BC2, BC1 and c20 (tabs. S62, S69, S76, figs. S44, S49, S54), ranging between 4,6 and 30,7%. Mean diameter ranges between 3,8 ϕ (very fine sand) and 8,3 ϕ (clay). The sediments are mainly poorly sorted with poorly sorted intervals in the upper and middle slope, while the lower slope is characterised by poorly sorted sediments with very poorly sorted intervals. Skewness highlighted that distribution curves are mainly negative asymmetric in BC3 (tab. S55, fig. S39) and BC1 (tab. S69, fig. S49), while curves are mainly symmetric in BC2 (tab. S62, fig. S44) and core c20 (tab. S76, fig. S54). Md shows a constant trend in the lower part of the box cores and it increases in the upper 10 cm. The primary mode (tabs. S55, S62, S69, S76, figs. S40, S45, S50, S55) of the box cores and the core ranges between 7,5 and 8,5 ϕ with a unimodal distribution. Moving up core, the primary mode changes to an interval 0f 4,0 – 7,5 ϕ with enrichments of coarse material and reaching a bimodal distribution in the upper part of the cores. The upper 6cm of BC3 (tab. S55, fig. S40) are even coarser (2,0 2,5 ϕ) and the upper 2 cm of this box core shows again a unimodal distribution.

7.5.3 Chemical and Geochemical analyses – Elemental analyses, Organic matter and Biomarkers

The correlation (tabs. S56, S63, S70, S77) among Al, Si, K, Ca, Ti, Fe, Rb, Sr, Zr is moderate to strong, in particular near the upper slope (BC3) (tab. S56), but moving downslope some elements show a good correlation only with some of them. For instance, BC1 shows a good correlation of SI with K and Fe. Ti shows a good correlation with these two elements as well. Ca correlates with Sr, Zr and Ba. Ba is characterised by anticorrelation with Rb and Si, while Br shows anticorrelation with Sr and Zr. Ti (cps) varies down slope, showing a decrease in the upper/middle slope and a more constant (c20) (fig. S51) to slightly increasing (BC1) (fig. S56) trend in the lower slope. Zr/Rb increases toward the top of box cores/gravity cores. Lithogenic elements (Si, Fe, K) mainly decrease up to the core. Ba/Ti and Ca/Ti are characterised by low constant values that increase in the upper part of the cores. Br/Ti shows a similar trend in BC3 (fig. S41) and BC2 (fig. S46), but it slightly decreases in BC1 (fig. S51) and c20 (fig. S56). Mn/Ti presents a peak, occupying a wider interval in c20 (fig. S56) and BC3 (fig. S41).

The organic matter content of core c20 (tab. S78, fig. S57) was performed only in the upper 55 cm. TOC content ranges between 0,12 and 0,42%. TOC is higher in the lower part of BC3 (tab. S57, fig. S42), BC2 (tab. S64, fig. S47) and c20 (tab. S78, fig. S57), showing an increase only in the upper part. BC1 (tab. S71, fig. S52) is characterised by an increasing up core trend. C/N decreases toward the top (tabs. S57, S71, S78, figs. S42, S52, S57). BC2 (tab. S64, fig. S47) shows a slight increase of this ratio at the top. $CaCO_3$ content (tabs. S57, S64, S71, S78, figs. S42, S47, S52, S57) is characterised by very low values and it was not measurable in the majority of samples. BC3 shows a decreasing trend (tab. S57, fig. S42) of calcium carbonate. Biogenic silica (BioSi) (tabs. S57, S64, S71, S78, figs. S42, S47, S52, S57) is characterised by low values (<5%) in all box cores and cores except BC3 (tab. S57, fig. S42), which presents higher values. HBI diene II and sterols show a very low concentration in all the samples (tabs. S58, S65, S72, figs. S42, S47, S52), but it increases toward the top of the box cores.

7.6 Slope and rise - sedimentary facies

The complete dataset (texture, physical parameters, element composition, organic matter) have been used to identify 3 facies described in this chapter. Only the upper 55 cm of the core c20 have been considered to make a comparison with the box cores.

Facies 1sr: Laminated clayey silt

This facies is made of laminated muddy sediments with silt/sandy silt intervals. Laminae are weak, parallel, millimetric to centimetric and horizontal in BC2 and C20 and slightly oblique in BC1. This facies is interpreted as the results of bottom currents, characterised by alternated periods of stronger (slightly coarse laminae, basal portion of BC1) and weaker (muddy laminated intervals) activity.

Facies 2sr: Massive sandy silt

This facies is characterised by a massive aspect. Clasts are abundant and sand content increases as confirmed also by the high magnetic susceptibility. The number of clasts slightly decreases moving toward the lower part of the slope because of the distance from the sediment source. Lithogenic elements (XRF data) show high values. This facies is thinner in the lower slope (5 cm in BC1) than in the middle slope (28 cm in BC3). In core c20, this facies shows the largest thickness (30 cm) because it was recovered on a mound of sediments. An important feature is the presence of Mn/Ti peaks.

Facies 3sr: Sandy silt with IRD

This facies is mainly characterised by olive brown sandy silt sediments. Magnetic susceptibility is higher than in the facies 2sr, because of the higher presence of sand and clasts at the top of the cores, in particular at the top of the BC2 (tabs. S59, S62, figs. S43, S44). The strong presence of coarse fraction is reflected by a bi-modal grain size distribution (figs. S40, S45, S50, S55), like facies 4cs-b in the outer shelf. The increasing values of TOC, biomarkers concentration and biogenic elements (Ba/Ti, Br/Ti and Ca/Ti) highlight a productivity increase.

8. Discussion

In this chapter, the sedimentary facies identified in the gravity cores and box cores are discussed and interpreted in relation to the morphological characters of the seafloor where the cores were collected. In order to distinguish between the facies of the continental shelf and the ones on the slope and rise, the formers are reported with initials “cs” (continental shelf), while the latters are reported with the initials “sr” (slope and rise).

8.1 Glomar Challenger Basin – Geophysical data

Sub-bottom profiles interpretation allowed us to recognise a discontinuous unconformity (fig. 7 and 8) covered by a drape of sediments in the inner continental shelf (fig. 7) and by mounded deposits in the middle outer continental shelf (fig. 8). The unconformity marked with a red dotted line in the figures from 11 to 17 was reached only with two of the gravity cores in the inner continental shelf (figs. 11 and 12). This unconformity, previously identified in the Glomar Challenger Basin and in other sectors of the Ross Sea, has been interpreted as the LGM unconformity, a seismic reflector representing the advance of the ice sheet across the continental shelf during the LGM (e.g. Shipp et al., 1999; Mosola & Anderson, 2006; Anderson et al., 2019). The blue dotted line (figs. 11-17) marks the upper limit of the overlying sedimentary facies described in the next chapter. Shipp et al. (1999) firstly interpreted these sediments as glaciomarine and marine sediments. Ó Cofaigh et al. (2007), studying geophysical data and sediment cores from the Antarctic Peninsula (Pine Island Bay, Belgica Trough, Marguerite Bay and Robertson Trough) identified an unconformity, similar to the one identified in the Ross Sea, dividing soft and stiff till. They suggested that it may be related to different processes of till deposition or deformation, or it may also divide pre-LGM from LGM sediments. Halberstadt et al. (2018) considered these hypotheses valid for the unconformity identified in the Glomar Challenger Basin, but the answer is not known yet.

In the inner sector of the Glomar Challenger Basin, an irregular morphology characterises the seafloor (fig. 7), interpreted as glacial morphologies associated with a bedrock near the seafloor. In fact, Anderson (1999) and Shipp et al. (1999) report the presence of bedrock near the seafloor in this portion of the continental shelf. Shipp & Anderson (1997) interpreted these features as drumlins. This geomorphological feature was reported by other authors (e.g. Mosola & Anderson, 2006; Halberstadt et al., 2016) and marks areas of different ice flow velocities due to the changes

from a bed with an exposed or nearly exposed bedrock to a soft sediments bed (Anderson et al., 2019 and references therein).

Mounded deposits interpreted as mega scale glacial lineations (MSGL) were identified in the sub bottom profiles acquired in the middle to outer shelf and studied for this work. These features, delimited at the lower end by the aforementioned unconformity highlighted with a red dotted line, are visible in figs. 8, 14-16. MSGLs were reported in this area by several authors (e.g. Mosola & Anderson, 2006; Halberstadt et al., 2016; Anderson et al., 2019). Another important feature identified in the middle shelf above the unconformity is a grounding zone wedge (GZW) (fig. 8), characterised by an irregular topset, gentle forest and toe. This GZW could be associated with the GZW previously identified in this part of the Glomar Challenger (e.g. Mosola & Anderson, 2006; Bart & Owolana, 2012; Halberstadt et al., 2016; Danielson and Bart, 2023). GZWs are also reported near the shelf edge (e.g. Mosola & Anderson, 2006; Halberstadt et al., 2016; Danielson & Bart, 2023). The seismic surveys used for this thesis did not show any additional GZWs to those previously recognized.

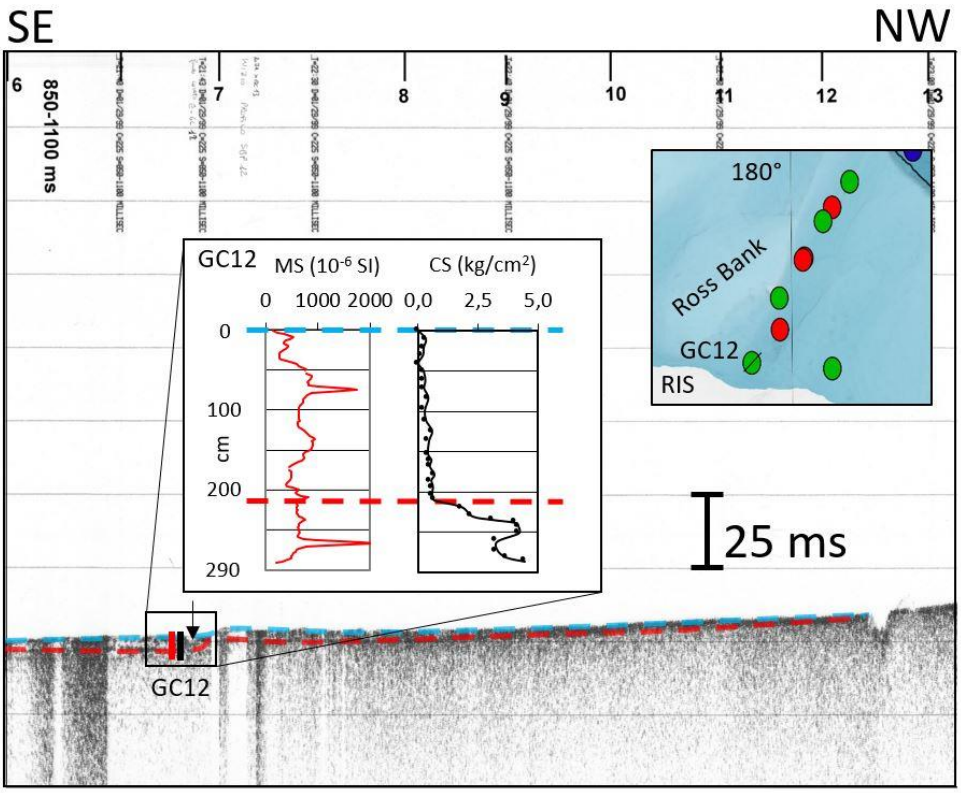

Figure 11 Correlation of the magnetic susceptibility (MS) and compressive strength (CS) with sub bottom profile (SBP) 11/12. The dotted red line is an erosive surface. The dotted blue line is the seafloor. Depth in SBP is reported in milliseconds (ms), while depth of GC12 is reported in centimetres (cm). The bathymetric map is a zoom of fig. 6.

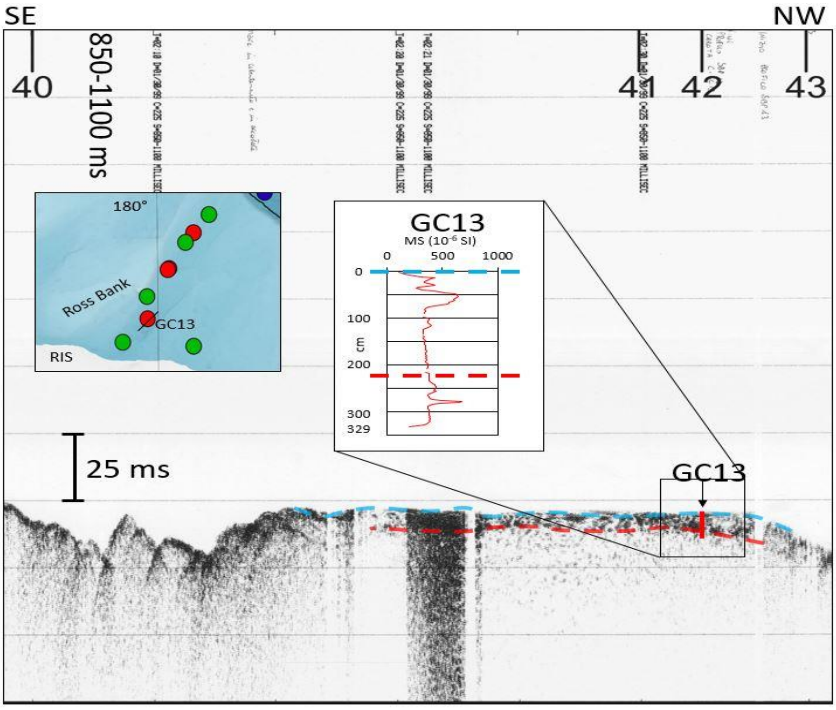

Figure 12 Correlation of the magnetic susceptibility with sub bottom profile (SBP) 11/12. The dotted red line is an erosive surface. The dotted blue line is the seafloor. Depth in SBP is reported in milliseconds (ms), while depth of GC13 is reported in centimetres (cm). The bathymetric map is a zoom of fig. 6.

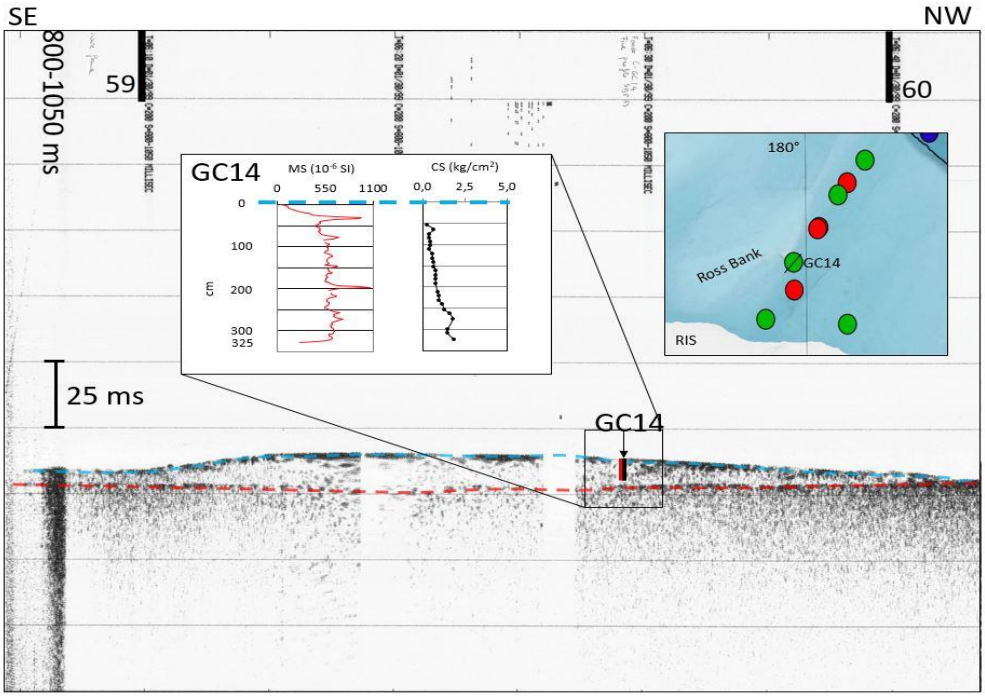

Figure 13 Correlation of the magnetic susceptibility (MS) and compressive strength (CS) with sub bottom profile (SBP) 13/14. The red line is an erosive surface. The blue line is the seafloor. Depth in SBP is reported in milliseconds (ms), while depth of GC14 is reported in centimetres (cm). The bathymetric map is a zoom of fig. 6.

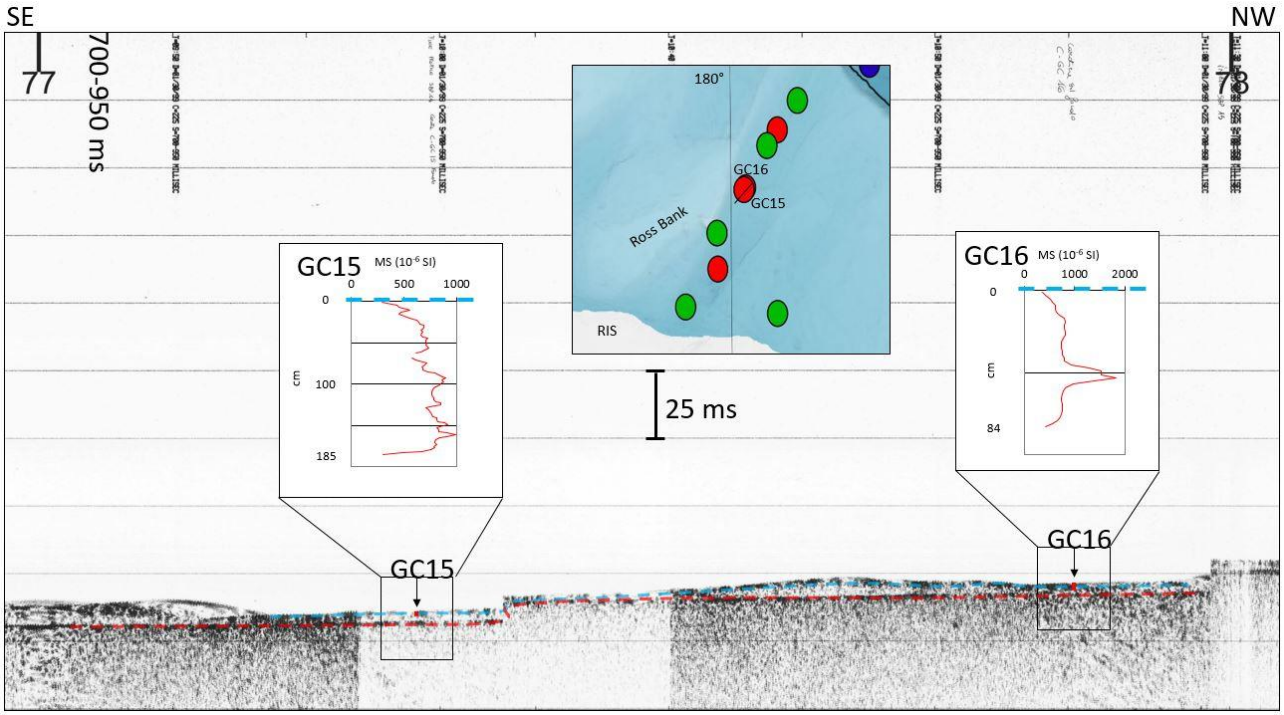

Figure 14 Correlation of the magnetic susceptibility (MS) and compressive strength (CS) with sub bottom profile (SBP) 14. The dotted red line is an erosive surface. The dotted blue line is the seafloor. Depth in SBP is reported in milliseconds (ms), while depth of GC15 and GC16 is reported in centimetres (cm). The bathymetric map is a zoom of fig. 6.

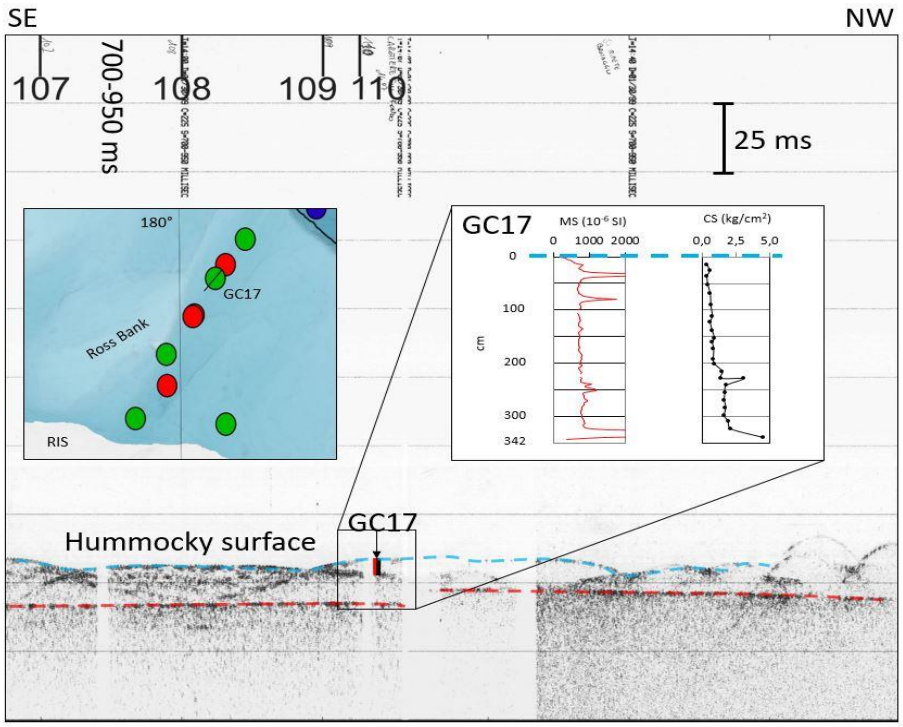

Figure 15 Correlation of the magnetic susceptibility (MS) and compressive strength (CS) with sub bottom profile (SBP) 15/16. The dotted red line is an erosive surface. The dotted blue line is the seafloor. Depth in SBP is reported in milliseconds (ms), while depth of GC17 is reported in centimetres (cm). The bathymetric map is a zoom of fig. 6.

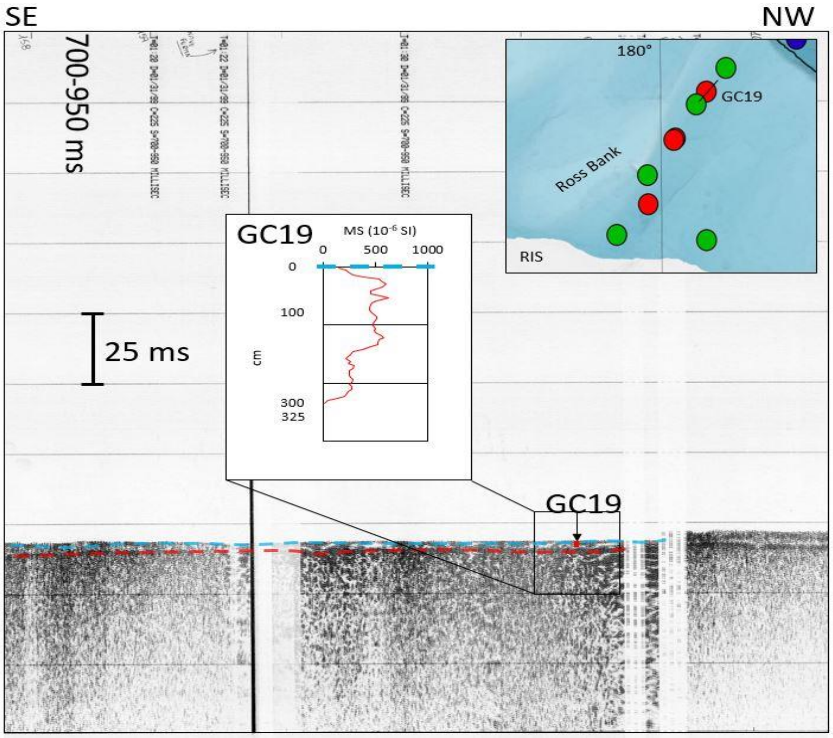

Figure 16 Correlation of the magnetic susceptibility (MS) and compressive strength (CS) with sub bottom profile (SBP) 19. The dotted red line is an erosive surface. The dotted blue line is the seafloor. Depth in SBP is reported in milliseconds (ms), while depth of GC19 is reported in centimetres (cm). The bathymetric map is a zoom of fig. 6.

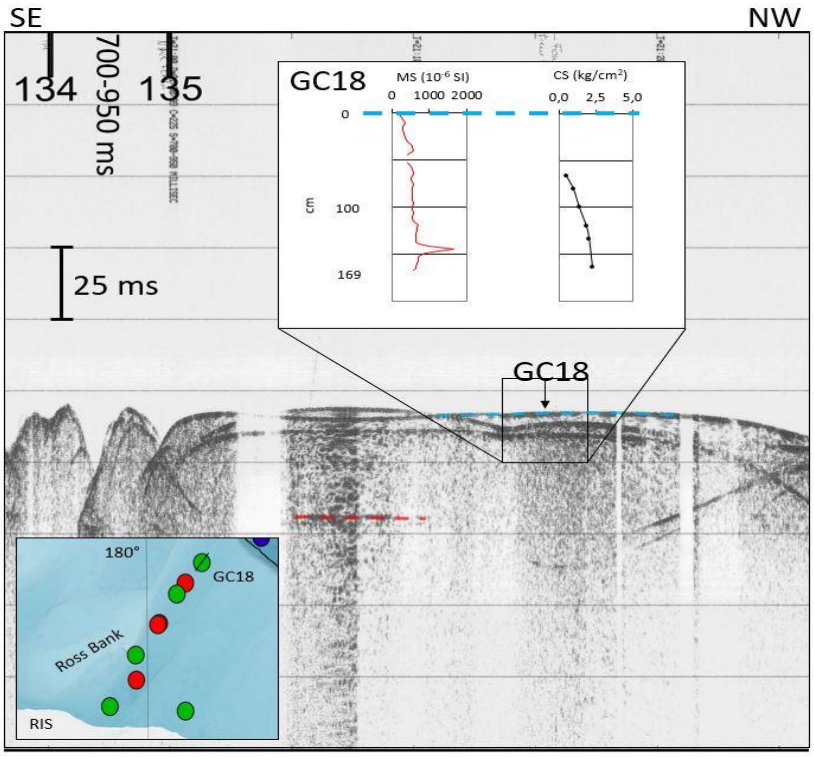

Figure 17 Correlation of the magnetic susceptibility (MS) and compressive strength (CS) with sub bottom profile (SBP) 17. The dotted red line is an erosive surface. The dotted blue line is the seafloor. Depth in SBP is reported in milliseconds (ms), while depth of GC18 is reported in centimetres (cm). The bathymetric map is a zoom of fig. 6.

8.2 Slope and rise area - Geophysical data

The interpretation of single channel seismic lines collected in the slope and rise area allowed us to identify three different sections (fig. 10). The upper slope, characterised by a steep profile, shows evidence of modern and paleo downslope processes (slides, gullies) that strongly influenced this part of the slope, as previously highlighted by Gales et al. (2021) and Ha et al. (2022). The middle slope and the lower slope, divided by a submerged mound, are characterised by deposits with discontinuous reflectors that lie above a strong irregular surface. These deposits may be associated with the downslope processes identified in the upper slope that filled the depressed part of the slope.

8.3 Glomar Challenger Basin – Sedimentary facies

The sedimentary facies identified in the gravity cores (tab. 7, fig. 18) allowed us to follow the evolution of the WAIS in the Glomar Challenger Basin since the pre-LGM.

Facies / Subfacies	Physical description	Physical parameters	Chemical and geochemical parameters	Biogenic component	Geomorphological context	Interpretation
1cs	Massive sandy silt with millimetric to pluri-centimetric clasts Dark grey	High MS with a constant trend: avg 488*10^-6 SI; st.dev. 121*10^-6 SI CS: avg 3,2 kg/cm2; st.dev. 1,2 kg/cm2 Water content: avg 23,8%; st.dev. 2,4% Sand/silt/clay: avg 24,7/68,0/7,4%; st.dev. 3,5/1,7/1,9%	XRF data show constant trend down core TOC not measured; HBI and sterols: not measured	Biogenic barren	Inner shelf (under the unconformity)	Subglacial stiff diamicton
2cs	Sandy silt with millimetric to pluri-centimetric clasts Grey to brownish grey Mainly massive. Iso-oriented clasts are present in GC14	High MS but more variable downcore: avg 602*10^-6 SI; st.dev. 170*10^-6 SI CS: avg 1,1 kg/cm2; st.dev. 0,7 kg/cm2 Water content: avg 27,5%; st.dev. 4,4% Sand/silt/clay: avg 20,6/72,6/6,8%; st.dev. 5,7/5,5/0,8%	XRF data show constant trend down core TOC avg 0,34%, st.dev. 0,07%; C/N>8, but <5 in core c04 HBI diene II and sterols: not measured except in a muddy interval (GC12): probably residual material	Sparse and damaged carbonate foraminifera, radiolarians, diatoms and sponge spicules	Ubiquitous	Subglacial soft diamicton
3cs	Sandy silt Grey to dark olive-brownish grey. High content of clasts. Mainly massive, but laminations are present in the cores GC13 and GC15	High MS: avg 681*10^-6 SI; st.dev. 131*10^-6 SI CS: avg 0,3 kg/cm2; st.dev. 0,1 kg/cm2 Water content: avg 29,6%; st.dev. 4,0% Sand/silt/clay: avg 16,9/74,0/9,1%; st.dev. 4,8/4,8/2,5%	XRF data show slightly higher values TOC avg 0,23%, st.dev. 0,06%; C/N>8 HBI diene II and sterols: almost absent, (residual material)	Very sparse and damaged carbonate foraminifera, radiolarians, diatoms and sponge spicules. Biogenic barren in the core c04	Inner/middle shelf	Sub Ice Shelf glaciomarine diamicton
4cs-a	Massive silty sediments with sparse clasts olive to olive green	Low MS: avg 323*10^-6 SI; st.dev. 95*10^-6 SI CS: avg 0,2 kg/cm2; st.dev. 0,1 kg/cm2 Water content: avg 46,9%; st.dev. 5,6% Sand/silt/clay: avg 4,9/85,6/9,5%; st.dev. 3,7/3,7/2,4%	XRF data show a slightly increase of Ba and Br; Elements related to lithological fraction decrease TOC avg 0,40%, st.dev. 0,14%; C/N <8 HBI diene II and sterols: low concentration	Sparse agglutinanated foraminifera, diatoms, sponge spicules and radiolarians. Siliceous oraganisms are more abundant in the core GC14	Draping unit Inner/middle shelf	Seasonal open marine condition Silt
4cs-b	Massive sandy silt with high sand content and presence of intervals of silty sand. Clasts presence decreases up core. From dark grey to olive grey to olive	High MS: avg 478*10^-6 SI; st.dev. 149*10^-6 SI CS: avg 0,5 kg/cm2; st.dev. 0,1 kg/cm2 Water content: avg 31,2%; st.dev. 4,8% Sand/silt/clay: avg 28,5/65,4/6,1%; st.dev. 12,0/11,0/1,9%	XRF data show a slightly increase of Ba and Br; Elements related to lithological fraction slightly increase TOC avg 0,35%, st.dev. 0,07%; C/N>7 HBI diene II and sterols: low concentration	Sparse agglutinanated foraminifera and slightly more abundat diatoms, sponge spicules, radiolarians in the upper part of the facies	Draping unit Middle/outer shelf	Seasonal open marine condition Winnowed sandy silt to silty sand

Table 7 Average values and standard deviations of parameters used to identify sedimentary facies cs (continental shelf).

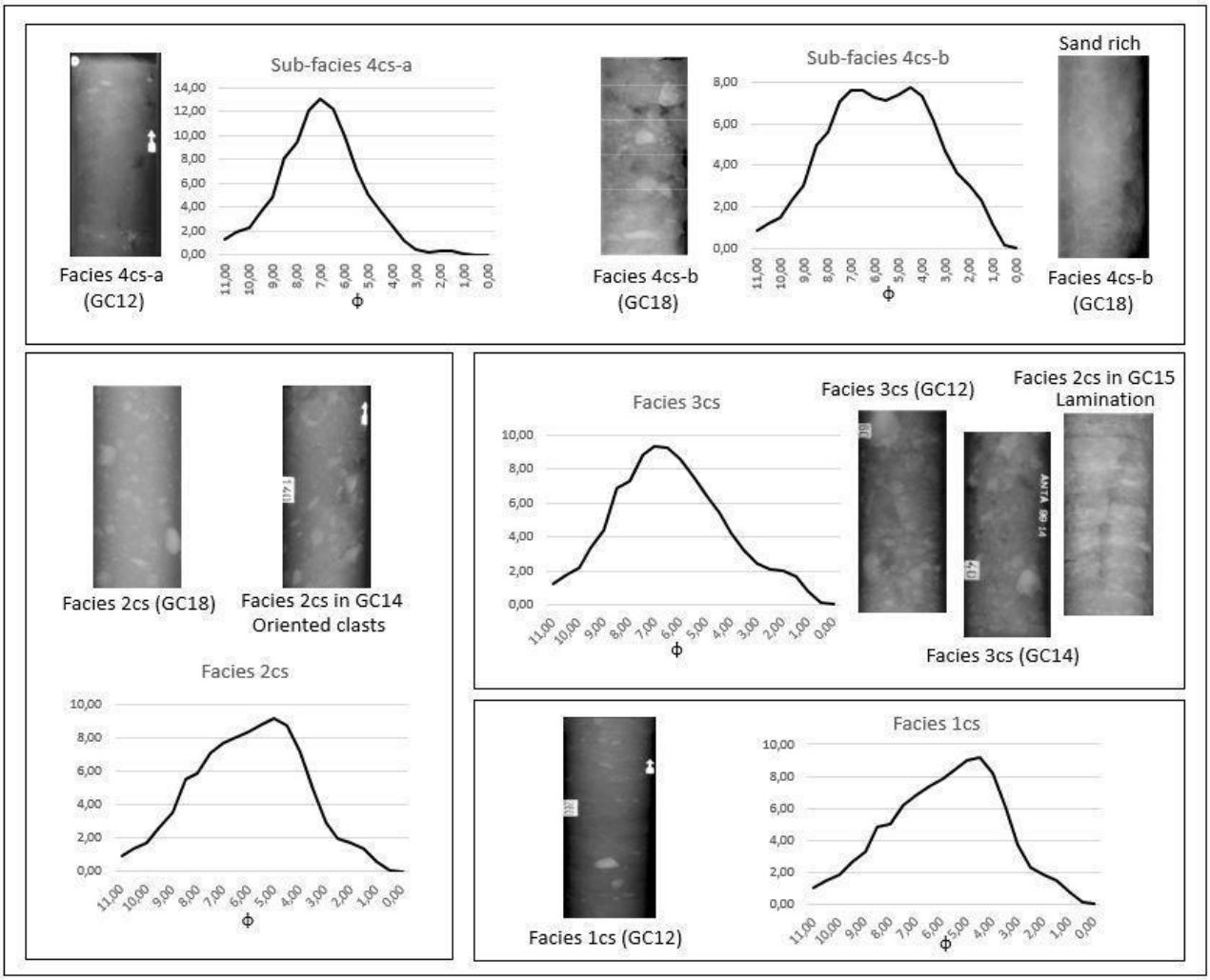

Figure 18 Radiographic images and average grain size (ϕ) distribution of the sedimentary facies/sub-facies (Glomar Challenger Basin).

Three stages were identified: glacial, deglacial and the Holocene.

Facies 1cs: Stiff diamicton

The facies 1cs (see chapter 7.4, tab. 7 and fig. 18) which is characterised by homogeneous grain size, magnetic susceptibility and low water content, is very similar to the “Facies 1” of Prothro et al. (2018). These authors found this facies on the topset of grounding zone wedges or in mega scale glacial lineation fields of the western sector of the Ross Sea continental shelf.

In addition, considering the homogeneity of this facies also considering the geochemical element distribution, its high compressive strength and the very sparse presence/absence of foraminifera mainly pertaining to the *Globocassidulina* and *Trifarina* genera, this facies can be interpreted as a

stiff subglacial diamicton, in agreement with Anderson (1999), McGlannan et al. (2017), Majewski et al. (2018), Prothro et al. (2018)**.** This facies, which represents sediments deposited when the ice sheet advanced across the continental shelf, was recovered only in GC12 and GC13 inner continental shelf cores under the erosive surface (unconformity) identified in the sub bottom profiles on a depth around 2 - 2,5 metres below sea floor (red dotted line of fig. 11 and fig. 12). This surface, identified in the sub bottom profiles in the other sectors of the Glomar Challenger Basin along the sampled transect, was not reached in the other studied cores: it lies under 2 to 4 metres of sediments in the site of cores GC14 (fig. 13) and GC17 (fig. 15), while the unconformity lies under 1-2 metres of sediments in the sites of cores GC15, GC16 (fig. 14) and GC19 (fig. 16). As aforementioned, this erosive surface was previously interpreted as the LGM unconformity (Anderson et al., 2019 and references therein). The radiocarbon date available for the GC12 core indicates that this facies in the inner continental shelf of the GCB has an age > 34,3 kyr BP. However, it should be considered that the age obtained by AIO may be older due to contamination with ancient organic matter, as also suggested by Domack et al. (1999)..

Facies 2cs: Soft diamicton

Considering the characteristics reported in chapters 7.3, 7.4 and in the supplementary 1 and in agreement with Anderson (1999), McGlannan et al. (2017), Prothro et al. (2018), this facies is here interpreted as a subglacial diamicton. In particular, considering the lower compressive strength, the position of this facies above the aforementioned unconformity and the work of Ó Cofaigh et al. (2007), it has been distinguished from facies 1cs and interpreted as **soft subglacial diamicton,** deposited under a grounded ice sheet during its progression across the shelf. McGlannan et al. (2017), studying cores collected in the Whales Deep Basin, reported the presence of a similar deposit on both grounding zone wedges and lineation fields, interpreting it as a till. They called it “grounding zone proximal till'' instead of “subglacial till” because of its similarity on topsets and foresets of grounding zone wedges. Prothro et al. (2018) also found a single facies for subglacial environments. Smith et al. (2019) also showed the presence of two distinguished diamicton in the subglacial environment. Ó Cofaigh et al. (2007) distinguished between stiff and soft diamicton using the previously described unconformity (e.g. Halberstadt et al., 2018; figs. 11 and 12 of this work) as a boundary between them. Both Ó Cofaigh et al. (2007) (Antarctic Peninsula) and Halberstadt et al. (2018) (Glomar Challenger Basin) also suggested that this interface might also be the boundary

between pre-LGM and LGM sediments, as previously interpreted by other authors (Shipp et al., 1999; Mosola & Anderson, 2006; Halberstadt et al., 2016; Anderson et al., 2019). The radiocarbon age obtained for core GC12 in the inner continental shelf of the GCB, indicates a pre-LGM age of 35,1 kyr BP. Considering the interpretation of the unconformity as a pre-LGM/LGM boundary, the possibility that the radiocarbon age was obtained by reworked organic matter must be considered, as suggested by Domack et al. (1999) for their cores.

Facies 3cs: Glaciomarine diamicton

This facies was identified only in the cores collected in the inner/middle shelf. It is mainly characterised by a silty primary mode, high and variable magnetic susceptibility, higher water content and low compressive strength. Elements distribution varies in this facies, and in particular a peak on Mn/Ti was identified. McGlannan et al. (2017 and references therein) identified a facies characterised by similar features (chapter 7.4, tab. 7 and fig. 18) in the Whales Deep Basin, interpreting it as proximal subglacial deposit, which can also be characterised by grain size similar to the subglacial facies (Prothro et al., 2018). McGlannan et al. (2017) and Prothro et al., (2018) interpreted this as a proof of the common origin of these deposits and the ones retrieved in the subglacial environment. Facies 3cs is interpreted as a **glaciomarine diamicton** deposited in a **sub ice shelf** environment.

A similar facies was described by Domack et al. (1999) in other cores of the Glomar Challenger Basin and named “granulated facies”. “Unit 2a” of McGlannan et al. (2017) and “facies 3” of Prothro et al. (2018) also share similar features. They interpreted this facies as proximal sub ice shelf facies.

Facies 4cs

-Sub-facies 4cs-a: Silt

In contrast with the other facies, this one is mainly represented by silt, and clasts >2 mm are very sparse to absent. The grain size variation is also reflected by a higher water content. Both TOC and biomarkers concentration show higher values in this facies. All these data likely indicate open marine conditions following the ice shelf retreat in agreement with Domack et al. (1999), McGlannan et al. (2017) and Prothro et al. (2018). These sediments are ubiquitous in the Ross Sea

and represent the most recent condition of the post-LGM glacial evolution. The only occurrence of the agglutinated taxa among the foraminifera have been documented in the diatomaceous sediments of the Ross Sea troughs by Melis & Salvi (2009), Majewski et al. (2018, 2020) and Melis et al. (2021) during the Late Pleistocene–Holocene transition, suggesting open marine conditions. The dominance of agglutinated foraminifera can be related to the influence of a bottom water mass characterised by a low carbonate concentration and a higher content of CO_2 due to the organic matter production and high diatoms occurrence (e.g. Majewski et al., 2020; Melis et al., 2021). Moreover, the presence of significant concentration of both HBI diene II ($IPSO_{25}$) and sterols (tabs. S7, S16 and S27) is interpreted as a signal of **seasonal open marine conditions,** since HBI diene II is a proxy for sea ice, while sterols are used as proxies for open waters (e.g. Lamping et al., 2021 and references therein) (fig. 4). The percentage of organic carbon in the facies 4cs-a increases in respect to the previous facies, reaching values between 0,44 and 0,65% in the upper part of the cores (tabs. S6, S15 and S26). Higher values of TOC are associated with a more open environment (e.g. Smith et al., 2019). The change in paleoproductivity is also suggested by the higher values of Br/Ti at the top of the cores. Ca/Ti, considering the scarcity of biogenic carbonate and its anomalous trend, may be interpreted as a lithogenic element.

-Sub-facies 4cs-b: Sandy silt with silty sand intervals

This facies represents the top of the cores collected in the middle/outer shelf and lies directly above diamicton facies. From a stratigraphical point of view, this facies is considered heteropic with respect to facies 4cs-a. Compared to the facies 4cs-a, the facies 4cs-b differs mainly in a less hydrated sediment (lower % water) where sand content increases and biomarker and TOC contents decrease. The reduced TOC and biomarkers content can be related to the higher content of sand and coarse material that dilute organic matter. The presence of the foraminifer *T. earlandi*-spinose morphotype at the bottom of this facies in the core GC18, might suggest a rapid transition from subglacial to a more open sea condition. In particular, Majewski et al. (2018) highlights that *T. earlandi*-spinose dominates in proximal sub-ice shelf and paleo-ice-shelf break up facies, both characterised by intense bottom currents. The similarity with the facies 4cs-a, leads to interpret this facies as a **seasonal open marine** facies but with higher content of the coarse fraction due to the **winnowing** operated by bottom currents, which affects the outer part of the shelf (McGlannan et al., 2017; Prothro et al., 2018).

8.4 Pre LGM to present continental shelf evolution

On the basis of the complete dataset and making a comparison with the previous studies, a reconstruction of the recognized events is proposed. A scheme representing the distribution of the sedimentary facies within the gravity cores is reported in fig. 19.

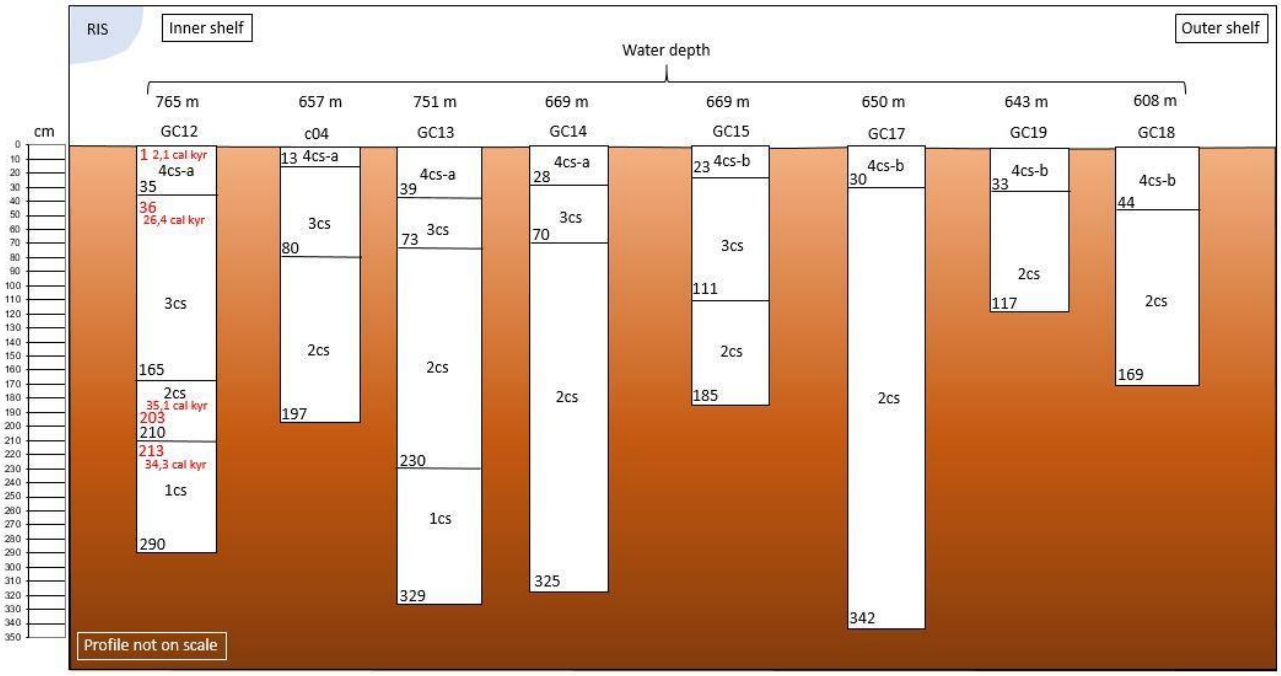

Figure 19 Scheme reporting distribution and thickness (in centimetres) of sedimentary facies identified on the continental shelf (profile not on scale). cs = continental shelf, RIS = Ross Ice Shelf. Red numbers represent depth (in cm) of dated samples.

Facies 1cs was identified in the basal part of the cores collected in the inner continental shelf. It was not identified in the core c04 (inner shelf) nor in the cores collected in the middle outer shelf, probably because the unconformity marking the upper limit of this facies was not reached during coring operation in the middle outer shelf (see figures 13-17), while the depth of this surface is unknown in the site of core c04. This facies is interpreted as **stiff diamicton** deposited in a subglacial environment. Facies 2cs prevails among the other facies and it is interpreted as **soft diamicton** which represents sediments deposited under the ice sheet. Facies 2cs was recovered above the facies 1cs in the core GC12 and GC13 and represents the basal unit of core c04 and the other cores collected in the middle/outer shelf. Both these facies are characterised by down core homogeneity, as similarly evidenced by other authors (e.g. Anderson, 1999; McGlannan et al., 2017; Prothro et al., 2018) in facies interpreted as subglacial diamicton, deposited when the ice sheet advanced across the continental shelf during the LGM and reached reaching the continental margin (e.g. Shipp et a.,

1999; Mosola & Anderson, 2006; Bart & Cone, 2012; Anderson et al., 2014; Halberstadt et al., 2016). In a similar way, the presence of these facies, or at least of the facies 2cs in all the studied cores confirms that the ice sheet reached the outer shelf of the GCB. However, the absence of radiocarbon ages in this dataset, except in the innermost core, doesn't permit to chronologically constrain this advancing phase.

A radiocarbon date obtained at the top of the facies 1cs, in the inner GCB, provided an age of 34,3 kyr BP (212-213 cm). This age set this unit in the pre-LGM. This interpretation is in line with that of the unconformity identified in the SBPs (red line, figs. 11-17), as this facies is normally found below the recognized unconformity, which records the advance of the LGM ice sheet. However, Halberstadt et al. (2018) suggested that this unconformity can also be the limit between stiff and soft diamicton (Ó Cofaigh et al., 2007). Other authors (i.e. Domack et al. 1999), studying sediment cores collected in the Glomar Challenger, considered similar old ages as a possible contamination by reworked organic matter. For this reason, the inverted age of 35,1 kyr BP obtained above the upper limit of facies 1cs, in core GC12, could indicate contamination with reworked organic matter.

Facies 3cs was identified in cores collected in the inner and middle shelf and represents a proximal sub ice shelf environment, indicating the proximity of the grounding line and suggesting the destabilisation of the ice sheet during the first retreat phases. A variation in the elements trends has been recorded in this facies. Facies 1cs and 2 cs are characterised by a constant trend of both lithogenic elements (Al, SI, K, Fe, Ti) and elemental ratios considered in this work. Facies 3cs shows slightly changes, in particular a decrease of Ca/Ti in the cores c04 and GC14, Ti (cps) in the core GC12 and an increase of Ca/Ti in the core GC12, K/Ti in the core c04, Ti (cps) and Ba/Ti in the core GC14. The sudden increase of Mn/Ti (fig. 20) in the upper part of this facies is very important to evidence the onset of deglaciation. This facies is widespread in the Ross Sea and was already recognized in the Glomar Challenger Basin (Domack et al., 1999), Whales Deep basin (McGlannan et al., 2017) and in the Western Ross Sea (Prothro et al., 2018). This facies was not identified in cores collected in the outer shelf. This could be related to the quick retreat of the ice sheet in the ERS (e.g. Mosola & Anderson, 2006; Halberstadt et al., 2016, Prothro et al., 2018), **but could also indicate a reduced ice shelf extent.**

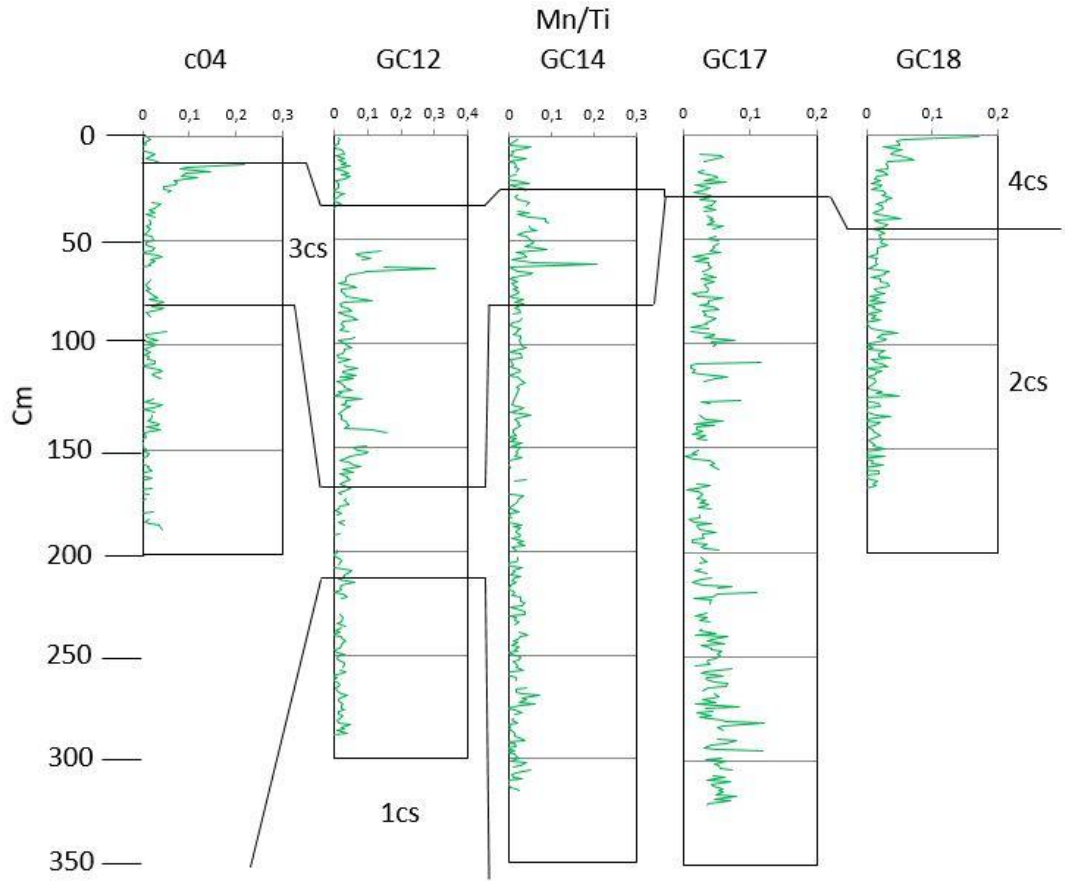

Figure 20 Mn/Ti trend of the shelf cores. Facies distribution is also reported.

In relation to the WAIS dynamic, Bart & Cone (2012) argued that the ice sheet never reached the shelf edge but was grounded in the middle shelf around 27,5 kyr BP and then retreated. However, other studies suggest that the ice sheet reached the shelf edge (e.g. Shipp et al., 1991; Mosola & Anderson, 2006; Halberstadt et al., 2016, Anderson et al., 2019) and started to retreat at 14,7 kyr BP (Bart et al., 2018) from the Whales Deep Basin first and then from the Glomar Challenger Basin (Danielson & Bart, 2023). The radiocarbon age of our glaciomarine sediments (26,3 kyr BP) obtained in the upper part of facies 3c in GC12 core, is similar to that obtained by Bart and Cone (2012) for their glaciomarine sediments, but unfortunately the lack of further radiocarbon ages in this facies of the other cores used for this thesis, prevents to confirm one of these two hypotheses.

The discrepancy between the recorded age of the sub ice shelf sediments (26,3 kyr BP, top of facies 3cs) and the age of the retreat onset from the shelf edge (e.g. Bart et al., 2018; Danielson & Bart, 2023) suggest that between the facies 3cs and the deposition of the facies 4cs-a there is a hiatus probably caused by erosional events related to the ice sheet retreat. A similar hiatus was previously reported by Licht et al. (1996) and Tolotti et al. (2013). Tolotti et al. (2013) suggested that this hiatus could be associated with the export of HSSW started during the onset of the modern conditions.

However, the presence of reworked older organic matter conditioning the age cannot be excluded (Andrews et al., 1999; Domack et al., 1999). As previously reported by several authors (e.g. Halberstadt et al., 2016; Anderson et al., 2019; Danielson & Bart, 2023), the retreat phase did not start at the same time and had different timings in each basin/trough.

The two sub-facies (4cs-a and 4cs-b) identified at the top of all cores are probably heteropic, and represent the same paleoenvironmental conditions in the inner and the outer shelf. Facies 4cs represents a seasonal open marine environment established when the ice sheet retreated from the shelf edge, similarly recognised by McGlannan et al. (2017) in the Whales Deep Basin and by Prothro et al. (2018) in the WRS. The presence of sands and clasts can be related to ice rafting, but also to other processes like winnowing and distinguishing the origin of this material can be tough, but a multiproxy approach can help to distinguish between these processes (McKay et al., 2022). Biomarkers are important indicators of paleoceanographic conditions (e.g. Müller et al., 2011; Lamping et al., 2021 and references therein). In this work, this kind of analysis was applied for the first time in the Glomar Challenger Basin. This analysis highlighted that both HBI diene II (sea ice proxy) and sterols (open marine proxy) showed an important increase of concentration, supporting the interpretation of this facies as seasonal open marine (figs. 4 and 20). The onset of a more open environment in all the GCB is also confirmed by the increase in TOC (%) (fig. 21) that correlates with the biomarkers trend. C/N ratio decreases to values lower than 10, indicating a marine origin of organic matter (Stein, 1991). Even though the peak of Mn/Ti was considered as a possible signal of deglaciation, the presence of a peak of Mn/Ti at the top of core GC18 can be related to Mn mobility under a continue sedimentation (Hillenbrand et al., 2021). The increased sand content in outer shelf cores can be related to material transported by icebergs and/or winnowing operated by bottom currents. Higher sand and IRD content caused by iceberg transit and currents winnowing was also reported on the outer shelf by e.g. McGlannan et al. (2017) in the Whales Deep Basin, Prothro et al. (2018) in several sectors of the Ross Sea.

Moving southward toward the current location of the Ross Ice Shelf, sand and IRD content decreases and biomarkers signals, representing the stronger presence of sea ice close to the ice shelf, move stratigraphically toward the top of the core (fig. 22). Also considering that the thicknesses of the open water facies are greatest in the outer shelf sector and tend to decrease toward the inner part of the shelf, this could indicate that the RIS retreat is time-transgressive, as indeed already demonstrated by Halberstadt et al. (2016).

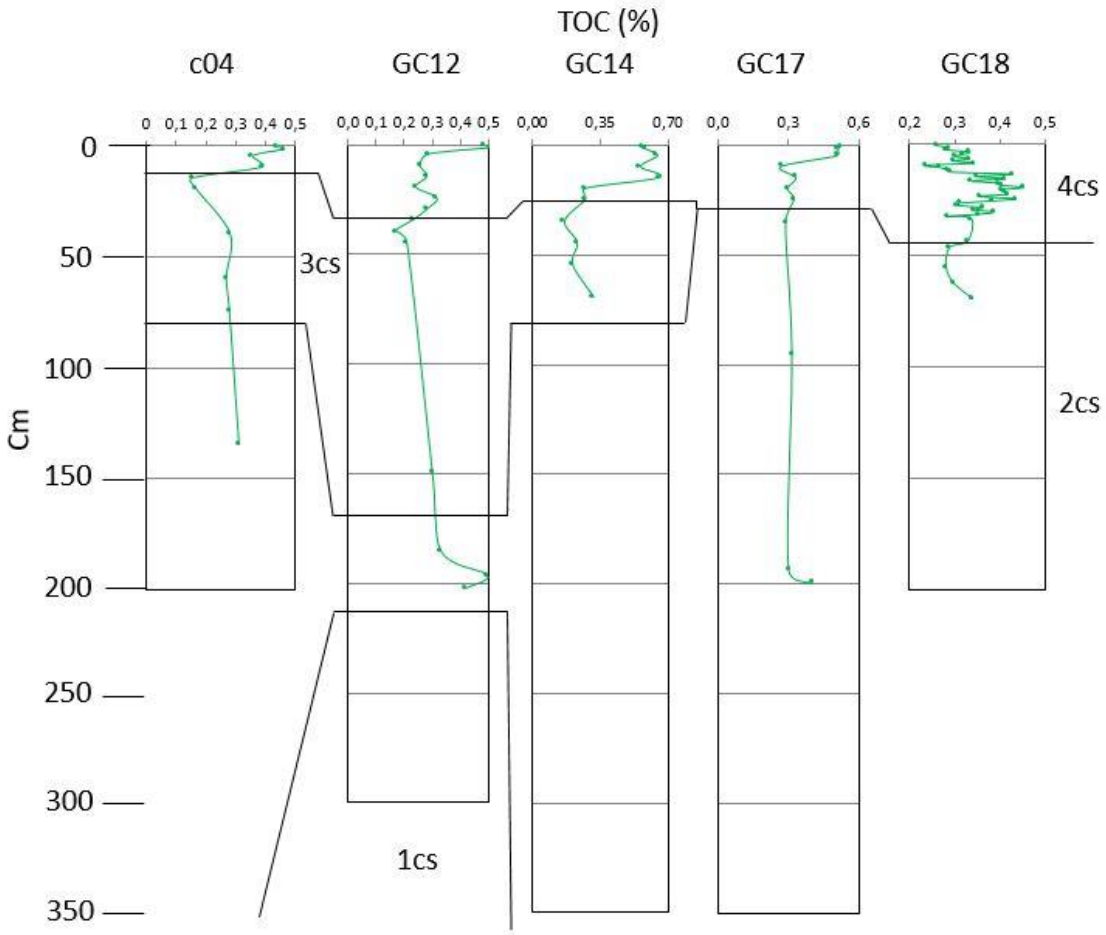

Figure 21 Percentage of TOC in the shelf cores. Distribution of the facies is also reported.

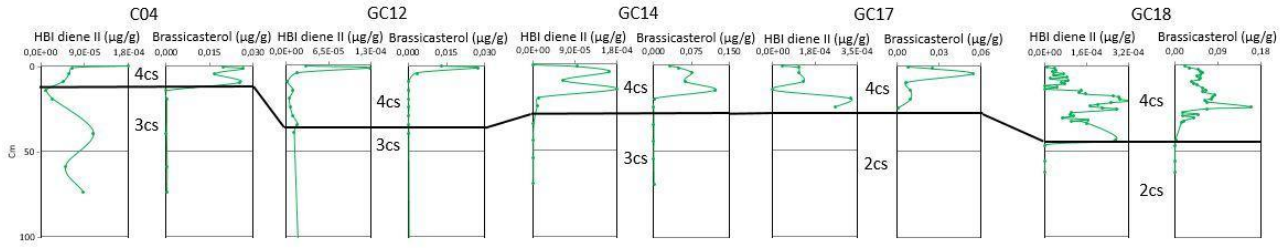

Figure 22 Variation of the concentration of HBI diene II (sea ice) and Brassicasterol (open water) from the outer shelf (GC18) to the inner continental shelf (c04 and GC12).

The strong presence of sea ice in the Glomar Challenger and the eastern Ross Sea was proposed by Anderson et al. (2014 and references therein) to explain the abundance of terrigenous material compared to diatoms-rich sediments recovered in the Western Ross Sea, where more open water conditions favour their productivity (e.g. Prothro et al., 2018). The upper part of this facies represents a more open water environment that favoured the presence of agglutinated foraminifera (tabs. S8, S17, S28, S40, S49) (Melis & Salvi, 2009; Majewski et al., 2018, 2020; Melis et al., 2021). The presence of agglutinated foraminifera can be also associated with the transition to

the Holocene (e.g. Brambati et al., 2002; Melis et al., 2021). Regarding the ages of facies 4cs, only one radiocarbon age is available for this dataset: 2,1 kyr BP. This calibrated age indicates that probably the sediment-water interface was lost during core recovery because of the methodology used (gravity core).

8.5 Slope and rise area - sedimentary facies

Three different facies (tab. 8, fig. 23) were identified by studying the three box cores and the upper 55 cm of the gravity core c20, collected in the slope and rise area. The thickness of these intervals was slightly modified from those previously identified by Ha et al. (2022) using new data.

Facies	Physical description	Physical parameters	Chemical and geochemical parameters	Geomorphological context	Interpretation
1sr	Laminated clayey silt Sparse clasts Olive brown/dark greyish brown/dark grey	High MS with a constant downcore trend: avg 427*10^-6 SI; st.dev. 167*10^-6 SI Water content: avg 42,2%; st.dev. 4,6% Sand/silt/clay: avg 4,4/71,2/24,4%; st.dev. 5,1/5,3/4,2%	XRF data shows high values of lithogenic elements and low values of biogenic elements TOC avg 0,24%, st.dev. 0,09%; C/N variable, with higher values (>10) in the coarser interval of BC1 and in core c20; HBI and sterols: not measured	Middle/lower slope	Laminated clayey silt Bottom currents Glacial
2sr	Massive sandy silt with clasts. Grey/brown/olive in BC3, dark brown/dark yellowish brown in BC2	Low MS but more variable downcore: avg 542*10^-6 SI; st.dev. 301*10^-6 SI Water content: avg 29,8%; st.dev. 7,9% Sand/silt/clay: avg 12,6/75,6/11,8%; st.dev. 4,7/4,8/3,6%	XRF data: lithogenic elements show high values with some fluctuation; low values of Br/Ti; Peak of Mn/Ti TOC avg 0,20%, st.dev. 0,05%; C/N>9 in the BC3 and between 6 and 9 in BC2, BC1, c20; HBI diene II and sterols: very low concentration	Ubiquitous	Glacigenic sediments Deposited by debris flow and ice rafting Deglacial
3sr	Sandy silt with a higher content of sand and IRD. Olive brown in BC2, BC1 and c20, dark greyish brown in BC3	Low MS: avg 401*^-6 SI; st.dev. 140*10^-6 SI Water content: avg 34,0%; st.dev. 8,7% Sand/silt/clay: avg 23,7/69,7/6,7%; st.dev. 13,8/11,9/2,7%	XRF data show a slightly increase of Ba and Br Elements related to lithological fraction decrease TOC avg 0,25%, st.dev. 0,06%; C/N <8, except 9,8 at the top of BC3; HBI diene II and sterols: low concentration	Ubiquitous	Sandy silt with IRD Seasonal open marine Holocene

Table 8 Average values and standard deviations of parameters used to identify sedimentary facies sr (slope and rise).

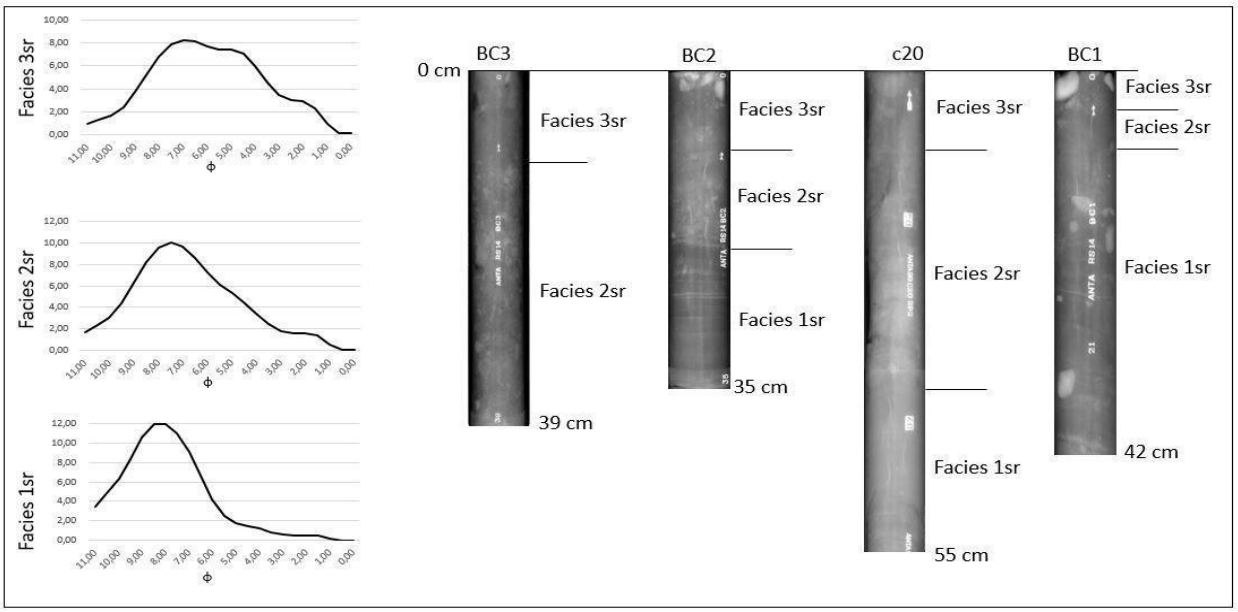

Figure 23 Radiographic images and average grain size distribution (ϕ) of the sedimentary facies. (slope and rise area).

Ha et al. (2022) studied three gravity cores collected in the same sites of the three box cores presented in this thesis. They identified three units: “A”, “B1” and “B2”, associated to three different phases: Holocene, deglacial and glacial respectively.

Facies 1sr: Laminated clayey silt

This is the facies characterised by the lower mean diameter (tabs. S62, S69, S76). The presence of the IRD in the laminated interval of BC1 (fig. 23) suggests icebergs supply. XRF data shows higher values of lithogenic elements (Ti, Si, Fe, K) than the biogenic ones (Ba, Br, Ca). Radiocarbon ages obtained in this interval show ages associated with the pre-LGM (27,1 kyr BP in BC2) and LGM period (23,3 kyr BP in c20). Considering these ages, this facies may have been deposited since the pre-LGM and during the LGM in the middle (BC2) and lower slope (c20 and BC1). It is not identified in the BC3 (tab. 8, fig. 23). Thickness of this facies ranges between 16 cm (BC2 and c20) and 32 cm (BC1). This facies represents the **glacial** period.

Facies 2sr: Massive sandy silt

Facies 2sr was identified in all the box cores and in the core c20, and its features are reported in tab. 8. One of the main distinctive features is represented by peaks of Mn/Ti. This is a signal of bottom water oxygenation (e.g. Jimenez-Espejo et al., 2020 and references therein). Both $IPSO_{25}$ (sea ice) and sterols (open waters) are present, indicating that the glacial cover was not perennial in this period (e.g. Lamping et al., 2021 and references therein). This facies is interpreted as **glacigenic sediments** deposited through debris flows and by icebergs during the **deglaciation**. Radiocarbon ages range from 20,8 kyr BP (BC3) to 13,6 kyr BP (BC1). These dates align with those found by Ha et al. (2022) and interpreted as a deglacial phase. The older age of 27,4 kyr BP (BC3), considering the location of the box core, may suggest the presence of reworked material.

Gales et al. (2021), studying gullies and paleo-gullies at the mouth of the Glomar Challenger Basin, considered previously available grain size data interpreting the lower part of the BC3 as glacigenic sediments. Considering the new grain size analyses that highlight a sand content increase at 11 cm and XRF data that point out rapid changes at the same depth (e.g. Zr/Rb, Si/Ti, Fe/Ti) (see tab. 8 and fig. S41) the upper limit of this facies is here better defined.

Facies 3sr: Sandy silt with IRD

Considering all the characteristics: increase of sand, clasts content, magnetic susceptibility, TOC, and biomarkers (chapter 7.6, tab. 8 and fig. 23), this facies can be interpreted as seasonal **open marine** facies. This is also confirmed by the decrease of lithogenic elements and the increase of biogenic ones, even though the increase of biogenic elements is less evident in the BC1. This facies (tab. 8, fig. 23) is present at the top of each box core and at the top of the gravity core c20 with a thickness ranging around 10 cm in BC3, BC2 and c20, and it is 5 cm thick in the BC1. Radiocarbon ages, ranging between 11,4 kyr (BC2) and the present place this facies in the Holocene. The relatively old radiocarbon age obtained at the top of core c20 (5,0 kyr BP) is probably due to the sampling methodology (gravity core) that tends to lose the top. This age is consistent with the top age of gravity cores studied by Ha et al. (2022) in the same area e (RS14-GC2 of 5,7 kyr BP).

8.6 Pre LGM to present evolution of the slope and rise area

Considering the all dataset (supplementary 2 and tab. 8) and the facies distribution (fig. 24), a reconstruction of the slope and rise evolution since the pre-LGM is here proposed.

According to the radiocarbon ages (tab. 5), the facies 1sr was deposited since the pre-LGM and during the LGM, when the ice sheet advanced across the continental shelf and reached the shelf edge (Shipp et al., 1999; Mosola & Anderson, 2006; Halberstadt et al., 2016). Radiocarbon ages suggest that the glacial phase lasted at least until 23,3 kyr BP (c20). The high sediments input from the shelf (Ha et al., 2022 and references therein) prevented the recovery of this facies in the BC3, collected near the upper slope. Preservation of laminations of this facies are associated with a reduced productivity (e.g. Lucchi et al., 2002) due to the perennial ice cover. TOC (%) is higher in this facies (fig. 25), but C/N ratio is higher as well. This is likely related to the presence of reworked organic matter, as suggested also by Ha et al., 2022. Ba/Ti of box cores and c20 shows low values and this might confirm the low productivity conditions.

Then, when the ice sheet began to retreat, the slope and rise area started to experience a seasonal ice cover, highlighted by several parameters. Peaks of Mn/Ti (fig. 26) were identified in the all dataset. In particular in core c20, Mn/Ti peaks were measured in an interval characterised by oxidised laminae. This represents the reoxygenation of the bottom waters during this phase (e.g. Jimenez-Espejo et al., 2020 and references therein).

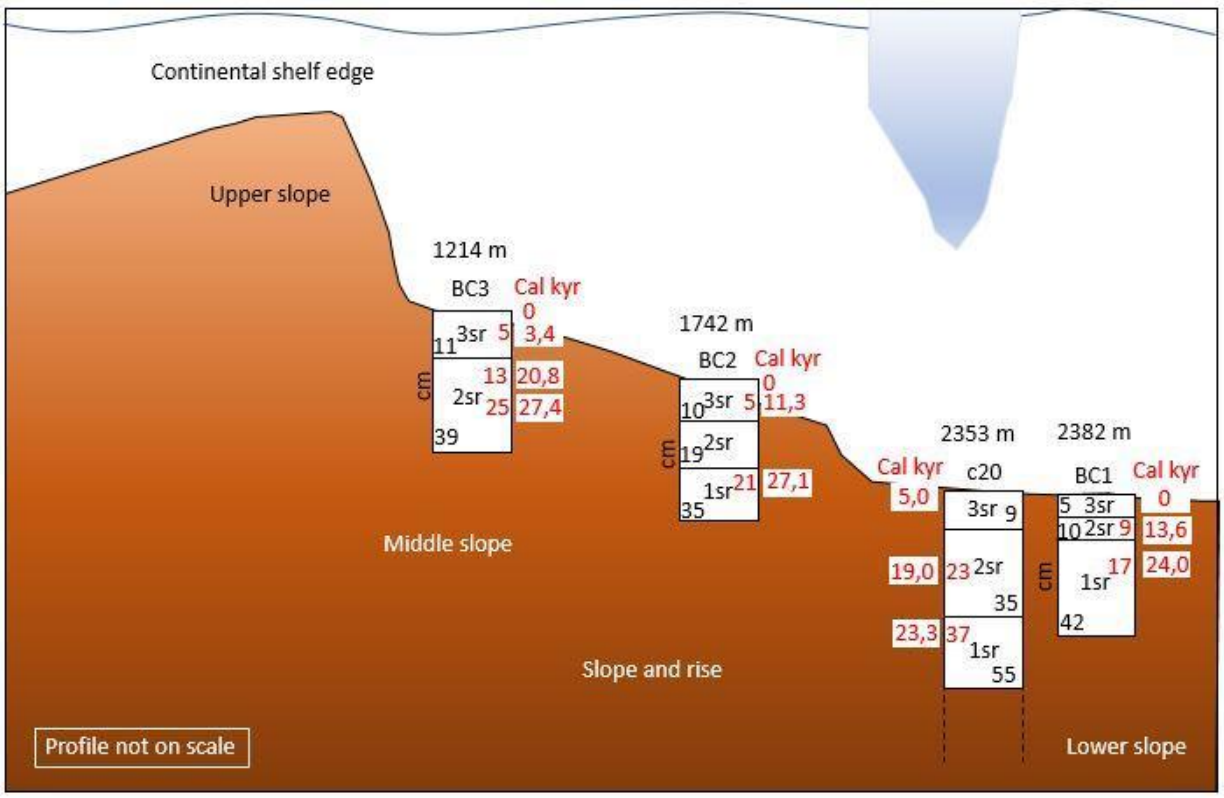

Figure 24 Scheme reporting distribution and thickness of sedimentary facies identified in the slope and rise area (profile not on scale). sr = slope and rise. Red numbers reported inside core frames represent depth (in cm) of dated samples.

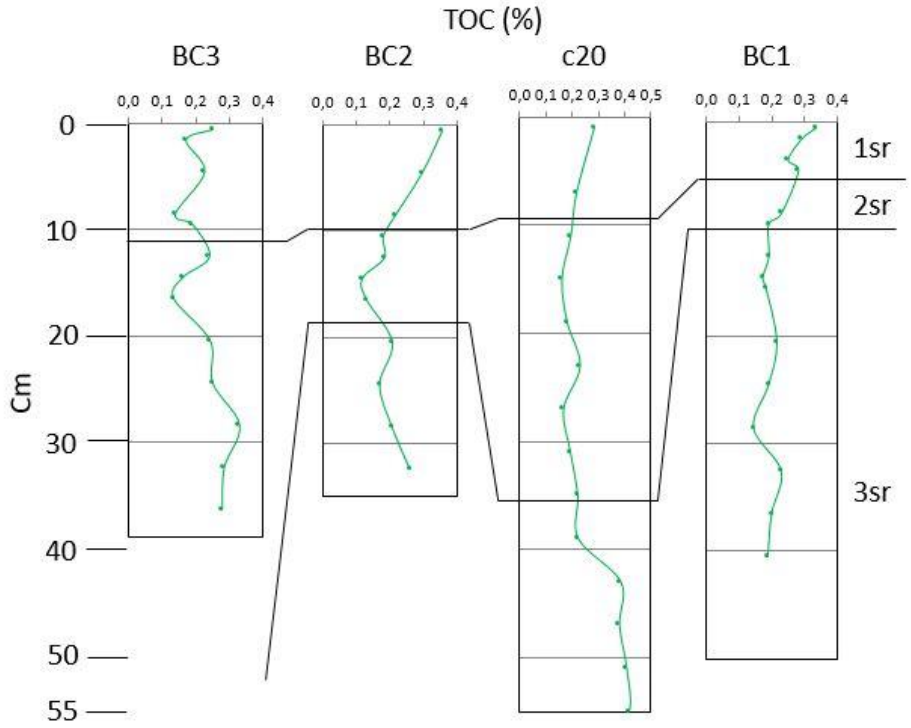

Figure 25 TOC (%) of the box cores and the gravity core collected in the slope and rise area. Facies distribution is also reported.

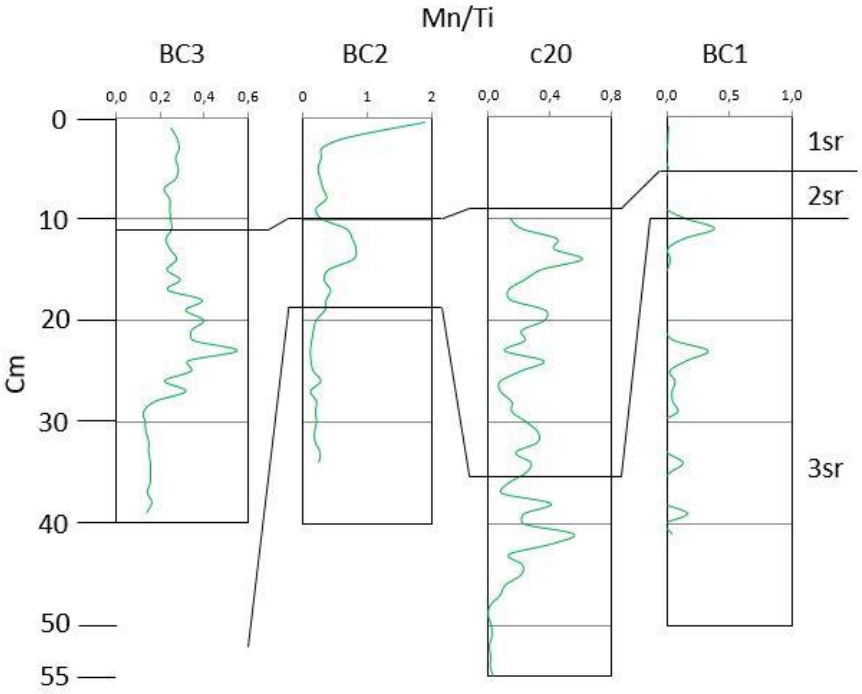

Figure 26 Mn/Ti ratio in the box cores and the gravity cores collected in the slope and rise area. Facies distribution is also reported.

The increased occurrence of the biomarkers (both $IPSO_{25}$ and sterols) (fig. 27) together with the C/N ratio decrease, support an increase in marine productivity. Strong presence of clasts (tab. 8, fig. 23) also represents a signal of a seasonal cover with floating icebergs (e.g. Melis et al., 2021). The increased content of the coarse fraction, in particular in the box cores collected closer to the shelf edge, can also be delivered to the slope from the shelf via mass movements (Pudsey, 2000, Ha et al., 2022).

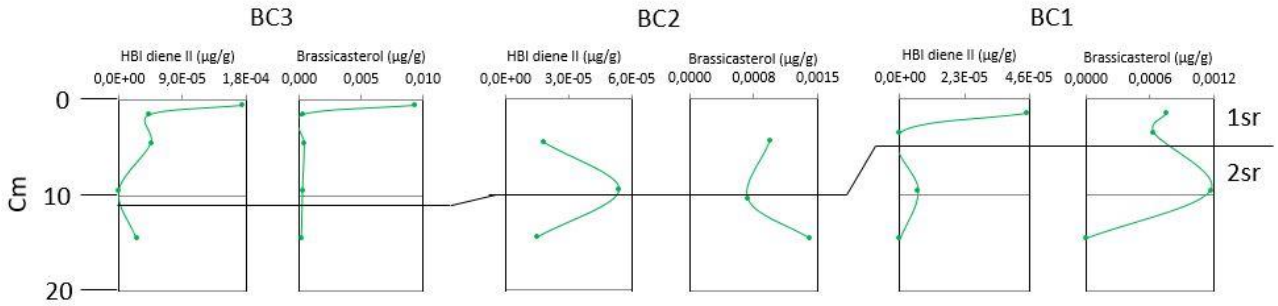

Figure 27 Biomarker concentration (HBI diene II and Brassicasterol) of the three box cores.

Radiocarbon ages are older in the BC3 (27,4 kyr BP at 24-25 cm and 20,8 kyr BP at 12-13 cm) and in c20 (24,4 kyr BP at 36-37 cm and 20,0 kyr BP at 22-23 cm), than in BC1 (13,6 kyr BP at 8-9 cm). This wide range of ages is consistent with radiocarbon ages obtained by Ha et al. (2022). Older ages are probably caused by reworked organic matter coming from the shelf edge due to the ice sheet destabilisation, considering the nature of this facies, while the age obtained for the BC1 is more consistent with a deglacial phase settled between the LGM and the Holocene and is coherent with the similar age (around 14,7 kyr BP) proposed by Bart et al. (2018) in the Whales Deep for the ice sheet retreat start. Golledge et al. (2014) suggested that the largest moment of the ice sheet retreat happened during the meltwater pulse 1A (MWP-1A) between 15 and 13 kyr BP. Their model also suggested that the retreat of the ice sheet was accelerated by subsurface ocean warming and by the restart of the Atlantic Meridional Overturning Circulation. However, sea level rise associated with MWP-1A did not seem to be strongly influenced by the AIS retreat that happened during this time frame (Prothro et al., 2020; Danielson & Bart, 2023). Considering MWP-1A, the ice sheet destabilisation may have started after the LGM, starting to retreat during the MWP-1A, as also suggested by the increase in sand and clasts (>2 mm) content. The radiocarbon ages obtained from facies 2sr of BC1 (13,6 kyr BP) is coherent with this event.

The ice sheet retreated from the shelf edge during the Holocene (11,4 kyr BP in BC2), as suggested by e.g. Danielson & Bart (2023). They proposed that the ice sheet first retreated in the WDB and formed an embayment around 11,5 cal kyr BP (Bart & Kratochvil, 2022) and then, after this phase, the ice sheet retreated also in the GCB. After that, seasonal open marine conditions were established in the outer shelf and the continental margin. as confirmed by the increasing of the productivity proxies (biomarkers, organic matters, Ba/Ti) at the top of the box cores.

9. Conclusions

The multidisciplinary study conducted in the framework of this thesis aims to propose the reconstruction of the events that have characterised the Western Antarctic Ross sheet and shelf dynamic in the Glomar Challenger Basin and the adjacent slope and rise area. Geophysical data helped to characterise geomorphological features of the studied area, and to identify an unconformity in the shelf area, previously interpreted as the LGM unconformity (e.g. Anderson et

al., 2019 and references therein). This unconformity represents the boundary between stiff and soft diamicton identified on the shelf cores and, considering the current interpretation proposed in the Ross Sea by some authors, the unconformity could be the boundary between pre-LGM and LGM sediments. For the slope and rise area, results previously published by Gales et al. (2021) and Ha et al. (2022) were improved with new data and radiocarbon ages.

Combining geophysical and sedimentological datasets and using several proxies/physical, chemical, geochemical, micropaleontological) allowed to 4 sedimentary facies, and two sub-facies, on the continental shelf (cs) and 3 facies in the slope and rise area (sr). These facies can be associated to three different phases: glacial, deglacial and seasonal open water conditions.

Using the sedimentary facies, an evolution model for both the Glomar Challenger Basin and the slope and rise area, since the last glacial, has been proposed.

Stiff and soft diamicton on the continental shelf and laminated clayey silt on the slope and rise were deposited during the glacial phase, when the ice sheet advanced on the shelf reaching the shelf edge, while the slope and rise was covered by perennial ice. Both stiff and soft diamicton, dated in the innermost core, report two pre-LGM ages: 34,3 kyr and 35,1 kyr BP respectively. While the age of the stiff diamicton is considered reliable since it was obtained from sediments recovered under the LGM unconformity, the age of the soft diamicton is not in stratigraphic order likely because of the presence of reworked organic matter in the sediments mixed by the advancing ice sheet, as suggested by Andrews et al. (1999) and Domack et al. (1999). Then, when the ice sheet reached the continental shelf edge (e.g. Halberstadt et al., 2016), a laminated clayey silt facies was deposited on the middle and lower slope and rise area. Radiocarbon ages of this facies range between 27,1 kyr to 23,3 kyr BP. According to these ages, this sediment was deposited during the LGM (26,5 - 19,0 kyr BP from Clark et al., 2009).

The deglacial phase started around the end of the LGM (20,8 to 13,6 kyr BP) and a massive sandy silt facies was deposited on the slope. Even older ages were obtained from the box core collected closer to the shelf edge, but considering that the upper slope is steep and characterised by gullies and slide scars (Gales et al., 2021), that older age (27,4 kyr BP) is probably related to reworked sediments. The other ages are more consistent with timing of retreat inferred by other authors, and in particular the age obtained in the deepest box core (13,6 kyr BP) is the most reliable, since it was less affected by shelf sediments considering its distance from the shelf edge and because its consistent with a larger phase of retreat set during MWP-1A, as proposed by Golledge et al. (2014).

According to Bart et al. (2018) the deglaciation started in the Whales Deep Basin around 14,7 cal kyr BP and the retreat in the Glomar Challenger started after 11,5 cal kyr BP, when an embayment opened in the Whales Deep. After that, the ice sheet started to retreat from the shelf edge, depositing a glaciomarine diamicton (sub ice shelf facies) on the continental shelf. The only radiocarbon age for this facies was obtained from the innermost core: 26,3 kyr BP. Such an old age probably indicates a hiatus between this facies and the seasonal open marine one, but it could also be related to reworked organic matter. The absence of the glaciomarine diamicton in the outer shelf cores may be related to erosive events of a rapid retreat of the ice sheet, in agreement with other authors (e.g. Mosola & Anderson, 2006; Tolotti et al., 2013; Halberstadt et al., 2016). When the ice sheet retreated, seasonal open marine conditions were established in the slope and rise area, where a sandy silt facies was deposited during the Holocene: 11,4 kyr BP to the present. On the shelf, the two heteropic sub-facies identified (sandy silt with high content of sand and clasts, in the middle/outer shelf, and silt with low sand and clasts, in the inner/middle shelf) are characterised by agglutinated foraminifera and biomarkers. These features allowed us to interpret these facies as seasonal open marine conditions established when the ice sheet retreated.

This model fits with those proposed by other authors (e.g. Danielson & Bart, 2023 and references therein). They proposed that the ice sheet advanced and retreated with a different timing in each trough/basin, due to their different characteristics. Considering radiocarbon ages obtained in the slope and rise area (this thesis), the retreat in the GCB started when the AIS was already retreating from other sectors of the Ross Sea (WRS and WDB). The lack of radiocarbon ages in the shelf cores prevents a more detailed reconstruction. As previously reported (e.g. Halberstadt et al., 2016; Danielson & Bart, 2023), the AIS retreat was quicker in the ERS than in the WRS during the Holocene. This is evidenced by the lack of the glaciomarine diamicton (facies 3cs) in the outer shelf gravity cores.

Supplementary

In this section, a more detailed description of sediment parameters is reported for each core with figures and tables.

Supplementary 1 - Glomar Challenger Basin

ANTA96-c04

This core has been collected in the inner continental shelf, in a secondary basin of the Glomar Challenger Basin (tab. 3, fig. 6). Geophysical data is not available for this site.

Core description and Radiography

The core (fig. S1) is characterised, from the bottom to 39/40 cm, by a sandy and gravelly material within a fine matrix in which several random oriented clasts are present (fig. S1). The colour changes from olive grey (5Y 4/2) to grey (5Y 5/1). They are characterised by dimension from sub centimetric to pluri-centimetric and a sub-angular shape, but rounded and angular clasts are also present. A muddy sediment with abundant millimetric to pluri-centimetric clasts (denser interval in the radiography) is present from 39/40 to 13 cm. This section is characterised by a brownish colour: light brownish grey (2,5Y 6/2) between 39 and 16 cm and light olive brown (2,5Y 5/4) between 16 and 13 cm. An irregular contact marks the transition with the above grey (5Y 5/1) more hydrated silt sediment characterising the top of the core (13-0 cm). Rare clasts are present in this interval. The upper 2,5 cm are made of hydrated oxidised (olive green, 5Y 5/3) clay.

Clasts have been counted using the method of Grobe (1987). The mobile average on an interval of 5 cm (tab. S1, fig. S1) shows a fluctuation in the number of clasts >2 mm from the bottom to 15 cm. The upper part of the core shows a rapid decrease in the number of clasts.

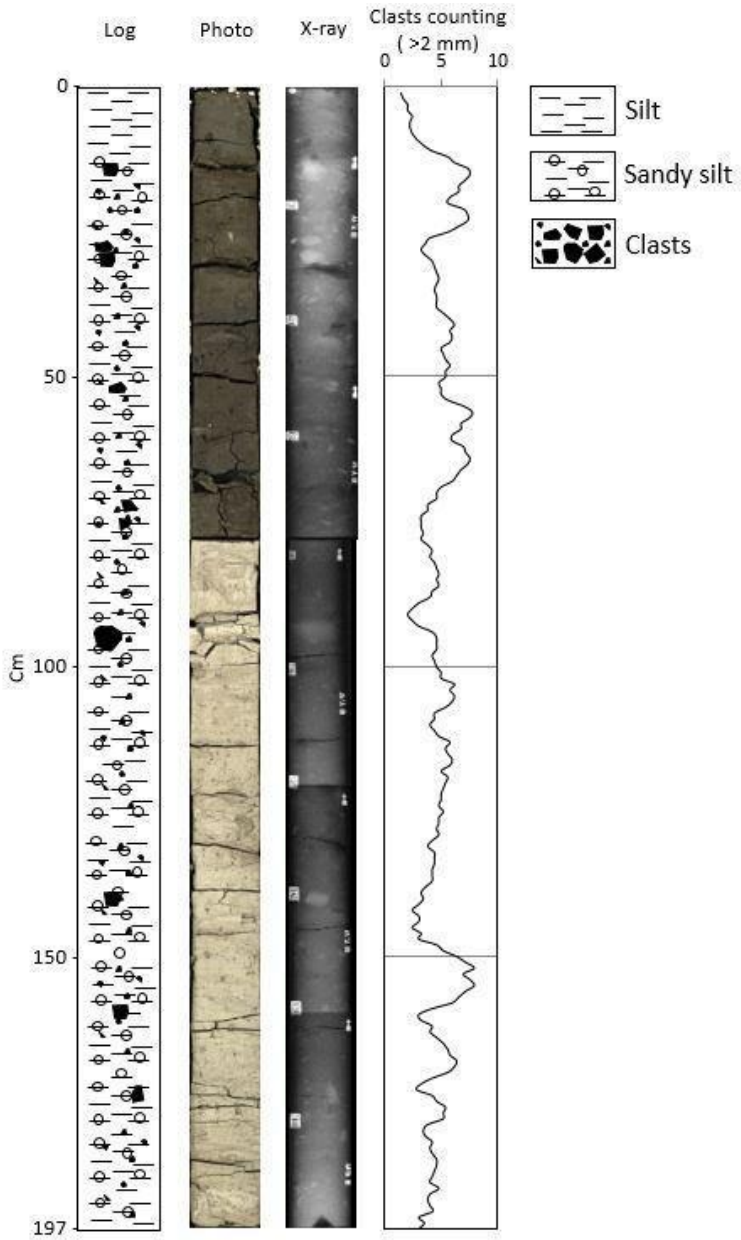

Figure S1 Lithologic log, photo, radiography, clasts counted using the Grobe (1987) method (mobile average interval: 5 cm) of the core c04.

Depth (cm)	Clasts >2mm (num.)	Mobile average	Depth (cm)	Clasts >2mm (num.)	Mobile average	Depth (cm)	Clasts >2mm (num.)	Mobile average
0-1	0	1,4	47-48	6	5,8	94-95	3	4,6
1-2	0	1,6	48-49	3	5,4	95-96	6	4,6
2-3	3	2,0	49-50	7	5,4	96-97	5	4,6
3-4	2	2,0	50-51	5	4,8	97-98	6	4,2
4-5	2	2,4	51-52	8	5,0	98-99	3	4,4
5-6	1	2,2	52-53	4	5,0	99-100	3	4,6
6-7	2	2,2	53-54	3	5,6	100-101	6	5,0
7-8	3	2,4	54-55	4	7,0	101-102	3	5,0
8-9	4	2,8	55-56	6	7,8	102-103	7	6,2
9-10	1	3,4	56-57	8	7,6	103-104	4	5,8
10-11	1	4,2	57-58	7	6,8	104-105	5	6,2
11-12	3	5,6	58-59	10	6,8	105-106	6	6,0
12-13	5	6,2	59-60	8	6,0	106-107	9	5,4
13-14	7	7,4	60-61	5	6,0	107-108	5	4,4
14-15	5	7,6	61-62	4	7,0	108-109	6	4,4
15-16	8	7,2	62-63	7	7,2	109-110	4	4,0
16-17	6	6,6	63-64	6	7,6	110-111	3	4,4
17-18	11	6,6	64-65	8	7,4	111-112	4	4,8
18-19	8	5,8	65-66	10	6,8	112-113	5	5,8
19-20	3	5,6	66-67	5	6,4	113-114	4	5,4
20-21	5	7,0	67-68	9	6,0	114-115	6	5,6
21-22	6	7,4	68-69	5	5,0	115-116	5	6,0
22-23	7	7,4	69-70	5	4,6	116-117	9	5,8
23-24	7	6,6	70-71	8	4,6	117-118	3	5,0
24-25	10	5,6	71-72	3	3,8	118-119	5	5,6
25-26	7	4,0	72-73	4	3,8	119-120	8	5,4
26-27	6	3,6	73-74	3	3,2	120-121	4	5,2
27-28	3	3,2	74-75	5	3,2	121-122	5	5,0
28-29	2	3,6	75-76	4	3,2	122-123	6	5,0
29-30	2	4,2	76-77	3	3,4	123-124	4	4,8
30-31	5	4,4	77-78	1	3,2	124-125	7	5,2
31-32	4	4,6	78-79	3	3,8	125-126	3	4,8
32-33	5	4,8	79-80	5	4,2	126-127	5	4,8
33-34	5	4,6	80-81	5	4,0	127-128	5	4,6
34-35	3	4,4	81-82	2	4,4	128-129	6	4,8
35-36	6	4,6	82-83	4	4,6	129-130	5	4,2
36-37	5	4,6	83-84	5	4,8	130-131	3	3,8
37-38	4	4,6	84-85	4	4,6	131-132	4	4,4
38-39	4	5,2	85-86	7	4,8	132-133	6	4,4
39-40	4	5,8	86-87	3	4,2	133-134	3	4,4
40-41	6	6,2	87-88	5	4,0	134-135	3	4,2
41-42	5	5,8	88-89	4	3,0	135-136	6	4,2
42-43	7	6,0	89-90	5	2,4	136-137	4	4,2
43-44	7	5,8	90-91	4	2,0	137-138	6	3,6
44-45	6	5,0	91-92	2	2,4	138-139	2	3,2
45-46	4	5,2	92-93	0	3,0	139-140	3	3,4
46-47	6	5,4	93-94	1	4,2	140-141	6	3,0

Depth (cm)	Clasts >2mm (num.)	Mobile average	Depth (cm)	Clasts >2mm (num.)	Mobile average	Depth (cm)	Clasts >2mm (num.)	Mobile average
141-142	1	2,4	160-161	3	3,2	179-180	5	3,4
142-143	4	3,0	161-162	4	4,2	180-181	3	3,6
143-144	3	3,0	162-163	1	4,0	181-182	4	4,2
144-145	1	2,4	163-164	2	4,6	182-183	3	4,0
145-146	3	3,2	164-165	6	5,2	183-184	2	4,2
146-147	4	3,0	165-166	8	5,6	184-185	6	4,6
147-148	4	4,6	166-167	3	5,8	185-186	6	4,6
148-149	0	5,2	167-168	4	6,4	186-187	3	4,4
149-150	5	6,4	168-169	5	6,2	187-188	4	4,2
150-151	2	7,2	169-170	8	5,6	188-189	4	4,0
151-152	12	8,0	170-171	9	4,2	189-190	6	4,8
152-153	7	7,0	171-172	6	3,2	190-191	5	4,0
153-154	6	7,6	172-173	3	2,8	191-192	2	3,8
154-155	9	8,0	173-174	2	4,2	192-193	3	4,0
155-156	6	7,2	174-175	1	4,6	193-194	8	4,3
156-157	7	6,6	175-176	4	5,4	194-195	2	3,0
157-158	10	6,0	176-177	4	5,2	195-196	4	3,5
158-159	8	4,2	177-178	10	5,2	196-197	3	3,0
159-160	5	3,0	178-179	4	3,8			

Table S1 Clasts >2 mm counted using the method of Grobe (1987) and mobile average (interval of 5 cm) of the core ANTA96-c04.

Physical analyses - Compression strength, Water content and Grain size

Compressive strength (CS) (tab. S2, fig. S2) shows a decreasing trend from the bottom to the top core with highest value at the bottom (2,3 kg/cm^2) and lowest value of 0,1 kg/cm^2 at the top core.

Water content (w%) (tab. S3, fig. S2) changes along the core, gradually increasing from the bottom of the core (19,5%) toward the top where it reaches the highest values (43,6%).

Grain size analyses (tab. S4, fig. S2) highlight that silt is the main sedimentary component along the core, varying from 88,0% to 65,1% (avg 74,1%). Sand varies from 24,7% to 4,7% (avg 15,1%). It tends to decrease toward the top core, while clay varies from 16,5% to 6,0% (avg 10,8%), highlighting the lowest values at the top and at the bottom core.

Mean diameter (Mz) shows values between 5,5 ϕ (coarse silt) and 7,2 ϕ (fine silt) (avg 6.38 ϕ - medium silt) and the trend of the parameter is fining up. The sediment of core C04 is generally very poorly sorted (avg 2,14 ϕ) and only the top core is characterised by a poorly sorted sediment. The average value of skewness (Sk) is -0,08. This core is characterised by negative asymmetry between 75 and 15 cm. Samples in the upper 15 cm and from the bottom to 75 cm shows symmetry. The median diameter (Md) shows a decreasing up core trend. See fig. S2 and tab. S4.

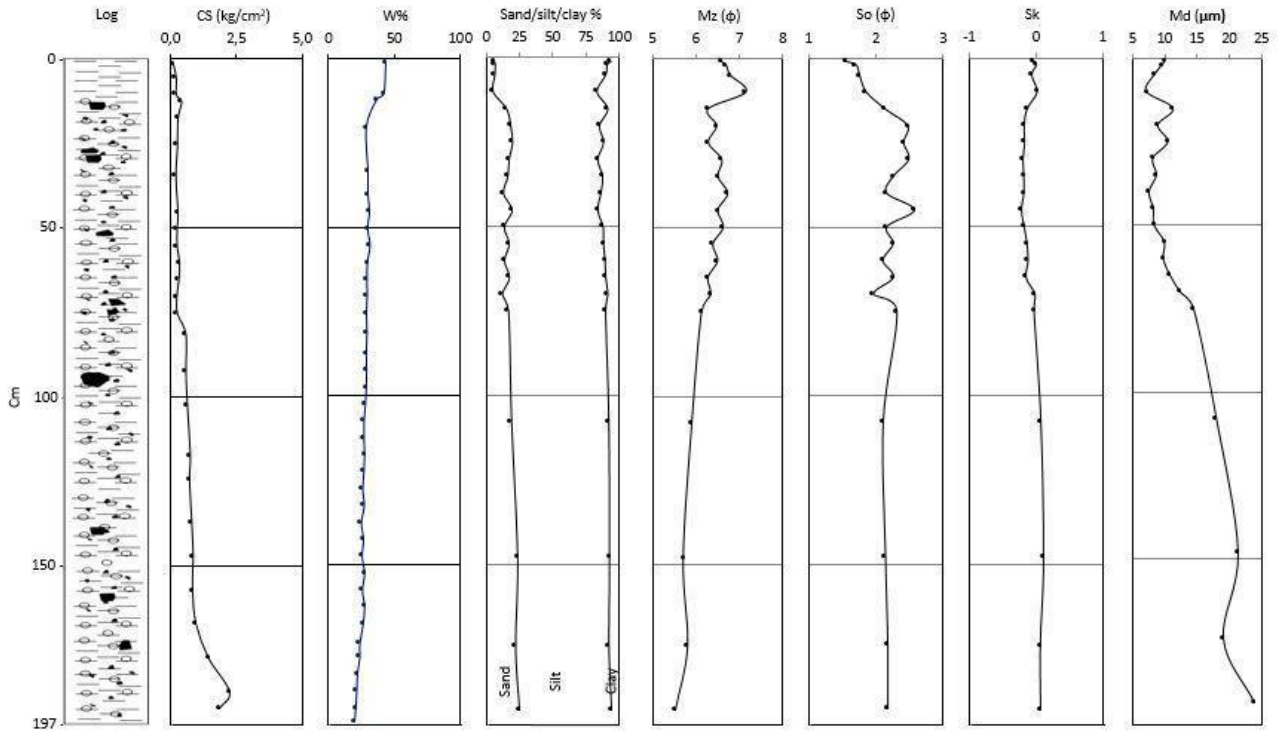

Figure S2 Physical parameters of the core c04.

Depth (cm)	CS (Kg/cm²)
1-2	0,1
5-6	0,2
10-11	0,2
12-13	0,4
17-18	0,3
25-26	0,2
34-35	0,2
45-46	0,3
50-51	0,2
55-56	0,2
60-61	0,3
65-66	0,3
70-71	0,2
75-76	0,2
81-82	0,6
92-93	0,6
102-103	0,6
117-118	0,7
124-125	0,7
137-138	0,8
147-148	0,8
157-158	0,8
167-168	1,0
177-178	1,4
187-188	2,3
192-193	1,9

Table S2 Compressive strength of the core ANTA96-c04.

Depth (cm)	W%
1-2	43,6
10-11	42,0
12-13	36,3
20-21	28,4
33-34	29,8
40-41	29,8
45-46	31,0
50-51	29,5
55-56	31,4
60-61	29,4
65-66	29,0
70-71	29,2
75-76	28,6
81-82	29,0
87-88	28,5
92-93	28,7
97-98	28,5
102-103	27,8
107-108	26,7
112-113	26,7
117-118	27,2
122-123	26,7
127-128	25,7
132-133	26,9
137-138	24,7
142-143	26,3
147-148	25,3
152-153	27,2
157-158	25,5
162-163	27,2
167-168	26,1
173-174	23,5
177-178	23,4
182-183	21,6
187-188	21,1
192-193	20,4
196-197	19,5

Table S3 Water content of the core ANTA96-c04.

Distribution curves (fig. S3) highlights different situations, starting with a unimodal distribution from the bottom to 108 cm. The primary mode varies between 4,5 and 5,0 ϕ (44,19 - 31,25 µm). Samples collected at 75 and 70 cm highlight a transition from the upper part of the core with a shift to finer sediment. These two samples have a mode between 6,0 and 6,5 ϕ (15,62 - 11,05 µm). From 65 to 60 cm and at 15 cm, the primary mode changes to 7,0 ϕ. From 55 to 20 cm, curves present a bi-modal distribution, with a primary mode between 7,0 and 7,5 ϕ (7,81 - 5,52 µm) and enrichments of coarse silt and sandy material. The upper part of the core (10-0 cm) highlights a greater presence of silt with unimodal distribution (mode around 7,0 ϕ (7,81 µm)).

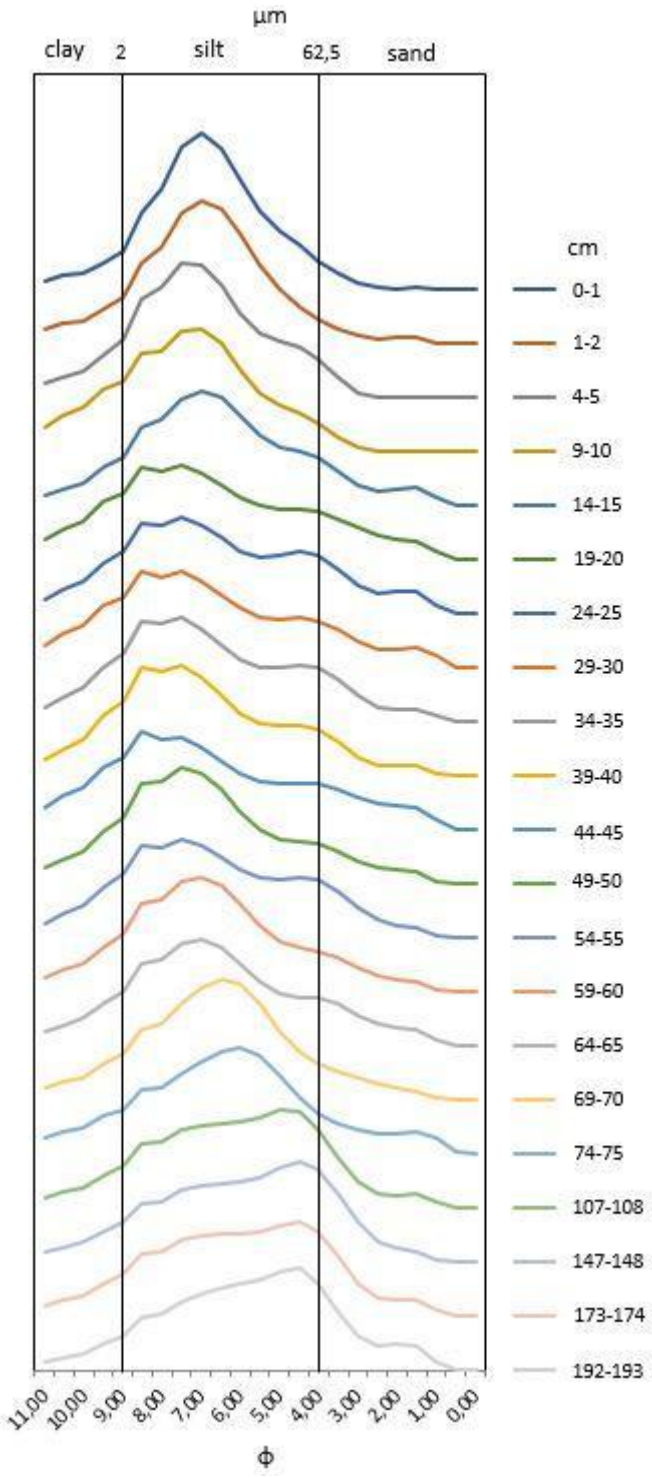

Figure S3 Grain size distribution curves of core c04.

c04	Sand (%)	Silt (%)	Clay (%)	Mz (φ)	So (φ)	Sk	Md (μm)	Primary mode (φ)
0-1	5,6	88,0	6,4	6,58	1,55	-0,05	10,0	7,00
1-2	6,3	84,6	9,1	6,70	1,70	0,01	9,6	7,00
4-5	5,9	83,9	10,2	6,79	1,75	-0,06	8,4	7,50
9-10	4,7	78,8	16,5	7,15	1,85	0,02	7,2	7,00
14-15	14,9	76,4	8,7	6,29	2,13	-0,14	11,3	7,00
19-20	18,0	67,3	14,6	6,48	2,47	-0,18	9,0	7,50
24-25	19,4	68,9	11,7	6,29	2,42	-0,17	10,5	7,50
29-30	16,8	67,2	15,9	6,60	2,49	-0,20	8,2	8,50
34-35	15,9	71,7	12,4	6,51	2,26	-0,19	8,8	7,50
39-40	12,5	73,8	13,7	6,73	2,16	-0,19	7,6	7,50
44-45	19,0	65,1	15,9	6,51	2,58	-0,22	8,3	8,50
49-50	13,2	74,7	12,1	6,63	2,16	-0,18	8,4	7,50
54-55	16,9	71,3	11,8	6,40	2,26	-0,14	10,0	7,50
59-60	13,3	76,0	10,7	6,50	2,10	-0,12	9,8	7,00
64-65	17,1	72,7	10,1	6,28	2,26	-0,15	10,9	7,00
69-70	11,8	79,5	8,7	6,35	1,96	-0,01	12,4	6,50
74-75	16,4	73,4	10,2	6,14	2,31	-0,03	14,5	6,00
107-108	18,8	73,3	7,9	5,91	2,11	0,08	18,0	5,00
147-148	23,3	69,3	7,4	5,72	2,14	0,12	21,3	4,50
173-174	21,8	70,4	7,8	5,82	2,18	0,07	19,1	4,50
192-193	24,7	69,3	6,0	5,54	2,18	0,07	23,9	4,50

Table S4 Grain size parameters of the core ANTA96-c04.

Chemical and geochemical analyses - Elemental analyses, Organic matter and Biomarkers

The correlation (tab. S5) between the elements highlighted a strong correlation between Al, Si, K, Ti, Fe, Rb, Zr, Sr and Ba. K, Fe and Rb show also a good correlation with Br. Ca does not correlate with other elements. Al, Si, K, Ti, Fe, Rb, Zr, Sr and Ba share the same lithogenic origin. Ti (cps) trend has been chosen to show the trend of this group of elements (fig. S4). Several element ratios have been chosen as well (fig. S4).

c04	Al_cps	Si_cps	K_cps	Ca_cps	Ti_cps	Fe_cps	Br_cps	Rb_cps	Sr_cps	Zr_cps	Ba50_cps
Al_cps		2,43E-89	2,93E-92	0,003807	6,75E-71	2,90E-72	1,17E-09	3,70E-65	7,05E-37	3,76E-39	1,74E-55
Si_cps	**0,96653**		1,43E-89	0,00024	7,94E-75	7,61E-76	4,34E-08	8,93E-65	8,13E-40	2,04E-41	5,08E-67
K_cps	**0,96948**	**0,96678**		0,080827	4,67E-101	7,51E-91	2,20E-11	8,76E-78	6,10E-38	1,19E-41	9,45E-61
Ca_cps	0,23492	0,2956	0,14302		0,016125	0,001272	0,013063	0,00374	6,28E-10	1,78E-06	3,37E-06
Ti_cps	**0,93979**	**0,94691**	**0,97688**	0,19618		9,57E-90	1,44E-10	6,73E-76	1,60E-43	8,32E-47	1,42E-63
Fe_cps	**0,94238**	**0,94861**	**0,96809**	0,26071	**0,96696**		1,43E-13	1,77E-88	2,47E-36	1,91E-36	2,61E-65
Br_cps	0,47114	0,42893	*0,51169*	-0,20225	0,49317	*0,55649*		1,54E-17	0,027299	0,023463	1,26E-08
Rb_cps	**0,92758**	**0,92668**	**0,9517**	0,23536	**0,9487**	**0,96561**	**0,62365**		1,21E-37	2,60E-37	3,22E-68
Sr_cps	**0,81489**	**0,83265**	**0,82155**	0,47782	**0,85242**	**0,81137**	0,18025	**0,81971**		4,86E-88	4,92E-51
Zr_cps	**0,82881**	**0,84153**	**0,84277**	0,3786	**0,86783**	**0,8121**	0,18495	**0,81763**	**0,96513**		1,32E-50
Ba50_cps	**0,90081**	**0,9318**	**0,91647**	0,36904	**0,92377**	**0,92794**	0,444	**0,93439**	**0,88516**	**0,88352**	

Table S5 Pearson elements correlation of the core c04. Bold and underlined values represent moderate to strong correlation. Underlined values in italics represent low correlation.

Ti (cps) is characterised by values that fluctuate along the core. Zr/Rb has a value of 1,5 from the bottom up to 10 cm. The upper part of the core is characterised by lower values. Si/Ti is characterised by a constant trend, which slightly drops between 100 cm and 80 cm. Fe/Ti has a constant trend. K/Ti shows a slightly increasing trend from the bottom of the core up to 150 cm. Then, it slightly decreases from 150 cm to 85 cm. After that, it slightly increases toward the top of the core. Br/Ti is characterised by a constant trend from the bottom to 13 cm and it increases in the upper part of the core. Ba/Ti shows a constant trend along the core. Ca/Ti is characterised by peaks form the bottom of the core up to 74 cm. The upper part of the core is characterised by low values of this ratio. Mn/Ti is characterised by low constant values along the core, but it increases at 24 cm and reaches a peak at 14 cm. The upper 14 cm of this core are characterised by low values of Mn.

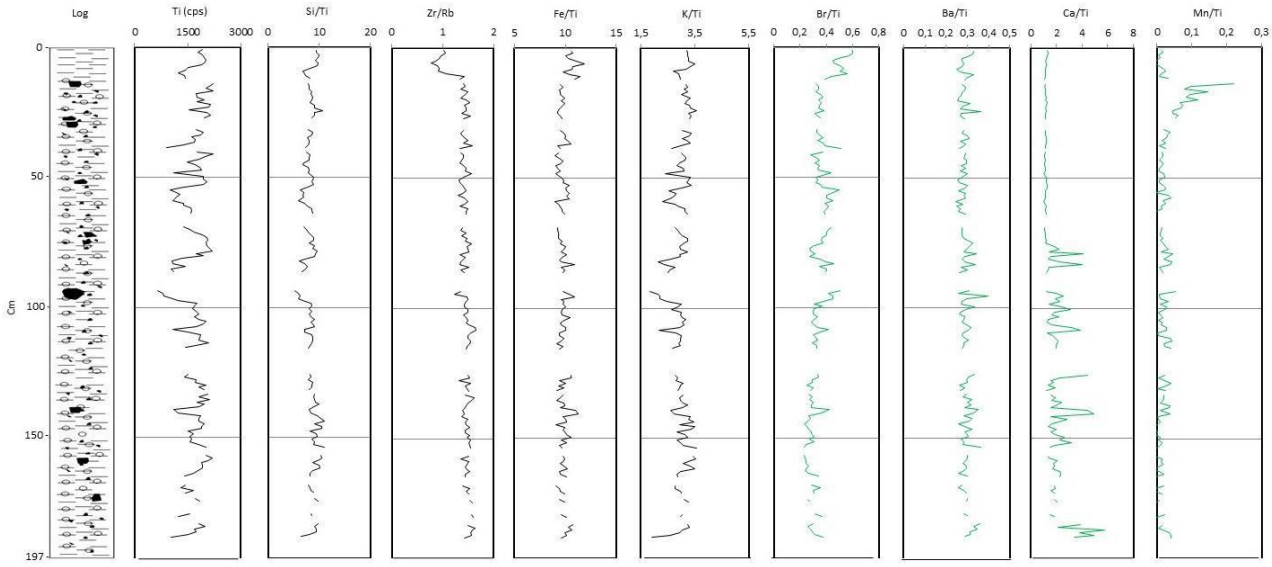

Figure S4 Elemental ratios of the core c04.

TOC (tab. S6, fig. S5) content in the core C04 ranges between 0,15 and 0,46% with an average value of 0,31%. The TOC trend is constant in the lower part of the core, shows a decrease around 10-15 cm, then increases with the highest values toward the top core.

The ratio C/N (avg 7.39) (shows an opposite trend with the lowest value at 135 cm (4,02), an increase of values in the central part of the core reaching the maximum values at 40 cm (10,28), a decrease around 15 cm and an increase at the top core (tab. S6, fig. S5).

HBI diene II (tab. S7, fig. S5) is present in this core with a very low concentration, with a max value of $1,79*10^{-4}$ µg/g at the top of the core and a min value of $1,09*10^{-5}$ µg/g at 15 cm. The average value is $6,96*10^{-5}$ µg/g.

Three sterols analysed (tab. S7, fig. S5) have a similar trend characterised by very low values between 75 cm and 15 cm and a higher concentration in the upper 15 cm with two peaks: at 10 cm ($8,58*10^{-3}$ µg/g for 22-dehydrocholesterol, $1,31*10^{-2}$ µg/g for cholesterol and $2,54*10^{-2}$ µg/g for brassicasterol), at 2 cm for brassicasterol ($2,65*10^{-2}$ µg/g), and at the top of the core for both 22-dehydrocholesterol ($9,13*10^{-3}$ µg/g) and cholesterol ($1,32*10^{-2}$ µg/g). The average value of each sterol is: $3,53*10^{-3}$ µg/g for 22-dehydrocholesterol, $6,14*10^{-3}$ µg/g for cholesterol and $9,85*10^{-3}$ µg/g for brassicasterol.

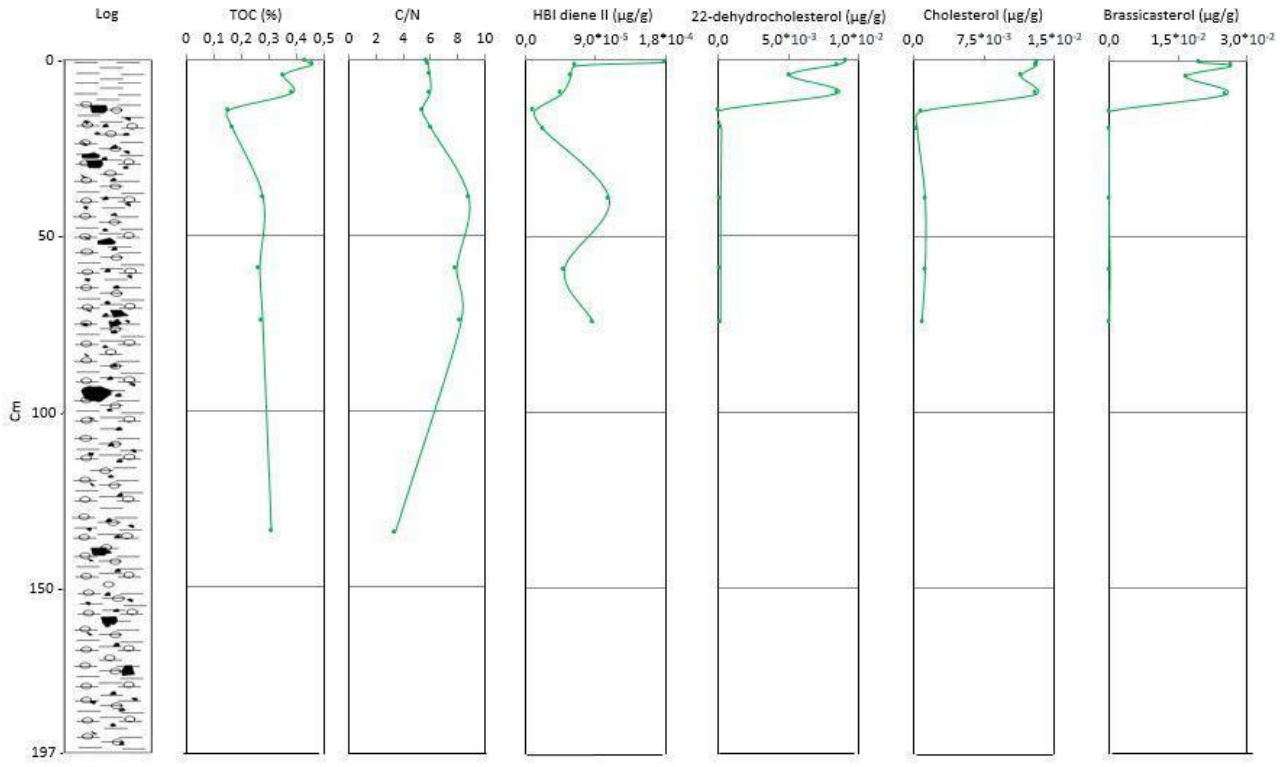

Figure S5 Organic matter and biomarkers parameters of the core c04.

c04	TOC (%)	TN (%)	C/N
0-1	0,44	0,08	6,67
1-2	0,46	0,08	6,81
4-5	0,36	0,06	6,96
9-10	0,39	0,06	6,99
14-15	0,15	0,03	6,30
19-20	0,17	0,03	7,05
39-40	0,28	0,03	10,28
59-60	0,27	0,03	9,23
74-75	0,28	0,03	9,60
134-135	0,31	0,09	4,02

Table S6 Organic matter parameters of the core ANTA96-c04.

c04	$IPSO_{25}$ (µg/g dry sedim.)	22-dehydrocholesterol (µg/g dry sedim.)	Cholesterol (µg/g dry sedim.)	Brassicasterol (µg/g dry sedim.)
0-1	$1,79*10^{-4}$	$9,13*10^{-3}$	$1,32*10^{-2}$	$1,96*10^{-2}$
1-2	$6,37*10^{-5}$	$8,54*10^{-3}$	$1,30*10^{-2}$	$2,65*10^{-2}$
4-5	$5,83*10^{-5}$	$5,08*10^{-3}$	$1,15*10^{-2}$	$1,67*10^{-2}$
9-10	$4,59*10^{-5}$	$8,58*10^{-3}$	$1,31*10^{-2}$	$2,54*10^{-2}$
14-15	$1,09*10^{-5}$	0	$7,52*10^{-4}$	0
19-20	$2,29*10^{-5}$	$1,56*10^{-4}$	$3,71*10^{-4}$	$7,25*10^{-5}$
39-40	$1,08*10^{-4}$	$9,53*10^{-5}$	$1,23*10^{-3}$	0
59-60	$4,98*10^{-5}$	$9,57*10^{-5}$	$1,21*10^{-3}$	$2,02*10^{-4}$
74-75	$8,76*10^{-5}$	$9,37*10^{-5}$	$8,77*10^{-4}$	$9,60*10^{-5}$

Table S7 Biomarkers parameters of the core ANTA96-c04.

Microscopy analyses - Sand and Foraminifera

Quartz grains with sharp to sub-rounded edges, rounded feldspar, micas and other femic minerals are present along the core. Lithic fragments are present as well, but they are less abundant at the top of the core. Biogenic component is generally scarce at the top of the core and made of agglutinated foraminifera, radiolarians, sponge spicules and diatoms. Below 10 cm, the sediments are almost biogenic barren. Foraminifera (tab. S8) reach a density of 10,5 specimens/g at the top of the core and are mainly represented by *Miliammina earlandi, Portatrochammina antarctica*, *P. bipolaris* and *Textularia earlandi*. Nine different species have been identified, belonging to 8 different genera. Foraminifera text fragmentation is around 40% at 10 cm and decreases to 25,8% at the top of the core.

C04	*Neogloboquadrina pachyderma*	Benthos/g	*Deuterammina grisea*	*Miliammina earlandi*	*Portatrochammina antarctica*	*Portatrochammina bipolaris*	*Reophax spiculifer*	*Spiroplectammina biformis*	*Textularia earlandi*	*Trifarina earlandi* (spinose)	Unknown	% fragmentation
1-2	0	10,5	2	25	6	5	0	1	8	0	2	25,8
9-10	0	4,1	0	8	1	3	1	0	9	0	0	42,1
14-15	0	0,0	0	0	0	0	0	0	0	0	0	0,0
19-20	0	0,0	0	0	0	0	0	0	0	0	0	0,0
29-30	0	0,0	0	0	0	0	0	0	0	0	0	0,0
24-25	0	0,0	0	0	0	0	0	0	0	0	0	0,0
39-40	0	0,0	0	0	0	0	0	0	0	0	0	0,0
49-50	0	0,0	0	0	0	0	0	0	0	0	0	0,0
59-60	0	0,0	0	0	0	0	0	0	0	0	0	0,0
69-70	0	0,0	0	0	0	0	0	0	0	0	0	0,0
95-96	0	0,0	0	0	0	0	0	0	0	0	0	0,0
107-108	0	0,0	0	0	0	0	0	0	0	0	0	0,0
147-148	1	0,05	0	0	0	0	0	0	0	1	0	33,3
173-174	0	0,0	0	0	0	0	0	0	0	0	0	0,0
192-193	0	0,0	0	0	0	0	0	0	0	0	0	0,0

Table S8 Foraminifera of the core ANTA96-c04.

ANTA99-GC12

This gravity core has been collected close to the modern limit of the RIS, in the inner continental shelf of the Glomar Challenger Basin (tab. 3, fig. 6). The seafloor is compact and characterised by a drape of glaciomarine sediments (fig. S6).

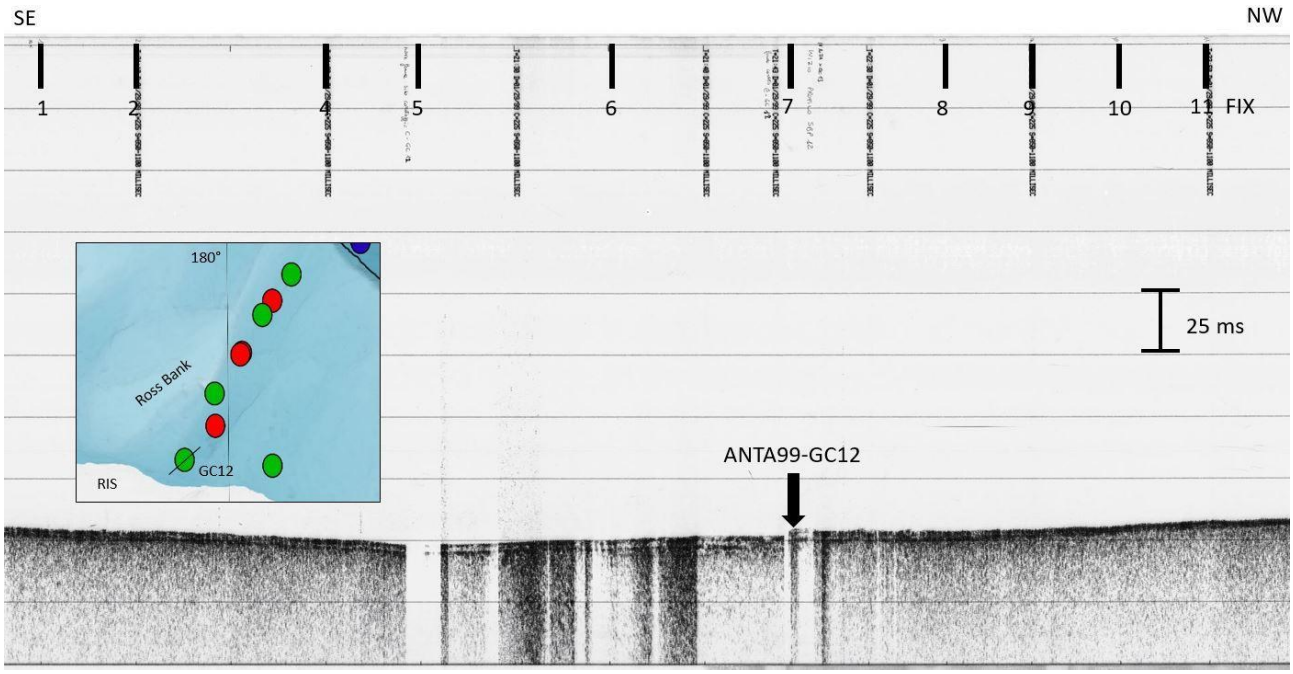

Figure S6 Section of the SBPs 11 and 12, with the location of the core GC12. Bathymetric map is a zoom of fig. 6.

Core description and Radiography

From the bottom to 209 cm, this core (fig. S7) is characterised by a dark grey (N4) very compact sandy and gravelly material within a fine matrix. Clasts are randomly oriented, characterised by dimensions from sub centimetric to pluri-centimetric. The shape of the clasts ranges from subangular to angular. The contact with the above sediments is sharp but irregular. A hydrated sandy silt layer (about 10 cm thick - 209-199 cm) divides the lower part of the core from the upper one. A thin silt laminated layer is present between 199 and 195 cm (5Y 4/2 - olive grey) that is characterised by low density in the radiography. A sharp contact characterises the lower limit of a four cm thick silty clay pocket (about 191-195 cm) (2.5Y 4/1, dark grey). Clasts are almost absent between 199 and 191 cm. Above this layer, sediments from 191 to 38 cm are characterised by a higher coarse fraction that increases up core, with millimetric to pluri-centimetric sub-angular clasts. Mud chips are present in this interval and are more abundant from 172 to 86 cm. Sediments are dark grey (5Y 4/1) from 191 to 84 cm. Colour changes toward the top of the core. Sediments are olive grey (5Y 4/2) from 84 to 65 cm, olive brown (2,5Y 4/4) from 65 to 53 cm and olive from 53 to 38 cm. The upper part of the core (38 cm top core) is a hydrated silty olive (5Y 4/3) sediment with sparse millimetre clasts. This part of the core is characterised by the presence of weak laminations with different colours: dark grey (5Y 4/1) at 37-38 cm, olive grey (5Y 5/2) between 37 and 34 cm There is also a dark grey (5y 4/1) layer between 6 and 3 cm.

The radiography was not acquired between 44 and 53 cm because of the presence of a massive clast. The presence of clasts >2 mm (tab. S9, fig. S7) is variable along the core. The interval between 199 and 191 cm is characterised by a reduced presence. The upper 50 cm also shows a reduced presence, but with two peaks around 36 and 17 cm.

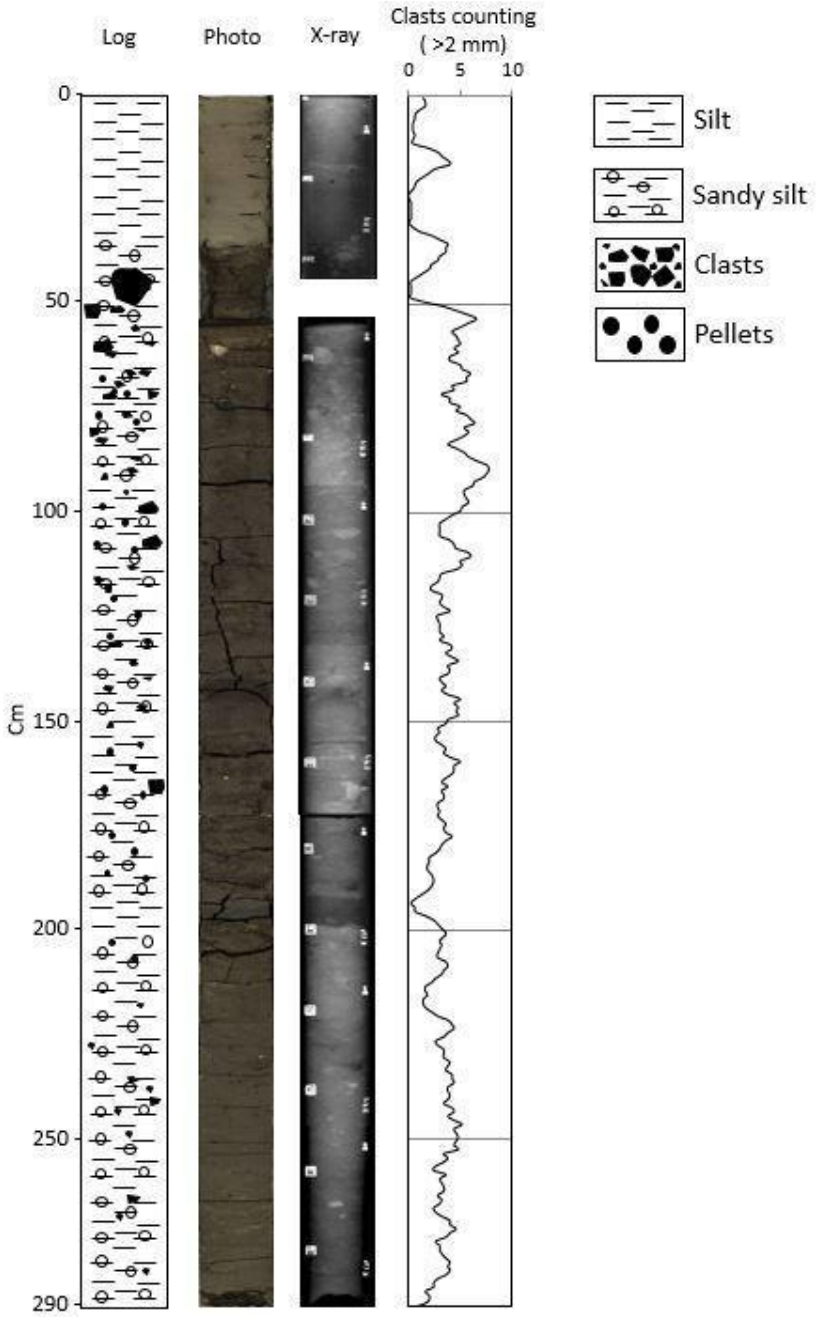

Figure S7 Lithologic log, photo, radiography, clasts counted using the Grobe (1987) method (mobile average interval: 5 cm) of the core GC12.

Depth (cm)	Clasts >2mm (num.)	Mobile average	Depth (cm)	Clasts >2mm (num.)	Mobile average	Depth (cm)	Clasts >2mm (num.)	Mobile average
0-1	0	1,2	47-48			94-95	5	5,0
1-2	1	1,4	48-49		8,0	95-96	6	5,2
2-3	3	1,4	49-50		9,0	96-97	5	5,0
3-4	1	0,8	50-51		8,0	97-98	4	5,2
4-5	1	0,8	51-52		7,5	98-99	5	4,8
5-6	1	0,6	52-53	8	7,0	99-100	6	4,0
6-7	1	0,6	53-54	10	6,0	100-101	5	3,4
7-8	0	0,6	54-55	6	4,8	101-102	6	2,8
8-9	1	0,8	55-56	6	4,4	102-103	2	2,2
9-10	0	0,6	56-57	5	3,8	103-104	1	2,6
10-11	1	0,6	57-58	3	4,4	104-105	3	2,8
11-12	1	0,6	58-59	4	4,8	105-106	2	3,0
12-13	1	2,0	59-60	4	4,8	106-107	3	3,4
13-14	0	2,6	60-61	3	4,6	107-108	4	4,0
14-15	0	3,2	61-62	8	5,2	108-109	2	4,4
15-16	1	3,8	62-63	5	4,6	109-110	4	5,4
16-17	8	3,8	63-64	4	4,4	110-111	4	5,6
17-18	4	2,6	64-65	3	5,0	111-112	6	5,6
18-19	3	1,8	65-66	6	5,2	112-113	6	5,0
19-20	3	1,2	66-67	5	4,8	113-114	7	4,2
20-21	1	0,6	67-68	4	5,4	114-115	5	3,6
21-22	2	0,4	68-69	7	5,6	115-116	4	3,2
22-23	0	0,0	69-70	4	4,8	116-117	3	2,8
23-24	0	0,0	70-71	4	4,4	117-118	2	3,0
24-25	0	0,2	71-72	8	4,2	118-119	4	3,2
25-26	0	0,2	72-73	5	3,4	119-120	3	3,4
26-27	0	0,2	73-74	3	3,4	120-121	2	3,0
27-28	0	0,2	74-75	2	3,8	121-122	4	3,2
28-29	1	0,2	75-76	3	4,8	122-123	3	3,0
29-30	0	0,0	76-77	4	5,0	123-124	5	3,0
30-31	0	0,2	77-78	5	5,8	124-125	1	2,2
31-32	0	0,6	78-79	5	6,2	125-126	3	2,8
32-33	0	1,2	79-80	7	6,2	126-127	3	3,2
33-34	0	2,4	80-81	4	5,4	127-128	3	3,8
34-35	1	3,0	81-82	8	5,4	128-129	1	4,0
35-36	2	3,6	82-83	7	4,4	129-130	4	4,2
36-37	3	3,8	83-84	5	3,8	130-131	5	4,2
37-38	6	3,4	84-85	3	3,8	131-132	6	4,6
38-39	3	2,6	85-86	4	4,8	132-133	4	4,4
39-40	4	2,5	86-87	3	5,6	133-134	2	4,2
40-41	3	2,0	87-88	4	6,2	134-135	4	4,6
41-42	1	1,5	88-89	5	6,4	135-136	7	4,4
42-43	2	2,0	89-90	8	6,6	136-137	5	3,8
43-44			90-91	8	6,0	137-138	3	3,8
44-45			91-92	6	5,6	138-139	4	3,4
45-46			92-93	5	5,4	139-140	3	3,0
46-47			93-94	6	5,2	140-141	4	3,4

Depth (cm)	Clasts >2mm (num.)	Mobile average	Depth (cm)	Clasts >2mm (num.)	Mobile average	Depth (cm)	Clasts >2mm (num.)	Mobile average
141-142	5	3,4	191-192	3	0,8	241-242	3	4,4
142-143	1	3,2	192-193	0	0,2	242-243	4	4,4
143-144	2	4,2	193-194	1	0,2	243-244	3	4,6
144-145	5	4,8	194-195	0	0,4	244-245	5	5,2
145-146	4	4,4	195-196	0	0,6	245-246	7	4,4
146-147	4	4,8	196-197	0	1,6	246-247	3	4,0
147-148	6	4,8	197-198	0	2,6	247-248	5	4,0
148-149	5	5,0	198-199	2	3,6	248-249	6	3,2
149-150	3	4,6	199-200	1	3,8	249-250	1	2,6
150-151	6	4,4	200-201	5	4,0	250-251	5	3,6
151-152	4	3,6	201-202	5	3,2	251-252	3	3,4
152-153	7	3,4	202-203	5	2,6	252-253	1	3,6
153-154	3	2,8	203-204	3	2,2	253-254	3	3,4
154-155	2	2,8	204-205	2	2,0	254-255	6	3,4
155-156	2	3,6	205-206	1	2,6	255-256	4	2,6
156-157	3	3,8	206-207	2	3,8	256-257	4	2,4
157-158	4	4,6	207-208	3	4,0	257-258	0	2,8
158-159	3	4,8	208-209	2	3,4	258-259	3	3,6
159-160	6	5,4	209-210	5	3,8	259-260	2	3,6
160-161	3	5,2	210-211	7	3,2	260-261	3	3,8
161-162	7	5,2	211-212	3	2,4	261-262	6	3,8
162-163	5	4,4	212-213	0	2,2	262-263	4	2,8
163-164	6	4,2	213-214	4	2,2	263-264	3	2,0
164-165	5	3,4	214-215	2	1,6	264-265	3	1,6
165-166	3	3,0	215-216	3	1,8	265-266	3	1,6
166-167	3	2,8	216-217	2	1,6	266-267	1	1,8
167-168	4	2,8	217-218	0	1,8	267-268	0	2,0
168-169	2	2,6	218-219	1	2,2	268-269	1	2,2
169-170	3	2,6	219-220	3	2,4	269-270	3	2,0
170-171	2	3,0	220-221	2	2,6	270-271	4	1,8
171-172	3	2,8	221-222	3	3,0	271-272	2	1,8
172-173	3	2,6	222-223	2	3,0	272-273	1	2,6
173-174	2	2,6	223-224	2	2,8	273-274	0	3,2
174-175	5	2,4	224-225	4	2,8	274-275	2	4,2
175-176	1	1,6	225-226	4	2,2	275-276	4	4,4
176-177	2	1,8	226-227	3	2,4	276-277	6	5,0
177-178	3	2,0	227-228	1	2,8	277-278	4	4,8
178-179	1	2,2	228-229	2	2,8	278-279	5	4,4
179-180	1	2,2	229-230	1	3,0	279-280	3	3,8
180-181	2	2,4	230-231	5	3,6	280-281	7	3,6
181-182	3	2,2	231-232	5	3,6	281-282	5	2,8
182-183	4	2,0	232-233	1	3,4	282-283	2	2,6
183-184	1	1,4	233-234	3	3,4	283-284	2	2,6
184-185	2	2,0	234-235	4	3,2	284-285	2	2,8
185-186	1	2,4	235-236	5	3,2	285-286	3	2,8
186-187	2	2,8	236-237	4	3,2	286-287	4	2,8
187-188	1	3,0	237-238	1	3,0	287-288	2	2,3
188-189	4	2,8	238-239	2	3,6	288-289	3	2,5
189-190	4	2,2	239-240	4	3,8	289-290	2	2,0
190-191	3	1,4	240-241	5	4,0			

Table S9 Clasts >2 mm counted using the method of Grobe (1987) and mobile average (interval of 5 cm) of the core ANTA99-GC12. Levels highlighted in yellow were not counted because the radiography was not acquired.

Physical analyses - Magnetic susceptibility, Compression strength, Water content and Grain size

Magnetic susceptibility (MS) (tab. S10, fig. S8) ranges between 400 and 650*10^6 SI from the bottom to 175 cm, with few higher values of 700-800*10^6 SI. There is a peak of 2100*10^6 SI at 267 cm (clast). MS slightly increases from 175 to 47 cm to 650-900*10^6 SI, with a peak of 1740*10^6 SI at 75 cm (clasts). The upper part of the core is characterised by a decreasing trend reaching a value of 130*10^6 SI at the top.

Depth (cm)	MS (10^{-6}SI)	Depth (cm)	MS (10^{-6}SI)	Depth (cm)	MS (10^{-6}SI)	Depth (cm)	MS (10^{-6}SI)
0-1	130	72-73	1610	144-145	910	218-219	610
2-3	230	74-75	1740	146-147	890	220-221	600
4-5	340	76-77	1200	148-149	880	222-223	600
6-7	460	78-79	870	150-151	820	224-225	610
8-9	520	80-81	790	152-153	760	226-227	600
10-11	460	82-83	780	154-155	720	228-229	600
12-13	390	84-85	740	156-157	720	230-231	610
14-15	350	86-87	710	158-159	740	232-233	640
16-17	350	88-89	710	160-161	740	234-235	690
18-19	420	90-91	710	162-163	700	236-237	760
20-21	420	92-93	680	164-165	630	238-239	710
22-23	390	94-95	650	166-167	560	240-241	660
24-25	340	96-97	630	168-169	510	242-243	640
26-27	290	98-99	630	170-171	440	244-245	630
28-29	270	100-101	630	172-173	360	246-247	620
30-31	270	102-103	630	174-175	450	248-249	630
32-33	260	104-105	630	176-177	480	250-251	640
34-35	270	106-107	630	178-179	490	252-253	650
36-37	300	108-109	630	180-181	480	254-255	630
38-39	380	110-111	640	182-183	490	256-257	620
40-41	520	112-113	650	184-185	480	258-259	620
42-43	590	114-115	620	186-187	470	260-261	710
44-45	640	116-117	610	188-189	440	262-263	960
46-47	680	118-119	620	190-191	410	264-265	1800
48-49	780	120-121	640	192-193	380	266-267	2100
50-51	760	122-123	680	194-195	410	268-269	1180
52-53	440	124-125	740	196-197	500	270-271	770
54-55	770	126-127	760	198-199	630	272-273	640
56-57	890	128-129	800	300-201	620	274-275	600
58-59	870	130-131	810	202-203	570	276-277	570
60-61	850	132-133	830	204-205	590	278-279	530
62-63	840	134-135	920	206-207	670	280-281	510
64-65	800	136-137	940	208-209	810	282-283	490
66-67	820	138-139	890	210-211	700	284-285	480
68-69	820	140-141	900	212-213	610	286-287	430
70-71	1010	142-143	900	214-215	590	288-289	330
				216-217	590	290-291	200

Table S10 Magnetic susceptibility of the core ANTA99-GC12. Yellow levels the end of each core section or peaks related to clasts.

This core is characterised by high values (higher than 3,0 kg/cm^2) of compressive strength (CS) (tab. S11, fig. S8) in the lower 50 cm, with two peaks higher than 4,0 kg/cm^2 at the bottom of the core and between 252 and 238 cm. CS rapidly decreases to 0,7 kg/cm^2 at 210-211 cm. CS gradually decreases in the upper part of the core, reaching 0,0 kg/cm^2 at the top of the core.

Depth (cm)	CS (Kg/cm²)
1-2	0,0
10-11	0,3
20-21	0,2
30-31	0,2
40-41	0,0
50-51	0,2
62-63	0,3
71-72	0,2
83-84	0,4
98-99	0,3
111-112	0,3
124-125	0,6
136-137	0,4
152-153	0,4
160-161	0,5
168-169	0,5
178-179	0,7
185-186	0,5
193-194	0,6
203-204	0,6
210-211	0,7
218-219	1,8
230-231	2,3
234-235	3,0
238-239	4,1
243-244	4,2
251-252	4,2
261-262	3,3
272-273	3,3
281-282	3,7
286-287	4,4

Table S11 Compressive strength of the core ANTA99-GC12.

Water content (w%) (tab. S12, fig. S8) has the highest values (52,3%) at the bottom of the core. W% values range between 20 and 35 % from 274 to 41 cm. There is a peak of 49,4% at 197 cm. The upper 40 cm of the core shows a rapid increase (values higher than 44%), reaching 50,6% at the top of the core.

The main sedimentary (tab. S13, fig. S8) component along the core is silt (avg 76,7%). It varies from 90,0% to 64,1%. Sand (avg 14,8%) has a max of 28,2% and it is almost absent between 35 cm and 10 cm. Clay (avg 8,5%) varies from 11,2% to 5,5%.

Depth (cm)	W%
1-2	50,6
10-11	46,4
20-21	44,0
30-31	49,7
40-41	33,2
50-51	27,1
54-55	25,3
64-65	26,4
74-75	24,7
84-85	27,8
94-95	28,5
104-105	28,5
114-115	27,3
124-125	28,1
134-135	28,4
142-143	25,9
153-154	25,8
163-164	32,8
169-170	28,6
182-183	24,4
192-193	44,9
196-197	49,4
202-203	29,1
212-213	28,0
222-223	26,0
232-234	23,8
242-243	22,4
253-254	21,4
263-264	23,2
273-274	21,9
285-286	52,3

Table S12 Water content of the core ANTA99-GC12.

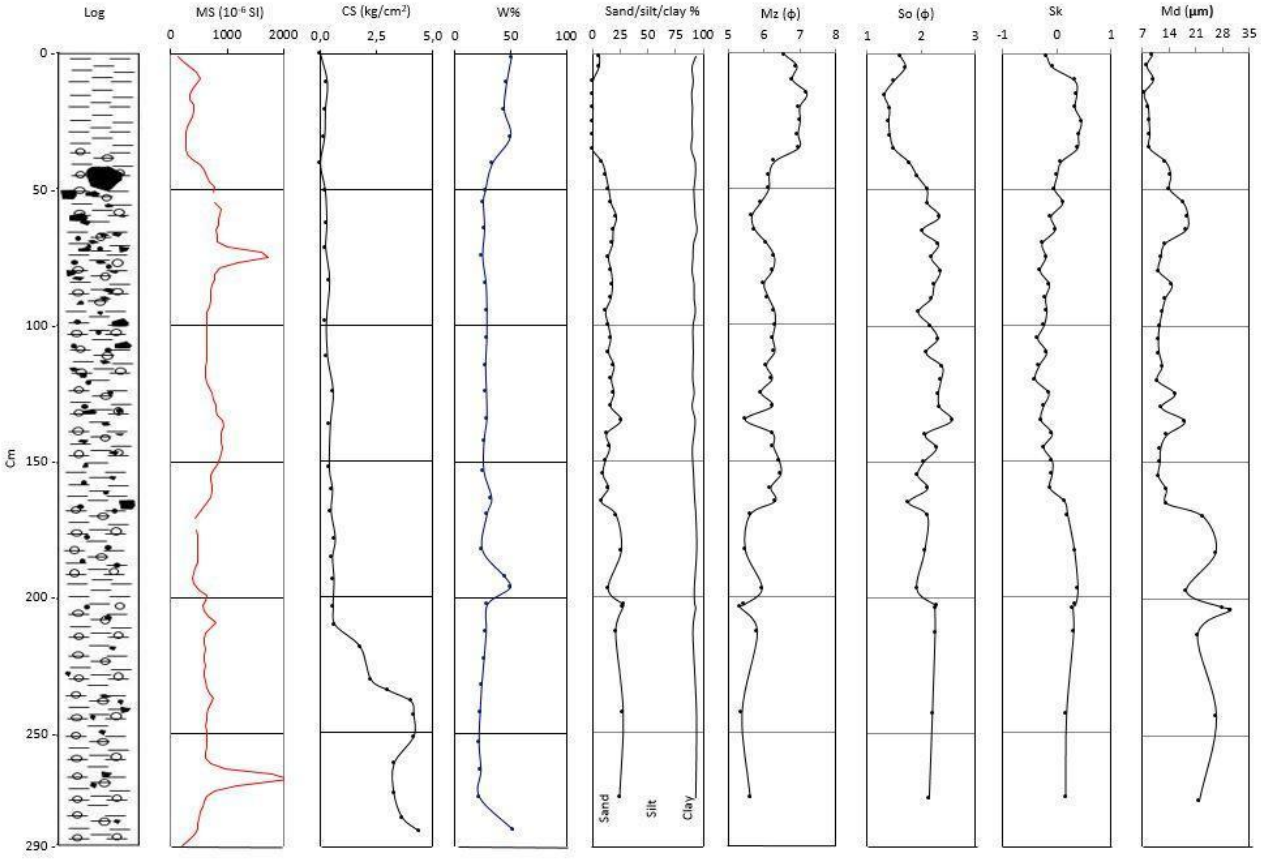

Figure S8 Physical parameters of the core GC12.

GC12	Sand (%)	Silt (%)	Clay (%)	Mz (φ)	So (φ)	Sk	Md (µm)	Primary mode (φ)
0-1	6,8	86,6	6,6	6,58	1,62	-0,09	9,6	7,00
4-5	6,2	83,4	10,4	6,91	1,71	-0,04	8,2	7,00
9-10	0,8	89,9	9,2	6,78	1,50	0,17	9,9	6,50
14-15	0,1	89,1	10,8	7,18	1,32	0,19	7,5	7,00
19-20	1,0	89,1	9,9	6,99	1,41	0,17	8,6	7,00
24-25	0,0	89,4	10,5	7,00	1,40	0,23	8,8	6,50
29-30	0,0	90,0	10,0	6,94	1,43	0,20	9,0	6,50
34-35	0,0	88,8	11,2	6,96	1,51	0,19	8,9	6,50
39-40	9,1	83,7	7,2	6,30	1,78	0,04	13,2	6,50
44-45	12,7	80,3	7,1	6,14	1,93	0,01	14,5	6,00
49-50	15,1	76,3	8,6	6,14	2,12	-0,02	14,1	6,50
54-55	17,1	74,9	8,0	5,92	2,12	0,06	17,8	5,50
59-60	21,9	70,9	7,2	5,67	2,35	-0,05	19,0	6,00
64-65	19,1	75,5	5,5	5,74	2,02	-0,02	18,5	6,00
69-70	18,5	72,6	8,9	6,06	2,32	-0,14	12,9	7,00
74-75	14,8	75,7	9,4	6,28	2,19	-0,10	11,9	7,00
79-80	17,2	72,3	10,4	6,24	2,36	-0,15	11,3	7,00
84-85	18,4	73,4	8,3	6,00	2,25	-0,07	14,8	6,50
89-90	17,0	74,6	8,3	6,12	2,19	-0,10	13,0	7,00
94-95	12,3	80,6	7,1	6,29	1,95	-0,09	12,2	6,50
99-100	14,7	76,0	9,4	6,30	2,18	-0,12	11,5	7,00
104-105	16,8	73,8	9,4	6,24	2,31	-0,17	11,2	7,00
109-110	14,8	76,1	9,1	6,30	2,09	-0,09	11,4	7,00
114-115	19,8	70,7	9,5	6,06	2,40	-0,16	12,2	7,00
119-120	17,3	73,0	9,7	6,23	2,38	-0,20	10,9	7,00
124-125	19,8	71,9	8,3	5,91	2,32	-0,08	15,6	6,50
129-130	16,7	72,9	10,3	6,23	2,35	-0,12	12,0	7,00
134-135	26,2	66,6	7,2	5,48	2,57	-0,15	18,2	6,50
139-140	13,1	78,5	8,3	6,23	2,08	-0,04	13,4	6,50
144-145	16,1	73,9	10,1	6,26	2,29	-0,12	11,8	6,50
149-150	11,9	78,4	9,7	6,42	2,06	-0,04	11,6	6,50
154-155	9,8	81,3	8,9	6,47	1,94	-0,04	11,2	7,00
159-160	14,6	76,9	8,4	6,19	2,13	-0,06	13,3	6,50
164-165	8,3	84,2	7,6	6,31	1,77	0,07	13,4	6,00
169-170	21,7	71,7	6,6	5,61	2,12	0,10	23,1	5,00
182-183	26,4	67,9	5,8	5,48	2,07	0,16	26,3	4,50
196-197	14,4	77,5	8,1	5,94	1,92	0,20	18,5	5,00
202-203	28,2	64,1	7,6	5,46	2,28	0,17	28,0	4,50
203-204	27,7	65,7	6,7	5,34	2,26	0,15	30,3	4,50
212-213	21,2	69,2	9,6	5,81	2,26	0,16	21,5	4,50
242-243	28,1	66,0	6,0	5,39	2,21	0,09	26,5	4,50
273-274	24,7	68,7	6,7	5,62	2,15	0,08	21,9	4,50

Table S13 Grain size parameters of the core ANTA99-GC12.

Mean diameter (Mz) (tab. S13, fig. S8) shows values between 5,34 ϕ (coarse silt) and 7,18 ϕ (fine silt) with an average of 6,18 ϕ (medium silt). Mz trend shows the lowest values below 170 cm and gradually increases toward the top highlighting a fining up trend. Sediments are very poorly sorted from the bottom of the core to 50 cm. The upper 50 cm of the core are poorly sorted (tab. S13, fig. S8). The average value of sorting is 2,04 ϕ. The average value of skewness (Sk) is 0,00. This core

shows positive asymmetry from the bottom up to 196 cm and between 35 and 10 cm (tab. S13, fig. S8). Grain size distribution between 197 and 70 cm shows an alternation of negative asymmetric and symmetric samples. Sediment from 70 to 35 and the upper part of the core shows a symmetric distribution. The median diameter (Md) is characterised by decreasing up core trend with a drop between 170 and 165 cm (tab. S13, fig. S8).

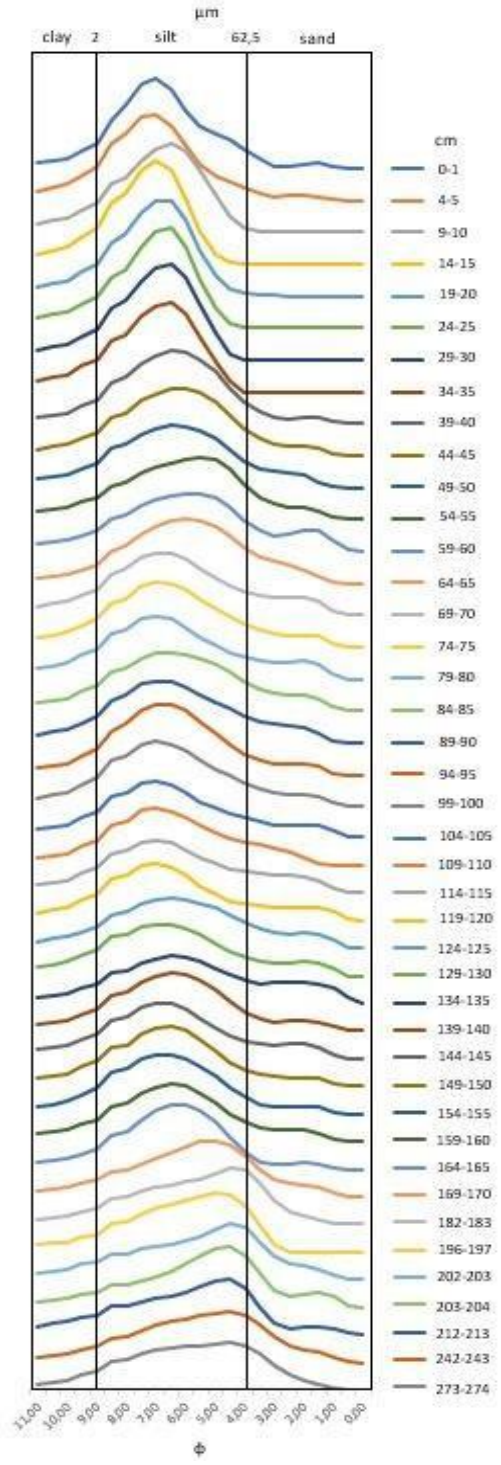

Figure S9 Grain size distribution curves of core GC12.

Distribution curves (fig. S9) of the interval from the bottom to 170 cm is characterised by an unimodal distribution, with a main mode between 4,5 and 5,0 ϕ (44,19 - 31,25 µm). Distribution curves changes to a primary mode of 6,5 - 7,0 ϕ (11,05 - 7,81 µm) from 165 to 70 cm and at 40 cm. Curves show enrichments of sandy material. The interval between 65 and 45 cm is characterised by a primary mode between 5,5 and 6,5 ϕ (22,09 - 11,05 µm). The upper part of the core is characterised by a unimodal distribution. The primary mode (tab. S13) is 6,5 - 7,0 ϕ (11,05 - 7,81 µm). The sandy fraction is almost absent in this interval, and it shows a slight increase in the upper 5 cm.

Chemical and geochemical analyses - Elemental analyses, Organic matter and Biomarkers

Al, Si, Ti, K, Fe and Rb show a good correlation (tab. S14). These elements, except the iron, also correlate with Zr. Ba correlates weakly with Al, Si, K, Fe, Rb, Sr and Zr, while Br correlates with K, Ti, Fe and Zb. Sr correlates with Al and Ca. Ca shows also a good correlation with Zr.

GC12	Al_cps	Si_cps	K_cps	Ca_cps	Ti_cps	Fe_cps	Br_cps	Rb_cps	Sr_cps	Zr_cps	Ba50_cps
Al_cps		6,56E-62	9,27E-60	5,87E-12	6,18E-33	1,80E-45	0,000323	4,64E-37	7,41E-30	3,48E-36	1,20E-21
Si_cps	**0,82958**		7,90E-119	0,34021	5,72E-81	4,23E-74	2,17E-16	1,65E-76	2,44E-16	2,77E-33	6,56E-21
K_cps	**0,82154**	**0,94695**		0,70468	9,61E-128	5,11E-148	3,40E-28	1,55E-114	1,03E-10	3,56E-19	9,50E-20
Ca_cps	0,42605	0,061958	-0,02464		0,000864	0,29636	1,44E-15	0,15611	7,87E-38	3,59E-19	9,72E-08
Ti_cps	**0,6734**	**0,88577**	**0,95558**	-0,21411		4,03E-141	1,85E-52	3,16E-109	4,35E-05	2,35E-11	8,50E-14
Fe_cps	**0,75578**	**0,86826**	**0,97027**	-0,06783	**0,96593**		2,29E-43	4,76E-117	8,00E-08	3,78E-13	4,07E-17
Br_cps	0,23067	0,49808	**0,63328**	-0,48596	**0,79089**	**0,74389**		9,67E-40	0,30697	0,6175	0,000209
Rb_cps	**0,70383**	**0,87471**	**0,9422**	-0,09203	**0,93571**	**0,94503**	**0,72173**		2,04E-09	7,91E-18	8,91E-24
Sr_cps	**0,64804**	0,49734	0,40231	**0,70911**	0,26119	0,33863	-0,06636	0,37544		2,09E-57	9,06E-34
Zr_cps	**0,69768**	**0,67612**	*0,53598*	*0,53594*	0,41479	0,44713	0,032465	*0,51825*	**0,81226**		3,90E-28
Ba50_cps	*0,56604*	*0,55738*	*0,54323*	0,33654	0,45802	*0,50845*	0,23761	*0,58968*	**0,67986**	**0,63273**	

Table S14 Pearson elements correlation of the core GC12. Bold and underlined values represent moderate to strong correlation. Underlined values in italics represent low correlation.

Ti (cps) is reported to represent lithogenic elements. Elemental ratios are reported as well (fig. S10). Ti (cps) shows a slightly decreasing trend from the bottom of the core to 57 cm and the upper 35 cm are characterised by higher values. Zr/Rb has values around 1,5 from the bottom up to 57 cm, but it drops to 0,75 between 200 cm and 190 cm. The upper part of the core is characterised by lower values, which increase toward the top. Si/Ti is characterised by a constant trend. The upper 35 cm has lower values. Fe/Ti has a slightly increasing trend from the bottom up to 57 cm. The upper 35 cm has a slightly decreasing trend. K/Ti has an increasing trend from the bottom up to 57 cm, with a drop between 200 cm and 190 cm. The upper 35 cm has very low values of this ratio. Ca/Ti is

characterised by an increasing trend from the bottom up to 94 cm. This trend is interrupted by a drop between 200 cm and 190 cm and several peaks. The trend is slightly decreasing between 94 cm and 57 cm. The upper 35 cm of the core has lower values. Mn/Ti has a constant trend from the bottom up to 57 cm, but it drops between 200 cm and 190 cm. There are two peaks: between 154 cm and 141 cm and at 64 cm. Then, it increases from 35 cm to 20 cm. After that, it decreases toward the top.

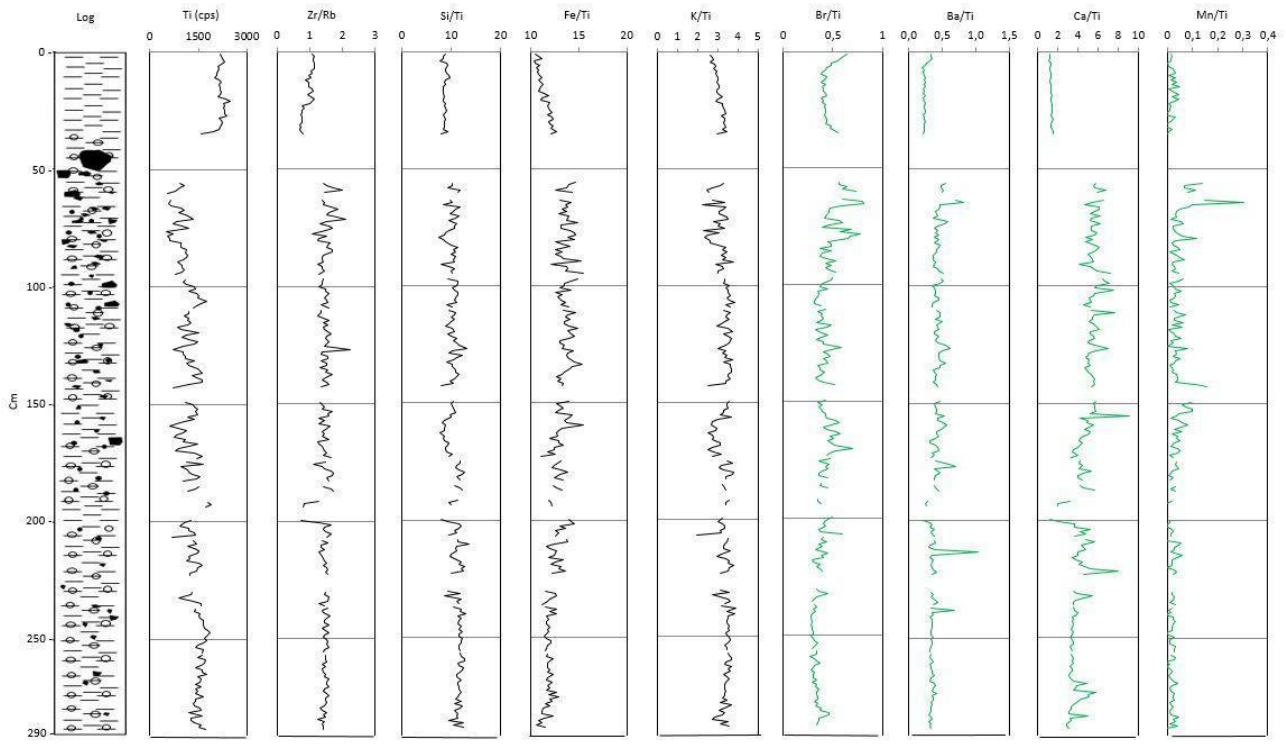

Figure S10 Elemental ratios of the core GC12.

TOC (avg 0,32%) (tab. S15, fig. S11) ranges between 0,17 and 0,50%. The TOC content is relatively high in the 4 deepest samples (values from 0,49 to 0,30%). The upper part of the core is characterised by a rapid increase of TOC reaching the highest values at the top core (0,50%)

C/N (avg 9,98) (tab. S15, fig. S11) is characterised by an opposite trend with increasing values from the bottom (around 10-11) toward the top core (24,50 at 45cm). C/N drops to values between 7,00 and 8,00, in the upper part of the core.

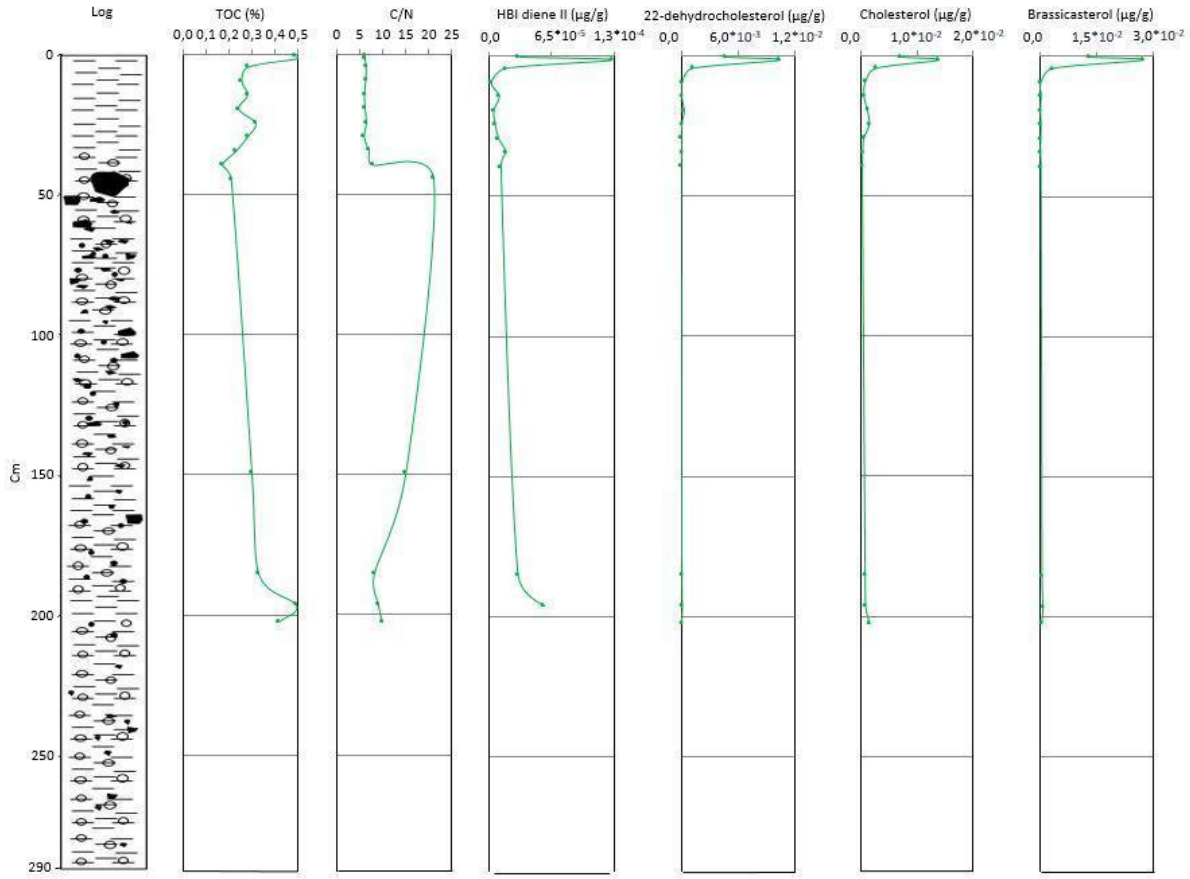

Figure S11 Organic matter and biomarkers parameters of the core GC12.

GC12	TOC (%)	TN (%)	C/N
0-1	0,49	0,08	7,38
1-2	0,50	0,08	7,19
4-5	0,28	0,04	7,53
9-10	0,26	0,04	7,42
14-15	0,28	0,05	7,09
19-20	0,24	0,04	7,28
24-25	0,32	0,05	7,58
29-30	0,28	0,05	7,04
34-35	0,23	0,03	8,23
39-40	0,17	0,02	9,17
44-45	0,21	0,01	24,50
149-150	0,30	0,02	17,50
185-186	0,33	0,04	9,56
196-197	0,49	0,05	10,63
202-203	0,42	0,04	11,55

Table S15 Organic matter parameters of the core ANTA99-GC12.

GC12	$IPSO_{25}$ (µg/g dry sedim.)	22-dehydrocholesterol (µg/g dry sedim.)	Cholesterol (µg/g dry sedim.)	Brassicasterol (µg/g dry sedim.)
0-1	$3,07*10^{-5}$	$4,61*10^{-3}$	$7,18*10^{-3}$	$1,28*10^{-2}$
1-2	$1,28*10^{-4}$	$1,04*10^{-2}$	$1,38*10^{-2}$	$2,73*10^{-2}$
4-5	$1,68*10^{-5}$	$1,20*10^{-3}$	$2,72*10^{-3}$	$3,35*10^{-3}$
9-10	$1,82*10^{-6}$	$1,06*10^{-4}$	$8,68*10^{-4}$	$1,17*10^{-4}$
14-15	$9,93*10^{-6}$	$5,69*10^{-5}$	$6,46*10^{-4}$	$2,06*10^{-4}$
19-20	$4,21*10^{-6}$	$3,13*10^{-4}$	$1,24*10^{-3}$	0
24-25	$5,63*10^{-6}$	$6,04*10^{-5}$	$1,56*10^{-3}$	$1,88*10^{-4}$
29-30	$9,26*10^{-6}$	$2,73*10^{-5}$	$5,77*10^{-4}$	$7,90*10^{-5}$
34-35	$1,69*10^{-5}$	$8,05*10^{-5}$	$4,26*10^{-4}$	0
39-40	$1,17*10^{-5}$	0	$3,33*10^{-4}$	$1,65*10^{-4}$
185-186	$2,95*10^{-5}$	$6,87*10^{-5}$	$8,35*10^{-4}$	$4,61*10^{-4}$
196-197	$5,73*10^{-5}$	$1,12*10^{-4}$	$9,20*10^{-4}$	$6,87*10^{-4}$
202-203	$1,74*10^{-4}$	$3,08*10^{-5}$	$1,64*10^{-3}$	$3,54*10^{-4}$

Table S16 Biomarkers of the core ANTA99-GC12.

HBI diene II (avg $3,82*10^{-5}$ µg/g) (tab. S16, fig. S11) shows a very low concentration, with a max value of $1,74*10^{-4}$ µg/g at 203 cm and a peak of $1,28*10^{-4}$ µg/g at 2 cm. The concentration in all the other samples is very low, with a minimum concentration of $9,93*10^{-6}$ µg/g at 15 cm.

Sterols (avg: $1,32*10^{-3}$ µg/g for 22-dehydrocholesterol, $2,52*10^{-3}$ µg/g for cholesterol and $3,52*10^{-3}$ µg/g for brassicasterol) (tab. S16, fig. S11) have a similar trend characterised by very low values between 203 cm and 186 cm and between 45 cm and 10 cm, and a peak of concentration in the upper 15 cm. All of them reaches a peak of concentration at 2 cm ($1,04*10^{-2}$ µg/g for 22-dehydrocholesterol, $1,38*10^{-2}$ µg/g for cholesterol and $2,73*10^{-2}$ µg/g for brassicasterol) and decreases at the top of the core.

Microscopy analyses - Sand and Foraminifera

Sand, analysed under a stereomicroscope, have shown presence of quartz grains with sharp to sub-rounded edges, rounded feldspar, micas and other femic minerals along the core. Lithic fragments are present but less abundant at the top of the core and around 197 cm. Biogenic component is generally scattered in the upper 80 cm and around 197 cm. Siliceous organisms include radiolarians, sponge spicules and diatoms that are poorly preserved between 40 and 182 cm. Samples are completely barren from a biogenic point of view below 200 cm. Only a few calcareous benthic foraminifera (tab. S17) have been recovered at 197 cm and between 80 cm and 20 cm, normally poorly preserved. Agglutinated foraminifera represented by *M. earlandi*, *P. antarctica* and

Spiroplectammina biformis have been recovered in the upper 10 cm. Foraminifera density increases toward the top, reaching 3,1 specimens/g. Fragmentation rate is higher than 50% at 197 cm. It increases to 100% between 182 and 20 cm, and higher than 40% at the top of the core.

GC12	Benthos/g	*Globocassidulina subglobosa*	*Miliammina earlandi*	*Portatrochammina antarctica*	*Portatrochammina bipolaris*	*Portatrochammina wiesneri*	*Pseudotrochammina bullata*	*Spiroplectammina bullata*	*Stainforthia concava*	*Textularia earlandi*	Unknown	% fragmentation
1-2	3,1	0	12	3	2	1	2	5	-	1	2	42,9
9-10	1,1	0	1	2	0	0	0	0	0	0	0	0,0
19-20	0,0	0	0	0	0	0	0	0	0	0	0	0,0
29-30	0,0	0	0	0	0	0	0	0	0	0	0	0,0
30-31	0,0	1	0	0	0	0	0	0	0	0	0	0,0
39-40	0,0	0	0	0	0	0	0	0	0	0	0	0,0
49-50	0,0	0	0	0	0	0	0	0	0	0	0	0,0
50-51	0,0	0	0	0	0	0	0	0	0	0	0	0,0
59-60	0,0	0	0	0	0	0	0	0	0	0	0	0,0
69-70	0,0	0	0	0	0	0	0	0	0	0	0	0,0
79-80	0,0	0	0	0	0	0	0	0	0	0	0	0,0
89-90	0,0	0	0	0	0	0	0	0	0	0	0	0,0
99-100	0,0	0	0	0	0	0	0	0	0	0	0	0,0
109-110	0,0	0	0	0	0	0	0	0	0	0	0	0,0
119-120	0,0	0	0	0	0	0	0	0	0	0	0	0,0
129-130	0,0	0	0	0	0	0	0	0	0	0	0	0,0
139-140	0,0	0	0	0	0	0	0	0	0	0	0	0,0
149-150	0,0	0	0	0	0	0	0	0	0	0	0	0,0
159-160	0,0	0	0	0	0	0	0	0	0	0	0	0,0
169-170	0,0	0	0	0	0	0	0	0	0	0	0	0,0
181-182	0,0	0	0	0	0	0	0	0	0	0	0	0,0
196-197	0,4	3	0	0	0	0	0	0	2	0	0	54,5
202-203	0,0	0	0	0	0	0	0	0	0	0	0	0,0
212-213	0,0	0	0	0	0	0	0	0	0	0	0	0,0
242-243	0,0	0	0	0	0	0	0	0	0	0	0	0,0
273-274	0,0	0	0	0	0	0	0	0	0	0	0	0,0

Table S17 Foraminifera of the core ANTA99-GC12.

ANTA99-GC13

This core has been collected in the inner-middle continental shelf (tab. 3, fig. 6). This area is characterised by a compact and irregular sea floor (fig. S12).

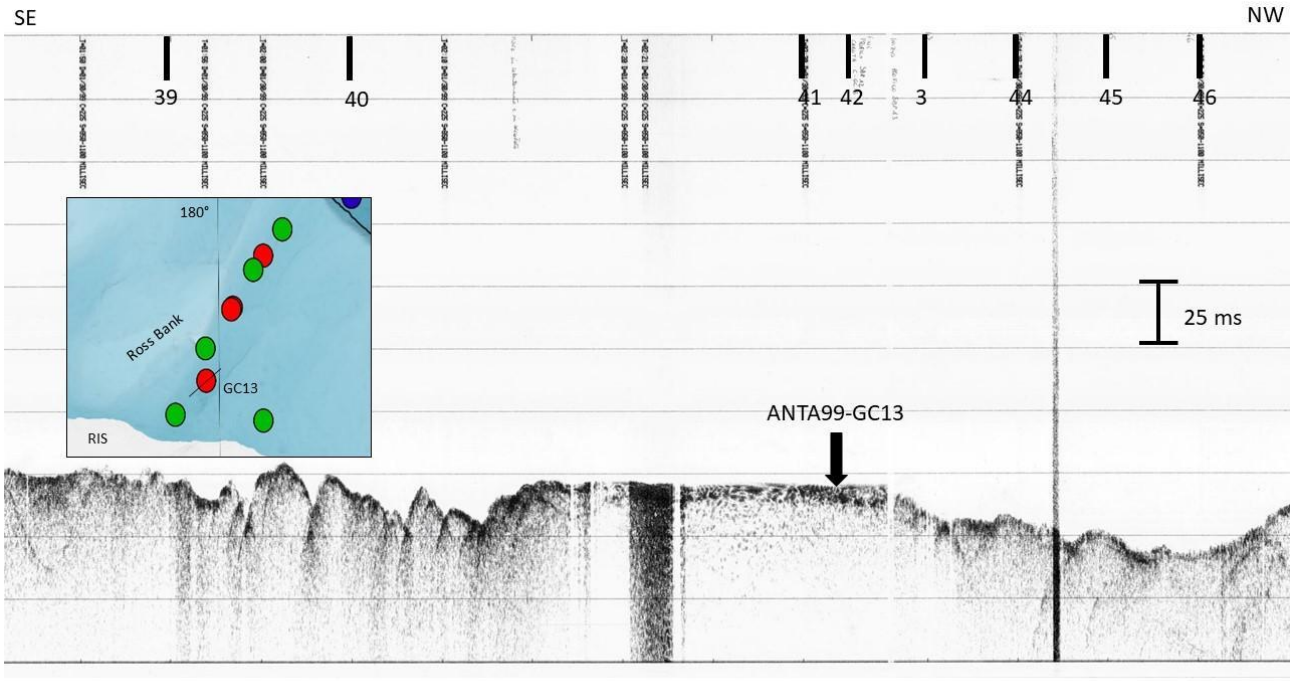

Figure S12 Section of the SBPs 12 and 13, with the location of the core GC13. Bathymetric map is a zoom of fig. 6.

Core radiography

Sediment (fig. S13) characterised by gravel dispersed in a homogeneous matrix is present from the bottom core until 106 cm. In this portion denser homogeneous sediments are present, with weak laminations around 321-319 cm. The upper part of the core is characterised by dense gravel-rich sediments with laminations at 101-97 cm, 90-72 cm and 45-42 cm. The upper 42 cm are characterised by density decreasing up core, with low density sediments at the top with sparse and mainly millimetric clasts. A denser and dishomogeneous level is present at 30-28 cm.

The mobile average of clasts >2 mm is characterised by fluctuating values along the core (tab. 16, fig. S18).

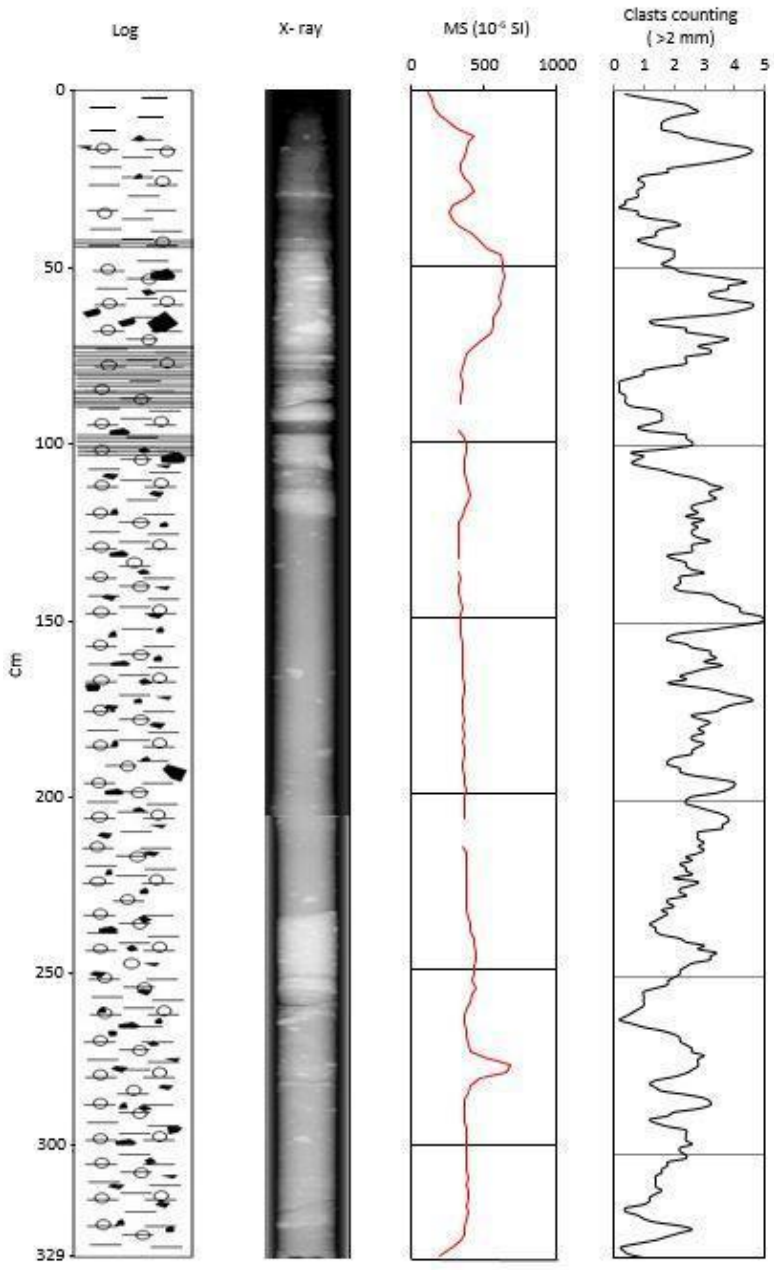

Figure S13 Descriptive log, radiography, magnetic susceptibility and clasts counted using the Grobe (1987) method (mobile average interval: 5 cm) of the core GC13.

Depth (cm)	Clasts >2mm (num.)	Mobile average	Depth (cm)	Clasts >2mm (num.)	Mobile average	Depth (cm)	Clasts >2mm (num.)	Mobile average
0-1	0	0,4	47-48	2	1,8	94-95	2	0,8
1-2	0	1,0	48-49	3	1,6	95-96	0	1,2
2-3	1	1,8	49-50	2	2,0	96-97	0	2,4
3-4	1	2,4	50-51	1	2,2	97-98	0	2,4
4-5	0	2,6	51-52	1	3,0	98-99	2	2,6
5-6	3	2,8	52-53	1	3,8	99-100	4	2,6
6-7	4	2,2	53-54	5	4,4	100-101	6	1,8
7-8	4	1,8	54-55	3	3,8	101-102	0	0,6
8-9	2	1,6	55-56	5	3,8	102-103	1	1,0
9-10	1	1,6	56-57	5	3,2	103-104	2	0,8
10-11	0	1,6	57-58	4	3,2	104-105	0	0,6
11-12	2	2,2	58-59	2	3,8	105-106	0	1,0
12-13	3	2,4	59-60	3	4,6	106-107	2	1,6
13-14	2	3,0	60-61	2	4,6	107-108	0	2,0
14-15	1	3,6	61-62	5	4,2	108-109	1	2,6
15-16	3	4,4	62-63	7	3,6	109-110	2	3,0
16-17	3	4,6	63-64	6	2,2	110-111	3	3,2
17-18	6	4,4	64-65	3	1,2	111-112	4	3,6
18-19	5	4,0	65-66	0	1,4	112-113	3	3,2
19-20	5	3,4	66-67	2	2,4	113-114	3	3,2
20-21	4	2,6	67-68	0	2,4	114-115	3	3,4
21-22	2	1,8	68-69	1	3,2	115-116	5	3,0
22-23	4	1,8	69-70	4	3,8	116-117	2	2,6
23-24	2	1,0	70-71	5	3,4	117-118	3	2,6
24-25	1	0,8	71-72	2	2,8	118-119	4	2,8
25-26	0	1,0	72-73	4	3,2	119-120	1	2,4
26-27	2	1,0	73-74	4	3,2	120-121	3	3,0
27-28	0	0,8	74-75	2	2,4	121-122	2	2,6
28-29	1	0,8	75-76	2	2,4	122-123	4	2,8
29-30	2	0,8	76-77	4	2,4	123-124	2	2,6
30-31	0	0,4	77-78	4	1,6	124-125	4	2,6
31-32	1	0,4	78-79	0	1,0	125-126	1	2,8
32-33	0	0,2	79-80	2	1,0	126-127	3	3,2
33-34	1	0,8	80-81	2	0,6	127-128	3	2,6
34-35	0	0,8	81-82	0	0,2	128-129	2	2,6
35-36	0	1,2	82-83	1	0,2	129-130	5	2,6
36-37	0	2,0	83-84	0	0,2	130-131	3	1,8
37-38	3	2,2	84-85	0	0,2	131-132	0	2,0
38-39	1	1,6	85-86	0	0,4	132-133	3	2,4
39-40	2	1,4	86-87	0	0,4	133-134	2	2,4
40-41	4	1,4	87-88	1	0,4	134-135	1	2,6
41-42	1	0,8	88-89	0	0,6	135-136	4	3,0
42-43	0	1,0	89-90	1	1,4	136-137	2	2,2
43-44	0	1,4	90-91	0	1,6	137-138	3	2,2
44-45	2	2,0	91-92	0	1,6	138-139	3	2,2
45-46	1	2,0	92-93	2	1,6	139-140	3	2,0
46-47	2	2,0	93-94	4	1,2	140-141	0	2,2

Depth (cm)	Clasts >2mm (num.)	Mobile average	Depth (cm)	Clasts >2mm (num.)	Mobile average	Depth (cm)	Clasts >2mm (num.)	Mobile average
141-142	2	3,2	188-189	1	1,8	235-236	3	1,4
142-143	3	3,4	189-190	2	1,8	236-237	0	1,4
143-144	2	3,6	190-191	2	2,2	237-238	1	1,6
144-145	4	4,0	191-192	1	2,2	238-239	1	2,2
145-146	5	4,2	192-193	3	2,6	239-240	2	2,4
146-147	3	4,2	193-194	1	3,4	240-241	3	3,0
147-148	4	4,8	194-195	4	4,0	241-242	1	2,8
148-149	4	5,0	195-196	2	4,0	242-243	4	3,4
149-150	5	4,8	196-197	3	3,8	243-244	2	3,2
150-151	5	4,0	197-198	7	3,4	244-245	5	3,2
151-152	6	3,2	198-199	4	2,6	245-246	2	2,6
152-153	5	2,2	199-200	4	2,4	246-247	4	2,4
153-154	3	1,8	200-201	1	2,4	247-248	3	2,2
154-155	1	1,8	201-202	1	2,8	248-249	2	2,2
155-156	1	2,4	202-203	3	3,2	249-250	2	2,0
156-157	1	2,6	203-204	3	3,6	250-251	1	1,8
157-158	3	3,2	204-205	4	3,8	251-252	3	1,8
158-159	3	3,2	205-206	3	3,8	252-253	3	1,4
159-160	4	3,4	206-207	3	3,6	253-254	1	1,0
160-161	2	3,0	207-208	5	3,6	254-255	1	1,0
161-162	4	3,6	208-209	4	2,8	255-256	1	1,0
162-163	3	3,0	209-210	4	2,8	256-257	1	1,0
163-164	4	2,6	210-211	2	2,8	257-258	1	1,0
164-165	2	2,2	211-212	3	3,0	258-259	1	0,8
165-166	5	2,4	212-213	1	2,8	259-260	1	0,6
166-167	1	1,8	213-214	4	3,0	260-261	1	0,4
167-168	1	2,6	214-215	4	2,8	261-262	1	0,2
168-169	2	3,4	215-216	3	2,4	262-263	0	0,6
169-170	3	3,8	216-217	2	2,6	263-264	0	1,0
170-171	2	4,4	217-218	2	2,2	264-265	0	1,6
171-172	5	4,6	218-219	3	2,4	265-266	0	2,0
172-173	5	4,0	219-220	2	2,4	266-267	3	2,2
173-174	4	3,6	220-221	4	2,6	267-268	2	2,2
174-175	6	3,4	221-222	0	2,0	268-269	3	2,4
175-176	3	2,6	222-223	3	2,8	269-270	2	2,6
176-177	2	2,8	223-224	3	2,6	270-271	1	2,6
177-178	3	3,2	224-225	3	2,2	271-272	3	3,0
178-179	3	3,0	225-226	1	2,2	272-273	3	2,8
179-180	2	2,8	226-227	4	2,4	273-274	4	2,8
180-181	4	3,0	227-228	2	1,8	274-275	2	2,8
181-182	4	2,6	228-229	1	1,8	275-276	3	2,6
182-183	2	2,6	229-230	3	2,0	276-277	2	2,4
183-184	2	3,0	230-231	2	1,6	277-278	3	2,0
184-185	3	2,8	231-232	1	1,8	278-279	4	1,4
185-186	2	2,6	232-233	2	1,6	279-280	1	1,2
186-187	4	2,6	233-234	2	1,4	280-281	2	1,4
187-188	4	2,0	234-235	1	1,2	281-282	0	1,6

Depth (cm)	Clasts >2mm (num.)	Mobile average	Depth (cm)	Clasts >2mm (num.)	Mobile average	Depth (cm)	Clasts >2mm (num.)	Mobile average
282-283	0	2,4	**298-299**	1	2,2	**314-315**	1	0,4
283-284	3	3,0	**299-300**	3	2,4	**315-316**	0	0,4
284-285	2	3,2	**300-301**	4	2,4	**316-317**	1	0,8
285-286	3	3,2	**301-302**	1	1,8	**317-318**	0	1,0
286-287	4	2,8	**302-303**	2	1,8	**318-319**	0	1,4
287-288	3	2,0	**303-304**	2	1,6	**319-320**	1	2,2
288-289	4	1,8	**304-305**	3	1,6	**320-321**	2	2,6
289-290	2	1,2	**305-306**	1	1,4	**321-322**	2	2,2
290-291	1	1,4	**306-307**	1	1,4	**322-323**	2	1,8
291-292	0	1,8	**307-308**	1	1,4	**323-324**	4	1,4
292-293	2	2,4	**308-309**	2	1,4	**324-325**	3	0,8
293-294	1	2,4	**309-310**	2	1,6	**325-326**	0	0,3
294-295	3	2,4	**310-311**	1	1,4	**326-327**	0	0,3
295-296	3	2,4	**311-312**	1	1,2	**327-328**	0	0,5
296-297	3	2,6	**312-313**	1	1,2	**328-329**	1	1,0
297-298	2	2,2	**313-314**	3	1,0			

Table S18 Clasts >2 mm counted using the method of Grobe (1987) and mobile average (interval of 5 cm) of the core ANTA99-GC13.

Physical analyses - Magnetic susceptibility

Magnetic susceptibility (tab. S19, fig. S13) is characterised by a constant trend with values around 300-400*10^{-6} SI from the bottom to 75 cm, with a peak of 680*10^{-6} SI around 277 cm. Then, MS increases reaching values higher than 600*10^{-6} SI from 61 to 47 cm, where the radiographic image shows a dense interval with clasts. In the upper part of the core, it decreases reaching 110*10^{-6} SI at the top. There are two peaks of 430*10^{-6} SI at 29 (dense interval) and 13 cm (clasts).

Depth (cm)	MS (10^{-6}SI)	Depth (cm)	MS (10^{-6}SI)	Depth (cm)	MS (10^{-6}SI)	Depth (cm)	MS (10^{-6}SI)
0-1	110	84-85	350	168-169	360	252-253	420
2-3	140	86-87	340	170-171	360	254-255	440
4-5	160	88-89	340	172-173	350	256-257	420
6-7	200	90-91	310	174-175	350	258-259	400
8-9	250	92-93	250	176-177	350	260-261	380
10-11	310	94-95	240	178-179	360	262-263	370
12-13	430	96-97	330	180-181	350	264-265	370
14-15	390	98-99	370	182-183	360	266-267	380
16-17	380	100-101	380	184-185	350	268-269	380
18-19	360	102-103	380	186-187	360	270-271	390
20-21	340	104-105	370	188-189	360	272-273	410
22-23	340	106-107	370	190-191	350	274-275	500
24-25	370	108-109	370	192-193	350	276-277	680
26-27	410	110-111	380	194-195	360	278-279	650
28-29	430	112-113	390	196-197	370	280-281	470
30-31	360	114-115	400	198-199	380	282-283	410
32-33	280	116-117	390	300-201	370	284-285	390
34-35	260	118-119	370	202-203	370	286-287	370
36-37	290	120-121	350	204-205	370	288-289	370
38-39	320	122-123	330	206-207	360	290-291	370
40-41	420	124-125	330	208-209	330	292-293	370
42-43	470	126-127	330	210-211	250	294-295	380
44-45	520	128-129	330	212-213	290	296-297	380
46-47	610	130-131	330	214-215	350	298-299	380
48-49	630	132-133	330	216-217	380	300-301	380
50-51	630	134-135	140	218-219	380	302-303	380
52-53	640	136-137	330	220-221	380	304-305	380
54-55	630	138-139	340	222-223	380	306-307	380
56-57	610	140-141	330	224-225	380	308-309	390
58-59	600	142-143	330	226-227	380	310-311	380
60-61	610	144-145	340	228-229	380	312-313	390
62-63	590	146-147	350	230-231	380	314-315	390
64-65	560	148-149	340	232-233	380	316-317	380
66-67	560	150-151	340	234-235	390	318-319	390
68-69	550	152-153	340	236-237	400	320-321	380
70-71	490	154-155	340	238-239	410	322-323	370
72-73	430	156-157	350	240-241	430	324-325	360
74-75	380	158-159	350	242-243	430	326-327	340
76-77	360	160-161	350	244-245	440	328-329	270
78-79	350	162-163	350	246-247	440	330-331	200
80-81	340	164-165	350	248-249	430		
82-83	350	166-167	350	250-251	430		

Table S19 Magnetic susceptibility of the core ANTA99-GC13. Yellow levels the end of each core section or peaks related to clasts.

ANTA99-GC14

This core has been collected in the inner-middle continental shelf, at the base of the Ross Bank (tab. 3, fig. 6). Bulges of glaciomarine sediments cover the seafloor (fig. S14).

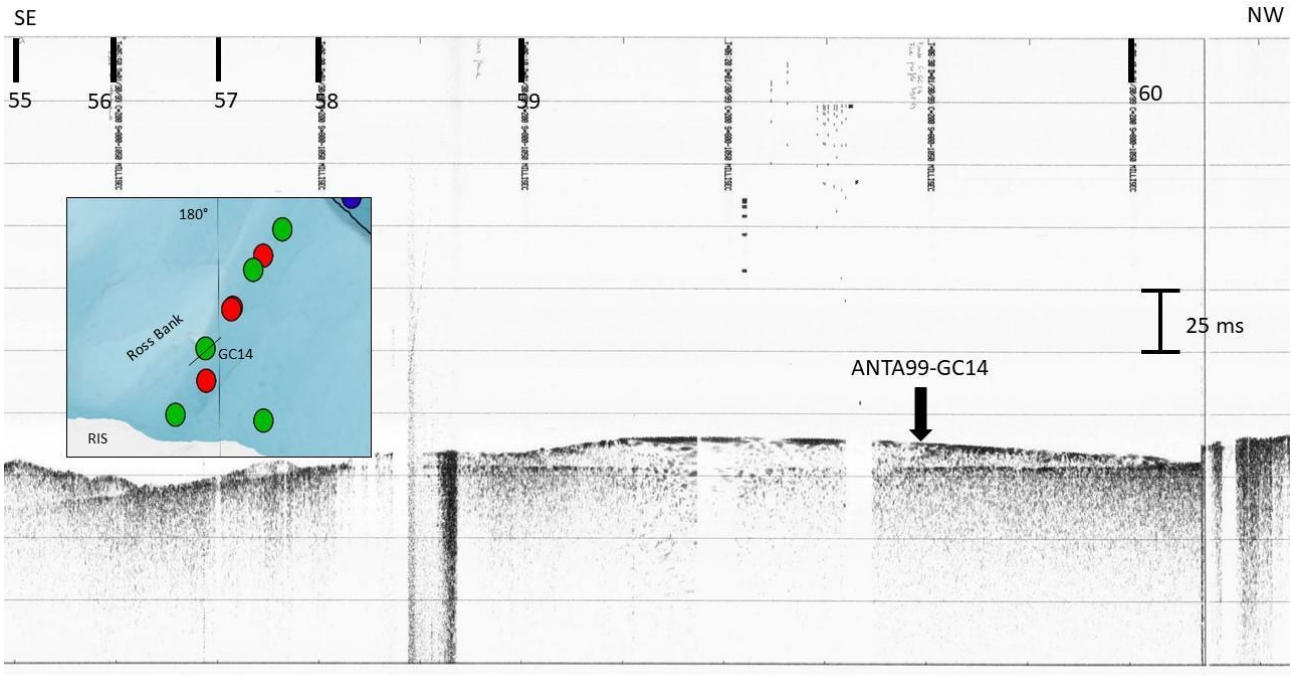

Figure S14 Section of the SBPs 13 and 14, with the location of the core GC14. Bathymetric map is a zoom of fig. 6.

Core description and Radiography

Dark grey (5Y 4/1) sandy and gravelly material surrounded by a fine matrix characterises this core from the bottom (325 cm) to 87 cm. This material has abundant randomly oriented clasts. Their dimension goes from millimetric to pluri-centimetric. In the interval between 200 and 100 cm clasts have an oblique orientation. Then, from 87 to 28 cm, the core is made of sandy mud with mm to pluri-cm clasts. Colour changes from dark grey (2,5Y 4/0) (87-68 cm) to olive grey (5Y 5/2) with dark greyish brown stains (2,5Y 4/2) (68-47 cm), to dark greyish brown (2,5Y 4/2) (47-28 cm). This last interval (47-28 cm) is highly hydrated, denser and clast-rich (sub centimetric to pluri-centimetric). It is separated from the lower one by a U-shaped detachment. A 1 cm thick clayey layer is present at 44,5-43,5 cm. The contact with the overlying sediment is sharp. The upper part of the core is made of silty clay with sparse clasts. Density of this section is lower. Colour changes from greyish brown (2,5Y 5/2) (28-20 cm) to dark grey (5Y 4/1) (20-18 cm) to olive (5Y 4/3) (18 cm - top of the core).

Clasts of this core are mainly sub-angular, but angular and rounded clasts are present. Photo and radiographic image in fig. S15.

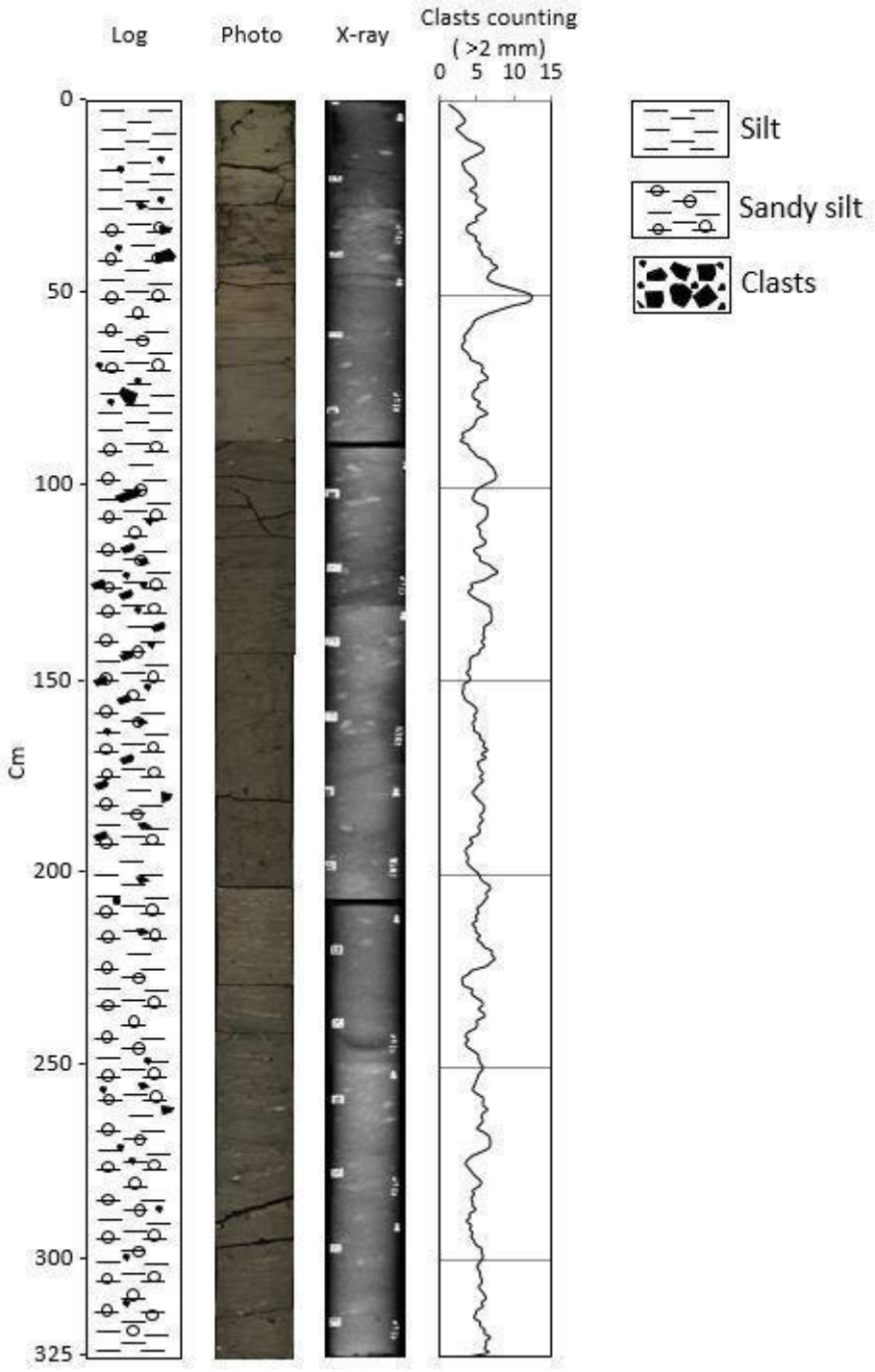

Figure S15 Lithologic log, photo, radiography, clasts counted using the Grobe (1987) method (mobile average interval: 5 cm) of the core GC14.

Clasts counted using the method of Grobe and elaborated using the mobile average on intervals of 5 cm highlighted a constant presence of clasts >2 mm, with a peak around 50 cm (tab. S20, fig. S15).

Depth (cm)	Clasts >2mm (num.)	Mobile average	Depth (cm)	Clasts >2mm (num.)	Mobile average	Depth (cm)	Clasts >2mm (num.)	Mobile average
0-1	0	1,2	47-48	4	8,8	94-95	6	7,2
1-2	0	2,0	48-49	6	10,6	95-96	5	7,4
2-3	1	2,6	49-50	8	12,2	96-97	8	7,6
3-4	2	3,0	50-51	10	12,4	97-98	9	7,4
4-5	3	3,4	51-52	16	12,0	98-99	8	6,4
5-6	4	3,0	52-53	13	9,8	99-100	7	5,4
6-7	3	2,2	53-54	14	8,2	100-101	6	4,8
7-8	3	2,6	54-55	9	6,6	101-102	7	4,6
8-9	4	3,2	55-56	8	5,4	102-103	4	4,4
9-10	1	3,8	56-57	5	4,6	103-104	3	5,0
10-11	0	5,0	57-58	5	4,4	104-105	4	6,2
11-12	5	5,8	58-59	6	4,0	105-106	5	6,4
12-13	6	5,8	59-60	3	3,6	106-107	6	6,4
13-14	7	4,8	60-61	4	3,2	107-108	7	6,2
14-15	7	3,8	61-62	4	3,4	108-109	9	5,6
15-16	4	3,0	62-63	3	3,0	109-110	5	5,0
16-17	5	3,2	63-64	4	3,0	110-111	5	5,4
17-18	1	3,4	64-65	1	3,6	111-112	5	5,4
18-19	2	4,0	65-66	5	4,0	112-113	4	5,6
19-20	3	4,6	66-67	2	4,2	113-114	6	6,2
20-21	5	4,8	67-68	3	5,4	114-115	7	5,8
21-22	6	4,8	68-69	7	5,8	115-116	5	4,6
22-23	4	4,0	69-70	3	5,6	116-117	6	4,8
23-24	5	4,8	70-71	6	6,2	117-118	7	5,4
24-25	4	5,0	71-72	8	6,4	118-119	4	5,4
25-26	5	4,8	72-73	5	5,2	119-120	1	6,6
26-27	2	5,4	73-74	6	5,2	120-121	6	7,2
27-28	8	6,2	74-75	6	4,6	121-122	9	7,8
28-29	6	5,6	75-76	7	4,4	122-123	7	6,8
29-30	3	4,8	76-77	2	4,6	123-124	10	6,0
30-31	8	5,0	77-78	5	5,4	124-125	4	4,2
31-32	6	3,8	78-79	3	5,0	125-126	9	4,4
32-33	5	3,6	79-80	5	5,8	126-127	4	3,8
33-34	2	3,8	80-81	8	6,4	127-128	3	4,2
34-35	4	4,8	81-82	6	5,2	128-129	1	5,0
35-36	2	4,8	82-83	3	4,8	129-130	5	6,0
36-37	5	5,4	83-84	7	4,6	130-131	6	6,8
37-38	6	5,2	84-85	8	4,0	131-132	6	6,8
38-39	7	5,6	85-86	2	3,0	132-133	7	7,0
39-40	4	5,8	86-87	4	3,2	133-134	6	7,0
40-41	5	6,8	87-88	2	2,8	134-135	9	6,8
41-42	4	7,0	88-89	4	3,8	135-136	6	6,0
42-43	8	7,8	89-90	3	4,0	136-137	7	6,0
43-44	8	7,0	90-91	3	4,6	137-138	7	5,8
44-45	9	6,6	91-92	2	5,0	138-139	5	6,0
45-46	6	6,4	92-93	7	6,2	139-140	5	5,6
46-47	8	7,2	93-94	5	6,6	140-141	6	6,0

Depth (cm)	Clasts >2mm (num.)	Mobile average	Depth (cm)	Clasts >2mm (num.)	Mobile average	Depth (cm)	Clasts >2mm (num.)	Mobile average
141-142	6	5,4	188-189	5	5,4	235-236	5	5,8
142-143	8	5,2	189-190	9	5,0	236-237	7	6,0
143-144	3	4,2	190-191	4	4,0	237-238	6	5,0
144-145	7	4,0	191-192	5	4,4	238-239	4	5,0
145-146	3	4,0	192-193	4	3,8	239-240	7	4,8
146-147	5	4,0	193-194	3	3,4	240-241	6	3,8
147-148	3	3,6	194-195	4	3,6	241-242	2	3,4
148-149	2	4,0	195-196	6	3,8	242-243	6	3,8
149-150	7	4,0	196-197	2	3,6	243-244	3	3,4
150-151	3	3,2	197-198	2	4,0	244-245	2	3,8
151-152	3	3,2	198-199	4	4,6	245-246	4	4,6
152-153	5	3,0	199-200	5	5,2	246-247	4	5,2
153-154	2	3,2	200-201	5	5,4	247-248	4	5,2
154-155	3	3,4	201-202	4	5,8	248-249	5	5,4
155-156	3	4,2	202-203	5	6,6	249-250	6	5,8
156-157	2	4,8	203-204	7	6,8	250-251	7	5,6
157-158	6	5,0	204-205	6	6,2	251-252	4	5,2
158-159	3	4,6	205-206	7	6,4	252-253	5	5,0
159-160	7	4,8	206-207	8	6,0	253-254	7	4,8
160-161	6	4,4	207-208	6	5,6	254-255	5	4,6
161-162	3	4,6	208-209	4	5,0	255-256	5	4,4
162-163	4	4,6	209-210	7	5,2	256-257	3	5,0
163-164	4	5,4	210-211	5	4,8	257-258	4	5,8
164-165	5	5,4	211-212	6	5,0	258-259	6	5,8
165-166	7	6,0	212-213	3	4,4	259-260	4	5,8
166-167	3	5,8	213-214	5	4,8	260-261	8	6,4
167-168	8	6,4	214-215	5	4,8	261-262	7	5,8
168-169	4	5,6	215-216	6	5,4	262-263	4	5,6
169-170	8	6,2	216-217	3	5,0	263-264	6	5,8
170-171	6	5,2	217-218	5	5,6	264-265	7	5,4
171-172	6	5,2	218-219	5	6,0	265-266	5	5,0
172-173	4	5,4	219-220	8	7,0	266-267	6	6,0
173-174	7	5,8	220-221	4	7,0	267-268	5	6,6
174-175	3	5,4	221-222	6	7,4	268-269	4	6,8
175-176	6	5,8	222-223	7	6,8	269-270	5	6,8
176-177	7	5,2	223-224	10	6,2	270-271	10	6,6
177-178	6	4,8	224-225	8	4,4	271-272	9	5,6
178-179	5	4,4	225-226	6	3,8	272-273	6	4,4
179-180	5	4,8	226-227	3	3,0	273-274	4	3,8
180-181	3	5,2	227-228	4	3,0	274-275	4	3,4
181-182	5	5,8	228-229	1	3,2	275-276	5	3,8
182-183	4	6,0	229-230	5	4,4	276-277	3	4,2
183-184	7	5,8	230-231	2	4,2	277-278	3	4,6
184-185	7	5,4	231-232	3	4,8	278-279	2	5,2
185-186	6	5,8	232-233	5	5,6	279-280	6	5,6
186-187	6	5,4	233-234	7	5,8	280-281	7	5,2
187-188	3	5,2	234-235	4	5,2	281-282	5	4,4

Depth (cm)	Clasts >2mm (num.)	Mobile average	Depth (cm)	Clasts >2mm (num.)	Mobile average	Depth (cm)	Clasts >2mm (num.)	Mobile average
282-283	6	4,6	297-298	3	5,6	312-313	6	5,0
283-284	4	4,2	298-299	5	5,8	313-314	6	4,8
284-285	4	4,4	299-300	8	5,6	314-315	3	4,6
285-286	3	4,4	300-301	8	5,2	315-316	6	5,4
286-287	6	4,8	301-302	4	5,0	316-317	4	5,4
287-288	4	4,0	302-303	4	5,4	317-318	5	6,0
288-289	5	4,0	303-304	4	5,4	318-319	5	6,0
289-290	4	3,6	304-305	6	5,6	319-320	7	6,8
290-291	5	4,2	305-306	7	5,6	320-321	6	6,2
291-292	2	4,0	306-307	6	5,2	321-322	7	6,3
292-293	4	4,4	307-308	4	5,6	322-323	5	6,0
293-294	3	4,2	308-309	5	6,0	323-324	9	6,5
294-295	7	4,6	309-310	6	6,2	324-325	4	4,0
295-296	4	4,8	310-311	5	5,6			
296-297	4	5,6	311-312	8	5,8			

Table S20 Clasts >2 mm counted using the method of Grobe (1987) and mobile average (interval of 5 cm) of the core ANTA99-GC14.

Physical analyses - Magnetic susceptibility, Compression strength, Water content and Grain size

Magnetic susceptibility (MS) (tab. S21, fig. S16) has values comprised between $450*10^6$ SI and $750*10^6$ SI from the bottom up to 27 cm. There are three peaks (clasts): $1060*10^6$ SI at 197 cm, $710*10^6$ SI at 77 cm and $970*10^6$ SI at 31 cm. After that, it rapidly decreases toward the top, reaching $40*10^6$ SI.

Compressive strength (CS) (tab. S22, fig. S16) of this core shows a decreasing up core trend, from 1,9 kg/cm^2 to 0,3 kg/cm^2.

A slightly increasing trend characterises the water content (w%) (tab. S23, fig. S16) of this core from the bottom to 50 cm. W% reaches a peak of 45,2% at 45 cm. Then, it drops to 24,4% at 41 cm. In the upper part of the core, w% rapidly increases again, reaching 54,3% at the top of the core.

Silt is the main sedimentary component (tab. S24, fig. S16) with an average value of 75,8% (max: 88,6%, min: 62,1%). Sand, with an average value of 17,2% (max 33%, min 5,1%) is the second component. Its presence decreases at the top of the core. Clay, with an average value of 6,9% (max 10,8%, min 4%), is characterised by a constant trend along the core (tab. S24, fig. S16).

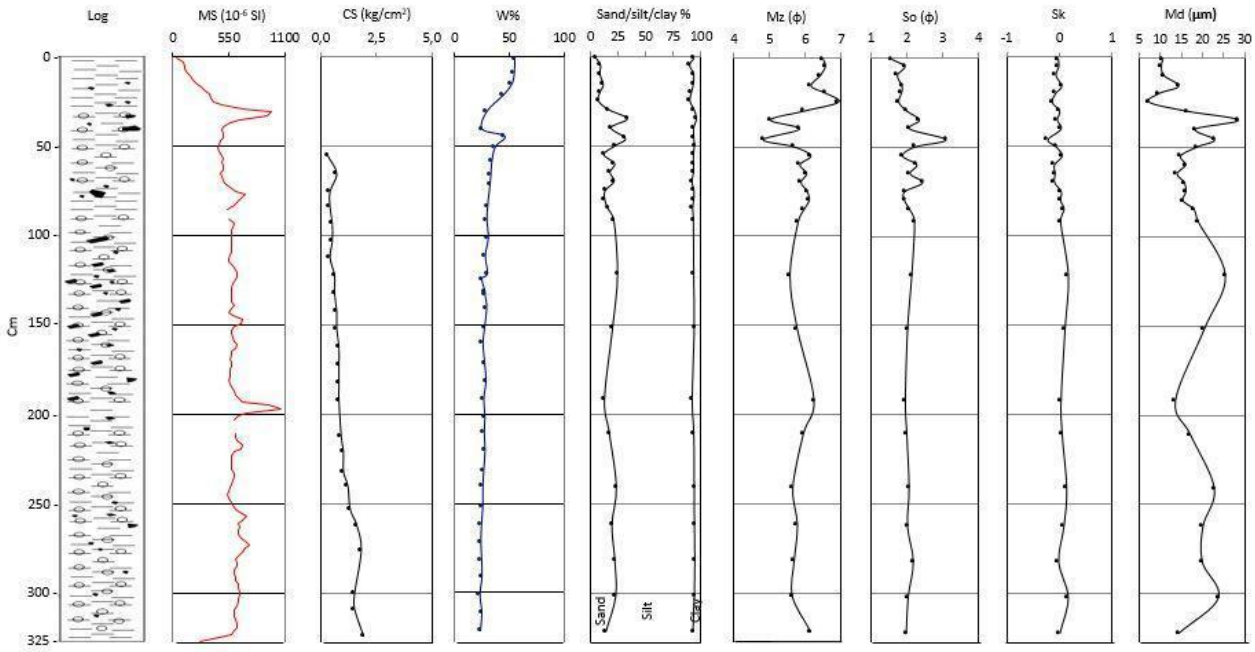

Figure S16 Physical parameters of the core GC14.

Mean diameter (Mz) shows values between 4,81 ϕ (coarse silt) and 6,92 ϕ (fine silt). The average value is 5,94ϕ. Sorting (So), with an average value of 2,06 ϕ, is very poorly sorted. The upper 25 cm are poorly sorted. Skewness (Sk) has an average value of -0,01. This core (tab. S24, fig. S16) is characterised by a symmetric distribution along the core, with positive asymmetric samples from the bottom to 122 cm, while there are few negative asymmetric intervals in the upper 60 cm. Higher fluctuating values characterise the median diameter (Md) from the bottom to 35 cm, while Md shows lower values in the upper part of the core (tab. S24, fig. S16).

Samples collected at 322 cm and between 211 and 192 cm are characterised by a primary mode of 6,5 ϕ (11,05 µm) and an unimodal distribution (fig. S17). Samples collected between 302 and 241 cm and between 152 and 92 cm show a main mode between 4,5 and 5,0 ϕ (44,19 - 31,25 µm). Then, the primary mode increases, ranging between 5,5 and 6,5 ϕ (22,09 - 11,05 µm) from 85 to 35 cm, with an interval around 7,0 ϕ (7,81 µm) between 65 and 60 cm. There is a bimodal interval at 45-46 cm, with the primary mode at 6,5 ϕ (11,05 µm) and the secondary mode at 0,5 ϕ (707,11 µm). Curve of the sample collected at 35 cm is sand-rich. The upper part of the core shows a primary mode (tab. S22) between 7,0 and 7,5 ϕ (7,81 - 5,52 µm), with curves characterised by an unimodal distribution. Sample collected at 16 cm shows a primary mode (tab. S24) of 6,5 ϕ (11,05 µm).

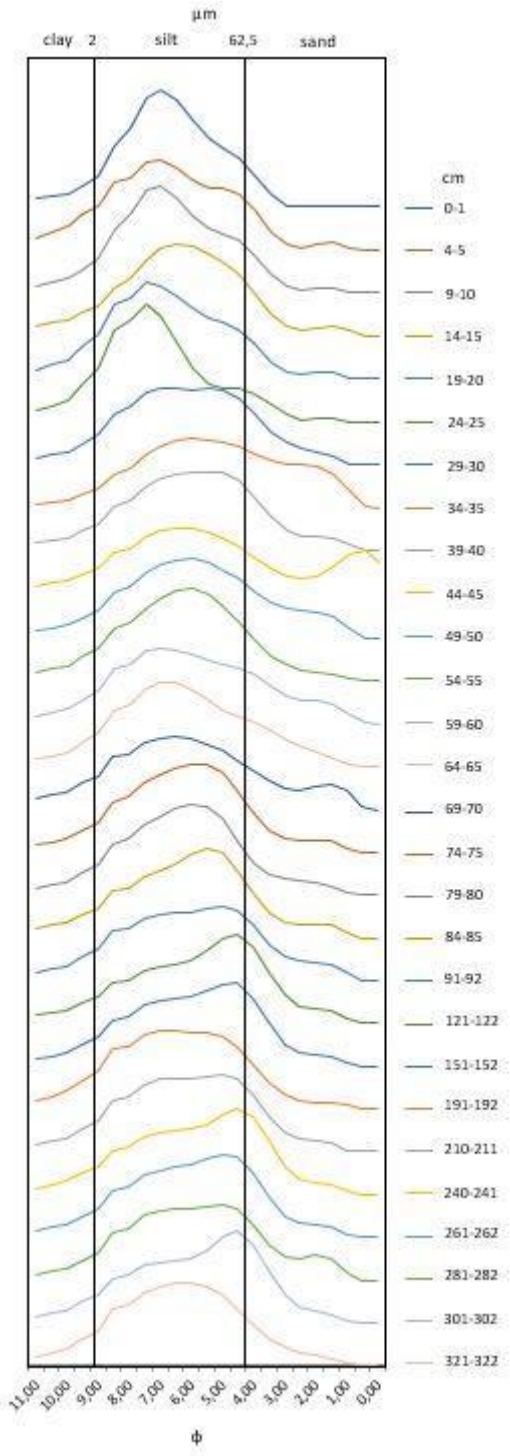

Figure S17 Grain size distribution core GC14.

Depth (cm)	MS (10^{-6}SI)	Depth (cm)	MS (10^{-6}SI)	Depth (cm)	MS (10^{-6}SI)	Depth (cm)	MS (10^{-6}SI)
0-1	40	94-95	590	188-189	620	282-283	630
2-3	100	96-97	570	190-191	640	284-285	630
4-5	120	98-99	570	192-193	690	286-287	610
6-7	120	100-101	570	194-195	940	288-289	610
8-9	140	102-103	580	196-197	1060	290-291	620
10-11	170	104-105	580	198-199	720	292-293	620
12-13	200	106-107	580	300-201	650	294-295	640
14-15	240	108-109	580	202-203	600	296-297	640
16-17	280	110-111	560	204-205	490	298-299	660
18-19	320	112-113	550	206-207	330	300-301	660
20-21	360	114-115	550	208-209	490	302-303	650
22-23	380	116-117	590	210-211	620	304-305	640
24-25	400	118-119	620	212-213	620	306-307	630
26-27	480	120-121	630	214-215	630	308-309	600
28-29	680	122-123	630	216-217	680	310-311	600
30-31	970	124-125	620	218-219	670	312-313	600
32-33	930	126-127	590	220-221	610	314-315	620
34-35	660	128-129	580	222-223	580	316-317	630
36-37	560	130-131	570	224-225	570	318-319	630
38-39	500	132-133	570	226-227	570	320-321	610
40-41	480	134-135	570	228-229	570	322-323	570
42-43	500	136-137	580	230-231	570	324-325	450
44-45	500	138-139	600	232-233	600	326-327	260
46-47	470	140-141	570	234-235	600		
48-49	450	142-143	550	236-237	590		
50-51	440	144-145	590	238-239	580		
52-53	460	146-147	690	240-241	560		
54-55	480	148-149	670	242-243	550		
56-57	490	150-151	600	244-245	540		
58-59	480	152-153	580	246-247	550		
60-61	490	154-155	580	248-249	580		
62-63	490	156-157	590	250-251	590		
64-65	470	158-159	600	252-253	620		
66-67	480	160-161	630	254-255	660		
68-69	490	162-163	620	256-257	720		
70-71	510	164-165	580	258-259	680		
72-73	560	166-167	570	260-261	650		
74-75	620	168-169	560	262-263	660		
76-77	710	170-171	570	264-265	650		
78-79	670	172-173	580	266-267	640		
80-81	640	174-175	560	268-269	670		
82-83	610	176-177	560	270-271	710		
84-85	530	178-179	560	272-273	750		
86-87	410	180-181	550	274-275	710		
88-89	420	182-183	560	276-277	680		
90-91	550	184-185	580	278-279	640		
92-93	600	186-187	600	280-281	620		

Table S21 Magnetic susceptibility of the core ANTA99-GC14. Yellow levels the end of each core section or peaks related to clasts.

Depth (cm)	CS (Kg/cm²)
54-55	0,3
65-66	0,7
75-76	0,4
83-84	0,4
92-93	0,5
102-103	0,5
111-112	0,4
121-122	0,6
131-132	0,6
141-142	0,7
151-152	0,7
161-162	0,8
171-172	0,8
181-182	0,8
191-192	0,8
211-212	0,9
220-221	1,0
231-232	1,0
239-240	1,2
252-253	1,3
261-262	1,6
275-276	1,8
299-300	1,5
308-309	1,5
323-324	1,9

Table S22 Compressive strength of the core ANTA99-GC14.

Depth (cm)	W%
1-2	54,3
09-10	53,9
15-16	51,5
21-22	43,9
30-31	29,0
40-41	24,4
44-45	45,2
50-51	36,5
58-59	33,3
66-67	32,4
71-72	31,7
83-84	29,5
91-92	28,8
101-102	30,1
111-112	27,4
121-122	29,3
124-125	24,2
131-132	27,1
133-134	27,1
140-141	28,6
151-152	26,7
160-161	25,3
171-172	26,8
181-182	28,0
191-192	26,0
201-202	27,0
210-211	26,4
220-221	27,1
231-232	26,0
240-241	25,2
251-252	25,1
261-262	23,9
271-272	23,3
281-282	24,0
291-292	24,3
301-302	22,5
311-312	24,2
321-322	22,9

Table S23 Water content of the core ANTA99-GC14.

GC14	Sand (%)	Silt (%)	Clay (%)	Mz (φ)	So (φ)	Sk	Md (μm)	Primary mode (φ)
0-1	5,1	88,6	6,3	6,49	1,57	-0,03	10,5	7,00
4-5	9,1	80,1	10,8	6,55	1,94	-0,02	10,1	7,00
9-10	8,6	84,7	6,7	6,41	1,73	-0,08	10,7	7,00
15-16	11,7	81,1	7,2	6,15	1,86	0,03	14,3	6,50
19-20	8,8	82,4	8,8	6,56	1,84	-0,08	9,7	7,50
24-25	7,2	82,4	10,5	6,92	1,77	-0,15	7,3	7,50
29-30	16,7	77,1	6,2	5,95	2,00	-0,01	16,3	7,00
34-35	33,0	63,0	4,0	5,01	2,34	-0,05	28,5	6,00
39-40	18,5	74,9	6,6	5,83	2,08	0,02	18,3	5,50
45-46	31,4	62,1	6,5	4,81	3,08	-0,23	22,8	6,50
49-50	22,2	71,9	5,9	5,66	2,22	-0,07	18,6	6,00
54-55	12,1	80,9	7,0	6,14	1,87	0,04	14,7	6,00
59-60	21,7	71,5	6,8	5,84	2,27	-0,11	15,9	7,00
64-65	17,6	75,7	6,8	6,02	2,08	-0,10	13,9	7,00
69-70	21,3	70,2	8,5	5,86	2,43	-0,10	15,7	6,50
74-75	13,5	80,1	6,4	6,04	1,94	0,02	16,0	5,50
79-80	12,8	80,6	6,6	6,10	1,93	0,01	15,3	6,00
84-85	15,6	76,7	7,7	5,95	2,07	0,08	18,0	5,50
91-92	21,1	72,0	7,0	5,79	2,21	0,01	19,0	5,00
121-122	24,3	69,1	6,6	5,56	2,13	0,16	25,4	4,50
151-152	19,9	73,9	6,2	5,76	2,01	0,10	20,3	4,50
191-192	12,6	79,2	8,2	6,23	1,95	0,02	13,5	6,50
210-211	17,1	76,4	6,6	5,93	1,99	0,04	17,1	6,50
240-241	23,2	70,7	6,1	5,64	2,06	0,13	22,8	4,50
261-262	19,3	74,7	5,9	5,76	2,01	0,08	20,1	5,00
281-282	21,9	72,6	5,5	5,67	2,17	-0,03	19,9	5,00
301-302	22,7	71,3	6,0	5,62	2,03	0,16	23,8	4,50
321-322	13,9	78,7	7,4	6,14	1,98	0,00	14,3	6,50

Table S24 Grain size parameters of the core ANTA99-GC14.

Chemical and Geochemical analyses - Elemental analyses, Organic matter and Biomarkers

There is a high correlation between Al, Si, Ti, K, Fe, Rb, Sr, Zr and Ba. Ca is also correlated with these elements, except for Ti and Rb. In this core, Br does not correlate with other elements. See tab. S25.

Ti (cps) shows slightly fluctuating values with a decreasing trend in the upper 45 cm. Zr/Rb has values higher than 1,5 from the bottom up to 45 cm. The interval between 45 cm and 30 cm has values around 1,5. The upper part of the core is characterised by lower values. Si/Ti is characterised by a constant trend, with several oscillations mainly below 180 cm and above 50 cm. Fe/Ti has a constant trend. K/Ti shows an increasing trend from the bottom up to 200 cm. Then, it has a constant trend from 200 cm to 26 cm. After that, K/Ti slightly decreases toward the top of the core. Ca/Ti is characterised by a constant trend from the bottom up to 75 cm, with a peak at 95 cm. Next, it decreases toward 49 cm. Then, Ca/Ti increases again between 49 and 31 cm. In the upper part of

the core, Ca/Ti is characterised by a decreasing trend. Mn/Ti is characterised by low constant values, with a peak at 62 cm. Then, it has a decreasing trend toward the top of the core. See fig. S18 for graphics of Ti (cps) as representative of lithogenic elements and several elemental ratios.

GC14	Al_cps	Si_cps	K_cps	Ca_cps	Ti_cps	Fe_cps	Br_cps	Rb_cps	Sr_cps	Zr_cps	Ba50_cps
Al_cps		1,87E-104	4,84E-99	4,73E-55	7,36E-70	8,44E-87	0,014697	3,95E-70	5,99E-92	5,50E-86	8,71E-61
Si_cps	**0,90625**		5,00E-153	1,20E-30	6,06E-104	6,78E-123	0,006604	3,49E-114	2,67E-80	2,22E-79	5,20E-96
K_cps	**0,89681**	**0,95967**		5,71E-24	1,55E-155	1,04E-206	0,018639	6,88E-147	9,91E-82	5,06E-77	1,91E-83
Ca_cps	**0,76844**	**0,61952**	*0,5578*		3,14E-16	1,16E-22	3,46E-16	5,00E-18	7,17E-60	9,39E-48	1,68E-24
Ti_cps	**0,82496**	**0,9054**	**0,96137**	0,46524		4,55E-180	7,96E-05	2,41E-115	2,33E-70	4,21E-62	5,81E-74
Fe_cps	**0,87156**	**0,93214**	**0,98384**	*0,54402*	**0,97459**		0,025284	1,42E-123	6,27E-82	5,33E-73	8,69E-77
Br_cps	-0,14673	0,16314	0,14154	-0,46465	0,23522	0,13465		4,87E-06	0,27414	0,33538	0,000582
Rb_cps	**0,82584**	**0,92099**	**0,95519**	0,48939	**0,92258**	**0,93294**	0,27117		1,32E-74	2,38E-71	1,06E-95
Sr_cps	**0,88291**	**0,85551**	**0,85922**	**0,78885**	**0,82658**	**0,85973**	-0,06605	**0,83965**		2,65E-104	4,07E-78
Zr_cps	**0,86966**	**0,85307**	**0,8466**	**0,73295**	**0,7976**	**0,83484**	-0,0582	**0,82973**	**0,906**		8,74E-64
Ba50_cps	**0,79249**	**0,8911**	**0,86353**	*0,56321*	**0,83774**	**0,84594**	0,20577	**0,8905**	**0,84964**	**0,80392**	

Table S25 Elements correlation of the core GC14. Bold and underlined values represent moderate to strong correlation. Underlined values in italics represent low correlation.

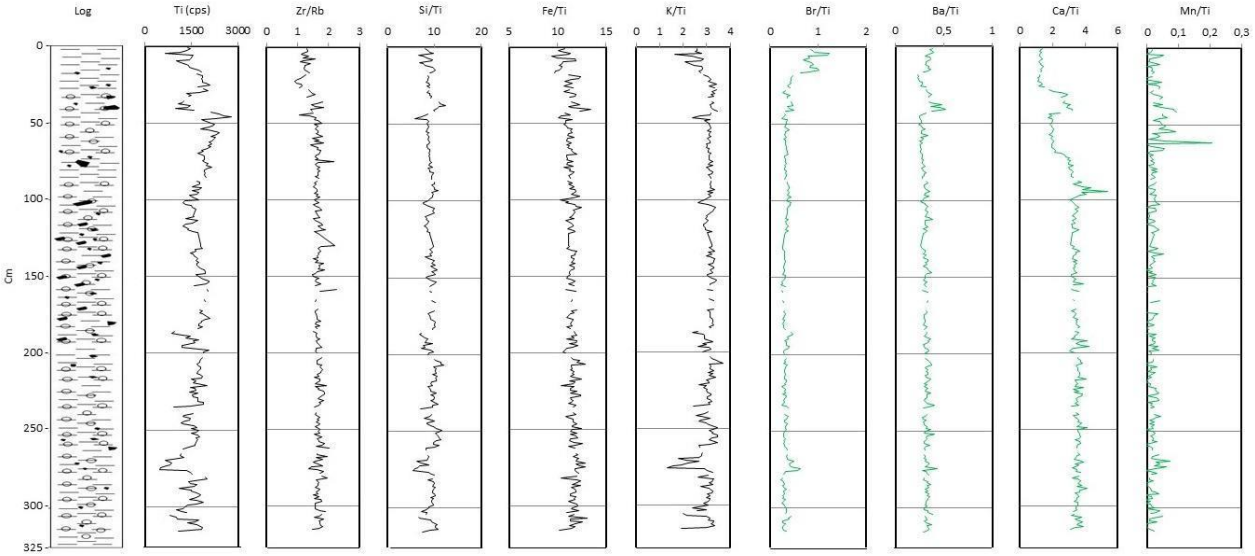

Figure S18 Elemental ratios of the core GC14.

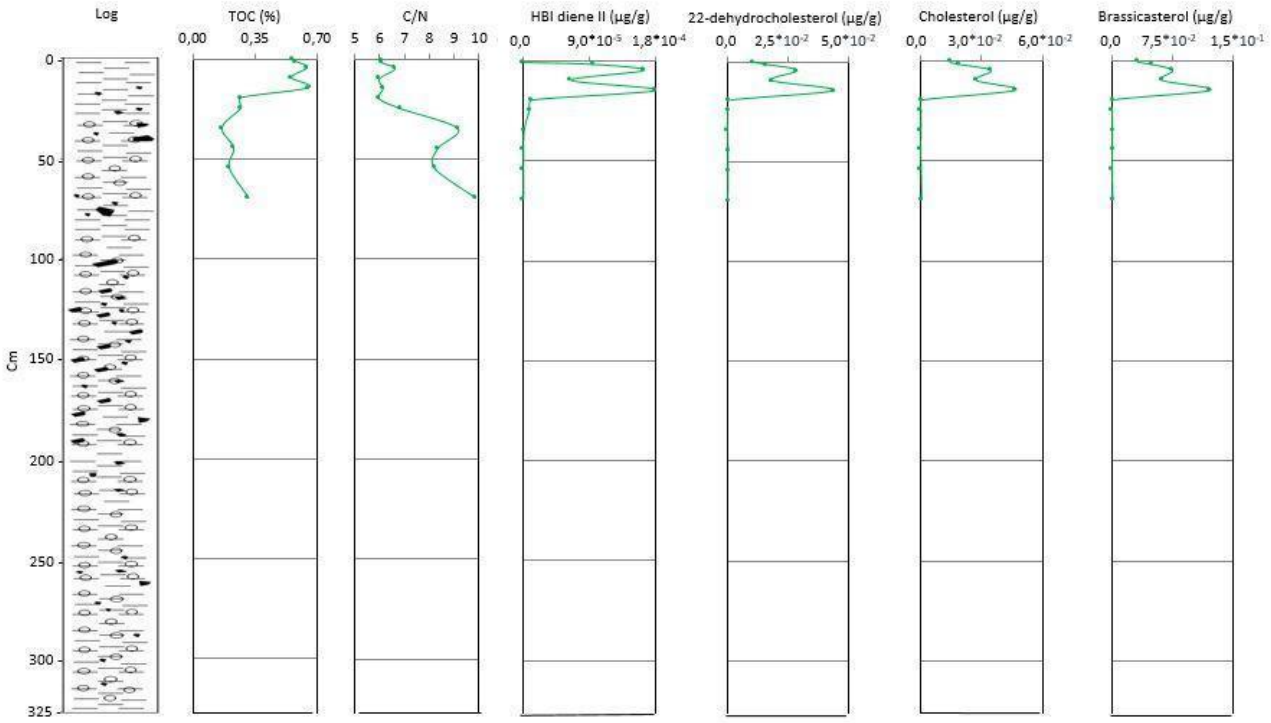

Figure S19 Organic matter and biomarkers parameters of the core GC14.

TOC values (tab. S26, fig. S19) range between 0,16 and 0,65% (avg 0,40%) and show a decreasing trend between 70 cm and 35 cm. Then, it rises to values higher than 0,55% in the upper 15 cm, with two peaks at 15 and 5 cm (0,65 and 0,64% respectively).

C/N (tab. S26, fig. S19) shows a decreasing trend toward the top of the core. It ranges from values higher than 9,00 from 70 to 35 cm, to values around 7,00-8,00 in the upper part of the core. The average value is 8,42.

Both $IPSO_{25}$ (avg $4,76*10^{-5}$ µg/g) and sterols (avg $1,08*10^{-2}$ µg/g for 22-dehydrocholesterol, $1,33*10^{-2}$ µg/g for cholesterol and $3,11*10^{-2}$ µg/g for brassicasterol) (tab. S27, fig. S19) have a similar trend, with a very low concentration between 70 cm and 20 cm. HBI diene II has not been detected below 45 cm and at the top of the core. The highest values have been measured at 15 ($1,80*10^{-4}$ µg/g) and 5 cm ($1,63*10^{-4}$ µg/g). All three sterols has two peaks at 15 ($4,40*10^{-2}$ µg/g for 22-dehydrocholesterol, $4,70*10^{-2}$ µg/g for cholesterol and $1,22*10^{-1}$ µg/g for brassicasterol) and 5 cm ($2,88*10^{-2}$ µg/g for 22-dehydrocholesterol, $3,50*10^{-2}$ µg/g for cholesterol and $7,54*10^{-2}$ µg/g for brassicasterol).

GC14	TOC (%)	TN (%)	C/N
0-1	0,57	0,09	7,10
1-2	0,58	0,10	7,12
4-5	0,64	0,10	7,73
9-10	0,55	0,09	6,99
14-15	0,65	0,11	7,16
19-20	0,27	0,04	6,98
24-25	0,27	0,04	7,98
34-35	0,16	0,02	10,67
44-45	0,23	0,03	9,75
54-55	0,20	0,02	9,59
69-70	0,31	0,03	11,52

Table S26 Organic matter parameters of the core ANTA99-GC14.

GC14	$IPSO_{25}$ (µg/g dry sedim.)	22-dehydrocholesterol (µg/g dry sedim.)	Cholesterol (µg/g dry sedim.)	Brassicasterol (µg/g dry sedim.)
0-1	0	$1,06*10^{-2}$	$1,47*10^{-2}$	$3,21*10^{-2}$
1-2	$9,49*10^{-5}$	$1,62*10^{-2}$	$1,91*10^{-2}$	$4,90*10^{-2}$
4-5	$1,63*10^{-4}$	$2,88*10^{-2}$	$3,50*10^{-2}$	$7,54*10^{-2}$
9-10	$6,45*10^{-5}$	$1,84*10^{-2}$	$2,77*10^{-2}$	$6,22*10^{-2}$
14-15	$1,80*10^{-4}$	$4,40*10^{-2}$	$4,70*10^{-2}$	$1,22*10^{-1}$
19-20	$1,16*10^{-5}$	$2,28*10^{-4}$	$1,18*10^{-3}$	$6,52*10^{-4}$
24-25	$8,20*10^{-6}$	$7,29*10^{-5}$	$4,14*10^{-4}$	0
34-35	$7,72*10^{-7}$	0	$3,42*10^{-4}$	$1,25*10^{-4}$
44-45	0	$1,18*10^{-4}$	$2,30*10^{-4}$	$3,45*10^{-5}$
54-55	0	$9,72*10^{-5}$	$4,31*10^{-4}$	0
69-70	0	$8,67*10^{-5}$	$6,49*10^{-4}$	$4,69*10^{-4}$

Table S27 Biomarkers of the core ANTA99-GC14.

Microscopy analyses - Sand and Foraminifera

Quartz grains with both angular to sub-rounded edges, rounded feldspar, micas and other femic minerals are present along the core. Lithic fragments are less abundant at the top of the core. Biogenic component is generally sparse in the upper 60 cm. Radiolarians, sponge spicules and diatoms represent the siliceous component.

Sparse calcareous foraminifera (tab. S28) have been recovered between 302 cm and 92 cm and between 60 cm and 40 cm, mainly broken or not well preserved. Agglutinated foraminifera, represented by *M. earlandi* and *P. antarctica* have been recovered in the upper 10 cm.

Fragmentation rate ranges between 25 and 100%. 19 different species have been identified, belonging to 17 different genera. Density is higher in the upper part of the core (3,3 specimens/g at 10 cm). The planktic *Neogloboquadrina pachyderma* (adult form) is sparsely present.

GC14	*Neogloboquadrina pachyderma*	Benthos/g	*Astrononion antarcticus*	Bolivina sp.	Bolivinellina sp.	*Cassidulina carinata*	*Cassidulinoides parkerianus*	*Cassidulinoides porrectus*	Cibicides sp.	*Ehrembergina glabra*	*Globocassidulina subglobosa*	Lagena spp.	*Miliammina earlandi*	*Nonionella bradyi*	*Nonionella iridea*	*Parafissurina fusiformis*	*Portatrochammina antarctica*	*Textularia earlandi*	*Trifarina earlandi*	*Triloculina tricarinata*	% fragmentation
1-2	0	1,2	0	0	0	0	0	0	0	0	0	0	13	0	0	0	0	1	0	0	41,7
9-10	0	3,3	0	0	0	0	0	0	0	0	0	0	3	0	0	0	3	1	0	0	36,4
19-20	0	0,0	0	0	0	0	0	0	0	0	0	0	0	0	0	0	0	0	0	0	0,0
28-29	1	0,0	0	0	0	0	0	0	0	0	0	0	0	0	0	0	0	0	0	0	0,0
34-35	0	0,3	0	1	0	0	0	0	0	0	0	0	0	0	0	0	0	0	0	0	50,0
39-40	1	0,3	0	0	0	0	1	0	0	0	0	0	0	0	0	0	0	0	0	0	66,7
45-46	0	0,3	0	0	0	0	0	0	0	0	0	0	0	1	0	0	0	0	0	0	50,0
49-50	0	0,0	0	0	0	0	0	0	0	0	0	0	0	0	0	0	0	0	0	0	100
59-60	1	0,0	0	0	0	0	0	0	0	0	0	0	0	0	0	0	0	0	0	0	0,0
64-65	0	0,0	0	0	0	0	0	0	0	0	0	0	0	0	0	0	0	0	0	0	0,0
68-69	0	0,0	0	0	0	0	0	0	0	0	0	0	0	0	0	0	0	0	0	0	0,0
79-80	0	0,0	0	0	0	0	0	0	0	0	0	0	0	0	0	0	0	0	0	0	0,0
84-85	0	0,0	0	0	0	0	0	0	0	0	0	0	0	0	0	0	0	0	0	0	0,0
91-92	0	0,1	0	0	0	0	0	0	0	0	2	0	0	0	0	0	0	0	0	0	0,0
94-95	0	0,0	0	0	0	0	0	0	0	0	0	0	0	0	0	0	0	0	0	0	0,0
111-112	1	0,2	0	0	0	0	0	0	0	1	1	0	0	0	1	0	0	0	0	1	37,5
121-122	0	0,05	0	0	0	0	0	0	0	0	1	0	0	0	0	0	0	0	0	0	0,0
131-132	0	0,1	0	0	0	0	0	1	0	0	0	1	0	0	0	0	0	0	1	0	50,0
140-141	0	0,1	0	0	0	0	0	0	0	1	1	1	0	0	0	0	0	0	0	0	25,0
151-152	0	0,0	0	0	0	0	0	0	0	0	0	0	0	0	0	0	0	0	0	0	100
171-172	0	0,05	0	0	0	0	0	0	0	0	1	0	0	0	0	0	0	0	0	0	50,0
192-193	1	0,1	0	0	0	1	0	0	0	0	1	0	0	0	0	0	0	0	0	0	50,0
210-211	0	0,05	0	0	1	0	0	0	0	0	0	0	0	0	0	0	0	0	0	0	0,0
240-241	0	0,0	0	0	0	0	0	0	0	0	0	0	0	0	0	0	0	0	0	0	100
261-262	0	0,05	0	0	0	0	0	0	0	0	0	0	0	0	0	1	0	0	0	0	66,7
281-282	0	0,0	0	0	0	0	0	0	0	0	0	0	0	0	0	0	0	0	0	0	100
301-302	0	0,3	0	0	0	0	0	0	0	0	0	0	0	0	0	0	0	0	0	0	41,7
321-322	0	0,0	0	0	0	0	0	0	0	0	0	0	0	0	0	0	0	0	0	0	100

Table S28 Foraminifera of the core ANTA99-GC14.

ANTA99-GC15

This core has been collected in the middle continental shelf (tab. 3, fig. 6). Build-ups of glaciomarine sediments drape the sea floor (fig. S20).

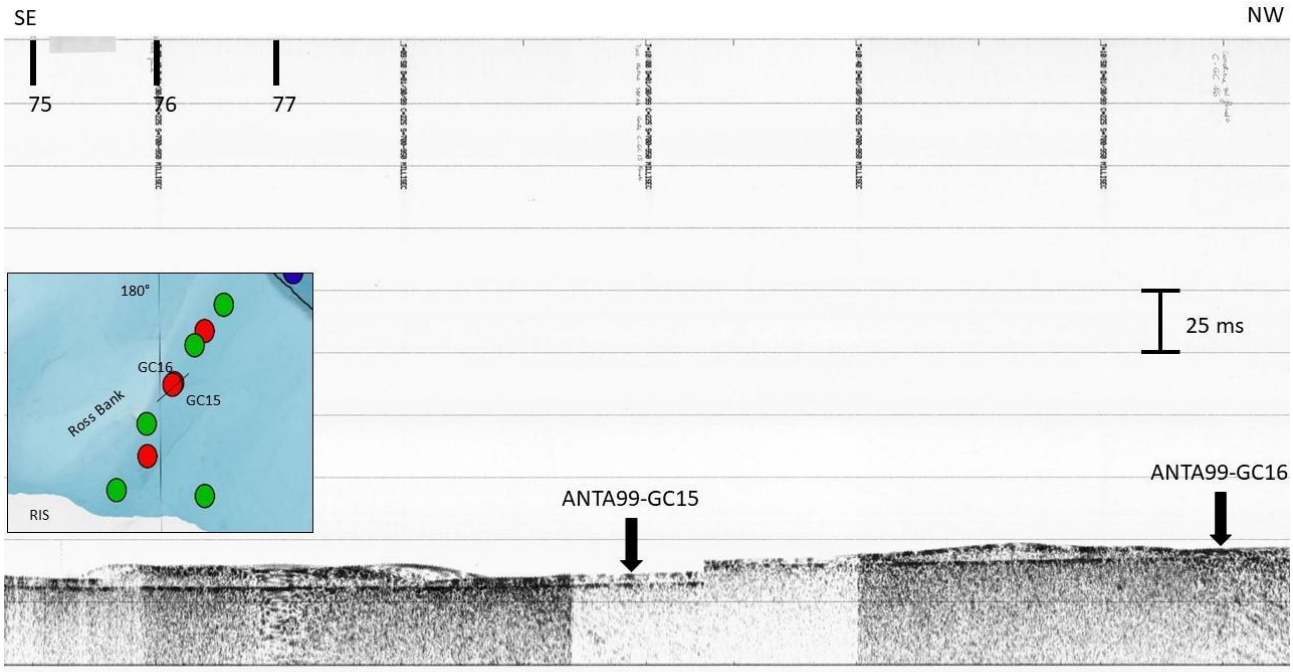

Figure S20 Section of the SBPs 14 and 15, with the location of the cores GC15 and GC16. Bathymetric map is a zoom of fig. 6.

Core radiography

The core (fig. S21) is 190 cm long, but the radiography shows that the upper 5 cm are empty. The description has been done considering the bottom of the core as 185 cm and 5 cm as the top of the core. Sediments (185 cm) are dense and made of sandy and gravelly material in a fine matrix. Dimensions of clasts range from millimetric to pluri-centimetric, while the shape ranges from rounded to sub-angular. A detachment at 110 cm divides the lower part of the core from a section (110-70 cm) characterised by lamination. From 82 to 70 cm, laminations are weaker and thinner.

Fluctuating values of the mobile average of clasts >2 mm characterises this core (tab. S29, fig. S21).

Physical analyses - Magnetic susceptibility

Magnetic susceptibility (MS) (tab. S30, fig. S21) rapidly increases from the bottom to 161 cm, reaching a peak of $994*10^{-6}$ SI (clasts). MS fluctuates between 700 and $900*10^{-6}$ SI from 161 to 85 cm. MS shows a decreasing trend in the upper part of the core, reaching the lowest value at the top: $290*10^{-6}$ SI.

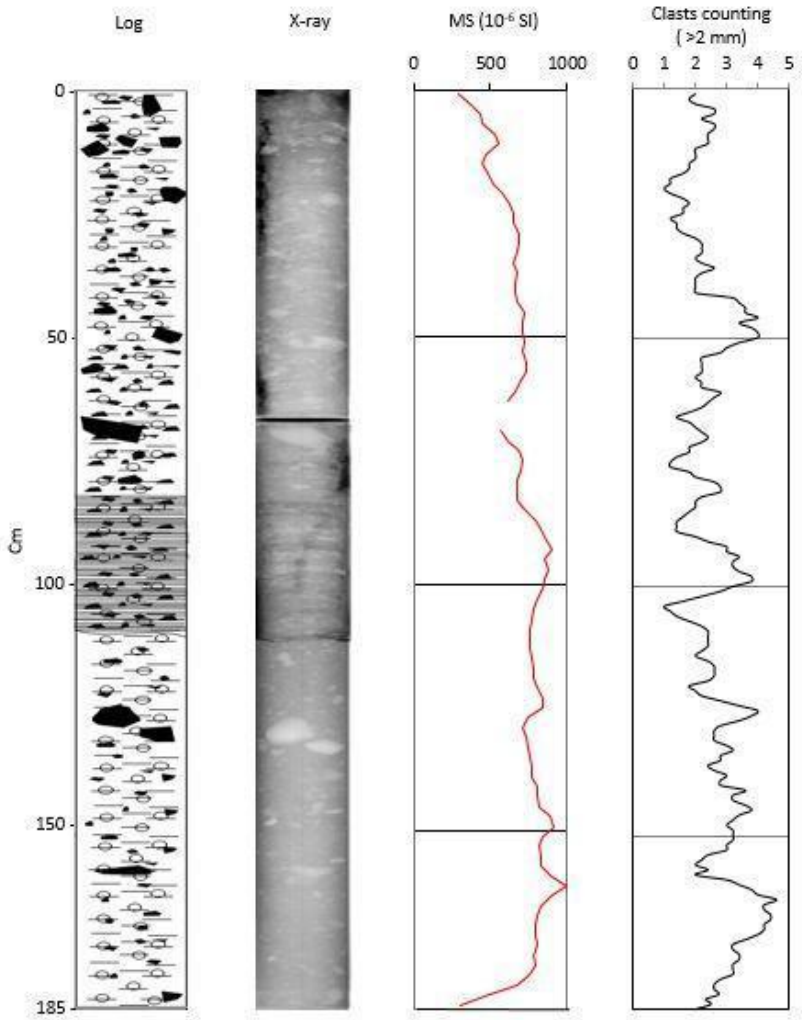

Figure S21 Descriptive log, radiography, magnetic susceptibility and clasts counted using the Grobe (1987) method (mobile average interval: 5 cm) of the core GC15.

Depth (cm)	Clasts >2mm (num.)	Mobile average	Depth (cm)	Clasts >2mm (num.)	Mobile average	Depth (cm)	Clasts >2mm (num.)	Mobile average
0-1	2	2,0	47-48	3	3,8	94-95	3	3,2
1-2	2	1,8	48-49	3	4,0	95-96	3	3,2
2-3	1	2,0	49-50	5	4,0	96-97	2	3,4
3-4	2	2,6	50-51	4	3,4	97-98	5	3,8
4-5	3	2,6	51-52	4	3,0	98-99	3	3,8
5-6	1	2,2	52-53	4	2,8	99-100	3	3,2
6-7	3	2,6	53-54	3	2,2	100-101	4	2,8
7-8	4	2,6	54-55	2	2,2	101-102	4	2,2
8-9	2	2,4	55-56	2	2,2	102-103	5	1,6
9-10	1	2,4	56-57	3	2,2	103-104	0	1,0
10-11	3	2,4	57-58	1	2,0	104-105	1	1,2
11-12	3	2,0	58-59	3	2,2	105-106	1	1,4
12-13	3	2,0	59-60	2	2,2	106-107	1	1,8
13-14	2	2,0	60-61	2	2,8	107-108	2	2,2
14-15	1	1,8	61-62	2	2,6	108-109	1	2,4
15-16	1	1,8	62-63	2	2,4	109-110	2	2,4
16-17	3	1,6	63-64	3	2,2	110-111	3	2,4
17-18	3	1,2	64-65	5	1,8	111-112	3	2,4
18-19	1	1,2	65-66	1	1,4	112-113	3	2,2
19-20	1	1,0	66-67	1	1,8	113-114	1	2,0
20-21	0	1,2	67-68	1	2,0	114-115	2	2,4
21-22	1	1,6	68-69	1	2,2	115-116	3	2,6
22-23	3	1,8	69-70	3	2,4	116-117	2	2,6
23-24	0	1,6	70-71	3	2,2	117-118	2	2,6
24-25	2	1,6	71-72	2	1,8	118-119	3	2,4
25-26	2	1,2	72-73	2	1,8	119-120	3	1,8
26-27	2	1,4	73-74	2	1,4	120-121	3	2,0
27-28	2	1,4	74-75	2	1,2	121-122	2	2,2
28-29	0	1,6	75-76	1	1,2	122-123	1	2,8
29-30	0	2,0	76-77	2	1,8	123-124	0	3,4
30-31	3	2,2	77-78	0	2,0	124-125	4	4,0
31-32	2	2,2	78-79	1	2,6	125-126	4	3,8
32-33	3	2,2	79-80	2	2,8	126-127	5	3,4
33-34	2	2,0	80-81	4	2,8	127-128	4	2,8
34-35	1	2,2	81-82	3	2,2	128-129	3	2,6
35-36	3	2,6	82-83	3	2,0	129-130	3	2,6
36-37	2	2,2	83-84	2	2,0	130-131	2	2,6
37-38	2	2,0	84-85	2	1,8	131-132	2	3,0
38-39	3	2,0	85-86	1	1,6	132-133	3	3,2
39-40	3	2,0	86-87	2	1,4	133-134	3	2,8
40-41	1	2,0	87-88	3	1,4	134-135	3	2,8
41-42	1	3,2	88-89	1	1,4	135-136	4	2,4
42-43	2	3,4	89-90	1	2,0	136-137	3	2,6
43-44	3	3,6	90-91	0	2,4	137-138	1	3,0
44-45	3	3,6	91-92	2	3,0	138-139	3	2,8
45-46	7	4,0	92-93	3	3,0	139-140	1	2,8
46-47	2	3,4	93-94	4	3,4	140-141	5	3,6

Depth (cm)	Clasts >2mm (num.)	Mobile average	Depth (cm)	Clasts >2mm (num.)	Mobile average	Depth (cm)	Clasts >2mm (num.)	Mobile average
141-142	5	3,2	**156-157**	4	2,4	**171-172**	4	3,2
142-143	0	3,2	**157-158**	0	2,0	**172-173**	3	3,2
143-144	3	3,6	**158-159**	3	3,0	**173-174**	4	3,4
144-145	5	3,8	**159-160**	2	3,4	**174-175**	3	3,4
145-146	3	3,4	**160-161**	3	3,8	**175-176**	2	3,2
146-147	5	3,2	**161-162**	2	4,0	**176-177**	4	3,2
147-148	2	3,0	**162-163**	5	4,6	**177-178**	4	3,2
148-149	4	3,2	**163-164**	5	4,2	**178-179**	4	2,8
149-150	3	3,2	**164-165**	4	4,2	**179-180**	2	2,6
150-151	2	3,2	**165-166**	4	4,4	**180-181**	2	2,6
151-152	4	3,0	**166-167**	5	4,4	**181-182**	4	2,8
152-153	3	3,0	**167-168**	3	4,2	**182-183**	2	2,3
153-154	4	2,4	**168-169**	5	4,2	**183-184**	3	2,5
154-155	3	2,2	**169-170**	5	4,0	**184-185**	2	2,0
155-156	1	2,0	**170-171**	4	3,6			

Table S29 Clasts >2 mm counted using the method of Grobe (1987) and mobile average (interval of 5 cm) of the core ANTA99-GC15.

Depth (cm)	MS (10^{-6}SI)	Depth (cm)	MS (10^{-6}SI)
0-1	290	94-95	857
2-3	381	96-97	878
4-5	431	98-99	858
6-7	451	100-101	839
8-9	532	102-103	799
10-11	552	104-105	780
12-13	472	106-107	770
14-15	452	108-109	761
16-17	483	110-111	761
18-19	523	112-113	762
20-21	583	114-115	772
22-23	624	116-117	783
24-25	644	118-119	783
26-27	654	120-121	804
28-29	684	122-123	844
30-31	685	124-125	845
32-33	675	126-127	745
34-35	655	128-129	706
36-37	676	130-131	736
38-39	666	132-133	747
40-41	656	134-135	757
42-43	677	136-137	768
44-45	727	138-139	768
46-47	707	140-141	809
48-49	707	142-143	809
50-51	718	144-145	820
52-53	708	146-147	890
54-55	728	148-149	911
56-57	739	150-151	841
58-59	699	152-153	812
60-61	659	154-155	832
62-63	609	156-157	833
64-65	410	158-159	903
66-67	461	160-161	994
68-69	571	162-163	904
70-71	612	164-165	835
72-73	682	166-167	805
74-75	713	168-169	796
76-77	693	170-171	796
78-79	673	172-173	807
80-81	674	174-175	787
82-83	674	176-177	788
84-85	725	178-179	758
86-87	795	180-181	669
88-89	826	182-183	489
90-91	866	184-185	300
92-93	897		

Table S30 Magnetic susceptibility of the core ANTA99-GC15. Yellow levels the end of each core section or peaks related to clasts.

ANTA99-GC16

This core has been collected in the middle continental shelf (tab. 3, fig. 6). Build-ups of glaciomarine sediments characterise this area (fig. S22).

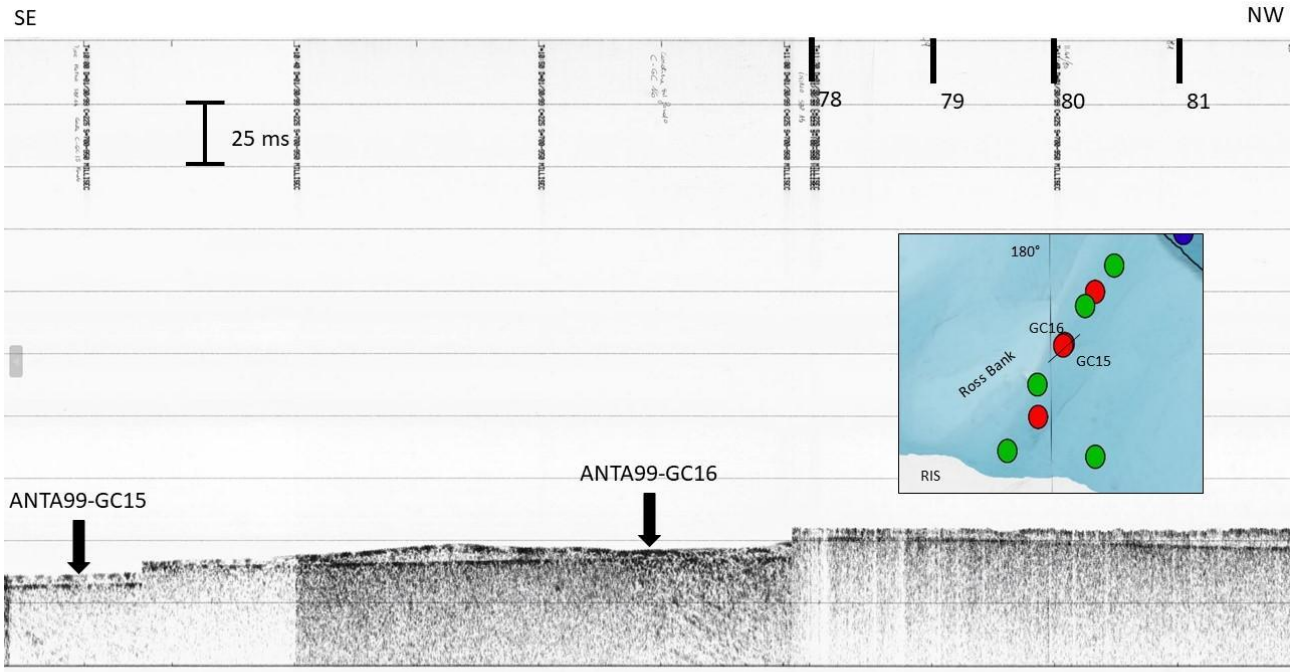

Fig. S22 Section of the SBPs 14 and 15, with the location of the cores GC15 and GC16. Bathymetric map is a zoom of fig.6.

Physical analyses - Magnetic susceptibility

Magnetic susceptibility (MS) (tab. S31, fig. S23) increases from the bottom, reaching values higher than $1000*10^{-6}$ SI in the interval from 55 to 47 cm (max $1820*10^{-6}$ SI at 53 cm)(probably related to clast concentration). MS decreases toward the top of the core (min $350*10^{-6}$ SI at the top).

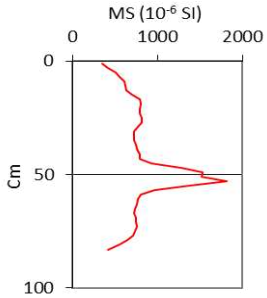

Figure S23 Magnetic susceptibility of the core GC16.

Depth (cm)	MS (10^{-6}SI)
0-1	350
2-3	420
4-5	510
6-7	560
8-9	610
10-11	620
12-13	630
14-15	700
16-17	800
18-19	810
20-21	790
22-23	790
24-25	820
26-27	820
28-29	770
30-31	730
32-33	730
34-35	730
36-37	750
38-39	760
40-41	790
42-43	800
44-45	930
46-47	1280
48-49	1530
50-51	1520
52-53	1820
54-55	1380
56-57	970
58-59	810
60-61	770
62-63	760
64-65	740
66-67	730
68-69	750
70-71	750
72-73	760
74-75	740
76-77	720
78-79	650
80-81	560
82-83	420

Table S31 Magnetic susceptibility of the core ANTA99-GC16. Yellow levels the end of each core section or peaks related to clasts.

ANTA99-GC17

This core has been collected in the outer continental shelf close to the junction of the Glomar Challenger Basin with the Pennell Trough (tab. 3, fig. 6). Core GC17 has been collected in a site characterised by a hummocky morphology (fig. S24).

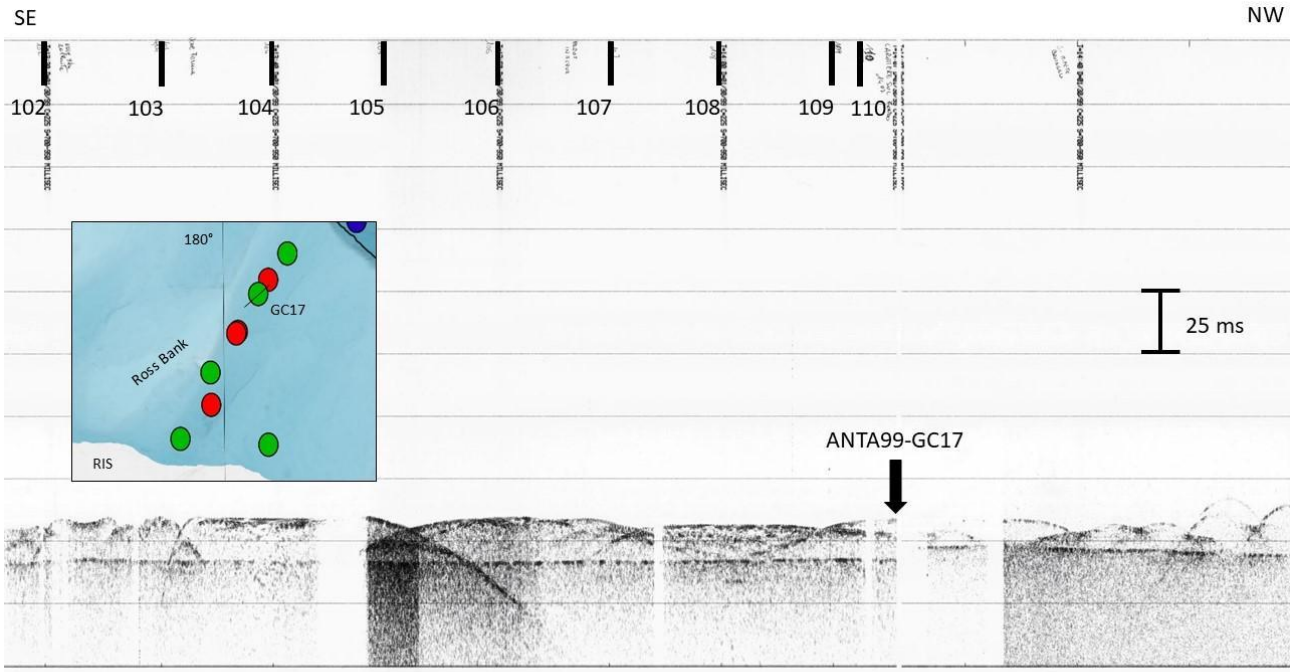

Figure S24 Section of the SBPs 15 and 16, with the location of the core GC17. Bathymetric map is a zoom of fig. 6.

Core description and Radiography

This core (fig. S25) is made of sandy and gravelly material within a fine matrix, with clasts from millimetric to pluri-centimetric, from the bottom to 30 cm. The colour is dark olive grey (5Y 3/2) from the bottom to 222 cm. The upper part of the deposit is dark grey (5Y 4/1). The upper 30 cm are made of sandy mud, with a muddy oblique layer around 15 cm. Colour changes from dark olive grey (5Y 3/2) from 30 to 23 cm, dark grey (5Y 4/1) from 23 to 10 cm, olive grey (5Y 4/2) from 10 to 4 cm and olive (5Y 3/4) in the upper 4 cm. The interval between 10 and 4 cm is coarser than the rest of the sediments of the upper part of the core. Pluri-centimetric clasts are also present in this interval. The upper 4 cm are hydrated. This core is characterised by sub-angular clasts, with also rounded and angular clasts.

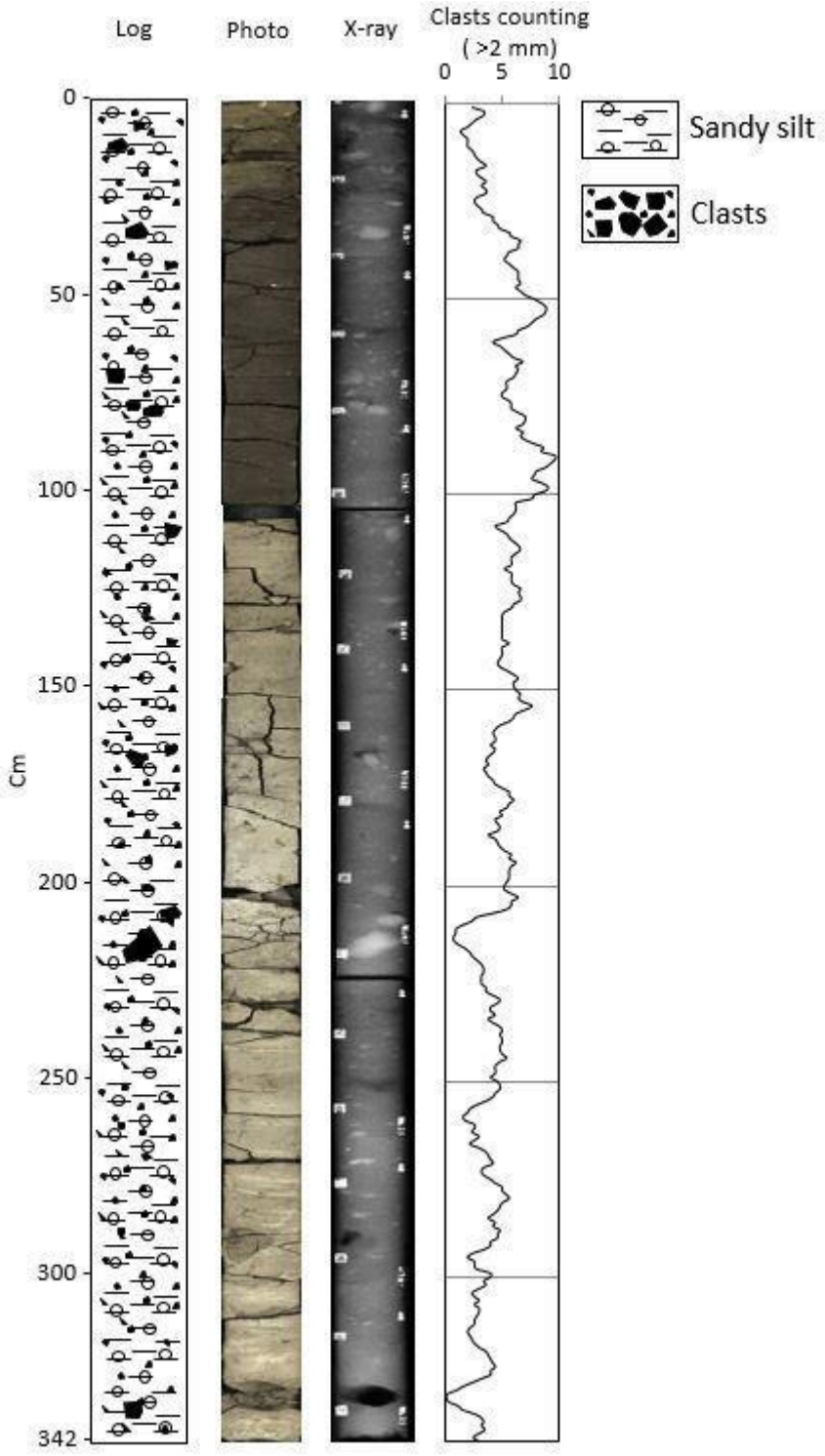

Figure S25 Lithologic log, photo, radiography, clasts counted using the Grobe (1987) method (mobile average interval: 5 cm) of the core GC17.

Fluctuating values of the mobile average of clasts >2 mm characterises this core, with a reduced presence of clasts around 335 cm and 217 cm where there are two large clasts and in the upper 30 cm (tab. S32, fig. S25).

Depth (cm)	Clasts >2mm (num.)	Mobile average	Depth (cm)	Clasts >2mm (num.)	Mobile average	Depth (cm)	Clasts >2mm (num.)	Mobile average
0-1	1	2,4	47-48	5	6,6	94-95	10	7,8
1-2	1	3,4	48-49	7	7,0	95-96	8	7,6
2-3	3	3,4	49-50	7	7,8	96-97	6	8,4
3-4	3	2,8	50-51	6	8,4	97-98	5	9,0
4-5	4	2,4	51-52	8	8,8	98-99	10	8,8
5-6	6	2,0	52-53	7	8,8	99-100	9	7,8
6-7	1	1,4	53-54	11	8,6	100-101	12	7,6
7-8	0	1,6	54-55	10	8,0	101-102	9	6,2
8-9	1	2,0	55-56	8	7,6	102-103	4	6,2
9-10	2	2,0	56-57	8	7,2	103-104	5	6,2
10-11	3	2,0	57-58	6	6,4	104-105	8	6,0
11-12	2	2,4	58-59	8	6,2	105-106	5	5,6
12-13	2	2,6	59-60	8	5,0	106-107	9	5,4
13-14	1	2,8	60-61	6	4,2	107-108	4	4,4
14-15	2	3,2	61-62	4	4,8	108-109	4	4,8
15-16	5	3,6	62-63	5	5,2	109-110	6	5,4
16-17	3	2,8	63-64	2	5,6	110-111	4	5,6
17-18	3	2,8	64-65	4	6,0	111-112	4	6,0
18-19	3	3,2	65-66	9	6,8	112-113	6	6,4
19-20	4	3,6	66-67	6	6,2	113-114	7	6,6
20-21	1	3,2	67-68	7	6,4	114-115	7	6,2
21-22	3	3,6	68-69	4	6,2	115-116	6	5,8
22-23	5	3,6	69-70	8	6,0	116-117	6	5,8
23-24	5	2,8	70-71	6	5,4	117-118	7	5,8
24-25	2	2,6	71-72	7	5,4	118-119	5	5,2
25-26	3	2,8	72-73	6	5,4	119-120	5	5,8
26-27	3	3,2	73-74	3	5,0	120-121	6	5,8
27-28	1	3,4	74-75	5	5,0	121-122	6	5,8
28-29	4	4,2	75-76	6	5,6	122-123	4	6,0
29-30	3	4,2	76-77	7	5,8	123-124	8	6,6
30-31	5	4,6	77-78	4	5,8	124-125	5	6,4
31-32	4	4,8	78-79	3	6,4	125-126	6	6,6
32-33	5	5,6	79-80	8	7,0	126-127	7	6,6
33-34	4	5,8	80-81	7	7,0	127-128	7	6,0
34-35	5	6,6	81-82	7	6,8	128-129	7	5,8
35-36	6	6,4	82-83	7	6,2	129-130	6	5,2
36-37	8	6,4	83-84	6	6,8	130-131	6	5,0
37-38	6	5,6	84-85	8	6,6	131-132	4	5,0
38-39	8	5,4	85-86	6	7,0	132-133	6	5,0
39-40	4	5,2	86-87	4	7,8	133-134	4	5,0
40-41	6	5,6	87-88	10	8,6	134-135	5	5,0
41-42	4	6,0	88-89	5	8,4	135-136	6	5,0
42-43	5	6,4	89-90	10	9,6	136-137	4	5,0
43-44	7	6,4	90-91	10	9,6	137-138	6	5,6
44-45	6	6,4	91-92	8	9,2	138-139	4	5,0
45-46	8	6,6	92-93	9	8,8	139-140	5	5,0
46-47	6	6,2	93-94	11	8,0	140-141	6	5,0

Depth (cm)	Clasts >2mm (num.)	Mobile average	Depth (cm)	Clasts >2mm (num.)	Mobile average	Depth (cm)	Clasts >2mm (num.)	Mobile average
141-142	7	4,8	188-189	6	4,6	235-236	4	4,8
142-143	3	4,6	189-190	4	4,8	236-237	6	5,0
143-144	4	4,8	190-191	2	5,2	237-238	3	4,8
144-145	5	5,4	191-192	7	5,8	238-239	5	5,0
145-146	5	6,0	192-193	4	5,6	239-240	6	5,0
146-147	6	6,4	193-194	7	6,2	240-241	5	4,8
147-148	4	6,0	194-195	6	5,8	241-242	5	4,8
148-149	7	6,0	195-196	5	5,6	242-243	4	5,0
149-150	8	6,2	196-197	6	5,6	243-244	5	5,4
150-151	7	6,6	197-198	7	5,6	244-245	5	4,8
151-152	4	6,4	198-199	5	5,4	245-246	5	4,4
152-153	4	6,8	199-200	5	5,2	246-247	6	4,4
153-154	8	7,6	200-201	5	5,2	247-248	6	4,4
154-155	10	7,0	201-202	6	5,8	248-249	2	4,0
155-156	6	6,2	202-203	6	6,4	249-250	3	4,6
156-157	6	6,0	203-204	4	5,8	250-251	5	4,8
157-158	8	5,6	204-205	5	5,8	251-252	6	4,8
158-159	5	4,8	205-206	8	5,4	252-253	4	4,4
159-160	6	4,4	206-207	9	4,2	253-254	5	4,2
160-161	5	4,2	207-208	3	2,8	254-255	4	3,6
161-162	4	4,4	208-209	4	2,4	255-256	5	2,8
162-163	4	4,4	209-210	3	1,6	256-257	4	2,2
163-164	3	4,0	210-211	2	1,0	257-258	3	2,0
164-165	5	4,4	211-212	2	1,0	258-259	2	1,6
165-166	6	4,2	212-213	1	0,8	259-260	0	1,8
166-167	4	3,8	213-214	0	0,8	260-261	2	2,6
167-168	2	3,6	214-215	0	1,2	261-262	3	2,6
168-169	5	3,8	215-216	2	1,8	262-263	1	2,4
169-170	4	3,4	216-217	1	2,2	263-264	3	3,0
170-171	4	3,6	217-218	1	2,4	264-265	4	2,6
171-172	3	3,8	218-219	2	2,8	265-266	2	2,2
172-173	3	4,2	219-220	3	3,2	266-267	2	3,0
173-174	3	4,4	220-221	4	3,4	267-268	4	3,6
174-175	5	5,0	221-222	2	3,4	268-269	1	3,8
175-176	5	5,6	222-223	3	3,2	269-270	2	4,0
176-177	5	5,6	223-224	4	3,2	270-271	6	4,2
177-178	4	6,0	224-225	4	3,2	271-272	5	3,4
178-179	6	5,6	225-226	4	3,6	272-273	5	3,2
179-180	8	5,4	226-227	1	3,6	273-274	2	3,4
180-181	5	4,8	227-228	3	4,2	274-275	3	4,0
181-182	7	5,0	228-229	4	4,8	275-276	2	4,4
182-183	2	4,4	229-230	6	4,6	276-277	4	5,0
183-184	5	4,6	230-231	4	4,0	277-278	6	5,0
184-185	5	4,8	231-232	4	4,0	278-279	5	5,4
185-186	6	4,6	232-233	6	4,4	279-280	5	5,6
186-187	4	3,8	233-234	3	3,8	280-281	5	5,0
187-188	3	4,4	234-235	3	4,2	281-282	4	4,8

Depth (cm)	Clasts >2mm (num.)	Mobile average	Depth (cm)	Clasts >2mm (num.)	Mobile average	Depth (cm)	Clasts >2mm (num.)	Mobile average
282-283	8	4,6	**302-303**	6	3,0	**322-323**	5	4,4
283-284	6	4,2	**303-304**	2	2,4	**323-324**	4	4,0
284-285	2	3,8	**304-305**	2	2,6	**324-325**	5	4,0
285-286	4	4,4	**305-306**	4	3,0	**325-326**	4	3,2
286-287	3	4,2	**306-307**	1	2,6	**326-327**	4	2,4
287-288	6	4,8	**307-308**	3	3,0	**327-328**	3	1,6
288-289	4	4,6	**308-309**	3	3,0	**328-329**	4	1,0
289-290	5	4,6	**309-310**	4	2,8	**329-330**	1	0,2
290-291	3	4,0	**310-311**	2	2,6	**330-331**	0	0,2
291-292	6	4,0	**311-312**	3	2,6	**331-332**	0	0,4
292-293	5	3,4	**312-313**	3	2,2	**332-333**	0	1,2
293-294	4	2,4	**313-314**	2	2,0	**333-334**	0	1,6
294-295	2	2,0	**314-315**	3	2,2	**334-335**	1	2,6
295-296	3	2,6	**315-316**	2	2,4	**335-336**	1	3,2
296-297	3	2,6	**316-317**	1	2,6	**336-337**	4	3,4
297-298	0	2,8	**317-318**	2	3,0	**337-338**	2	3,2
298-299	2	4,0	**318-319**	3	3,6	**338-339**	5	3,5
299-300	5	4,0	**319-320**	4	3,8	**339-340**	4	3,0
300-301	3	3,4	**320-321**	3	4,0	**340-341**	2	2,5
301-302	4	3,6	**321-322**	3	4,2	**341-342**	3	3,0

Table S32 Clasts >2 mm counted using the method of Grobe (1987) and mobile average (interval of 5 cm) of the core ANTA99-GC17.

Physical analyses - Magnetic susceptibility, Compression strength, Water content and Grain size

Magnetic susceptibility (MS) (tab. S33, fig. S26) shows values between 700 and 900*10^6 SI from the bottom of the core to 17 cm. There are several peaks exceeding 1000*10^6 SI (clasts). In particular three of them at 342-330 cm, 83-75 cm and 39-29 cm reaches 12000*10^6 SI, 1762*10^6 SI and 3437*10^6 SI respectively. MS drops in the upper part of the core, reaching 180*10^6 SI at the top.

Compressive strength (CS) (tab. S34, fig. S26) is characterised by a very high value at the bottom of the core: 4,52 kg/cm^2. CS drops to 2,15 kg/cm^2 around 324 cm and shows a decreasing trend. Around 269 cm, CS increases again, reaching a peak of 3,05 kg/cm^2 at 229 cm. Then, CS drops again to values lower than 1,0 kg/cm^2. The upper 2 metres of the core are characterised by a decreasing trend, reaching 0,35 kg/cm^2 at the top of the core.

Water content (w%) (tab. S35, fig. S26) is characterised by an increasing up-core trend from the bottom to 36 cm, with few less hydrate intervals from 250 to 150 cm. The upper part of the core is

characterised by a drop of water content (w%), from 34,1% (36 cm) to 24,5% (15 cm). W% reaches the highest value at the top of the core: 35,8%.

Depth (cm)	MS (10^{-6}SI)	Depth (cm)	MS (10^{-6}SI)	Depth (cm)	MS (10^{-6}SI)	Depth (cm)	MS (10^{-6}SI)
0-1	180	94-95	761	188-189	760	282-283	800
2-3	340	96-97	771	190-191	780	284-285	780
4-5	369	98-99	711	192-193	780	286-287	780
6-7	449	100-101	590	194-195	760	288-289	770
8-9	549	102-103	410	196-197	750	290-291	760
10-11	569	104-105	590	198-199	740	292-293	750
12-13	669	106-107	670	300-201	730	294-295	760
14-15	819	108-109	690	202-203	790	296-297	780
16-17	798	110-111	710	204-205	780	298-299	780
18-19	758	112-113	720	206-207	770	300-301	800
20-21	738	114-115	720	208-209	710	302-303	820
22-23	718	116-117	730	210-211	700	304-305	830
24-25	758	118-119	750	212-213	740	306-307	850
26-27	867	120-121	740	214-215	770	308-309	860
28-29	1087	122-123	740	216-217	780	310-311	860
30-31	1757	124-125	710	218-219	760	312-313	870
32-33	3397	126-127	690	220-221	670	314-315	840
34-35	3437	128-129	710	222-223	370	316-317	820
36-37	1726	130-131	740	224-225	680	318-319	840
38-39	1086	132-133	750	226-227	750	320-321	890
40-41	856	134-135	810	228-229	780	322-323	1080
42-43	766	136-137	800	230-231	750	324-325	1550
44-45	766	138-139	760	232-233	750	326-327	3330
46-47	766	140-141	720	234-235	770	328-329	7310
48-49	715	142-143	710	236-237	860	330-331	12060
50-51	715	144-145	710	238-239	1060	332-333	11220
52-53	725	146-147	720	240-241	990	334-335	5950
54-55	695	148-149	730	242-243	880	336-337	2870
56-57	695	150-151	730	244-245	870	338-339	1410
58-59	674	152-153	730	246-247	980	340-341	830
60-61	664	154-155	710	248-249	1150	342-343	380
62-63	674	156-157	710	250-251	1190		
64-65	694	158-159	710	252-253	1010		
66-67	694	160-161	710	254-255	840		
68-69	713	162-163	700	256-257	810		
70-71	763	164-165	700	258-259	820		
72-73	783	166-167	700	260-261	840		
74-75	863	168-169	720	262-263	860		
76-77	1213	170-171	720	264-265	850		
78-79	1763	172-173	710	266-267	870		
80-81	1262	174-175	710	268-269	950		
82-83	942	176-177	710	270-271	950		
84-85	792	178-179	720	272-273	880		
86-87	772	180-181	750	274-275	850		
88-89	742	182-183	790	276-277	840		
90-91	741	184-185	800	278-279	850		
92-93	751	186-187	780	280-281	830		

Table S33 Magnetic susceptibility of the core ANTA99-GC17. Yellow levels the end of each core section or peaks related to clasts.

Depth (cm)	CS (Kg/cm²)
14-16	0,4
25-27	0,6
35-37	0,4
52-54	0,4
68-70	0,6
89-91	0,6
110-112	0,8
121-123	0,6
138-140	0,7
152-154	0,9
159-161	0,8
172-174	0,9
191-193	0,8
200-202	0,9
214-216	1,5
227-229	1,4
228-229,5	3,1
240,5-242	1,8
254,5-256	1,7
267,5-269	1,6
282,5-284	1,8
297,5-299	1,6
307,5-309	1,9
322,5-324	2,1
338,5-340	4,5

Table S34 Compressive strength of the core ANTA99-GC17.

Depth (cm)	W%
1-2	35,8
14-15	24,5
25-26	29,5
35-36	34,1
44-45	33,0
55-56	32,4
65-66	31,0
75-76	31,0
85-86	30,8
95-96	30,2
103-104	30,4
113-114	30,4
123-124	30,7
133-134	30,2
143-144	30,1
153-154	29,0
163-164	29,8
174-175	30,5
183-184	29,1
193-194	27,5
203-204	26,6
213-214	27,5
226-227	24,5
237-238	25,1
246-247	26,2
256-257	26,3
266-267	25,8
276-277	25,9
286-287	26,3
296-297	25,9
306-307	24,9
316-317	24,6
326-327	24,1
338-339	20,9

Table S35 Water content of the core ANTA99-GC17.

The main sedimentary component (tab. S36, fig. S26) of this core is silt (avg 68,4%, max 79,4%, min 49,5%). The second component is sand (avg 24,8%, max 44,3%, min 13,4%). The least present component is clay (avg 6,8%, max 11,7%, min, 4,5%). Mean diameter (Mz) (avg 5,58 ϕ) shows values between 5 and 6 ϕ (medium silt). The Mz trend is almost constant from the bottom core to 30 cm. In the uppermost samples the parameter tends to reach the minimum values (4,69 ϕ - coarse silt - at 10cm) and to increase to fine silt toward the top core. Sediments are very poorly sorted (avg 2,16 ϕ), except for the sample collected at 40 cm, which is poorly sorted (tab. S36, fig. 26). The average value of skewness (Sk) is 0,11. Sediment distribution is symmetric at the bottom of the core, positive asymmetric from 287 to 40 cm and symmetric with few positive asymmetric intervals in the upper 40 cm. A constant trend characterises the median diameter (Md), with a peak around 10 cm (tab. S36, fig. 26).

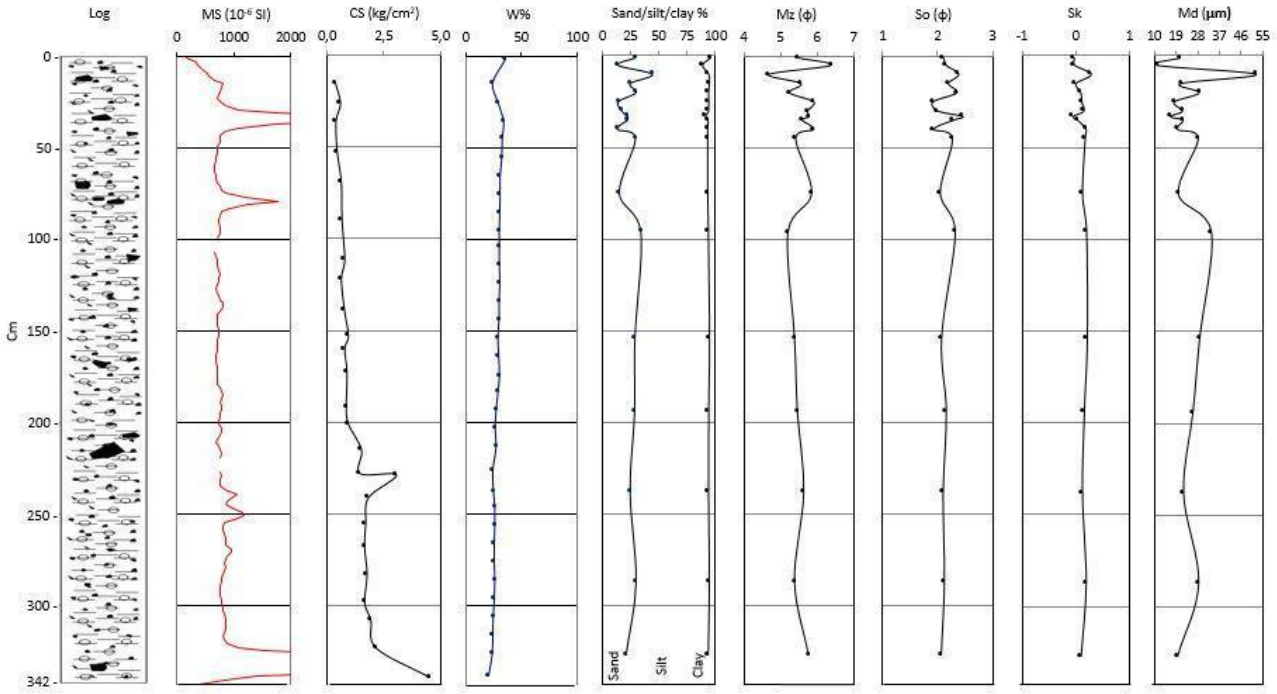

Figure S26 Physical parameters of the core GC17.

From the bottom of the core to 96 cm, distribution curves (fig. S27) show an unimodal distribution with a primary mode between 4,0 and 4,5 ϕ (62,50 - 44,19 µm). The primary mode ranges between 5,0 and 6,0 ϕ (31,25 - 15,62 µm) from 75 to 15 cm, except at 45 cm where it is 4,5 ϕ (44,19 µm). The sample collected at 10 cm is characterised by a primary mode of 4,0 ϕ (62,50 µm) with a great abundance of sandy and silty component. The upper part of the core is characterised by a primary

mode (tab. S33) of 7,0 ϕ (7,81 µm), but the top of the core is also characterised by a bimodal distribution, with the secondary mode at 4,0 ϕ (62,50 µm).

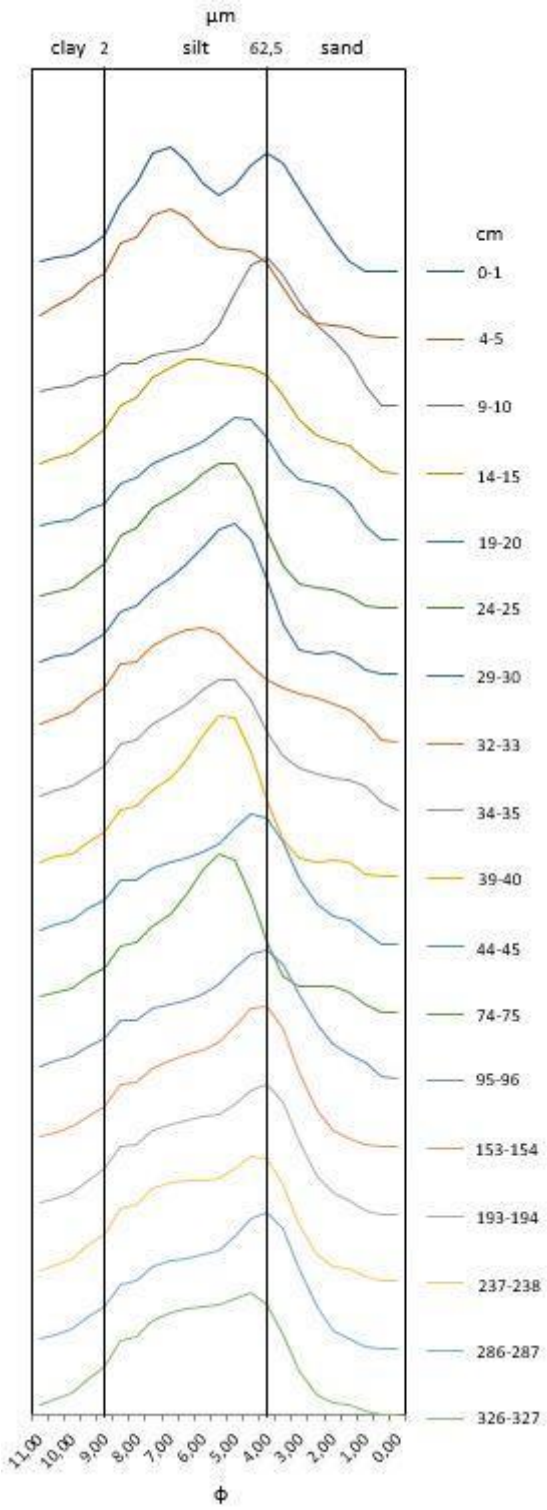

Figure S27 Grain size distribution core GC17.

GC17	Sand (%)	Silt (%)	Clay (%)	Mz (φ)	So (φ)	Sk	Md (μm)	Primary mode (φ)
0-1	29,3	66,2	4,5	5,49	2,11	-0,03	20,9	7,00
4-5	14,2	74,1	11,7	6,39	2,15	-0,03	11,3	7,00
9-10	44,3	49,5	6,2	4,69	2,38	0,28	52,1	4,00
14-15	25,0	69,3	5,7	5,57	2,19	0,00	21,1	6,00
19-20	29,9	63,7	6,4	5,25	2,35	0,09	28,7	5,00
24-25	14,3	79,4	6,2	5,92	1,91	0,10	18,4	5,50
29-30	17,5	75,9	6,5	5,74	2,00	0,14	21,7	5,00
32-33	22,6	68,4	9,0	5,79	2,45	-0,06	16,8	6,00
34-35	22,5	70,6	6,9	5,60	2,28	0,03	21,9	5,50
39-40	13,4	79,3	7,3	5,92	1,92	0,18	19,7	5,50
44-45	29,5	63,4	7,1	5,42	2,26	0,17	28,2	4,50
74-75	15,3	77,5	7,1	5,86	2,04	0,12	20,1	5,50
95-96	34,2	59,3	6,6	5,21	2,31	0,19	33,6	4,00
153-154	29,0	65,4	5,6	5,39	2,06	0,20	28,8	4,00
193-194	28,8	65,0	6,2	5,47	2,15	0,15	26,1	4,00
237-238	24,8	68,8	6,4	5,64	2,09	0,11	22,2	4,50
286-287	30,1	64,2	5,7	5,39	2,12	0,18	28,4	4,00
326-327	21,3	72,0	6,7	5,77	2,06	0,09	19,7	4,50

Table S36 Grain size parameters of the core ANTA99-GC17.

Chemical and Geochemical analyses - Elemental analyses, Organic matter and Biomarkers

Almost all the selected elements (Al, Si, Ti, K, Fe, Rb, Sr, Zr, Ba) show a good correlation (tab. S37). Br is correlated with these elements, except for Sr. Ca correlates with Sr.

GC17	Al_cps	Si_cps	K_cps	Ca_cps	Ti_cps	Fe_cps	Br_cps	Rb_cps	Sr_cps	Zr_cps	Ba50_cps
Al_cps		3,13E-148	5,55E-138	0,066683	3,71E-99	7,63E-96	8,23E-37	9,93E-88	1,83E-36	4,26E-63	1,67E-47
Si_cps	**0,96483**		1,18E-163	0,024536	2,40E-111	5,39E-112	1,10E-35	2,08E-102	1,06E-42	1,96E-79	7,42E-60
K_cps	**0,95743**	**0,97358**		0,94127	2,86E-160	7,09E-114	4,21E-45	2,22E-86	2,15E-32	2,30E-61	1,20E-46
Ca_cps	0,11525	0,14108	0,004646		0,68737	9,06E-06	3,69E-06	2,50E-09	2,66E-26	2,52E-10	2,38E-16
Ti_cps	**0,9114**	**0,92975**	**0,97187**	-0,02537		1,70E-113	5,94E-36	5,02E-70	9,54E-30	2,82E-49	4,48E-38
Fe_cps	**0,90558**	**0,93061**	**0,93304**	0,27448	**0,93256**		2,79E-22	2,49E-106	4,05E-52	3,04E-67	2,73E-62
Br_cps	**0,68701**	**0,67902**	**0,73889**	-0,28573	**0,68093**	*0,55902*		7,14E-26	9,48E-11	1,58E-25	1,34E-17
Rb_cps	**0,88958**	**0,91674**	**0,88665**	0,36303	**0,84367**	**0,92273**	*0,59654*		7,73E-65	2,03E-105	1,83E-93
Sr_cps	**0,68457**	**0,72503**	**0,65407**	**0,60071**	**0,63215**	**0,77489**	0,39185	**0,82654**		2,18E-72	3,39E-81
Zr_cps	**0,82033**	**0,8702**	**0,8139**	0,38352	**0,76106**	**0,83472**	*0,59315*	**0,92138**	**0,85084**		1,54E-96
Ba50_cps	**0,75193**	**0,8081**	**0,74738**	0,48441	**0,6957**	**0,81737**	*0,50172*	**0,90116**	**0,8746**	**0,90684**	

Table S37 Elements correlation of the core GC17. Bold and underlined values represent moderate to strong correlation. Underlined values in italics represent low correlation.

Ti (cps), as representative of lithogenic elements, is characterised by fluctuating values along the core, and they are slightly lower in the upper 30 cm. Zr/Rb has values around 1,5 from the bottom up to 22 cm. The upper part of the core is characterised by higher values. The trend of this ratio resembles the IRD content. Si/Ti shows a constant trend from the bottom to 27 cm. The upper part

of the core shows an increasing trend. Fe/Ti has a slightly decreasing trend with two small peaks: 220 cm and 28 cm. K/Ti has a constant trend with several drops. The upper 40 cm are characterised by a slightly increasing trend. Ca/Ti as a decreasing trend from the bottom toward the top of the core. It is characterised by a peak at 220 cm. Mn/Ti decreases from the bottom to 200 cm. Then, it increases upward to 109 cm, while the upper part of the core is characterised by a decreasing trend. See fig. S28 for the graphics.

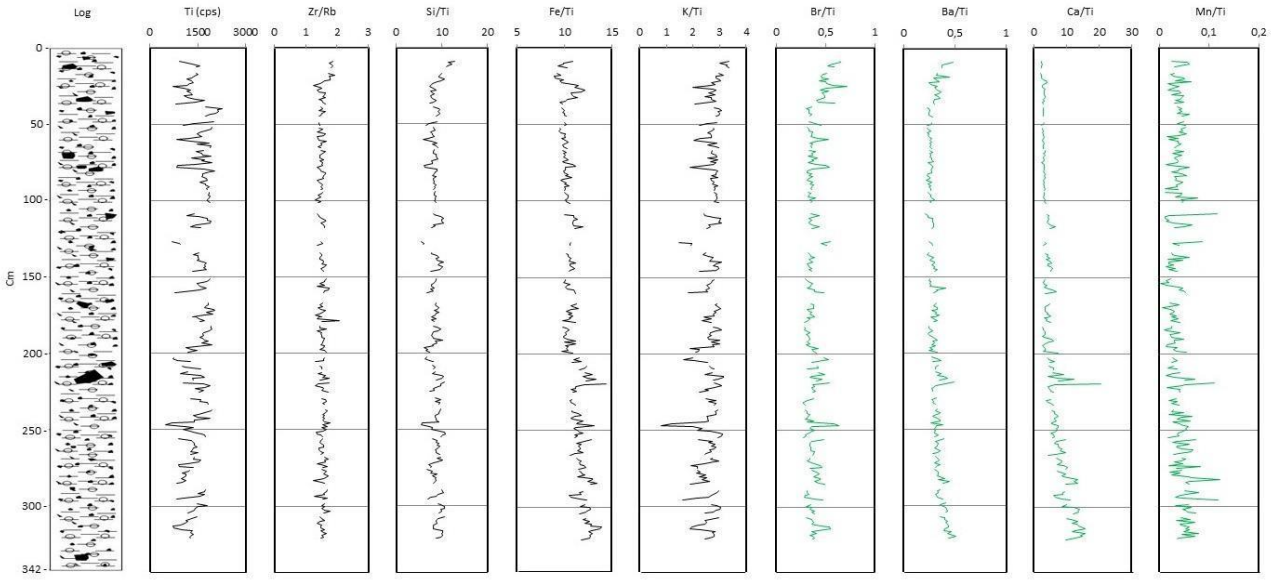

Figure S28 Elemental ratios of the core GC17.

The average value of TOC is 0,37% (max: 0,53% at the top of the core; min: 0,27% at 10 cm). TOC (tab. S38, fig. S29) is higher at 200 cm (0,41%). It shows a constant trend from 194 to 10 cm, with values around 0,30%. TOC reaches a peak in the upper 5 cm, with values higher than 0,50%.

The average value of C/N is 10,15 (max: 16,92 at 36 cm; min: 7,99 at 5 cm). C/N (tab. S38, fig. S29) has an increasing trend from 200 cm to 36 cm, where it reaches the max value. The upper part of the core is characterised by a drop of the values of C/N, reaching the min value. C/N slightly increases at the top of the core.

HBI diene II (tab. S39, fig. S29) is present in this core but with a very low concentration. The average value is $1,38*10^{-4}$ µg/g (max value: $3,21*10^{-4}$ µg/g at 20 cm; $IPSO_{25}$ has not been detected at 15 cm).

22-dehydrocholesterol, cholesterol and brassicasterol (tab. S39, fig. S29) have average values of: $5,70*10^{-3}$ µg/g, $1,03*10^{-2}$ µg/g and $1,62*10^{-2}$ µg/g respectively. They have a similar trend, with low concentrations from 25 to 10 cm and at the top of the core. All three sterols reach a peak at 5 cm

(2,02*10^{-2} µg/g for 22-dehydrocholesterol, 3,11*10^{-2} µg/g for cholesterol and 5,41*10^{-2} µg/g for brassicasterol).

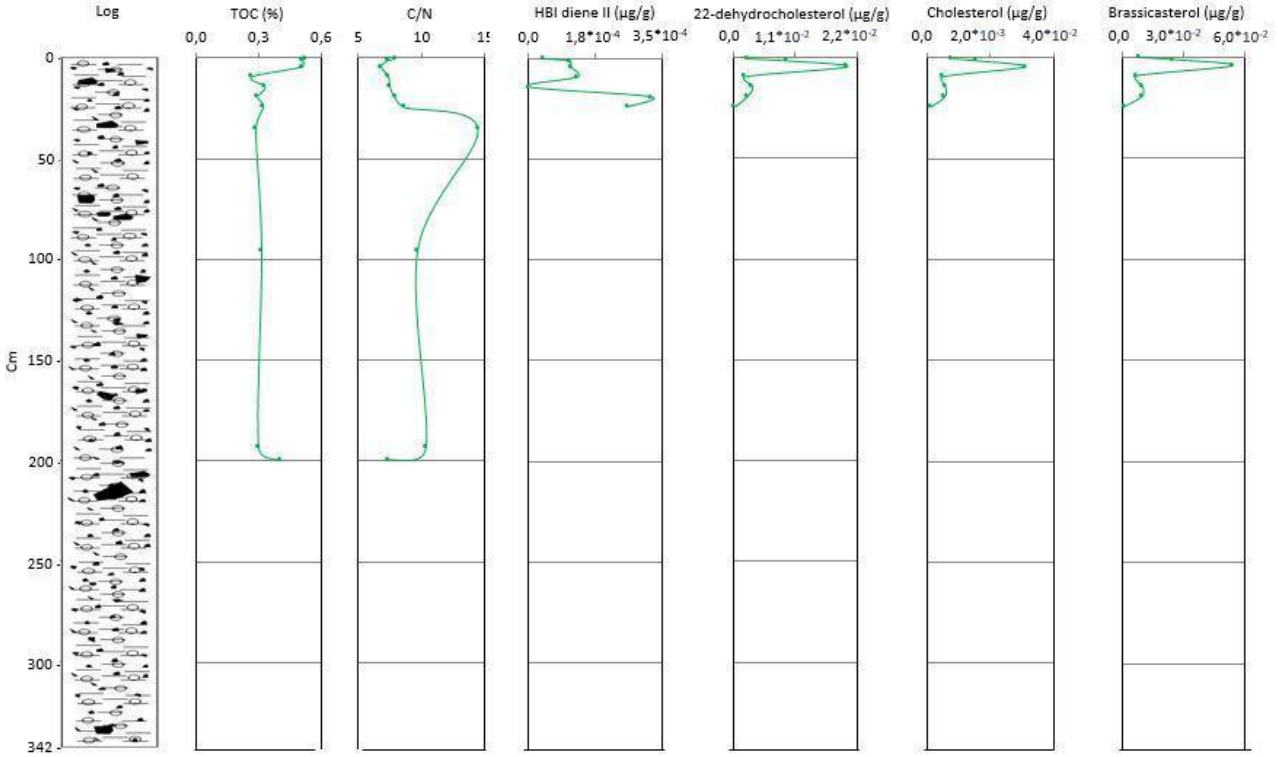

Figure S29 Organic matter and biomarkers parameters of the core GC17.

GC17	TOC (%)	TN (%)	C/N
0-1	0,53	0,07	9,34
1-2	0,51	0,07	8,54
4-5	0,51	0,07	7,99
9-10	0,27	0,04	8,67
14-15	0,33	0,04	8,78
19-20	0,30	0,04	9,21
24-25	0,33	0,04	10,11
35-36	0,29	0,02	16,92
95-96	0,32	0,03	11,35
193-194	0,30	0,03	12,11
199-200	0,41	0,06	8,61

Table S38 Organic matter parameters of the core ANTA99-GC17.

GC17	$IPSO_{25}$ (µg/g dry sedim.)	22-dehydrocholesterol (µg/g dry sedim.)	Cholesterol (µg/g dry sedim.)	Brassicasterol (µg/g dry sedim.)
0-1	$3,83*10^{-5}$	$2,36*10^{-3}$	$7,88*10^{-3}$	$7,97*10^{-3}$
1-2	$1,06*10^{-4}$	$9,43*10^{-3}$	$15,7*10^{-2}$	$2,48*10^{-2}$
4-5	$1,10*10^{-4}$	$2,02*10^{-2}$	$3,11*10^{-2}$	$5,41*10^{-2}$
9-10	$1,27*10^{-4}$	$1,95*10^{-3}$	$4,79*10^{-3}$	$6,59*10^{-3}$
14-15	0	$3,35*10^{-3}$	$5,76*10^{-3}$	$9,72*10^{-3}$
19-20	$3,21*10^{-4}$	$2,37*10^{-3}$	$5,48*10^{-3}$	$9,35*10^{-3}$
24-25	$2,61*10^{-4}$	$1,77*10^{-4}$	$1,27*10^{-3}$	$5,48*10^{-4}$

Table S39 Biomarkers of the core ANTA99-GC17.

Microscopy analyses - Sand and Foraminifera

Angular to sub-rounded quartz grains, rounded feldspar, micas, other femic minerals and lithic fragments are present along the core. Biogenic component is very sparse along the core. Radiolarians, sponge spicules and diatoms represent the siliceous component. Very sparse foraminifera were recovered.

GC17	*Neogloboquadrina pachyderma*	Benthos/g	*Globocassiduina biora* (pustolose)	*Globocassidulina subglobosa*	*Hormosinella ovicula gracilis*	*Miliammina earlandi*	*Nonionella bradyi*	Nonionella sp.	*Portatrochammina antarctica*	*Reophax scorpiurus*	*Spiroplectammina biformis*	Unknown	% fragmentation
1-2	0	0,4	0	0	1	2	0	0	0	0	2	1	50,0
4-5	0	1,2	0	0	0	4	0	0	0	0	0	0	20,0
9-10	0	0,0	0	0	0	0	0	0	0	0	0	0	0,0
19-20	1	0,3	0	0	0	0	1	0	0	0	0	0	0,0
29-30	0	0,0	0	0	0	0	0	0	0	0	0	0	0,0
39-40	0	0,0	0	0	0	0	0	0	0	0	0	0	0,0
44-45	0	0,0	0	0	0	0	0	0	0	0	0	0	0,0
74-75	0	0,0	0	0	0	0	0	0	0	0	0	0	0,0
95-96	0	0,0	0	0	0	0	0	0	0	0	0	0	0,0
153-154	0	0,0	0	0	0	0	0	0	0	0	0	0	0,0
193-194	0	0,05	0	1	0	0	0	0	0	0	0	0	50,0
199-200	0	0,0	0	0	0	0	0	0	0	0	0	0	0,0
219-220	0	0,0	0	0	0	0	0	0	0	0	0	0	0,0
237-238	0	0,1	0	1	0	0	0	1	0	0	0	0	33,3
286-287	0	0,1	1	0	0	0	0	0	0	0	0	1	50,0
326-327	0	0,0	0	0	0	0	0	0	0	0	0	0	0,0

Table S40 Foraminifera of the core ANTA99-GC17.

Benthic and planktonic (adult form of *Neogloboquadrina pachyderma*)) were identified. Agglutinated foraminifera are present in the upper 5 cm, mainly represented by *Miliammina earlandi*. Fragmentation rate ranges between 20,0% to 50,0%. 9 different genera have been identified, represented by 12 different species (tab. S36).

ANTA99-GC18

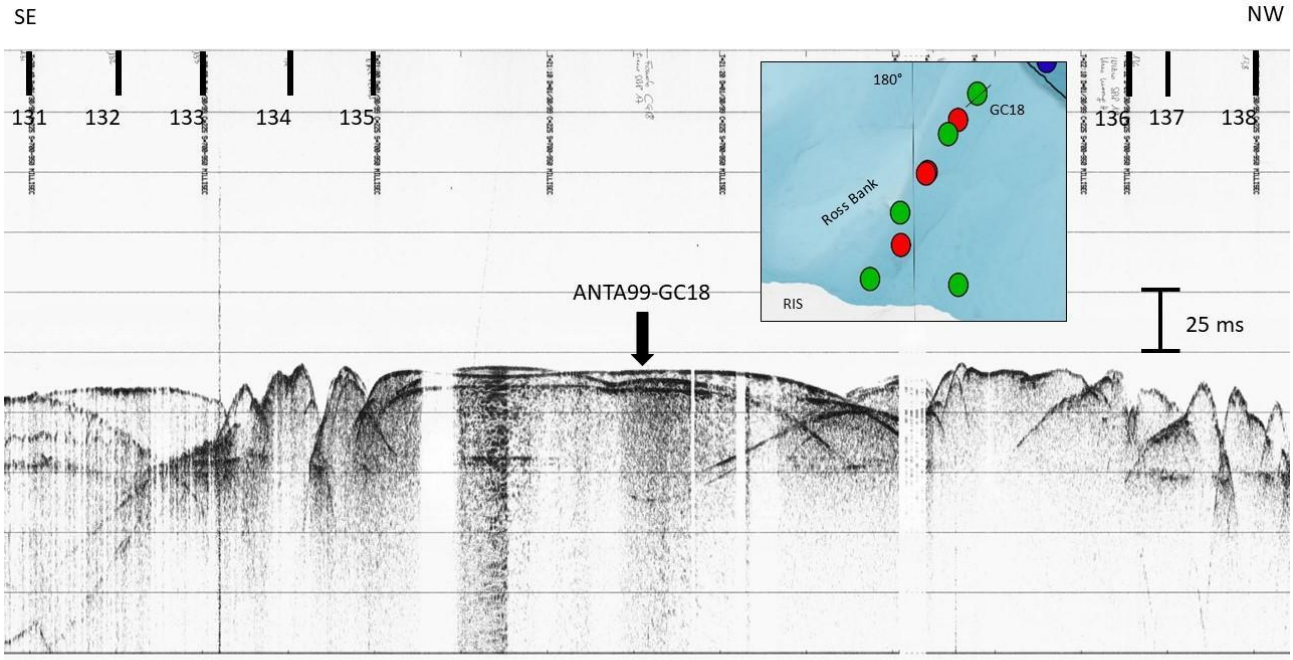

Figure S30 Section of the SBPs 17 and 18, with the location of the core GC18. Bathymetric map is a zoom of fig. 6.

This gravity core has been collected in the outer continental shelf. Considering this dataset, this is the core closer to the continental shelf break (tab. 3, fig. 6). A hummocky morphology characterises the sea floor in this site (fig. S30).

Core description and Radiography

This is a core (fig. S31) characterised by sandy and gravelly material within a fine matrix, from the bottom to 74 cm. Colours gradually change from very dark grey (5Y 3/1) to dark olive grey (5Y 3/2) to dark grey (5Y 4/1) to olive grey (5Y 4/2). Several clasts, from millimetric to pluri-centimetric, are present. Around 74 cm, sediment gradually changes to sandy mud. Millimetric to centimetric clasts are also present. The colour of sediments changes from olive grey (5Y 4/2) to olive (5Y 4/3) at 49

cm. A chromatic contact at 44 cm divides a 2 cm thick sandy mud layer from sediments below. Density decreases from the bottom to 42 cm. The colour of this interval is dark grey (5Y 4/1). The colour of sediments is still dark grey (5Y 4/1) from 42 to 5 cm. Density is higher in the upper part of the core. Sandy gravelly sediments are present from 42 to 35 cm. Above this interval, from 35 to 5 cm, sediments gradually change from muddy to sandy mud. The upper 5 cm are made of olive (5Y 4/3) sandy mud. Clasts of this core are mainly sub-angular to angular.

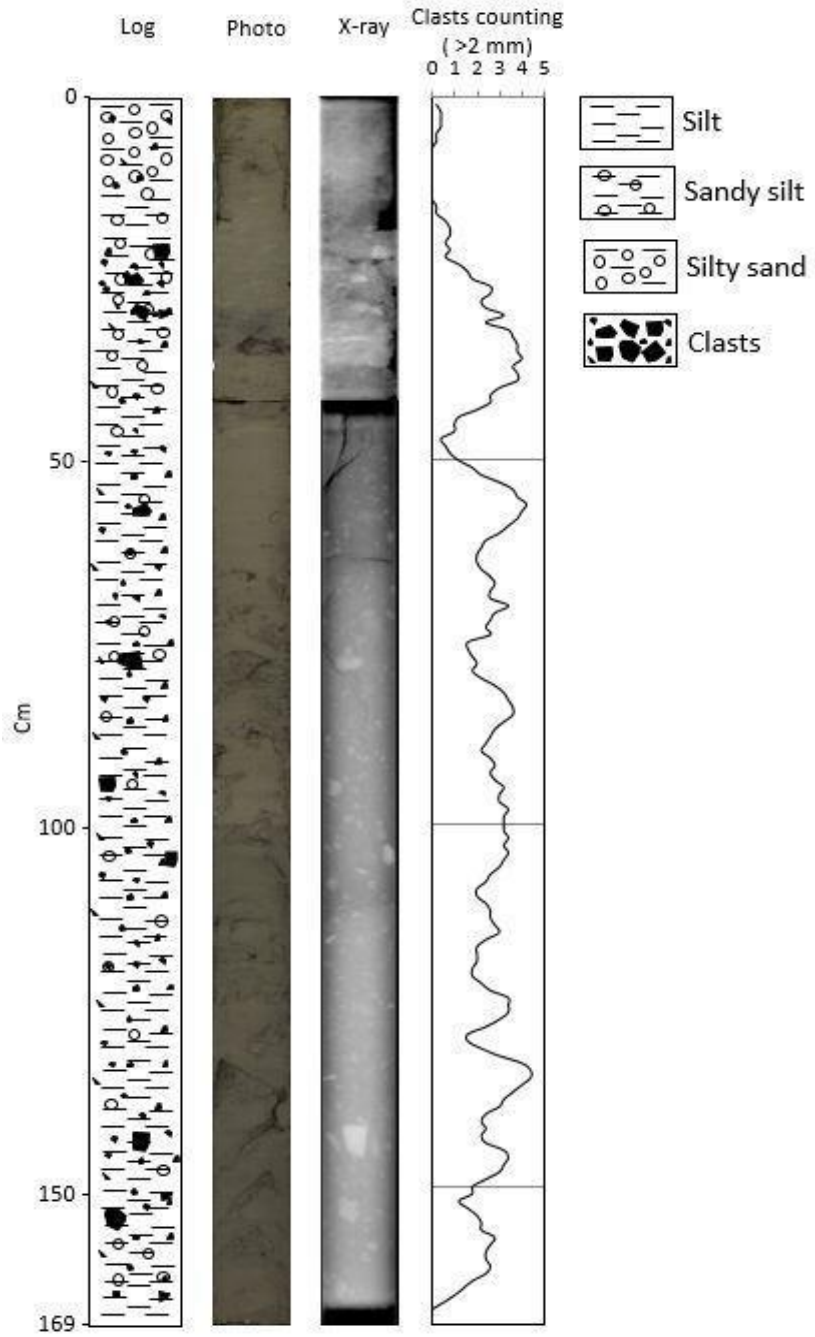

Figure S31 Lithologic log, photo, radiography, clasts counted using the Grobe (1987) method (mobile average interval: 5 cm) of the core GC18.

A minimum around 47 cm and in the upper 22 cm characterises the mobile average of clasts >2 mm. The rest of the core shows fluctuating values of this parameter (tab. S41, fig. S31).

Depth (cm)	Clasts >2mm (num.)	Mobile average	Depth (cm)	Clasts >2mm (num.)	Mobile average	Depth (cm)	Clasts >2mm (num.)	Mobile average
0-1	0	0,2	47-48	0	0,6	94-95	4	3,2
1-2	0	0,4	48-49	0	0,8	95-96	3	3,0
2-3	0	0,4	49-50	0	1,2	96-97	2	3,0
3-4	1	0,4	50-51	1	1,8	97-98	3	3,4
4-5	0	0,2	51-52	2	2,2	98-99	4	3,2
5-6	1	0,2	52-53	1	3,0	99-100	3	3,2
6-7	0	0,0	53-54	2	3,6	100-101	3	3,2
7-8	0	0,0	54-55	3	3,8	101-102	4	3,4
8-9	0	0,0	55-56	3	4,2	102-103	2	3,2
9-10	0	0,0	56-57	6	4,0	103-104	4	3,4
10-11	0	0,0	57-58	4	3,8	104-105	3	3,2
11-12	0	0,0	58-59	3	3,4	105-106	4	3,0
12-13	0	0,0	59-60	5	3,0	106-107	3	2,6
13-14	0	0,0	60-61	2	2,4	107-108	3	2,4
14-15	0	0,2	61-62	5	2,2	108-109	3	2,0
15-16	0	0,2	62-63	2	2,0	109-110	2	2,0
16-17	0	0,6	63-64	1	2,0	110-111	2	2,4
17-18	0	0,8	64-65	2	2,2	111-112	2	2,6
18-19	1	0,8	65-66	1	2,6	112-113	1	2,6
19-20	0	0,6	66-67	4	2,8	113-114	3	2,8
20-21	2	0,8	67-68	2	2,6	114-115	4	3,0
21-22	1	0,6	68-69	2	2,6	115-116	3	2,4
22-23	0	1,2	69-70	4	3,4	116-117	2	2,0
23-24	0	1,6	70-71	2	2,8	117-118	2	2,0
24-25	1	1,8	71-72	3	2,6	118-119	4	2,0
25-26	1	2,6	72-73	2	2,4	119-120	1	1,8
26-27	4	2,6	73-74	6	2,6	120-121	1	1,8
27-28	2	2,2	74-75	1	1,6	121-122	2	2,2
28-29	1	2,4	75-76	1	1,6	122-123	2	2,6
29-30	5	3,2	76-77	2	1,8	123-124	3	3,4
30-31	1	2,4	77-78	3	2,0	124-125	1	3,4
31-32	2	3,4	78-79	1	1,8	125-126	3	3,4
32-33	3	3,6	79-80	1	2,2	126-127	4	3,0
33-34	5	3,8	80-81	2	2,8	127-128	6	2,4
34-35	1	3,8	81-82	3	3,2	128-129	3	1,6
35-36	6	4,0	82-83	2	3,4	129-130	1	1,6
36-37	3	3,6	83-84	3	3,6	130-131	1	2,2
37-38	4	3,8	84-85	4	3,6	131-132	1	3,0
38-39	5	3,8	85-86	4	3,2	132-133	2	4,0
39-40	2	3,0	86-87	4	2,8	133-134	3	4,4
40-41	4	2,6	87-88	3	2,6	134-135	4	4,4
41-42	4	2,6	88-89	3	2,4	135-136	5	4,0
42-43	4	2,0	89-90	2	2,2	136-137	6	3,6
43-44	1	1,2	90-91	2	2,6	137-138	4	3,2
44-45	0	1,0	91-92	3	2,8	138-139	3	3,0
45-46	4	1,0	92-93	2	2,6	139-140	2	2,4
46-47	1	0,4	93-94	2	2,8	140-141	3	2,2

Depth (cm)	Clasts >2mm (num.)	Mobile average	Depth (cm)	Clasts >2mm (num.)	Mobile average	Depth (cm)	Clasts >2mm (num.)	Mobile average
141-142	4	2,4	**151-152**	2	1,2	**161-162**	3	2,4
142-143	3	2,2	**152-153**	1	1,6	**162-163**	2	1,8
143-144	0	2,4	**153-154**	1	2,0	**163-164**	2	1,4
144-145	1	3,2	**154-155**	2	2,2	**164-165**	3	1,0
145-146	4	3,4	**155-156**	0	2,2	**165-166**	2	0,5
146-147	3	3,2	**156-157**	4	2,8	**166-167**	0	0,0
147-148	4	3,0	**157-158**	3	2,6	**167-168**	0	0,0
148-149	4	2,4	**158-159**	2	2,4	**168-169**	0	0,0
149-150	2	1,8	**159-160**	2	2,4			
150-151	3	1,8	**160-161**	3	2,6			

Table S41 Clasts >2 mm counted using the method of Grobe (1987) and mobile average (interval of 5 cm) of the core ANTA99-GC18.

Physical analyses - Magnetic susceptibility, Compression strength, Water content and Grain size

Magnetic susceptibility (MS) (tab. S42, fig. S32) is characterised by values higher than $600*10^6$ SI from the bottom of the core to 117 cm. It reaches a peak of $1638*10^6$ SI (clast) from 147 to 143 cm in correspondence of a large clast. From 117 to 35 cm, MS shows values between 500 and 600 $*10^6$ SI. Lower values have been measured around 49 cm at the end of the core section. The upper 35 cm are characterised by a decreasing trend. MS reaches $160*10^6$ SI at the top of the core.

Compressive strength (CS) (tab. S43, fig. S32) shows a decreasing up-core trend. CS is 2,3 kg/cm^2 at the bottom of the core and decreases to 0,5 kg/cm^2 at 66 cm.

Water content (w%) (tab. S44, fig. S32) has a slightly increasing trend from the bottom (23,3%) to 45 cm (41,0%). In the upper part of the core, w% is characterised by values fluctuating between 20 and 40%.

Grain size analysis (tab. S45, fig. S32) highlighted that the main sedimentary component is silt (avg 70,1%), ranging from 81,7% to 44,6%. Sand is the second component (avg 23,7%), with values between 50,9 % and 11,1%. Clay (avg 6,2%) presents a range between 8,2% and 4,0%.

Mean diameter (Mz) shows values between 4,38 ϕ (coarse silt) and 6,19 ϕ (fine silt) and an average value of 5,65 ϕ (medium silt). The trend is almost constant from the bottom until 20 cm with mean diameter around 6 ϕ. The uppermost sediment is coarser (avg 4,72 ϕ). Sediments collected from

the bottom to 45 cm ranges between very poorly sorted and poorly sorted from the bottom to 45 cm. The upper part of the core is very poorly sorted. Skewness (Sk) has an average value of 0,02. From the bottom to 20 cm, sediment distributions are symmetric with few positive asymmetric samples from the bottom to 54 cm and few negative asymmetric samples from 54 to 20 cm. The upper part of the core is characterised by a positive asymmetric distribution. The median diameter (Md) shows a constant trend from the bottom to 20 cm, and it peaks to higher values in the upper part of the core. These data are reported in the tab. S45 and fig. S35.

Depth (cm)	MS (10^{-6}SI)	Depth (cm)	MS (10^{-6}SI)
0-1	160	94-95	564
2-3	240	96-97	564
4-5	270	98-99	554
6-7	300	100-101	544
8-9	330	102-103	555
10-11	340	104-105	565
12-13	330	106-107	575
14-15	300	108-109	555
16-17	300	110-111	535
18-19	300	112-113	535
20-21	310	114-115	566
22-23	330	116-117	636
24-25	340	118-119	706
26-27	350	120-121	656
28-29	380	122-123	656
30-31	420	124-125	656
32-33	480	126-127	647
34-35	540	128-129	647
36-37	550	130-131	637
38-39	580	132-133	637
40-41	560	134-135	627
42-43	470	136-137	647
44-45	410	138-139	728
46-47	350	140-141	978
48-49	280	142-143	1468
50-51	370	144-145	1638
52-53	421	146-147	1228
54-55	471	148-149	898
56-57	521	150-151	759
58-59	541	152-153	699
60-61	531	154-155	689
62-63	571	156-157	689
64-65	562	158-159	669
66-67	552	160-161	659
68-69	522	162-163	650
70-71	512	164-165	650
72-73	532	166-167	570
74-75	562		
76-77	593		
78-79	553		
80-81	533		
82-83	543		
84-85	543		
86-87	543		
88-89	553		
90-91	554		
92-93	554		

Table S42 Magnetic susceptibility of the core ANTA99-GC18. Yellow levels the end of each core section or peaks related to clasts.

Depth (cm)	CS (Kg/cm²)
65-67	0,5
79-81	1,0
99-101	1,4
119-121	1,9
133-135	2,1
163-165	2,3

Table S43 Compressive strength of the core ANTA99-GC18.

Depth (cm)	W%
0-1	29,9
4-5	27,1
9-10	24,0
14-15	31,6
19-20	39,3
24-25	36,1
29-30	34,5
33-34	33,6
36-37	28,8
44-45	41,0
53-54	38,5
59-60	32,7
64-65	33,1
69-70	31,5
76-77	29,1
81-82	28,3
94-95	26,6
109-110	27,7
124-125	24,4
131-132	24,5
138-139	24,6
150-151	24,3
160-161	23,2
166-167	23,3

Table S44 Water content of the core ANTA99-GC18.

The lower part of the core (fig. 33), from the bottom to 54 cm, is mainly characterised by a primary mode of 5,0 ϕ (31,25 µm), with fine intervals with a primary mode (tab. S45) of 6,5 - 7,0 ϕ (11,05 - 7,81 µm) at 167, 139 and 60 cm, and a coarser interval at 77 cm, with a primary mode of 4,5 ϕ (44,19 µm). Then, between 45 and 20 cm, the primary mode (tab. S41) shifts toward finer sediments from 5,5 to 7,0 ϕ (22,09 - 7,81 µm). Curves from the bottom of the core to 20 cm are characterised by an unimodal distribution. The upper 15 cm of the core are characterised by a coarser primary mode, between 3,5 and 4,5 ϕ (88,38 - 44,19 µm). Samples collected from 15 to 5 cm show a bimodal distribution, with a secondary mode between 6,5 and 7,0 ϕ (11,05 - 7,81 µm).

GC18	Sand (%)	Silt (%)	Clay (%)	Mz (φ)	So (φ)	Sk	Md (μm)	Primary mode (φ)
0-1	32,3	63,7	4,1	5,11	2,08	0,12	32,5	4,50
4-5	50,9	44,6	4,5	4,41	2,50	0,27	64,9	3,50
9-10	39,2	56,5	4,3	4,99	2,25	0,19	39,1	4,00
14-15	50,2	45,7	4,0	4,38	2,42	0,24	63,1	3,50
19-20	18,9	74,9	6,1	5,93	2,02	-0,06	15,1	7,00
24-25	22,9	68,9	8,2	5,85	2,43	-0,14	14,8	7,00
29-30	22,3	71,3	6,4	5,82	2,31	-0,19	14,4	7,00
33-34	18,8	75,4	5,9	5,91	2,13	-0,13	14,9	7,00
36-37	25,4	67,8	6,8	5,58	2,43	-0,10	18,7	6,50
44-45	11,1	81,7	7,2	6,19	1,87	0,05	14,3	5,50
53-54	14,6	79,6	5,7	5,83	1,84	0,17	20,3	5,00
59-60	19,6	72,5	7,9	5,99	2,31	-0,15	13,5	7,00
64-65	17,6	75,9	6,5	5,86	2,09	0,05	19,0	5,00
69-70	13,6	79,4	7,0	6,03	1,91	0,11	16,8	5,00
76-77	25,6	68,9	5,5	5,52	2,14	0,09	24,3	4,50
109-110	16,7	76,5	6,7	5,95	1,97	0,07	17,0	5,00
138-139	15,6	77,7	6,8	6,02	1,99	0,01	15,8	6,50
160-161	19,8	73,8	6,5	5,84	2,17	-0,02	17,8	5,00
166-167	15,8	76,6	7,6	6,18	2,09	-0,10	12,6	7,00

Table S45 Grain size parameters of the core ANTA99-GC18.

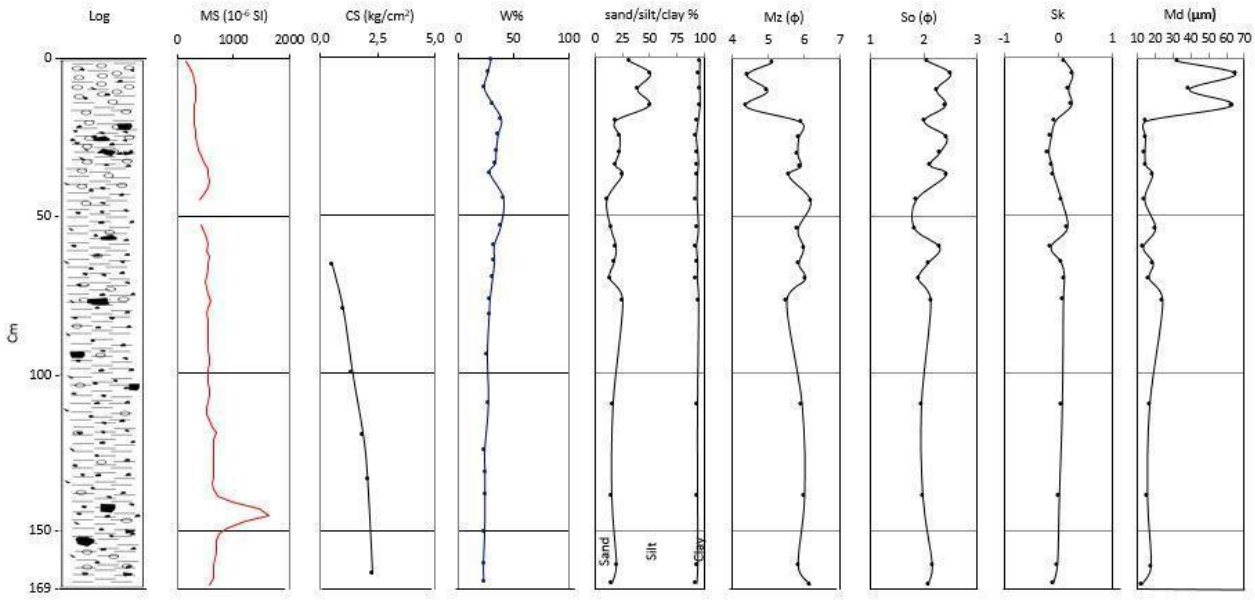

Figure S32 Physical parameters of the core GC18.

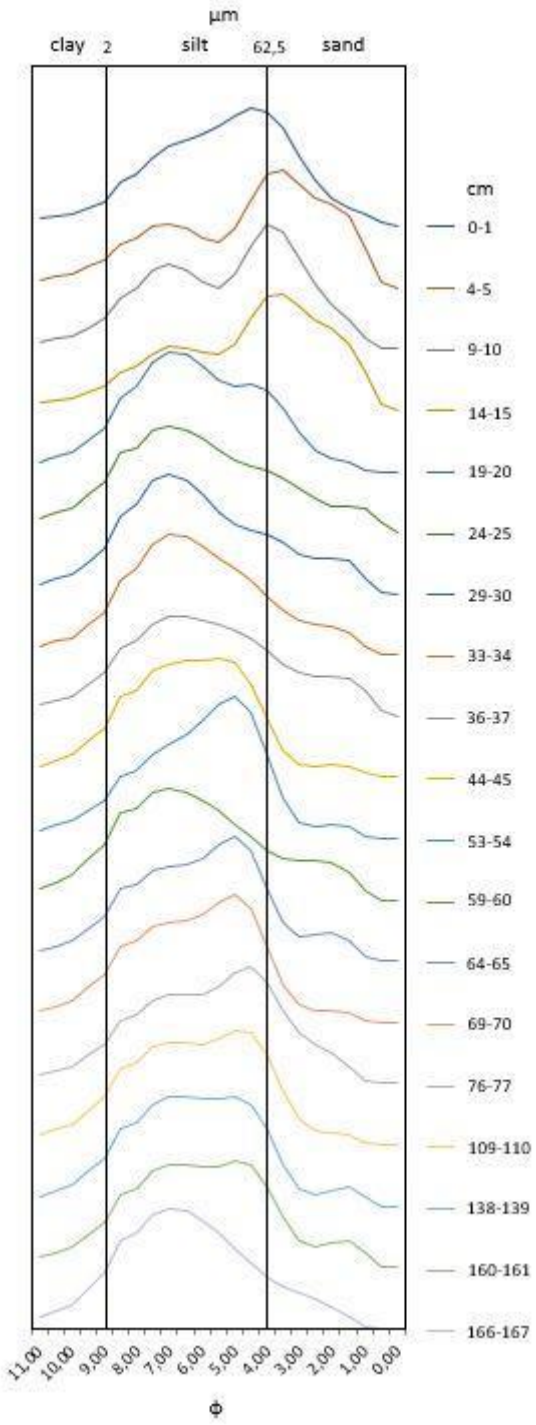

Figure S33 Grain size distribution curves of core GC18.

Chemical and Geochemical analyses - Elemental analyses, Organic matter and Biomarkers

This core is characterised by a good correlation (tab. S46) between Al, Si, Ti, K, Fe and Ca. Br correlates with Rb, Sr, Zr and Ba, while it anti-correlates with Al, Si and Ca. Ti, Sr and Zr show a good correlation with Rb.

GC18	Al_cps	Si_cps	K_cps	Ca_cps	Ti_cps	Fe_cps	Br_cps	Rb_cps	Sr_cps	Zr_cps	Ba50_cps
Al_cps		2,81E-81	1,48E-57	8,66E-53	4,68E-25	2,13E-25	4,19E-13	0,19166	0,060822	0,004625	0,61534
Si_cps	**0,9423**		5,77E-60	5,49E-75	5,61E-24	8,30E-26	9,78E-20	0,69218	0,021119	0,000428	0,81069
K_cps	**0,88576**	**0,89354**		5,21E-34	1,15E-68	9,28E-45	0,000171	1,14E-08	0,1547	0,98391	0,000524
Ca_cps	**0,86855**	**0,93098**	**0,76703**		2,19E-14	2,79E-22	1,98E-24	0,37963	0,010569	1,34E-05	0,62594
Ti_cps	**0,68828**	**0,67672**	**0,91726**	*0,54371*		7,50E-52	0,99475	8,83E-22	0,000264	0,050523	1,07E-06
Fe_cps	**0,69184**	**0,69603**	**0,83286**	**0,6574**	**0,86485**		0,003247	1,14E-09	0,7867	0,012115	0,41187
Br_cps	*-0,52025*	**-0,6255**	-0,28521	**-0,68164**	0,00051	-0,22516		5,85E-20	5,18E-23	9,25E-24	4,30E-12
Rb_cps	0,10093	0,030675	0,42155	-0,06801	**0,65142**	0,44672	**0,62845**		4,61E-33	3,90E-24	1,24E-29
Sr_cps	-0,14453	-0,17728	0,10996	-0,19621	0,27715	-0,02097	**0,66591**	**0,75994**		1,94E-56	2,19E-55
Zr_cps	-0,21686	-0,26796	0,001563	-0,32796	0,15068	-0,1926	**0,67432**	**0,67844**	**0,88196**		1,36E-45
Ba50_cps	0,038925	0,018562	0,26401	-0,03776	0,365	0,063531	*0,50037*	**0,73199**	**0,87825**	**0,83701**	

Table S46 Elements correlation of the core GC18. Bold and underlined values represent moderate to strong correlation. Underlined values in italics represent low correlation.

Ti (cps) has a constant trend from the bottom to 44 cm. Then it decreases between 44 and 40 cm. After that, Ti (csp) increases reaching the maximum around 26 cm. It decreases in the upper part of the core, with a drop at 12 cm. Zr/Rb has a value of 1,5 from the bottom up to 42 cm. Then, it fluctuates between 1,3 and 1,7 from 42 cm up to 19 cm. The upper 19 cm by values around 2. Si/Ti is characterised by a decreasing trend from the bottom to 28 cm. The upper part of the core is characterised by an increasing trend. Fe/Ti has a constant trend from the bottom up to 44 cm. Then, it decreases toward the top of the core. K/Ti shows a decreasing trend from the bottom of the core up to 29 cm. Then, it slightly increases from 29 cm to 25 cm. The upper 25 centimetres are characterised by a decreasing trend. Ca/Ti is characterised by a decreasing trend from the bottom up to 17 cm. It peaks at 12 cm and then, it decreases toward the top of the core. Mn/Ti increases upward reaching a peak at the top of the core. See fig. S34 for the graphics, where Ti (cps) represents lithogenic elements and various elemental ratios are reported as well.

TOC (tab. S47, fig. S35), with an average value of 0,34%, ranges from 0,23% to 0,45%. TOC is characterised by an increasing trend from 70 to 14 cm. Then, organic carbon percentage drops, reaching its minimum value at 10 cm. After that, TOC increases again to values equal or higher than 0,30%. The upper 3 cm shows values slightly lower than 0,30%.

C/N (tab. S47, fig. S35) shows a decreasing up-core trend. The highest value is 13,22 at 70 cm, while the lowest is 7,68 at 3 cm. C/N measured in the upper 2 cm shows values slightly higher than 8,00. The average value of the core is 8,88.

HBI diene II (tab. S48, fig. S35) has not been found in three samples collected at 63, 56 and 47 cm. It shows a decreasing trend from 44 to 27 cm. Higher concentration of $IPSO_{25}$ has been observed

from 26 to 18 cm (max 3,27*10^{-4} µg/g). The upper part of the core is characterised by a decreasing trend, with low values in the upper 14 cm. The average concentration is 1,18*10^{-4} µg/g.

Sterols (tab. S48, fig. S35) have a very low concentration from 63 cm to 34 cm. Then, all of them show an increasing trend and reach a peak at 25 cm (3,69*10^{-2} µg/g for 22-dehydrocholesterol, 7,16*10^{-2} µg/g for cholesterol and 1,58*10^{-1} µg/g for brassicasterol). All of them show a fluctuation of concentration between 24 cm and 13 cm. Sterols show a decreasing trend in the upper part of the core. The average concentration value is 1,43*10^{-2} µg/g for 22-dehydrocholesterol, 2,66*10^{-2} µg/g for cholesterol and 4,61*10^{-2} µg/g for brassicasterol.

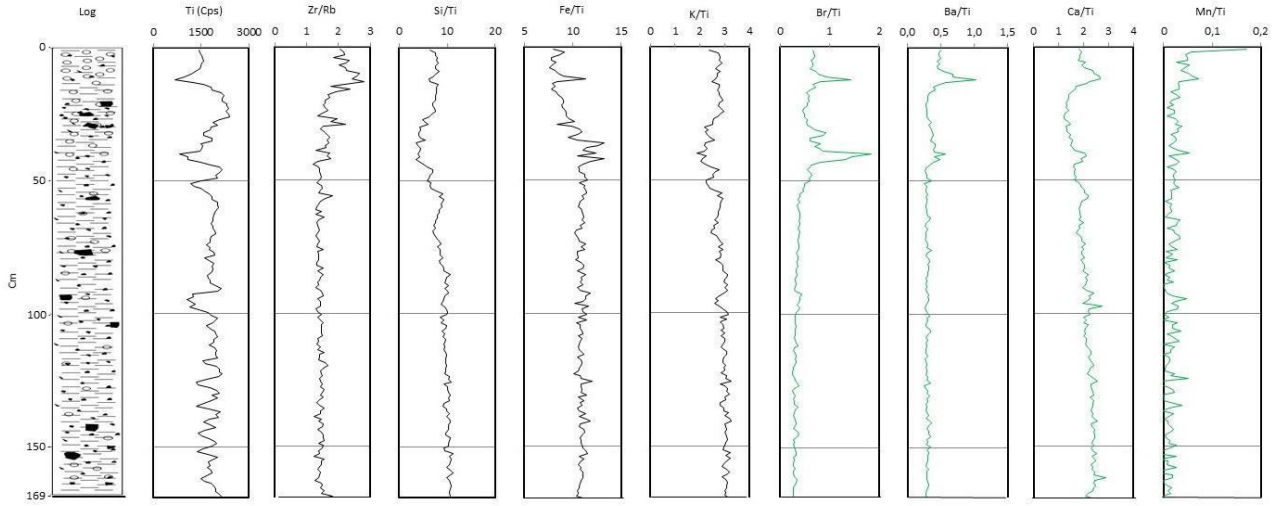

Figure S34 Elemental ratios of the core GC18.

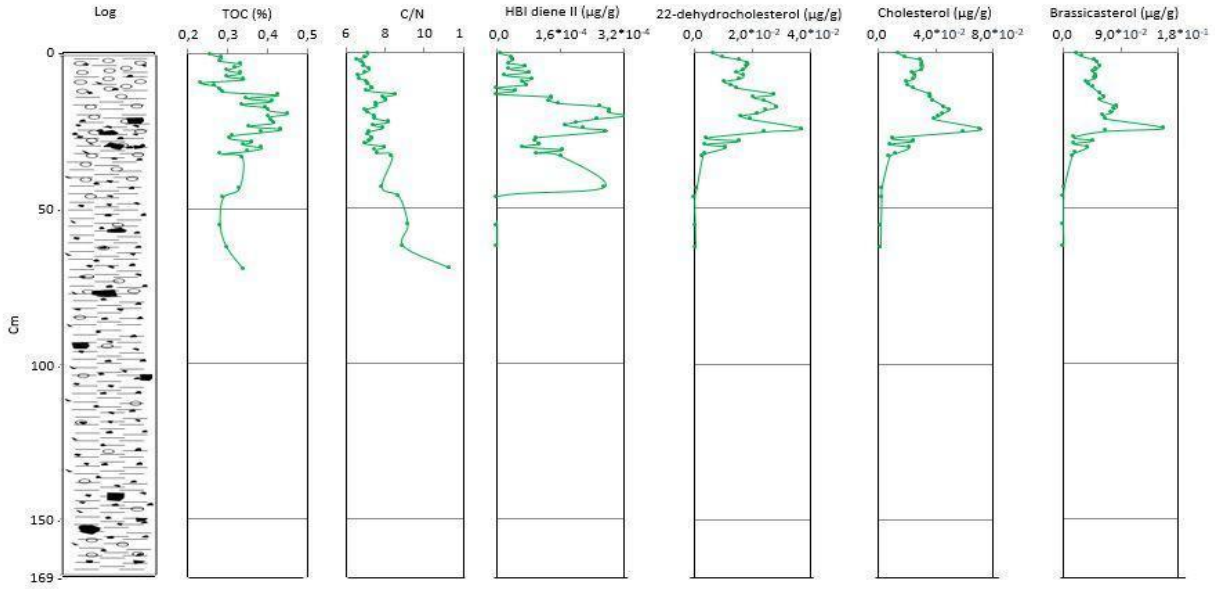

Figure S35 Organic matter and biomarkers parameters of the core GC18.

GC18	TOC (%)	TN (%)	C/N
0-1	0,26	0,04	8,32
1-2	0,29	0,04	8,19
2-3	0,28	0,04	7,68
3-4	0,33	0,05	8,05
4-5	0,32	0,05	8,13
5-6	0,30	0,04	8,41
6-7	0,33	0,05	8,17
7-8	0,30	0,04	7,73
8-9	0,34	0,05	7,82
9-10	0,23	0,03	8,30
10-11	0,27	0,04	8,37
11-12	0,28	0,04	8,62
12-13	0,29	0,04	8,21
13-14	0,43	0,05	9,96
14-15	0,35	0,04	9,26
15-16	0,41	0,05	9,42
16-17	0,34	0,04	8,79
17-18	0,40	0,05	8,83
18-19	0,40	0,06	8,17
19-20	0,45	0,06	8,38
20-21	0,40	0,05	8,74
21-22	0,41	0,05	8,77
22-23	0,42	0,05	9,60
23-24	0,36	0,05	8,64
24-25	0,44	0,06	9,21
25-26	0,38	0,05	8,46
26-27	0,31	0,04	8,33
27-28	0,31	0,04	8,59
28-29	0,36	0,05	8,43
29-30	0,34	0,05	8,16
30-31	0,39	0,05	9,33
31-32	0,35	0,05	8,78
32-33	0,28	0,04	8,96
33-34	0,34	0,04	9,77
43-44	0,33	0,04	9,13
46-47	0,29	0,03	10,17
55-56	0,28	0,03	10,69
62-63	0,30	0,03	10,44
69-70	0,34	0,03	13,22

Table S47 Organic matter parameters of the core ANTA99-GC18.

GC18	$IPSO_{25}$ (µg/g dry sedim.)	22-dehydrocholesterol (µg/g dry sedim.)	Cholesterol (µg/g dry sedim.)	Brassicasterol (µg/g dry sedim.)
0-1	$8,40*10^{-6}$	$6,79*10^{-3}$	$1,44*10^{-2}$	$2,12*10^{-2}$
1-2	$3,82*10^{-5}$	$9,81*10^{-3}$	$1,90*10^{-2}$	$3,11*10^{-2}$
2-3	$4,13*10^{-5}$	$1,58*10^{-2}$	$2,99*10^{-2}$	$4,93*10^{-2}$
3-4	$2,90*10^{-5}$	$1,86*10^{-2}$	$3,07*10^{-2}$	$5,45*10^{-2}$
4-5	$7,29*10^{-5}$	$1,80*10^{-2}$	$3,10*10^{-2}$	$5,73*10^{-2}$
5-6	$3,17*10^{-5}$	$1,69*10^{-2}$	$3,03*10^{-2}$	$5,28*10^{-2}$
6-7	$8,27*10^{-5}$	$1,46*10^{-2}$	$2,35*10^{-2}$	$4,74*10^{-2}$
7-8	$2,11*10^{-5}$	$1,69*10^{-2}$	$2,60*10^{-2}$	$5,24*10^{-2}$
8-9	$8,81*10^{-5}$	$1,58*10^{-2}$	$2,48*10^{-2}$	$5,01*10^{-2}$
9-10	$6,54*10^{-5}$	$1,02*10^{-2}$	$1,97*10^{-2}$	$3,58*10^{-2}$
10-11	$7,44*10^{-5}$	$1,30*10^{-2}$	$2,08*10^{-2}$	$4,07*10^{-2}$
11-12	0	$1,46*10^{-2}$	$2,46*10^{-2}$	$4,71*10^{-2}$
12-13	$4,65*10^{-5}$	$7,24*10^{-3}$	$1,23*10^{-2}$	$1,75*10^{-2}$
13-14	0	$2,73*10^{-2}$	$3,63*10^{-2}$	$5,90*10^{-2}$
14-15	$1,39*10^{-4}$	$2,03*10^{-2}$	$3,64*10^{-2}$	$6,48*10^{-2}$
15-16	$1,31*10^{-4}$	$2,42*10^{-2}$	$3,87*10^{-2}$	$5,81*10^{-2}$
16-17	$1,57*10^{-4}$	$7,12*10^{-3}$	$1,52*10^{-2}$	$1,87*10^{-2}$
17-18	$2,62*10^{-4}$	$2,84*10^{-2}$	$4,62*10^{-2}$	$8,45*10^{-2}$
18-19	$2,85*10^{-4}$	$2,48*10^{-2}$	$4,95*10^{-2}$	$7,93*10^{-2}$
19-20	$2,85*10^{-4}$	$2,20*10^{-2}$	$4,55*10^{-2}$	$7,62*10^{-2}$
20-21	$3,27*10^{-4}$	$1,60*10^{-2}$	$4,18*10^{-2}$	$6,36*10^{-2}$
21-22	$2,54*10^{-4}$	$1,92*10^{-2}$	$3,89*10^{-2}$	$6,76*10^{-2}$
22-23	$2,01*10^{-4}$	$5,68*10^{-3}$	$1,40*10^{-2}$	$1,94*10^{-2}$
23-24	$1,73*10^{-4}$	$9,96*10^{-3}$	$2,33*10^{-2}$	$3,44*10^{-2}$
24-25	$2,20*10^{-4}$	$3,69*10^{-2}$	$7,16*10^{-2}$	$1,58*10^{-1}$
25-26	$2,76*10^{-4}$	$2,43*10^{-2}$	$5,94*10^{-2}$	$6,65*10^{-2}$
26-27	0	$3,49*10^{-3}$	$9,34*10^{-3}$	$9,11*10^{-3}$
27-28	$1,02*10^{-4}$	$4,25*10^{-3}$	$9,93*10^{-3}$	$1,65*10^{-2}$
28-29	$9,63*10^{-5}$	$1,56*10^{-2}$	$2,50*10^{-2}$	$1,40*10^{-2}$
29-30	$1,08*10^{-4}$	$4,05*10^{-3}$	$8,43*10^{-3}$	$1,74*10^{-3}$
30-31	$6,63*10^{-5}$	$1,08*10^{-2}$	$2,17*10^{-2}$	$3,94*10^{-2}$
31-32	$1,66*10^{-4}$	$4,38*10^{-3}$	$1,61*10^{-3}$	$1,60*10^{-3}$
32-33	$1,01*10^{-4}$	$3,82*10^{-3}$	$1,20*10^{-2}$	$1,83*10^{-2}$
33-34	$1,61*10^{-4}$	$2,87*10^{-3}$	$7,86*10^{-3}$	$1,40*10^{-2}$
43-44	$2,71*10^{-4}$	$8,75*10^{-4}$	$2,44*10^{-3}$	$1,74*10^{-3}$
46-47	0	$1,55*10^{-4}$	$2,33*10^{-3}$	$6,82*10^{-4}$
55-56	0	$3,03*10^{-4}$	$1,93*10^{-3}$	$5,25*10^{-4}$
62-63	0	$4,90*10^{-4}$	$1,80*10^{-3}$	$6,38*10^{-4}$

Table S48 Biomarkers of the core ANTA99-GC18. Yellow samples are anomalous and were not considered.

Microscopy analyses - Sand and Foraminifera

Sand samples are characterised by the presence of quartz grains (angular to sub-rounded), feldspar (rounded), micas and other femic minerals and lithic fragments along the core. Biogenic component is sparse but present along the core. Radiolarians, sponge spicules and diatoms represent the siliceous component. Both benthic and planktonic (*Neogloboquadrina pachyderma*) foraminifera

(tab. S49) have been recovered (calcareous from the bottom to 37 cm and agglutinated in the upper 30 cm). Density is very low, exceeding 2 specimes/grams only at 77 cm and at the top of the core. 12 different genera (15 different species) have been identified. *Miliammina earlandi*, *Globocassidulina subglobosa* and *Trifarina earlandi* (costate and spinose morphotypes) are the most present species. Fragmentation rate is higher than 40,0%, except for the sample collected at 60 cm (28,6%).

GC18	*Neogloboquadrina pachyderma*	Benthos/g	*Astrononion antarcticus*	*Astrononion echolsi*	*Cassidulina carinata*	*Cassidulinoides parkerianus*	*Cassidulinoides porrectus*	*Cibicides refulgens*	*Ehrembergina glabra*	*Epistominella exigua*	*Globocassiduina biora* (smooth)	*Globocassiduina biora* (pustolose)	*Globocassidulina subglobosa*	Hyalinonetrion sp.	Lagena spp.	*Miliammina earlandi*	*Nonionella iridea*	Nonionella sp.	*Portatrochammina antarctica*	*Reophax scorpiurus*	*Trifarina earlandi (costate)*	*Trifarina earlandi (spinose)*	Unknown	% fragmentation
0-1	0	2,1	0	0	0	0	0	0	0	0	0	0	0	0	0	5	0	0	1	1	0	0	1	52,9
9-10	0	1,6	0	0	0	0	0	0	0	0	0	0	0	0	0	6	0	0	0	0	0	0	0	40,0
19-20	0	0,7	0	0	0	0	0	0	0	0	0	0	0	0	0	2	0	0	0	0	0	0	0	71,4
29-30	0	0,3	0	0	0	0	0	0	0	0	0	0	0	0	0	1	0	0	0	0	0	0	0	85,7
33-34	0	0,0	0	0	0	0	0	0	0	0	0	0	0	0	0	0	0	0	0	0	0	0	0	100
36-37	0	1,3	0	0	0	0	0	0	0	0	0	0	0	0	0	0	0	0	0	0	0	4	0	42,9
44-45	1	0,3	0	0	0	0	0	0	0	0	0	0	0	0	0	0	0	0	0	0	0	1	0	71,4
53-54	2	1,2	0	0	0	1	2	0	0	0	0	0	2	0	1	0	0	0	0	0	2	0	0	47,4
59-60	2	0,7	0	0	0	0	0	0	0	0	1	0	0	0	0	0	0	0	0	0	2	0	0	28,6
64-65	1	0,8	0	0	0	0	0	0	0	0	0	0	1	0	0	0	0	0	0	0	2	0	0	42,9
76-77	2	2,3	0	0	0	0	0	0	0	1	1	0	0	0	0	0	2	0	0	0	1	3	1	66,7
81-82	3	0,8	0	0	0	0	0	0	0	0	0	0	3	0	0	0	0	0	0	0	1	0	0	69,6
94-95	1	1,5	0	1	0	0	0	1	0	0	0	0	1	0	0	0	0	0	0	0	3	0	0	58,8
109-110	2	1,6	0	0	1	1	0	0	0	0	1	0	3	0	0	0	0	0	0	0	0	1	0	47,1
124-125	0	0,7	1	0	0	0	0	0	0	0	0	0	2	0	0	0	0	0	0	0	0	0	0	72,7
131-132	2	1,0	0	0	0	0	1	1	0	0	0	0	2	0	0	0	0	0	0	0	0	0	0	53,8
138-139	1	0,9	0	0	0	0	0	0	0	0	2	1	0	0	0	0	0	0	0	0	1	0	0	50,0
150-151	0	0,7	0	0	0	0	0	0	0	0	0	0	2	0	0	0	0	1	0	0	0	0	0	72,7
160-161	2	1,8	0	0	1	0	0	0	1	0	1	1	1	0	1	0	0	0	0	0	1	0	1	56,5
166-167	1	1,7	0	0	0	0	0	0	0	0	1	1	0	1	0	0	2	0	0	0	1	0	0	50,0

Table S49 Foraminifera of the core ANTA99-GC18.

ANTA99-GC19

This gravity core has been collected in the outer continental shelf, between the GC17 and GC18 sites (tab. 3, fig. 6). The area is characterised by glaciomarine build-ups (fig. S36).

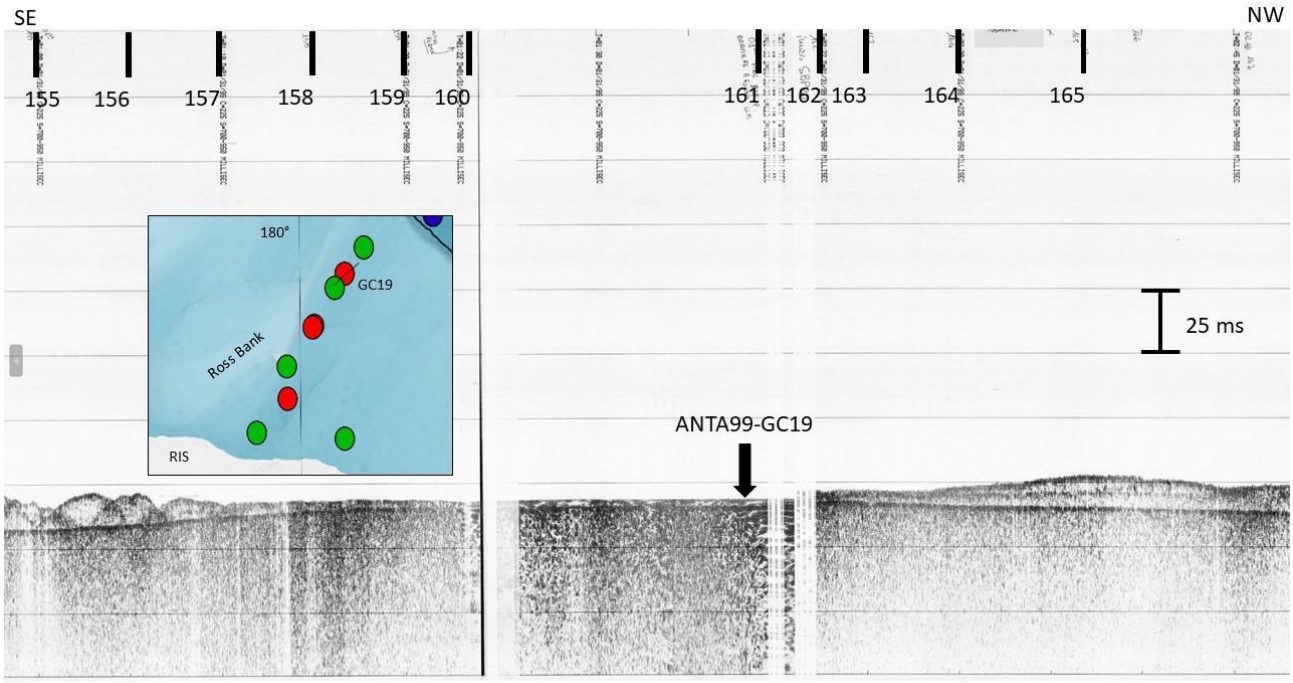

Figure S36 Section of the SBPs 19 and 20, with the location of the core GC19. Bathymetric map is a zoom of fig. 6.

Core radiography

The core (fig. S37) is made of gravelly and sandy material within a fine matrix. Clasts range from millimetric to pluri-centimetric and from rounded to angular, but they are mainly sub-angular. This interval occupies the major part of the core, from the bottom to 8 cm. A denser layer with abundant clasts is present between 19 and 8 cm. The upper part of the core is characterised by a less dense sediment with lower amount of clasts.

The lower part of the core shows fluctuating values of the mobile average of clasts >2 mm (tab. S50, fig. S37), with the highest peak between 26 and 23 cm. Then, it drops to lower values in the upper part of the core, except for a small peak around 11 cm.

Depth (cm)	Clasts >2mm (num.)	Mobile average	Depth (cm)	Clasts >2mm (num.)	Mobile average	Depth (cm)	Clasts >2mm (num.)	Mobile average
0-1	0	1,4	39-40	2	3,2	78-79	3	2,2
1-2	1	1,8	40-41	2	4,4	79-80	3	2,8
2-3	2	1,8	41-42	5	4,8	80-81	1	3,4
3-4	1	1,4	42-43	5	6,2	81-82	1	3,8
4-5	3	1,2	43-44	2	6,0	82-83	3	3,6
5-6	2	0,8	44-45	8	6,2	83-84	6	3,8
6-7	1	1,0	45-46	4	5,4	84-85	6	3,6
7-8	0	1,8	46-47	12	5,2	85-86	3	3,2
8-9	0	2,8	47-48	4	3,6	86-87	0	3,2
9-10	1	3,6	48-49	3	3,0	87-88	4	3,6
10-11	3	3,8	49-50	4	3,4	88-89	5	3,2
11-12	5	3,8	50-51	3	3,8	89-90	4	2,2
12-13	5	3,2	51-52	4	3,8	90-91	3	1,8
13-14	4	2,2	52-53	1	4,2	91-92	2	1,6
14-15	2	2,0	53-54	5	4,8	92-93	2	2,0
15-16	3	2,6	54-55	6	4,2	93-94	0	2,4
16-17	2	2,4	55-56	3	4,0	94-95	2	3,0
17-18	0	3,2	56-57	6	4,0	95-96	2	3,0
18-19	3	4,4	57-58	4	4,0	96-97	4	3,8
19-20	5	5,6	58-59	2	4,2	97-98	4	4,0
20-21	2	5,6	59-60	5	4,6	98-99	3	4,0
21-22	6	6,6	60-61	3	4,4	99-100	2	4,4
22-23	6	7,0	61-62	6	4,8	100-101	6	4,8
23-24	9	6,6	62-63	5	4,4	101-102	5	3,8
24-25	5	6,8	63-64	4	4,6	102-103	4	3,8
25-26	7	7,0	64-65	4	5,2	103-104	5	3,6
26-27	8	6,6	65-66	5	5,8	104-105	4	4,0
27-28	4	5,8	66-67	4	6,0	105-106	1	4,2
28-29	10	5,6	67-68	6	6,6	106-107	5	4,8
29-30	6	4,2	68-69	7	5,8	107-108	3	5,0
30-31	5	3,8	69-70	7	5,4	108-109	7	5,0
31-32	4	3,2	70-71	6	4,4	109-110	5	4,8
32-33	3	2,6	71-72	7	4,0	110-111	4	4,2
33-34	3	2,8	72-73	2	3,4	111-112	6	4,2
34-35	4	3,2	73-74	5	4,0	112-113	3	3,6
35-36	2	2,8	74-75	2	3,6	113-114	6	3,8
36-37	1	2,8	75-76	4	3,8	114-115	2	3,0
37-38	4	3,6	76-77	4	3,2	115-116	4	3,5
38-39	5	3,8	77-78	5	2,6	116-117	3	3,0

Table S50 Clasts >2 mm counted using the method of Grobe (1987) and mobile average (interval of 5 cm) of the core ANTA99-GC19.

Physical analyses - Magnetic susceptibility

Magnetic susceptibility (tab. S51, fig. S37) is characterised by an increasing trend from the bottom to the interval between 27 and 15 cm (coarser interval and clasts). This section presents two peaks of 620 and 600*10^{-6} SI respectively. The upper part of the core is characterised by a decreasing trend (150*10^{-6} SI at the top).

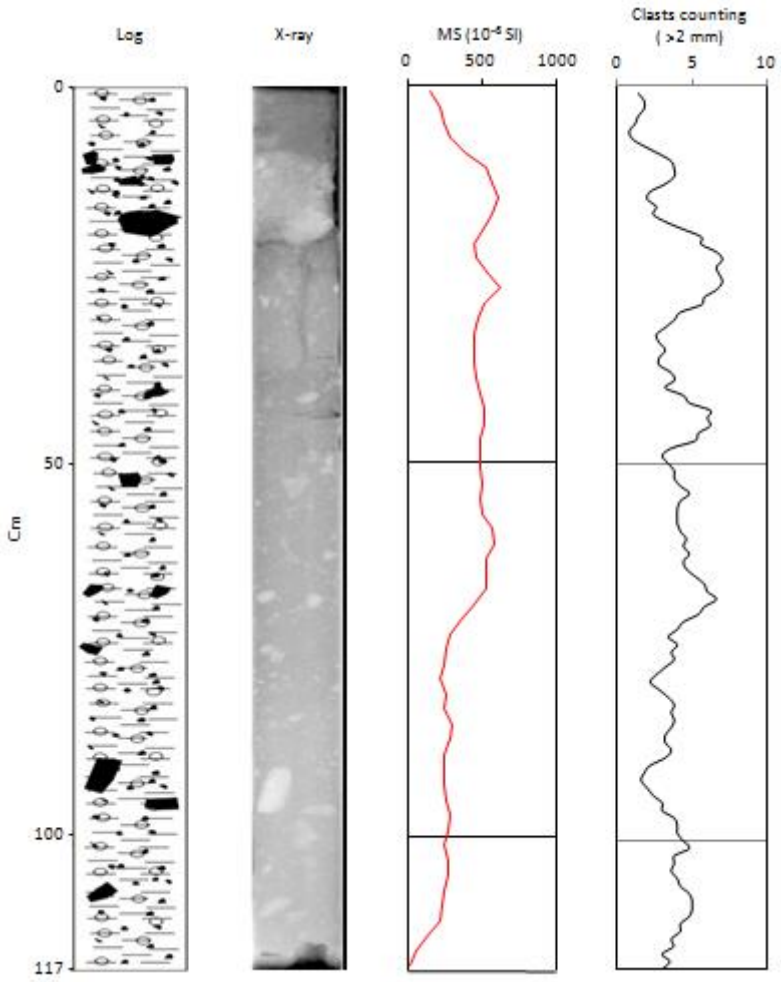

Figure S37 Descriptive log, radiography, magnetic susceptibility and clasts counted using the Grobe (1987) method (mobile average interval: 5 cm) of the core GC19.

Depth (cm)	MS (10^{-6}SI)	Depth (cm)	MS (10^{-6}SI)
0-1	150	94-95	260
2-3	220	96-97	290
4-5	240	98-99	270
6-7	290	100-101	250
8-9	390	102-103	270
10-11	530	104-105	270
12-13	570	106-107	240
14-15	600	108-109	230
16-17	570	110-111	210
18-19	510	112-113	140
20-21	450	114-115	50
22-23	460	116-117	10
24-25	540		
26-27	620		
28-29	510		
30-31	470		
32-33	450		
34-35	440		
36-37	440		
38-39	460		
40-41	490		
42-43	510		
44-45	510		
46-47	490		
48-49	480		
50-51	480		
52-53	500		
54-55	490		
56-57	500		
58-59	560		
60-61	580		
62-63	530		
64-65	520		
66-67	520		
68-69	450		
70-71	370		
72-73	290		
74-75	260		
76-77	240		
78-79	220		
80-81	260		
82-83	240		
84-85	300		
86-87	280		
88-89	250		
90-91	250		
92-93	250		

Table S51 Magnetic susceptibility of the core ANTA99-GC19. Yellow levels the end of each core section or peaks related to clasts.

Supplementary 2 - Slope and rise area

RS14-BC3

This box core has been collected in the middle continental slope (tab. 3, figs. 6 and 10).

Core description and Radiography

This box core (fig. S38) is 39 cm long. From the bottom to 31 cm, greenish grey (10Y 4/1) muddy sediment. Millimetric and centimetric clasts are present. From 31 to 25 cm, and the colour changes to dark grey (5Y 4/1). Olive (5Y 4/3) muddy stains are present. Clasts are less abundant from 29 to 26 cm. The interval from 25 t0 15 cm is made of gravel surrounded by a muddy sandy matrix and its colour is grey (2,5Y 5/1) with sparse brown (10YR 3/3) stains. Pluri-centimetric clasts are present. The sandy component increases in the upper 15 cm. In the upper 10 cm, colour changes to greyish brown (2,5Y 4/2). The muddy component is more abundant, while clasts are less present and density is slightly lower between 10 and 4 cm. The top of the core is made of sand with clasts. Clasts are mainly angular and subangular.

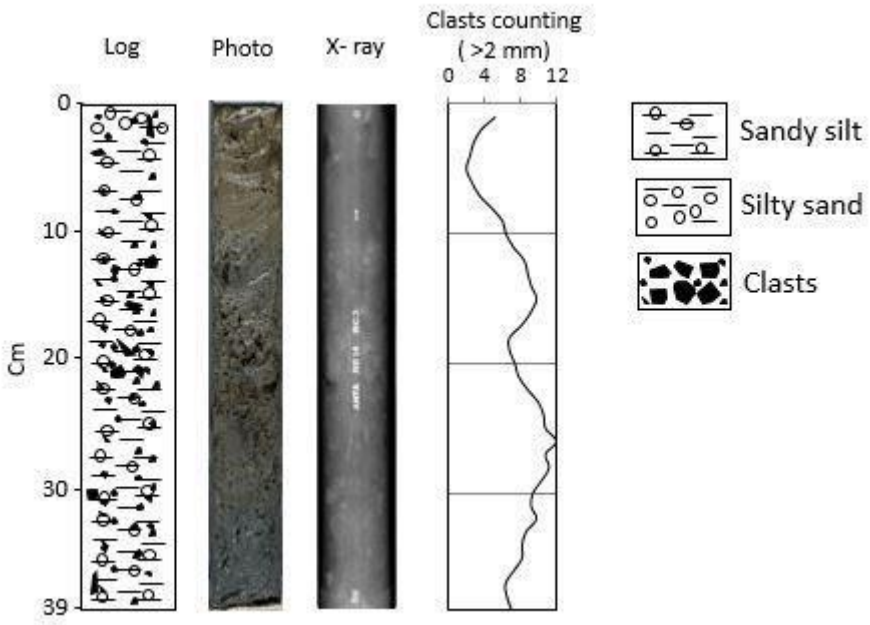

Figure S38 Lithologic log, photo, radiography and clasts counted using the Grobe (1987) method (mobile average interval: 5 cm) of the box core BC3.

Counting clasts (tab. S52, fig. S38), highlighted a higher number of clasts from the bottom to 14 cm. The number decreases in the upper part of the core, before increasing again toward the top.

Depth (cm)	Clasts >2mm (num.)	Mobile average
0-1	11	5,2
1-2	6	3,6
2-3	3	2,8
3-4	5	2,4
4-5	1	2,0
5-6	3	2,6
6-7	2	3,4
7-8	1	4,8
8-9	3	6,0
9-10	4	6,4
10-11	7	7,2
11-12	9	8,4
12-13	7	8,8
13-14	5	9,2
14-15	8	9,8
15-16	13	9,2
16-17	11	8,2
17-18	9	6,8
18-19	8	6,8
19-20	5	7,4
20-21	8	7,8
21-22	4	8,8
22-23	9	10,0
23-24	11	10,6
24-25	7	10,8
25-26	13	12,0
26-27	10	10,8
27-28	12	11,2
28-29	12	10,4
29-30	13	9,4
30-31	7	9,2
31-32	12	9,8
32-33	8	8,6
33-34	7	8,2
34-35	12	8,2
35-36	10	7,3
36-37	6	6,3
37-38	6	6,5
38-39	7	7,0

Table S52 Clasts >2 mm counted using the method of Grobe (1987) and mobile average (interval of 5 cm) of the box core RS14-BC3.

Physical analyses - Magnetic susceptibility, Water content and Grain size

Magnetic susceptibility (MS) (tab. S53, fig. S39) is very low at the bottom of the core. MS increases and, from 32 cm to the top of the core, it shows values between 280 and 330*10^6 SI.

Water content (w%) (tab. S54, fig. S39) has a constant trend along the core with values between 20 and 30%, except for the lowest and the highest values. The min value: 17,0% has been measured at 35 cm. The max value%: 31,9 has been measured at 9 cm.

Silt is the main sedimentary component (avg 70,3%, max 81,8%, min 36,4%). Sand varies between 60,7%, and 8,3%, with an average value of 20,9%. Clay has an average value of 8,8%, varying from 16,1% to 2,9% (tab. S55, fig. S39).

Mean diameter (Mz) shows values between 3,76 ϕ (very fine sand) and 6,94 ϕ (fine silt). The average value is 5,97 ϕ (medium silt). Sediments are very poorly sorted (avg 2,25 ϕ), with few poorly sorted intervals. The average value of skewness (Sk) is -0,09. Distributions curves are mainly negative asymmetric, with few samples characterised by a symmetric distribution. A constant trend of median diameter (Md) characterises the core from the bottom to 9 cm. Then, Md rapidly increases in the upper part of the core. See tab. S55 and fig. S39 for the graphics.

Depth (cm)	MS (10^{-6}SI)
0-1	315
2-3	318
4-5	326
6-7	322
8-9	320
10-11	305
12-13	306
14-15	297
16-17	296
18-19	294
20-21	294
22-23	294
24-25	301
26-27	328
28-29	314
30-31	298
32-33	288
34-35	248
36-37	166
38-39	68

Table S53 Magnetic susceptibility of the box core RS14-BC3. Yellow levels the end of the core section.

Grain size distribution curves from the bottom to 9 cm are mainly unimodal with a primary mode between 7,5 and 7,0 ϕ (5,52 - 7,81 µm), with finer intervals (8,0 ϕ - 4,00 µm) and coarser ones (from 6,5 to 5,0 ϕ - from 11,05 to 31,25 µm). Some samples, collected at 12-13 cm and between 8 and 6 cm, are characterised by a bimodal distribution, with a secondary mode between 2,5 and 2,0 ϕ (176,77 - 250,00 µm).

Depth (cm)	W%
0-1	22,9
1-2	22,7
2-3	24,2
3-4	21,8
4-5	26,1
5-6	25,1
6-7	25,4
7-8	26,7
8-9	31,9
9-10	27,1
10-11	25,5
11-12	24,6
12-13	22,3
13-14	25,0
14-15	24,8
15-16	24,8
16-17	25,3
17-18	23,3
18-19	23,2
19-20	24,2
20-21	25,0
21-22	24,6
22-23	24,2
23-24	23,1
24-25	24,3
25-26	26,1
26-27	24,0
27-28	25,0
28-29	23,4
29-30	22,8
30-31	23,0
31-32	23,8
32-33	25,0
33-34	24,5
34-35	17,0
35-36	23,1
36-37	24,3
37-38	22,5
38-39	24,3

Table S54 Water content of the box core RS14-BC3.

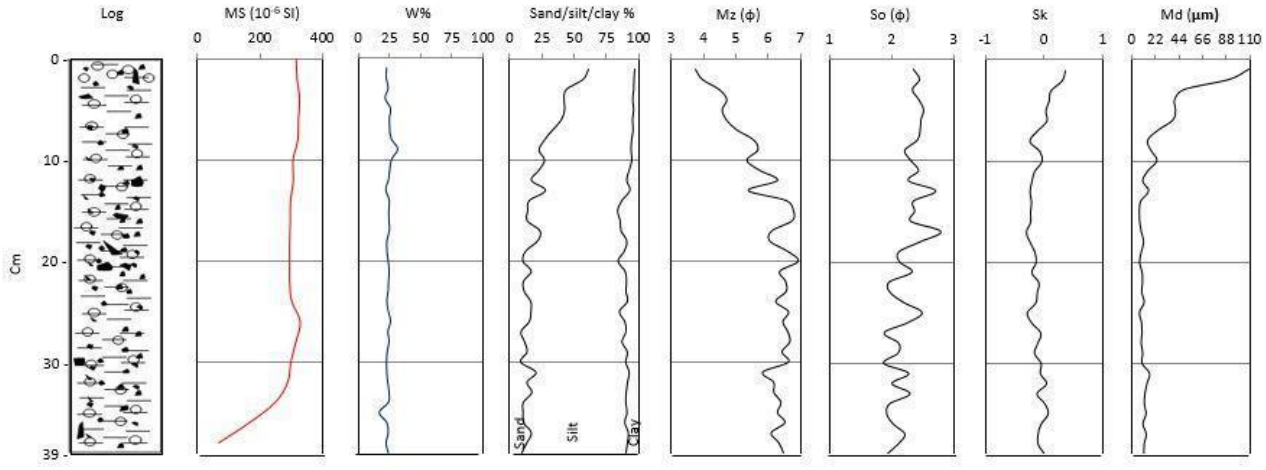

Figure S39 Physical parameters of the box core BC3.

The upper 6 cm are characterised by coarser sediments, with a primary mode between 2,5 and 2,0 ϕ (176,77 - 250,00 µm), except for the samples collected at 2-3 cm, which is characterised by a

primary mode of 4,5 ϕ (44,19 µm). These samples are mainly characterised by a bimodal distribution, while the upper 2 cm are characterised by an unimodal distribution. The primary mode is in table S55 and curves are reported in fig. S40.

BC3	Sand (%)	Silt (%)	Clay (%)	Mz (φ)	So (φ)	Sk	Md (µm)	Primary mode (φ)
0-1	60,7	36,4	2,9	3,76	2,35	0,37	109,2	2,00
1-2	56,6	40,0	3,4	3,97	2,45	0,32	90,7	2,00
2-3	43,6	52,7	3,7	4,49	2,33	0,12	48,6	4,50
3-4	41,9	53,6	4,5	4,73	2,44	0,09	40,0	2,50
4-5	42,3	54,0	3,7	4,59	2,51	0,03	40,8	2,00
5-6	39,8	55,6	4,6	4,72	2,47	0,05	38,5	5,00
6-7	33,0	62,8	4,2	5,04	2,46	-0,12	24,8	6,50
7-8	26,7	68,0	5,3	5,56	2,41	-0,25	14,8	7,00
8-9	22,5	71,7	5,8	5,69	2,21	-0,07	18,0	6,50
9-10	26,8	68,1	5,1	5,35	2,31	-0,04	23,6	5,00
10--11	22,4	70,4	7,2	5,74	2,43	-0,16	15,2	7,00
11--12	16,7	74,3	9,1	6,30	2,27	-0,21	10,3	7,50
12-13	27,5	65,9	6,6	5,40	2,71	-0,24	15,8	7,00
13-14	14,9	72,1	12,9	6,58	2,35	-0,22	8,5	7,50
14-15	13,8	70,1	16,1	6,80	2,37	-0,23	7,2	8,00
15-16	13,4	72,4	14,2	6,76	2,30	-0,23	7,5	7,50
16-17	23,3	63,3	13,4	6,13	2,79	-0,31	8,9	8,00
17-18	21,4	69,6	9,1	6,06	2,47	-0,24	11,1	7,50
18-19	12,3	76,8	10,9	6,60	2,11	-0,16	9,1	7,50
19-20	10,1	74,1	15,8	6,94	2,12	-0,14	7,3	7,50
20-21	16,5	73,1	10,4	6,37	2,32	-0,21	9,7	7,50
21-22	10,4	80,3	9,3	6,55	1,95	-0,09	10,1	7,00
22-23	11,1	79,2	9,7	6,57	1,97	-0,12	9,4	7,50
23-24	16,1	75,4	8,5	6,25	2,19	-0,14	11,6	7,00
24-25	16,3	68,8	14,8	6,64	2,49	-0,29	7,3	8,00
25-26	14,9	74,6	10,5	6,47	2,26	-0,21	9,3	7,50
26-27	8,5	81,7	9,8	6,62	1,87	-0,05	9,7	7,00
27-28	11,4	75,8	12,8	6,68	2,11	-0,11	8,8	7,50
28-29	13,2	78,2	8,6	6,44	2,10	-0,16	10,3	7,00
29-30	8,3	81,8	9,9	6,64	1,86	-0,05	9,6	7,00
30-31	20,1	72,7	7,2	5,84	2,27	-0,06	16,7	6,00
31-32	13,2	78,3	8,5	6,19	2,00	0,04	14,3	5,50
32-33	17,0	73,6	9,5	6,19	2,30	-0,12	12,4	7,00
33-34	10,3	79,9	9,8	6,41	1,96	0,02	11,8	7,00
34-35	10,2	80,9	8,9	6,30	1,91	0,07	13,4	5,50
35-36	10,5	78,9	10,6	6,53	2,02	-0,05	10,5	7,00
36-37	16,6	75,6	7,8	6,11	2,21	-0,10	13,6	7,00
37-38	13,1	78,3	8,6	6,35	2,10	-0,10	11,6	7,00
38-39	9,1	81,2	9,7	6,49	1,91	0,01	11,3	6,50

Table S55 Grain size parameters of the box core RS14-BC3.

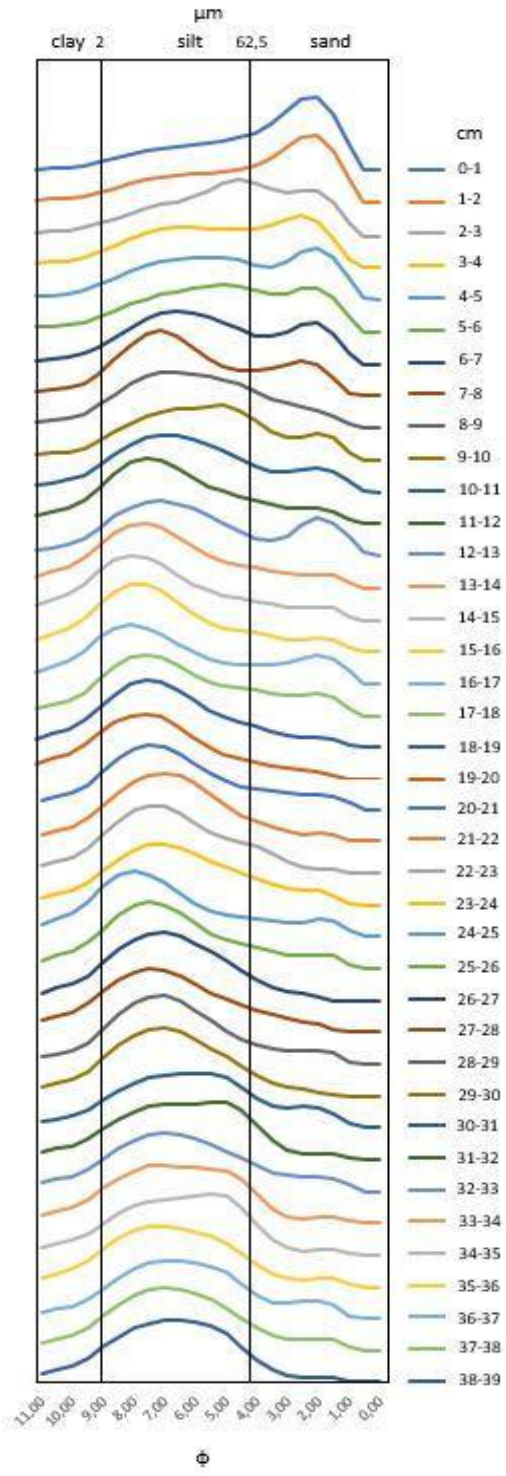

Figure S40 Grain size distribution curves of box core BC3

Chemical and Geochemical analyses - Elemental analyses, Organic matter and Biomarkers

Al, SI, K, Fe, Ti, Rb, Sr, Ca and Zr show a good correlation, but Zr does not correlate with Al and Si. Rb, Sr and Zr also correlate with Ba and Br. See tab. S56.

BC3	Al_cps	Si_cps	K_cps	Ca_cps	Ti_cps	Fe_cps	Br_cps	Rb_cps	Sr_cps	Zr_cps	Ba50_cps
Al_cps		6,55E-33	2,66E-23	2,62E-12	6,97E-16	9,53E-20	0,5067	8,56E-11	0,000783	0,007606	0,26616
Si_cps	**0,98979**		5,48E-27	2,59E-15	2,94E-16	6,06E-21	0,37121	2,02E-12	0,00024	0,004257	0,22202
K_cps	**0,96586**	**0,97855**		1,72E-14	3,05E-25	1,50E-32	0,075314	8,58E-18	9,06E-06	0,000282	0,037325
Ca_cps	**0,85903**	**0,9051**	**0,89434**		2,13E-11	1,07E-11	0,12596	6,39E-12	1,56E-06	0,00014	0,05055
Ti_cps	**0,91189**	**0,91606**	**0,97328**	**0,84072**		1,86E-24	0,004624	1,01E-21	7,69E-08	2,70E-06	0,001221
Fe_cps	**0,94639**	**0,95397**	**0,98932**	**0,84697**	**0,97049**		0,079278	1,07E-16	3,72E-05	0,00087	0,04676
Br_cps	0,10957	0,14719	0,2881	0,24926	0,44409	0,28442		0,000125	1,48E-10	1,77E-10	1,08E-13
Rb_cps	**0,82714**	**0,86114**	**0,93115**	**0,85153**	**0,95831**	**0,92071**	*0,57601*		2,30E-11	3,72E-08	8,13E-05
Sr_cps	*0,51551*	*0,55568*	**0,64565**	**0,68429**	**0,73918**	**0,61015**	**0,82146**	**0,84001**		2,46E-16	1,05E-11
Zr_cps	0,42102	0,44779	*0,55055*	*0,57255*	**0,67283**	*0,51171*	**0,81954**	**0,75067**	**0,9169**		3,84E-12
Ba50_cps	0,18249	0,20007	0,33463	0,31532	0,49904	0,32039	**0,88266**	*0,58851*	**0,84715**	**0,85586**	

Table S56 Elements correlation of the box core BC3. Bold and underlined values represent moderate to strong correlation. Underlined values in italics represent low correlation.

Ti (cps) is used to represent the lithogenic fraction, and it shows a decreasing trend with drops at 24 cm and in the upper part of the box core. Zr/Rb has values between 1,0 and 1,35 from the bottom up to 12 cm. Then, it increases to 1,4 at 11 cm. The upper part of the core is characterised by an increasing trend. Si/Ti has higher values from the bottom to 14 cm, where it drops. The upper part of the core shows lower values of Si/Ti. Fe/Ti shows a constant trend from the bottom to 13 cm, then, it drops between 13 cm and 10 cm. The upper part of the core shows a constant trend but characterised by lower values. K/Ti shows the same trend as Si/Ti. Ba/Ti is characterised by a constant trend from the bottom up to 14 cm and it increases in the upper part of the core. Br/Ti shows a similar trend. Ca/Ti is characterised by a decreasing trend from the bottom up to 5 cm. The upper part of the core is characterised by a slightly increasing trend. Mn/Ti slightly decreases from the bottom to 28 cm. Then, it fluctuates, reaching a peak at 23 cm. After that, Mn/Ti decreases, swinging up to 17 cm. The upper part of the core shows a constant trend. Graphics of elemental ratios are reported in fig. S41.

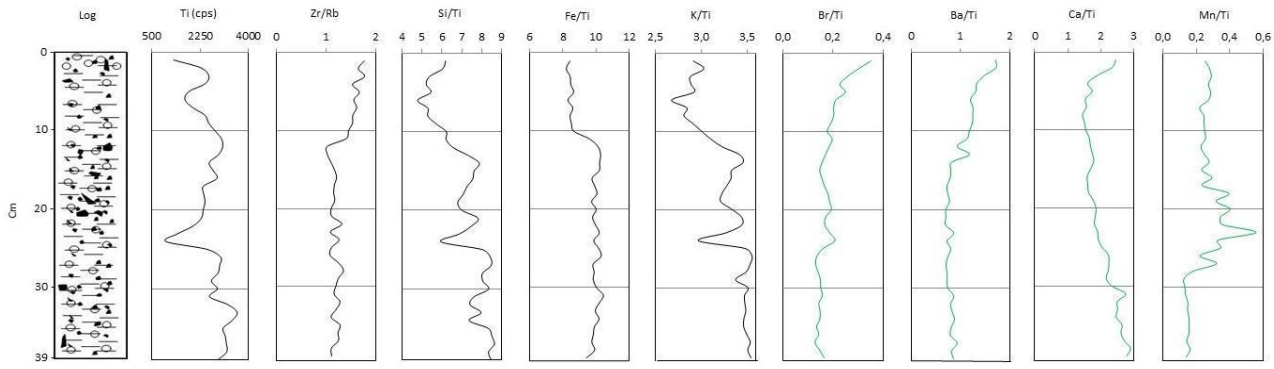

Figure S41 Elemental ratios of the box core BC3.

Total organic carbon (TOC) (tab. S57, fig. S42) has an average value of 0,22%, a max value of 0,33% and a min value 0,13%. TOC is characterised by an up-core decreasing trend, but it slightly increases at the top.

C/N (tab. S57, fig. S42) has an average value of 10,43. It shows a slightly increasing trend from the bottom to 21 cm (14,99). The upper part of the core (10-2 cm) is characterised by a decreasing trend, with values between 6 and 8 in the upper 10 cm. The top of the core has a higher value: 9,86.

$CaCO_3$ (tab. S57, fig. S42) is characterised by higher values in the lower part of the core (39-33 cm), with a max value of 2,39% at 33 cm. The upper part of the core shows a decreasing trend. The average value is: 0,83%.

Biogenic silica (BioSi) (tab. S57, fig. S42) has an average value of 7,33%. It is characterised by an increasing trend from the bottom to 21 cm. BioSi drops to 2,99% at 17 cm. It increases to 8,77% at 9 cm. The upper part of the core is characterised by slightly lower values.

$IPSO_{25}$ (tab. S58, fig. S42) has been detected in this core but with a very low concentration, with a max value of $4,54*10^{-5}$ µg/g at 2 cm. HBI diene II has not been detected at 10 cm. The average concentration is $2,79*10^{-5}$ µg/g.

22-dehydrocholesterol (tab. S58, fig. S42) has been only detected at the top of the core: $2,71*10^{-3}$ µg/g. Cholesterol (tab. 33, fig. 47) shows the highest value at 2 cm: $1,23*10^{-2}$ µg/g. The average concentration is $4,95*10^{-3}$ µg/g. Brassicasterol (tab. S52, fig. 51) shows the highest value at the top of the core: $9,38*10^{-3}$ µg/g (avg $2,12*10^{-3}$ µg/g).

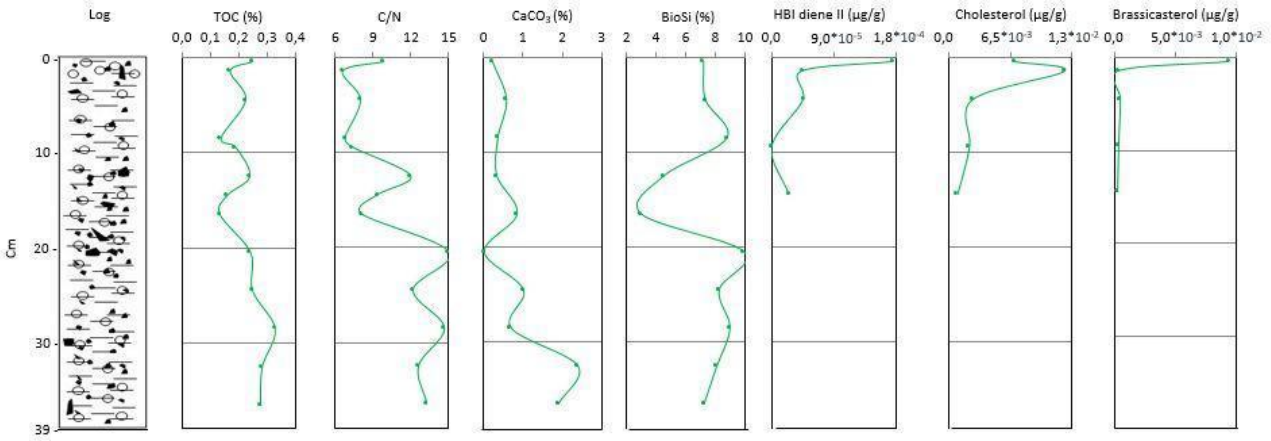

Figure S42 Organic matter and biomarkers parameters of the box core BC3.

BC3	TOC (%)	TN (%)	C/N	$CaCO_3$	SiBio
0-1	0,25	0,03	9,86	0,21	7,20
1-2	0,17	0,03	6,61	-	-
4-5	0,23	0,03	8,01	0,57	7,32
8-9	0,14	0,02	6,79	0,35	8,77
9-10	0,19	0,03	7,39	-	-
12-13	0,24	0,02	11,96	0,32	4,54
14-15	0,16	0,02	9,33	-	-
16-17	0,13	0,02	8,10	0,84	2,99
20-21	0,24	0,02	14,99	0,00	9,93
24-25	0,25	0,02	12,15	1,00	8,25
28-29	0,33	0,03	14,62	0,69	8,97
32-33	0,28	0,03	12,58	2,39	8,09
36-37	0,28	0,02	13,25	1,89	7,23

Table S57 Organic matter parameters of the box core RS14-BC3.

BC3	$IPSO_{25}$ (µg/g dry sedim.)	22-dehydrocholesterol (µg/g dry sedim.)	Cholesterol (µg/g dry sedim.)	Brassicasterol (µg/g dry sedim.)
0-1	$4,34*10^{-5}$	$2,71*10^{-3}$	$6,96*10^{-3}$	$9,38*10^{-3}$
1-2	$4,54*10^{-5}$	-	$1,23*10^{-2}$	$2,73*10^{-4}$
4-5	0	-	$2,47*10^{-3}$	$4,35*10^{-4}$
9-10	$2,49*10^{-5}$	-	$2,14*10^{-3}$	$2,93*10^{-4}$
14-15	$2,55*10^{-5}$	-	$8,73*10^{-4}$	$2,02*10^{-4}$

Table S58 Biomarkers of the box core RS14-BC3. 22-dehydrocholesterol was not measurable in four samples.

RS14-BC2

This box core has been collected in the middle continental slope (tab. 3, figs. 6 and 10).

Core description and Radiography

This box core (35 cm long) (fig. S43) is made of light olive brown (2,5Y 5/3) muddy sediment with sparse clasts from the bottom to 21 cm. The radiography highlights the presence of laminations in this layer. A sharp contact divides the lower part of the core from a sandy mud interval. The colour changes to dark yellowish brown (10YR 3/4) (21-15 cm) to dark brown (10YR 3/3) (15-11 cm). Millimetric and centimetric clasts are abundant. The upper part of the core is made of hydrated sandy mud. Millimetric and centimetric clasts are present, but more abundant in the upper part of

the core. Pluri-centimetric clasts are present in the upper 4 cm. The colour of the upper part of the core is olive brown (2,5Y 4/4). Clasts are mainly sub-angular.

Clasts counting (tab. S59, fig. S43) shows an increase of clasts presence between 17 and 10 cm. Number of clasts decreases in the upper part, but it shows a slightly increasing trend.

Depth (cm)	Clasts >2mm (num.)	Mobile average
0-1	7	3,8
1-2	4	2,8
2-3	1	3,2
3-4	5	3,6
4-5	2	2,6
5-6	2	2,4
6-7	6	2,2
7-8	3	1,8
8-9	0	1,8
9-10	1	2,8
10-11	1	5,4
11-12	4	7,2
12-13	3	7,6
13-14	5	7,8
14-15	14	7,0
15-16	10	4,4
16-17	6	2,4
17-18	4	1,4
18-19	1	0,6
19-20	1	0,4
20-21	0	0,2
21-22	1	0,2
22-23	0	0,0
23-24	0	0,0
24-25	0	0,2
25-26	0	0,2
26-27	0	0,2
27-28	0	0,2
28-29	1	0,2
29-30	0	0,0
30-31	0	0,0
31-32	0	0,0
32-33	0	0,0
33-34	0	0,0
34-35	0	0,0

Table S59 Clasts >2 mm counted using the method of Grobe (1987) and mobile average (interval of 5 cm) of the box core RS14-BC2.

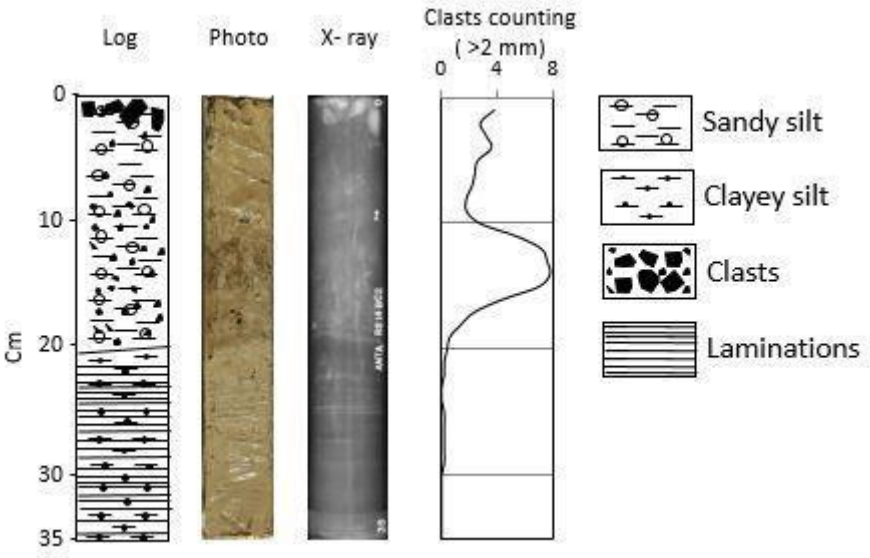

Figure S43 Lithologic log, photo, radiography clasts counted using the Grobe (1987) method (mobile average interval: 5 cm) of the box core BC2.

Physical analyses - Magnetic susceptibility, Water content, Grain size

This core has an increasing trend of magnetic susceptibility (MS) (tab. S60, fig. S44) from the bottom ($61*10^6$) toward the top ($818*10^6$).

Depth (cm)	MS (10^{-6}SI)
0-1	818
2-3	696
4-5	450
6-7	360
8-9	358
10-11	393
12-13	426
14-15	447
16-17	401
18-19	328
20-21	303
22-23	319
24-25	304
26-27	278
28-29	241
30-31	199
32-33	148
34-35	61

Table S60 Magnetic susceptibility of the box core RS14-BC2.

Water content (w%) (tab. S61, fig. S44) has a decreasing trend from the bottom toward the top. W% has values higher than 40% between 35 cm and 20 cm (max: 46,4% at 33 cm), except for a drop to 35,9% at 25 cm. The upper part of the core has values between 30% and 40%. The min value has been measured at 16 cm: 30,9%.

Depth (cm)	W%
0-1	32,9
1-2	31,1
2-3	38,6
3-4	31,8
4-5	37,8
5-6	39,0
6-7	39,6
7-8	38,0
8-9	37,0
9-10	36,3
10-11	35,5
11-12	34,2
12-13	31,7
13-14	33,2
14-15	31,4
15-16	30,9
16-17	31,4
17-18	33,1
18-19	35,8
19-20	45,0
20-21	44,0
21-22	41,7
22-23	40,3
23-24	42,2
24-25	35,9
25-26	44,7
26-27	44,4
27-28	43,5
28-29	43,9
29-30	44,0
30-31	44,4
31-32	44,5
32-33	46,4
33-34	44,4
34-35	45,4

Table S61 Water content of the box core RS14-BC2.

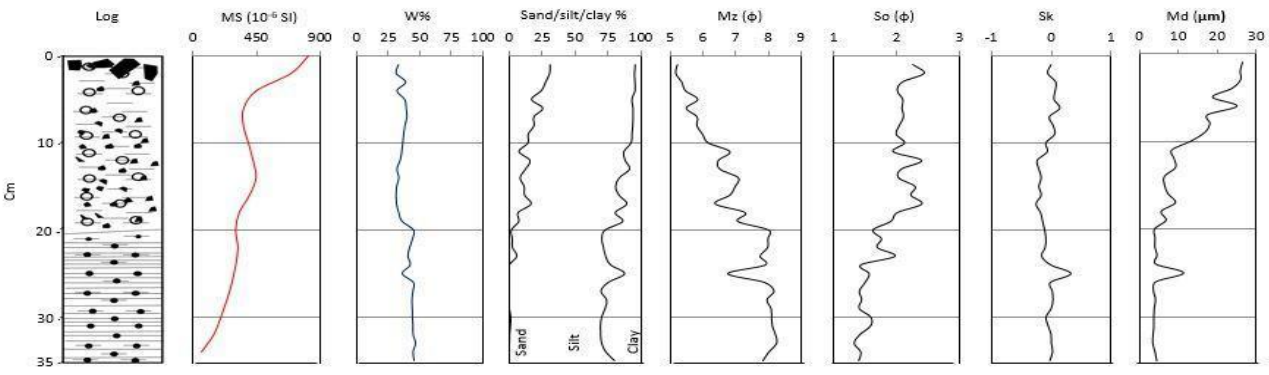

Figure S44 Physical parameters of the box core BC2.

The main sedimentary (tab. S62, fig. S44) component is silt (avg 72,5%). It ranges from 87,1% and 64,0%. The second component is clay (avg 17,5%), ranging from 30,7% to 4,6%. Sand (avg 9,9%) is present with a max of 31,1% and it is absent at 27-28 cm.

BC2	Sand (%)	Silt (%)	Clay (%)	Mz (φ)	So (φ)	Sk	Md (μm)	Primary mode (φ)
0-1	31,1	64,3	4,6	5,23	2,25	0,00	26,5	6,00
1-2	30,9	64,0	5,0	5,18	2,43	-0,06	25,9	6,50
2-3	27,8	67,4	4,8	5,36	2,09	0,07	26,0	4,50
3-4	24,6	70,7	4,7	5,48	2,01	0,07	23,8	4,50
4-5	17,3	75,7	7,0	5,85	2,10	0,05	18,8	5,00
5-6	25,7	68,2	6,1	5,50	2,08	0,14	25,1	4,50
6-7	19,0	74,9	6,1	5,83	2,11	-0,03	17,4	6,50
7-8	19,2	74,5	6,3	5,82	2,04	0,03	18,1	5,00
8-9	14,8	78,3	6,9	6,00	1,99	0,06	16,8	5,00
9-10	14,6	77,7	7,7	6,18	2,12	-0,09	13,2	7,00
10--11	7,9	79,1	13,1	6,83	1,94	-0,06	8,2	7,50
11--12	16,2	71,7	12,1	6,48	2,39	-0,23	8,8	7,50
12-13	12,8	78,5	8,8	6,53	2,07	-0,20	9,2	7,50
13-14	8,7	74,8	16,5	7,09	2,03	-0,17	6,3	8,00
14-15	11,8	69,0	19,2	6,99	2,29	-0,20	6,3	8,00
15-16	12,1	71,1	16,7	6,83	2,22	-0,17	7,3	8,00
16-17	16,9	72,2	10,9	6,38	2,40	-0,25	9,2	7,50
17-18	7,2	73,3	19,5	7,30	2,01	-0,18	5,5	8,00
18-19	7,8	78,3	13,9	7,07	1,91	-0,14	6,7	7,50
19-20	2,1	70,6	27,3	8,02	1,62	-0,11	3,8	8,50
20-21	2,8	67,5	29,6	7,99	1,76	-0,09	3,9	8,00
21-22	3,0	68,6	28,4	7,98	1,69	-0,10	3,8	8,50
22-23	6,3	66,9	26,8	7,75	1,97	-0,16	4,4	8,50
23-24	0,6	76,4	23,0	7,92	1,43	-0,01	4,1	8,50
24-25	0,3	87,1	12,5	6,77	1,57	0,33	11,3	6,50
25-26	0,1	75,2	24,7	7,88	1,50	-0,01	4,2	8,50
26-27	0,0	69,7	30,3	8,18	1,41	0,02	3,5	8,50
27-28	0,0	73,9	26,1	7,96	1,45	0,03	4,0	8,50
28-29	0,6	72,2	27,2	8,09	1,41	0,00	3,7	8,50
29-30	1,8	68,4	29,9	8,10	1,59	-0,09	3,6	8,50
30-31	1,5	67,8	30,7	8,12	1,59	-0,05	3,6	8,50
31-32	0,9	68,6	30,6	8,22	1,42	0,00	3,4	8,50
32-33	0,7	69,5	29,8	8,26	1,33	0,00	3,3	8,50
33-34	0,3	73,1	26,6	8,02	1,43	0,02	3,9	8,50
34-35	0,8	79,2	20,0	7,84	1,40	-0,02	4,3	8,00

Table S62 Grain size parameters of the box core RS14-BC2.

Mean diameter (Mz) (avg 7,00 ϕ, fine/very fine silt) is characterised by values between 5,18 ϕ (coarse silt) and 8,26 ϕ (clay) (tab. S62, fig. S44). Sediments are poorly sorted from the bottom to 19 cm. The upper part of the core is made of very poorly sorted sediments (avg 1,86 ϕ), with few levels of poorly sorted sediments (tab. S62, fig. S44). The average value of skewness (Sk) is -0,05. Sediment distribution (tab. S62, fig. S44) is symmetric from the bottom to 21 cm. The sample collected at 25 cm is characterised by a strong positive symmetry. Distribution curves are negative asymmetric, with intervals of symmetric distribution, from 21 to 12 cm. The upper part of the core

is characterised by a symmetric sediment distribution. Median diameter (Md) (tab. S62, fig. S44) shows an increasing up core trend, with a peak at 25 cm.

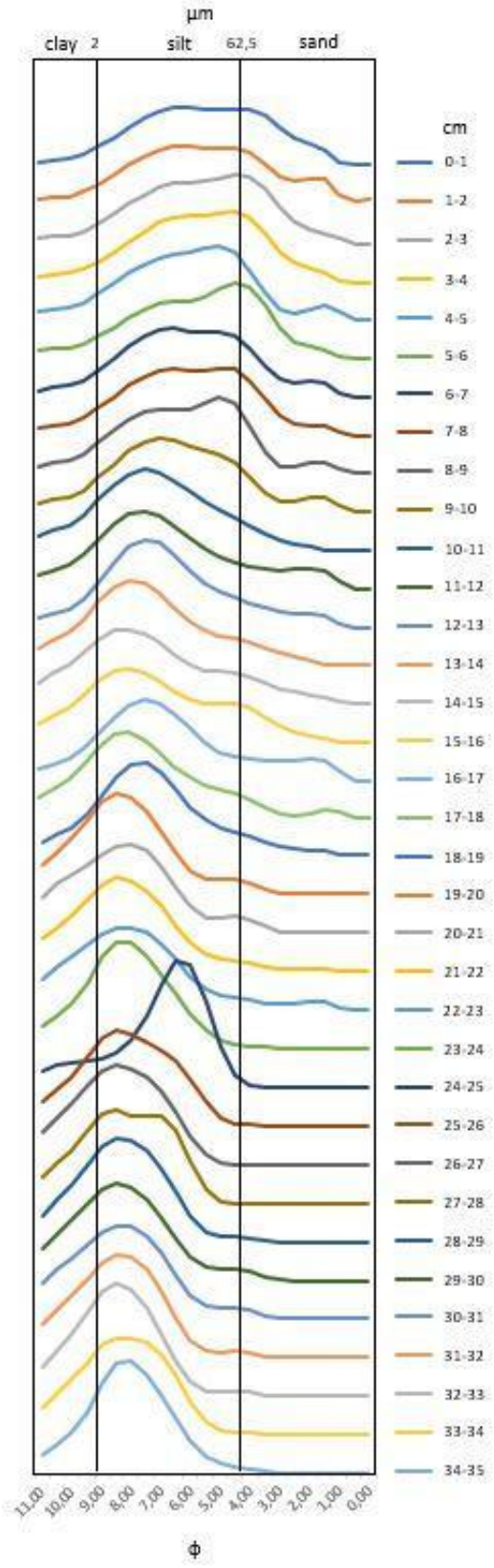

Figure S45 Grain size distribution curves of box core BC2.

Grain size distribution curves along the box core are reported in fig. S45. From the bottom to 19 cm, curves are mainly characterised by an unimodal distribution. The primary mode (tab. S56) is 8,5 - 8,0 ϕ (2,76 - 4,00 µm). Sample collected at 24-25 cm is an outlier (not included in the cluster analysis), with an unimodal distribution, a primary mode of 6,5 ϕ (11,05 µm). Samples collected between 19 to 11 cm are slightly coarser, with a primary mode between 8,0 and 7,5 ϕ (4,00 - 5,52 µm) and enrichments in coarse silt - sand. The upper 10 cm are coarser, with a primary mode that span between 7,0 and 4,5 ϕ (7,81 - 44,19 µm) and several samples are characterised by a bimodal distribution.

Chemical and Geochemical analyses - Elemental analyses, Organic matter and Biomarkers

In this core (tab. S63) there is a high correlation between Al, Si, K, Fe, Ti and Rb. Ba and Br correlate with Sr and Zr. Ba correlates weakly with Ca. There is also a weak correlation between Zr and K, Ti, Rb.

BC2	Al_cps	Si_cps	K_cps	Ca_cps	Ti_cps	Fe_cps	Br_cps	Rb_cps	Sr_cps	Zr_cps	Ba50_cps
Al_cps		2,22E-18	4,24E-14	0,013211	5,20E-08	5,68E-10	0,94102	4,61E-09	0,56588	0,1904	0,31846
Si_cps	**0,95453**		1,79E-15	9,34E-05	3,68E-09	1,26E-07	0,58869	1,83E-10	0,67264	0,009237	0,934
K_cps	**0,91424**	**0,93015**		0,00114	1,72E-10	1,55E-11	0,10422	2,23E-17	0,4905	0,002499	0,326
Ca_cps	0,42078	**0,61955**	*0,53411*		5,22E-06	0,050189	0,003213	0,000455	0,000378	4,25E-09	0,001997
Ti_cps	**0,78056**	**0,81731**	**0,85161**	**0,69445**		2,14E-11	0,011849	6,27E-08	0,29513	0,000616	0,1332
Fe_cps	**0,83913**	**0,7664**	**0,87364**	0,33853	**0,87089**		0,056212	2,03E-07	0,96287	0,14396	0,76633
Br_cps	-0,01318	0,096116	0,28349	0,49071	0,4267	0,33055		0,064402	1,84E-06	4,54E-06	5,08E-11
Rb_cps	**0,81445**	**0,85098**	**0,9473**	*0,56825*	**0,77766**	**0,75844**	0,32073		0,31582	0,000616	0,15924
Sr_cps	-0,10202	0,075173	0,12238	*0,57471*	0,18491	-0,00829	**0,71694**	0,17729		3,23E-06	5,22E-09
Zr_cps	0,23014	0,43987	*0,50178*	**0,81549**	*0,55739*	0,25597	**0,69756**	*0,55738*	**0,70506**		4,69E-09
Ba50_cps	-0,17634	0,014754	0,17366	*0,51134*	0,2628	0,05291	**0,86323**	0,24688	**0,81286**	**0,81426**	

Table S63 Elements correlation of the box core BC2. Bold and underlined values represent moderate to strong correlation. Underlined values in italics represent low correlation.

The representative element for the lithogenic fraction is Ti (cps). It increases from the bottom to 27 cm. Then, it shows a more constant trend before dropping in the upper 3 cm. Zr/Rb shows an increasing up-core trend, with values between 0,8 and 1,4 from the bottom to 4 cm, except for a small peak: 1,6 at 7 cm. Zr/Rb reaches 1,5 at 3 cm and increases toward the top. Si/Ti is characterised by fluctuations from the bottom up to 14 cm, with two peaks at 24 cm and 14 cm, and two drops at 27 cm and 21 cm. The upper part of the core shows a decreasing trend. Fe/Ti has a decreasing trend interrupted by a drop at 27 cm and by swinging values between 25 cm and 20 cm. K/Ti shows a

slightly increasing trend from the bottom of the core up to 17 cm, with a drop around 27 cm. Then, it decreases toward the top. Ba/Ti shows an increasing trend along the core and it reaches a peak at 2 cm. Then, it drops at the top of the core. Ca/Ti is characterised by an increasing trend along the core. Mn/Ti shows higher values between 15 and 10 cm and a peak at the top. Graphics are in fig. S46.

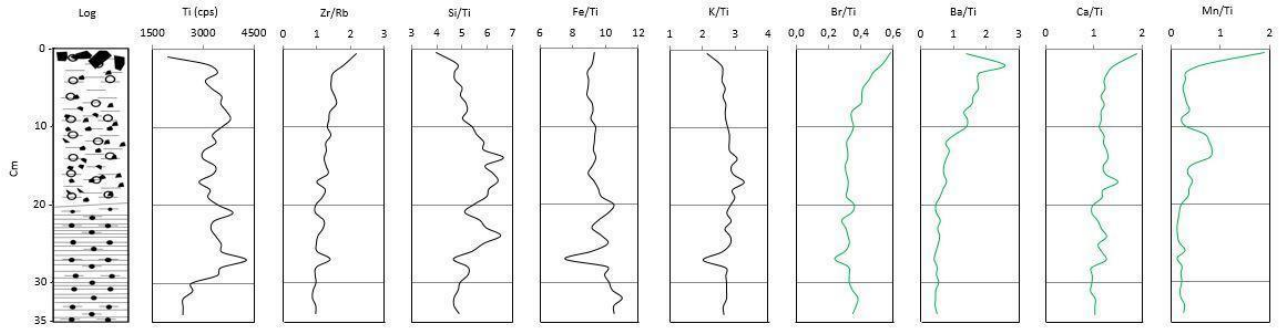

Figure S46 Elemental ratios of the box core BC2.

TOC (tab. S64, fig. S47) average value is 0,21%. It ranges between 0,12 and 0,36%. TOC decreases from the bottom to 15 cm. The upper 14 cm are characterised by an increasing trend.

C/N (avg 8,31) (tab. S64, fig. S47) has a decreasing trend from the bottom (max: 10,01 at 33 cm) to 11 cm (min: 6,71). C/N slightly increases in the upper part of the core.

$CaCO_3$ (tab. S64, fig. S47) shows very low values (avg 0,05%). The highest value is 0,12% (5 cm). Content of $CaCO_3$ was not measurable in some samples. Biogenic silica (tab. S64, fig. S47) has values fluctuating between 1,95 and 3,89% (avg 2,91%).

$IPSO_{25}$ (tab. S65, fig. S47) is present in this core but with a very low concentration, with a max value of $5,42*10^{-5}$ µg/g at 11 cm and a min value of $1,52*10^{-5}$ µg/g at 15 cm. The average value is $2,92*10^{-5}$ µg/g.

22-dehydrocholesterol has not been detected. Cholesterol (avg $2,01*10^{-3}$ µg/g) (tab. S65, fig. S47) shows a slightly decreasing up-core trend, with the highest value at 15 cm: $2,49*10^{-3}$ µg/g. The lowest value has been detected at 5 cm: $1,49*10^{-3}$ µg/g. Brassicasterol (avg$1,01*10^{-3}$ µg/g) (tab. S65, fig. S47) shows the highest value at 15 cm: $1,40*10^{-3}$ µg/g, and the lowest value at 10 cm: $6,86*10^{-4}$ µg/g.

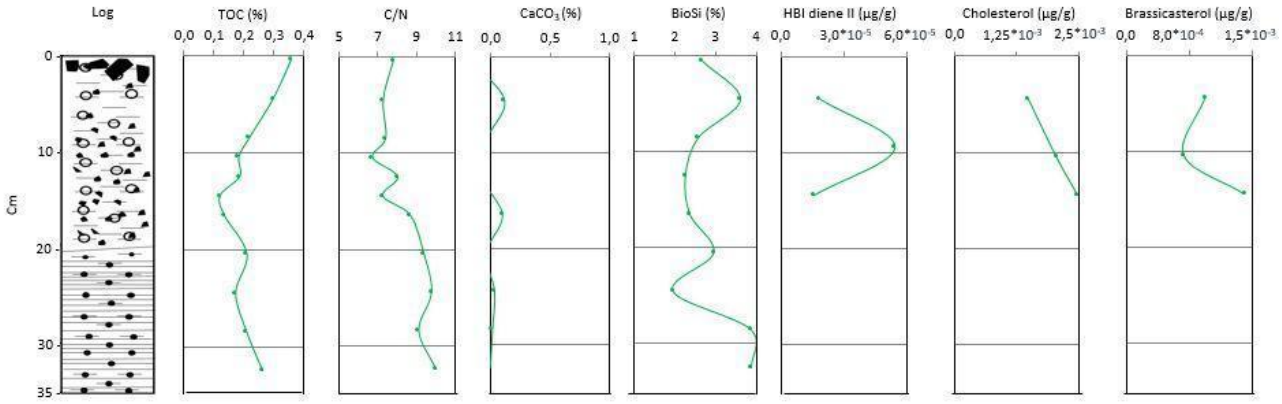

Figure S47 Organic matter and biomarkers parameters of the box core BC2.

BC2	TOC (%)	TN (%)	C/N	$CaCO_3$	SiBio
0-1	0,36	0,05	7,79	NM	2,68
4-5	0,30	0,05	7,27	0,12	3,62
8-9	0,22	0,03	7,40	NM	2,58
10-11	0,18	0,03	6,71	-	-
12-13	0,19	0,03	8,02	NM	2,26
14-15	0,12	0,02	7,24	-	-
16-17	0,13	0,02	8,67	0,10	2,37
20-21	0,21	0,03	9,38	NM	2,96
24-25	0,17	0,02	9,78	0,03	1,95
28-29	0,21	0,03	9,12	0,02	3,87
32-33	0,26	0,03	10,01	0,00	3,89

Table S64 Organic matter parameters of the box core RS14-BC2. NM = not measurable.

BC2	$IPSO_{25}$ (µg/g dry sedim.)	22-dehydrocholesterol (µg/g dry sedim.)	Cholesterol (µg/g dry sedim.)	Brassicasterol (µg/g dry sedim.)
4-5	$1,83*10^{-5}$	0	$1,49*10^{-3}$	$9,39*10^{-4}$
10-11	$5,42*10^{-5}$	0	$2,06*10^{-3}$	$6,86*10^{-4}$
14-15	$1,52*10^{-5}$	0	$2,49*10^{-3}$	$1,40*10^{-3}$

Table S65 Biomarkers of the box core RS14-BC2.

RS14-BC1

This box core has been collected in the lower continental slope (tab. 3, figs. 6 and 10).

Core description and Radiography

The lower part (42-28 cm) of this box core (length: 42 cm) is made of olive brown (2,5Y 4/3) muddy sediments with millimetric clasts. The colour is olive brown (2,5Y 4/3) from 42 to 35/34 cm and dark greyish brown (10YR 4/2) from 35/34 to 28 cm. Sandy material is more abundant between 40 and 38 cm. Oblique laminations characterise these muddy sediments. In the upper part of the core, Sediments are muddy. The sandy component is more present in the upper 9 cm. The colour of these sediments changes toward the top: olive (5Y 4/3) from 28 to 13 cm, olive brown (2,5Y 4/4) from 13 cm to the top of the core. Dark greyish brown (10YR 4/2) are present. The interval from 28 to 13 cm is characterised by weak laminations and by the presence of sparse millimetric to pluri-centimetric clasts. The upper 9 cm are characterised by sparse millimetric clasts, with centimetric and pluri-centimetric clasts in the upper 2 cm. Clasts of this core are mainly sub-rounded. Log, photo and radiographic image in the fig. S48.

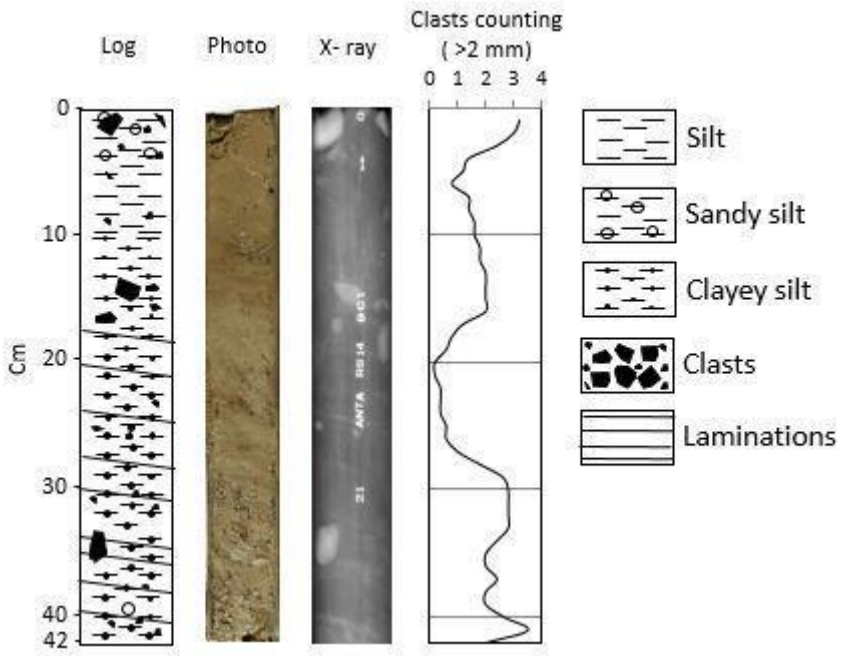

Figure S48 Lithologic log, photo, radiography and clasts counted using the Grobe (1987) method (mobile average interval: 5 cm) of the box core BC1.

Clasts counting (tab. S66, fig. S48) highlighted a higher number of clasts from the bottom to 29 cm, followed by an interval with a reduced presence. Number of clasts increases again from 16 cm, and in particular in the upper 4 cm.

Depth (cm)	Clasts >2mm (num.)	Mobile average
0-1	2	3,2
1-2	4	3,0
2-3	5	2,4
3-4	3	1,4
4-5	2	1,2
5-6	1	0,8
6-7	1	1,4
7-8	0	1,4
8-9	2	1,6
9-10	0	1,6
10-11	4	1,8
11-12	1	1,8
12-13	1	2,0
13-14	2	2,0
14-15	1	2,0
15-16	4	2,0
16-17	2	1,2
17-18	1	0,8
18-19	2	0,6
19-20	1	0,2
20-21	0	0,2
21-22	0	0,4
22-23	0	0,4
23-24	0	0,4
24-25	1	0,6
25-26	1	0,6
26-27	0	1,0
27-28	0	1,8
28-29	1	2,6
29-30	1	2,8
30-31	3	2,8
31-32	4	2,8
32-33	4	2,8
33-34	2	2,4
34-35	1	2,0
35-36	3	2,0
36-37	4	2,4
37-38	2	2,0
38-39	0	2,0
39-40	1	2,7
40-41	5	3,5
41-42	2	2,0

Table S66 Clasts >2 mm counted using the method of Grobe (1987) and mobile average (interval of 5 cm) of the box core RS14-BC1.

Physical analyses - Magnetic susceptibility, Water content, Grain size

Magnetic susceptibility (MS) (tab. S67, fig. S49) is low at the bottom ($78*10^6$ SI) and rapidly increases up core, reaching the highest value ($453*10^6$ SI) at 36 cm. The interval from 36 to 28 cm is characterised by high MS values. Then, it shows a decreasing trend from 28 to 12 cm. MS is slightly higher in the upper 10 cm.

Water content (w%) (tab. S68, fig. S49) is characterised by a slightly increasing up core trend. W% ranges between 29 and 50%, except for a sample collected at 2 cm: 14,0%.

Grain size analysis (tab. S69, fig. S49) has identified silt as the main sedimentary component (avg 71,5%, max 85,0%, min 59,6%). Clay has an average value of 20,1%, with a max of 29,9% and a min of 6,1%. Sand (avg 8,5%) varies between 27,9% and 0,2%.

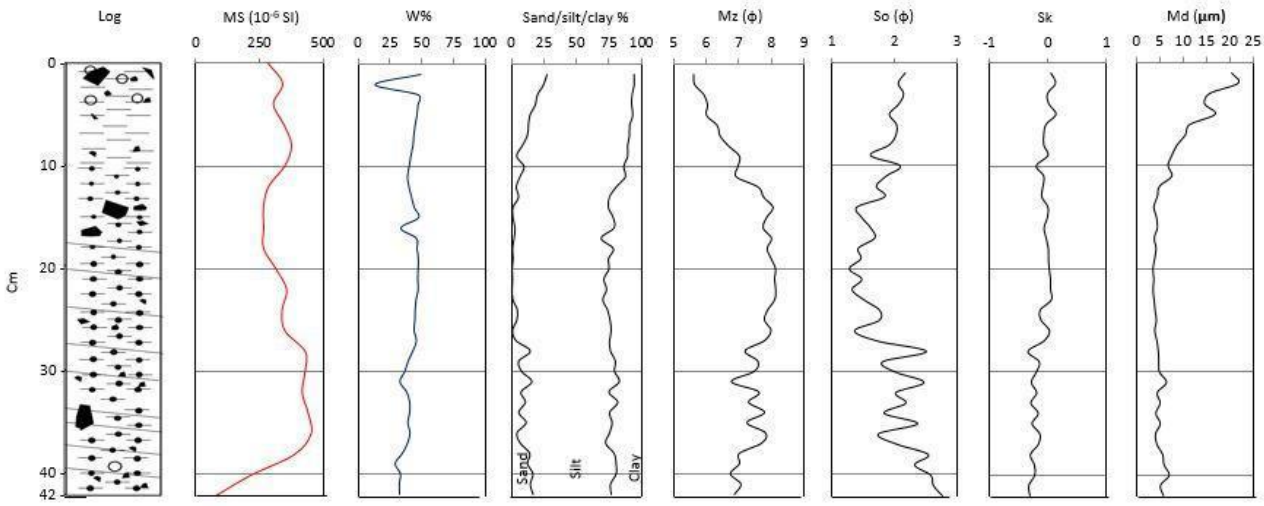

Figure S49 Physical parameters of the box core BC1.

Depth (cm)	MS (10^{-6}SI)
0-1	282
2-3	341
4-5	305
6-7	346
8-9	376
10-11	350
12-13	286
14-15	266
16-17	267
18-19	266
20-21	315
22-23	357
24-25	339
26-27	350
28-29	430
30-31	429
32-33	418
34-35	442
36-37	453
38-39	387
40-41	217
41-42	78

Table S67 Magnetic susceptibility of the box core RS14-BC1.

Depth (cm)	W%
0-1	49,7
1-2	14,0
2-3	47,6
3-4	47,4
4-5	46,6
5-6	45,1
6-7	44,1
7-8	43,5
8-9	41,7
9-10	40,5
10-11	39,2
11-12	40,4
12-13	42,4
13-14	44,5
14-15	47,8
15-16	33,9
16-17	46,2
17-18	46,7
18-19	47,6
19-20	47,5
20-21	47,2
21-22	47,5
22-23	45,9
23-24	45,2
24-25	45,0
25-26	44,3
26-27	46,2
27-28	43,4
28-29	39,7
29-30	37,2
30-31	33,3
31-32	38,6
32-33	40,9
33-34	41,0
34-35	39,5
35-36	41,2
36-37	39,3
37-38	35,2
38-39	29,6
39-40	33,8
40-41	32,7
41-42	33,1

Table S68 Water content of the box core RS14-BC1.

Values between 5,64 ϕ (coarse silt) and 8,14 ϕ (clay) represent the mean diameter (Mz) (tab. S69). The average value is 7.3 ϕ (very fine silt). Sediments are very poorly sorted from the bottom to 28 cm, poorly sorted from 28 to 2 cm and the upper 2 cm are very poorly sorted (tab. S69). The average value of sorting is 1,92 ϕ. Distribution curves are negative asymmetric, with few symmetric samples, from the bottom to 24 cm. In the upper part of the core, distribution curves are symmetric, with few positive asymmetric intervals toward the top. Skewness (Sk) (tab. S69) has an average value of -0,11. A constant trend characterised the median diameter (Md) from the bottom to 13 cm. Md increases in the upper part of the core. See tab. S69 and fig. S49.

BC1	Sand (%)	Silt (%)	Clay (%)	Mz (φ)	So (φ)	Sk	Md (µm)	Primary mode (φ)
0-1	27,9	65,8	6,3	5,61	2,17	0,04	20,5	4,00
1-2	25,3	68,6	6,1	5,64	2,06	0,12	21,9	4,00
2-3	20,4	71,8	7,7	5,93	2,14	-0,02	15,7	7,00
3-4	18,6	73,4	8,0	6,04	2,07	0,00	14,7	7,00
4-5	14,4	78,4	7,3	6,01	1,92	0,12	17,0	4,50
5-6	13,2	77,2	9,6	6,34	2,03	-0,04	11,5	7,50
6-7	12,3	77,9	9,7	6,43	2,02	-0,08	10,5	7,50
7-8	8,1	80,7	11,2	6,69	1,91	-0,08	8,7	7,50
8-9	3,9	85,0	11,1	7,03	1,62	-0,01	7,6	7,50
9-10	9,7	76,3	14,0	6,98	2,09	-0,20	6,8	7,50
10--11	6,5	80,7	12,9	6,93	1,87	-0,08	7,6	7,50
11--12	3,6	76,6	19,8	7,60	1,71	-0,09	5,0	8,00
12-13	5,4	69,7	24,9	7,77	1,84	-0,11	4,5	8,00
13-14	0,9	73,4	25,7	8,06	1,40	-0,01	3,8	8,50
14-15	0,9	77,1	22,0	7,86	1,48	-0,02	4,3	8,00
15-16	2,6	76,0	21,5	7,76	1,62	-0,07	4,5	8,00
16-17	1,9	67,0	31,2	8,01	1,68	-0,04	3,9	8,50
17-18	0,5	77,5	21,9	7,88	1,42	0,00	4,2	8,00
18-19	1,0	73,4	25,6	8,01	1,46	0,00	4,0	8,50
19-20	0,3	74,5	25,3	8,14	1,28	0,01	3,6	8,00
20-21	0,6	70,3	29,1	8,11	1,48	0,03	3,8	8,00
21-22	0,2	72,8	27,0	8,14	1,32	0,03	3,6	8,50
22-23	0,8	69,3	29,9	8,11	1,51	0,05	3,8	8,00
23-24	4,5	69,2	26,3	7,90	1,76	-0,14	4,0	8,50
24-25	4,0	71,6	24,4	7,80	1,75	-0,12	4,3	8,00
25-26	0,5	76,0	23,5	8,00	1,36	0,02	3,9	8,00
26-27	3,4	71,8	24,8	7,79	1,73	-0,08	4,4	8,00
27-28	14,7	61,2	24,1	7,20	2,50	-0,34	4,7	8,50
28-29	5,5	74,1	20,4	7,59	1,81	-0,15	4,8	8,00
29-30	7,9	71,1	21,0	7,48	2,01	-0,20	5,0	8,00
30-31	15,9	66,7	17,4	6,77	2,47	-0,29	6,5	8,00
31-32	7,3	67,4	25,2	7,63	2,02	-0,20	4,5	8,50
32-33	10,8	70,6	18,6	7,31	2,18	-0,29	5,1	8,00
33-34	5,5	69,8	24,7	7,80	1,83	-0,17	4,2	8,50
34-35	11,4	65,8	22,8	7,25	2,36	-0,27	5,1	8,50
35-36	4,1	71,1	24,8	7,83	1,74	-0,14	4,1	8,50
36-37	6,7	65,5	27,8	7,71	2,04	-0,17	4,4	8,50
37-38	14,3	64,3	21,3	7,02	2,54	-0,30	5,7	8,50
38-39	12,5	67,7	19,8	7,02	2,32	-0,24	6,0	8,50
39-40	16,8	63,4	19,8	6,75	2,57	-0,23	7,1	8,00
40-41	14,7	61,2	24,1	7,07	2,62	-0,33	5,2	8,50
41-42	16,9	59,6	23,5	6,87	2,76	-0,31	5,9	8,00

Table S69 Grain size parameters of the box core RS14-BC1.

Considering the grain size distribution curves (fig. 50), the lower part of the core, from the bottom to 12 cm is characterised by a primary mode between 8,5 and 8,0 ϕ (2,76 - 4,00 µm). This section shows curves with an unimodal distribution, and some of them are characterised by sand enrichments. A primary mode (tab. S62) of 7,5 ϕ (5,52 µm) and an unimodal distribution

characterise the interval between 11 and 8 cm. Curves of the upper part of the cores are characterised by a bimodal distribution. Both the primary mode and the secondary mode span between 7,5 and 4,0 ϕ (5,52 - 62,50 µm).

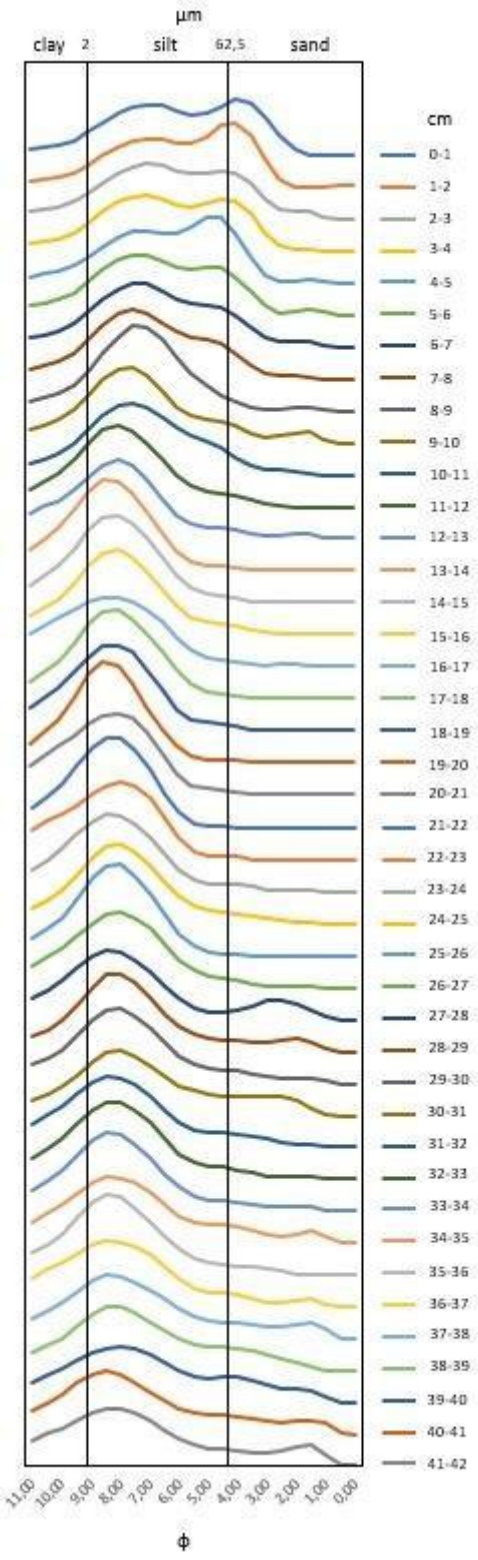

Figure S50 Grain size distribution curves of box core BC1.

Chemical and Geochemical analyses - Elemental analyses, Organic matter and Biomarkers

This core is different from BC3 and BC2 (tab. S70). There is a good correlation between Si, K, Fe and Rb. K and Fe also correlate with Ti. Si is anti-correlated with Ba. Ca, Sr and Ba show a good correlation. Ca and Sr are also correlated with Zr. Ba is anti-correlated with Si and Rb. Br is anti-correlated with Sr and Zr.

BC1	Si_cps	K_cps	Ca_cps	Ti_cps	Fe_cps	Br_cps	Rb_cps	Sr_cps	Zr_cps	Ba50_cps
Si_cps		3,19E-14	0,15182	0,01116	1,62E-07	0,040205	2,67E-10	0,004184	0,069341	1,34E-05
K_cps	**0,88063**		0,53698	2,92E-08	1,16E-11	0,002998	1,09E-08	0,010761	0,14114	0,075769
Ca_cps	-0,22791	-0,09925		0,079567	0,19706	0,009657	0,024205	1,35E-10	6,45E-07	9,71E-05
Ti_cps	0,39241	**0,74155**	0,27698		5,95E-05	0,007902	0,034979	0,98162	0,71656	0,013566
Fe_cps	**0,71372**	**0,83486**	-0,20566	*0,58474*		0,008068	1,13E-09	0,041054	0,35782	0,015304
Br_cps	0,32179	0,45217	-0,39953	0,40915	0,40817		0,041757	9,94E-06	2,94E-07	0,34953
Rb_cps	**0,80301**	**0,75613**	-0,35155	0,33022	**0,78608**	0,31945		0,005034	0,29217	8,64E-05
Sr_cps	-0,43798	-0,39422	**0,81047**	-0,00371	-0,3205	**-0,63052**	-0,42984		1,96E-14	0,000601
Zr_cps	-0,28652	-0,23385	**0,68867**	0,058461	-0,14738	**-0,70322**	-0,16854	**0,88375**		0,007102
Ba50_cps	**-0,62332**	-0,28041	*0,5709*	0,38256	-0,37634	-0,14991	*-0,57424*	*0,51318*	0,41416	

Table S70 Elements correlation of the box core BC1. Bold and underlined values represent moderate to strong correlation. Underlined values in italics represent low correlation.

Ti (cps) (lithogenic fraction representative element) is characterised by a constant trend with a little drop around 30 cm and a peak around 6 cm. A constant trend with some fluctuation of Zr/Rb characterises the bottom part of the core (12-42 cm). The upper part of the box core is characterised by greater fluctuations and higher values. Zr/Rb shows swinging values from the bottom to 28 cm, where it starts to decrease up to 21 cm. Then, Zr/Rb increases toward the top of the core. It has values around 1,5 between 17 cm and 13 cm. Si/Ti show a small peak at the bottom of the core. Next, it shows lower values with a constant trend from 39 cm to 29 cm. Then, both ratios increase and show a constant trend between 27 cm and 21 cm. The upper part of the core presents a decreasing trend. Fe/Ti values drop at 35 cm. Then, in the upper part of the core, Fe/Ti is characterised by a decreasing trend toward the top. K/Ti shows constant values pu-core and slightly decreases in the upper 8 cm. Ba/Ti shows a slightly decreasing trend from the bottom up to 14 cm. It increases toward the top in the upper part of the core. Ca/Ti is characterised by a decreasing trend from the bottom of the core up to 24 cm, but with a peak at 30-31 cm. The upper part of the core is characterised by an increasing trend. Mn/Ti is characterised by low values along the core. See fig. S51 for the graphics.

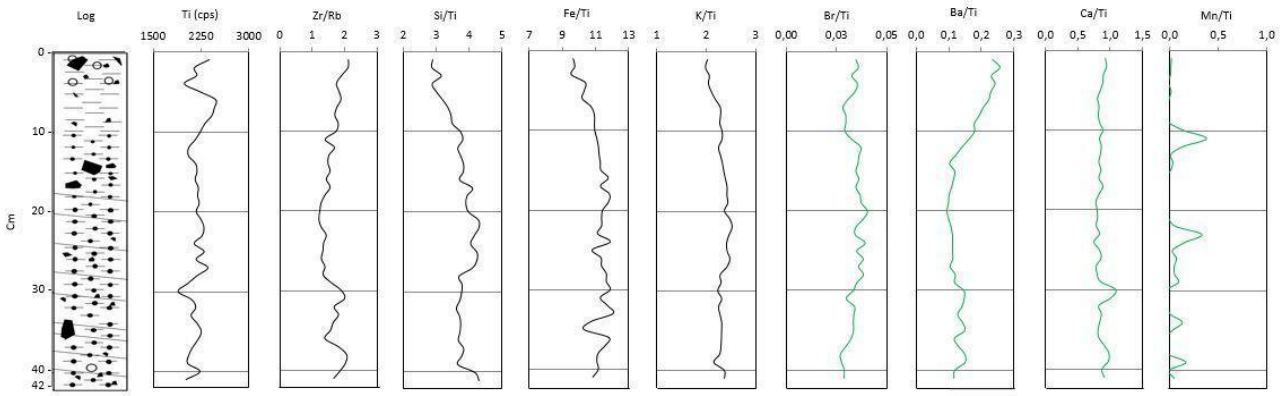

Figure S51 Elemental ratios of the box core BC1.

TOC (tab. S71, fig. S52) has a min value of 0,15% at 29 cm and a max value of 0,33% at the top of the core. The average value is 0,22%. TOC is characterised by an increasing trend from the bottom to 33 cm. It decreases, reaching the min value at 29 cm. Then, TOC shows an increasing up core trend.

C/N (tab. S71, fig. S52) has a decreasing trend along the core, with the highest value at 33 cm (11,66) and the lowest one at 4 cm (6,18). The average value is 8,05.

$CaCO_3$ was not measurable. Biogenic silica (tab. S71, fig. S52) is characterised by an increasing trend but with fluctuating values (max 6,30% at 21 cm; min 0,82% at 33 cm; avg 3,96%).

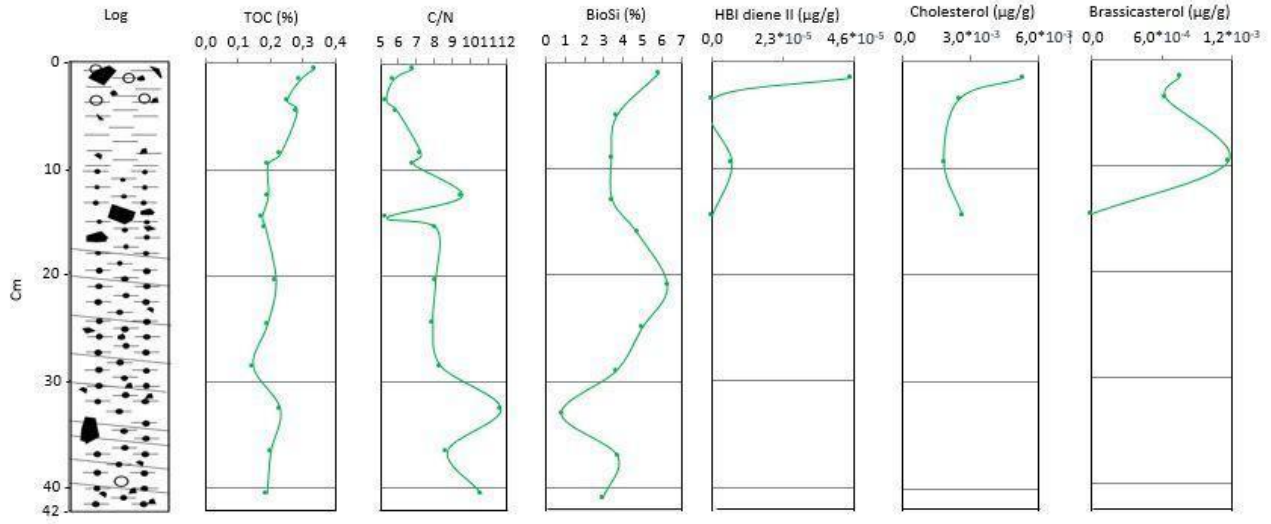

Figure S52 Organic matter and biomarkers parameters of the box core BC1.

$IPSO_{25}$ (tab. S72, fig. S52) has a very low concentration. The max value is $4{,}50*10^{-5}$ µg/g at 2 cm. HBI diene II has not been detected in two samples (15 and 5 cm).

22-dehydrocholesterol (tab. S72, fig. S52) has been only detected at the bottom of the core and that sample has a very low concentration ($3{,}16*10^{-5}$ µg/g). Both cholesterol and brassicasterol (tab. S72, fig. S52) have a very low concentration (avg $3{,}07*10^{-3}$ µg/g and $6{,}42*10^{-4}$ µg/g respectively). Cholesterol shows the highest value at 2 cm: $5{,}31*10^{-3}$ µg/g. Brassicasterol shows the highest value at 10 cm:$1{,}17*10^{-3}$ µg/g. It has not been detected at 15 cm.

BC1	TOC (%)	TN (%)	C/N	SiBio
0-1	0,33	0,06	6,79	5,85
1-2	0,29	0,05	6,65	-
3-4	0,25	0,05	6,18	
4-5	0,28	0,05	6,90	3,68
8-9	0,23	0,04	7,23	3,41
9-10	0,19	0,03	7,97	-
12-13	0,19	0,02	9,51	3,47
14-15	0,17	0,03	6,21	-
15-16	0,18	0,03	8,08	4,74
20-21	0,22	0,03	8,03	6,30
24-25	0,19	0,03	7,88	4,98
28-29	0,15	0,02	8,33	3,65
32-33	0,23	0,02	11,66	0,82
36-37	0,20	0,03	8,69	3,73
40-41	0,19	0,02	10,60	2,96

Table S71 Organic matter parameters of the box core RS14-BC1.

BC1	$IPSO_{25}$ (µg/g dry sedim.)	22-dehydrocholesterol (µg/g dry sedim.)	Cholesterol (µg/g dry sedim.)	Brassicasterol (µg/g dry sedim.)
1-2	$4{,}50*10^{-5}$	-	$5{,}31*10^{-3}$	$7{,}59*10^{-4}$
3-4	0	-	$2{,}49*10^{-3}$	$6{,}35*10^{-4}$
9-10	$6{,}41*10^{-6}$	-	$1{,}82*10^{-3}$	$1{,}17*10^{-3}$
14-15	0	$3{,}16*10^{-5}$	$2{,}65*10^{-3}$	0

Table S72 Biomarkers of the box core RS14-BC1. 22-dehydrocholesterol was not measurable in three samples.

ANTA99-c20

This gravity core has been collected in the middle-lower continental slope (tab. 3, figs. 6 and 10). In order to correlate this core with the three box cores RS14, only the analyses performed in the upper 55 cm are considered (grain size, element ratio and organic matter).

Core description and Radiography

Total length of the core is 202 cm (fig. S53). The lower part of the core (202-169 cm) is made of muddy sediments, with colour changing from olive (2,5Y 4/3; 202-195 cm) to olive grey (2,5Y 4/2; 195-169 cm). The coarse fraction is present in this section but it decreases up core.

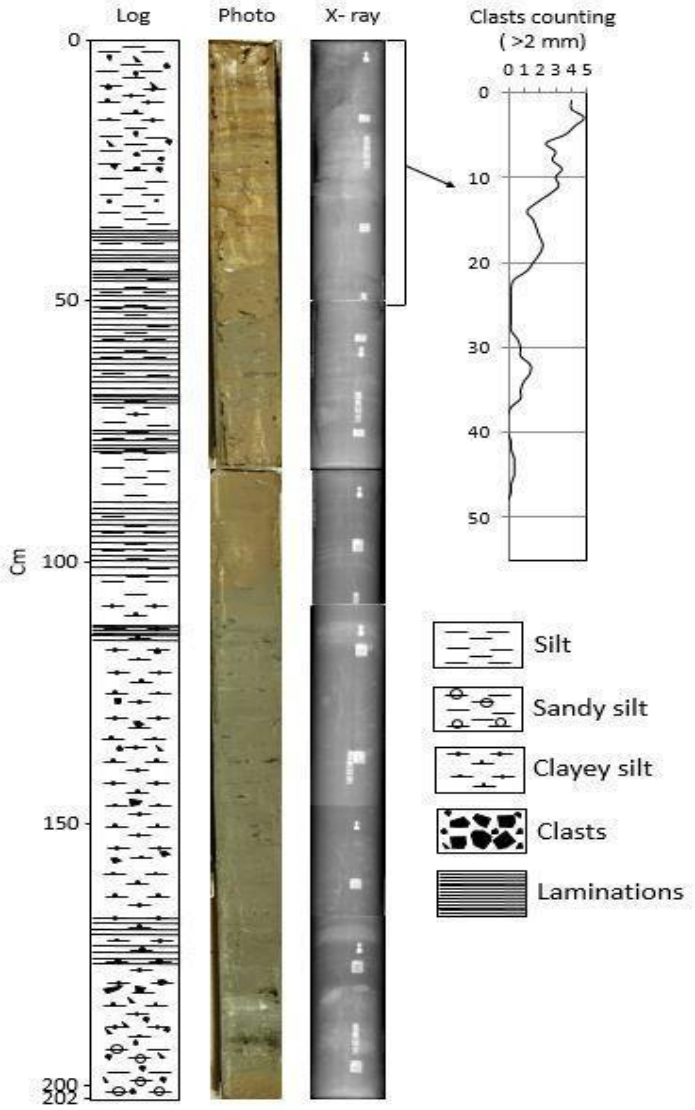

Figure S53 Lithologic log, photo, radiography and clasts counted using the Grobe (1987) method (mobile average interval: 5 cm) of the core c20.

Then, dark grey (2,5Y 4/1) sediments are present from 169 to 112 cm. These muddy sediments contain sandy and gravelly material that become sandier up core. There is a clayey layer at 115-113 cm. From 112 to 31 cm, dark grey (2,5Y 4/1) clayey mud is present with several oxidised olive (2,5Y 4/3) intervals. Weak laminations are visible in the radiography. The upper part of the core is made of laminated muddy sediments with levels characterised by a higher content of sandy/gravelly

material. Between 31 and 21 cm, muddy layers are light yellowish brown (2,5Y 6/3) while coarser levels are dark grey (5Y 4/1). In the upper 21 cm, muddy layers are olive brown (2,5Y 4/3), while coarser layers are dark olive brown (2,5Y 3/3). From 82 cm to the top of the core, muddy layers are characterised by dark olive brown (2,5Y 3/3) oxidised laminations. Weak laminations are visible in the radiography between 185 and 175 cm, 105 and 90 cm, 80 and 39 cm.

Clasts were counted using the method of Grobe (1987). The mobile average (interval of 5 cm) (tab. S73, fig. S53) shows an increasing trend toward the top of the core.

Depth (cm)	Clasts >2mm (num.)	Mobile average	Depth (cm)	Clasts >2mm (num.)	Mobile average	Depth (cm)	Clasts >2mm (num.)	Mobile average
0-1	3	4,0	**19-20**	2	1,6	**38-39**	0	0,0
1-2	2	4,0	**20-21**	4	1,2	**39-40**	0	0,0
2-3	4	4,8	**21-22**	2	0,4	**40-41**	0	0,2
3-4	5	4,2	**22-23**	0	0,2	**41-42**	0	0,2
4-5	6	3,6	**23-24**	0	0,2	**42-43**	0	0,4
5-6	3	2,4	**24-25**	0	0,2	**43-44**	0	0,4
6-7	6	3,0	**25-26**	0	0,2	**44-45**	1	0,4
7-8	1	2,8	**26-27**	1	0,2	**45-46**	0	0,2
8-9	2	3,4	**27-28**	0	0,2	**46-47**	1	0,2
9-10	0	3,0	**28-29**	0	0,6	**47-48**	0	0,0
10-11	6	3,2	**29-30**	0	0,8	**48-49**	0	0,0
11-12	5	2,6	**30-31**	0	0,8	**49-50**	0	0,0
12-13	4	1,8	**31-32**	1	1,4	**50-51**	0	0,0
13-14	0	1,2	**32-33**	2	1,4	**51-52**	0	0,0
14-15	1	1,6	**33-34**	1	1,0	**52-53**	0	0,0
15-16	3	1,8	**34-35**	0	0,8	**53-54**	0	0,0
16-17	1	2,0	**35-36**	3	0,8	**54-55**	0	0,0
17-18	1	2,2	**36-37**	1	0,2			
18-19	2	2,0	**37-38**	0	0,0			

Table S73 Clasts >2 mm counted using the method of Grobe (1987) and mobile average (interval of 5 cm) of the core ANTA99-c20.

Physical analyses - Magnetic susceptibility, Water content and Grain size

Magnetic susceptibility (tab. S74, fig. S54) shows values higher than $1000*10^{-6}$ SI from the bottom to 179 cm. There are two peaks of 2080 and $2150*10^{-6}$ in this interval. From 179 to 31 cm, MS is characterised by values fluctuating between 500 and $900*10^{-6}$ SI. There is a small peak of $1160*10^{-6}$ SI at 147 cm. MS increases from 29 to 21 cm, exceeding $1000*10^{-6}$ SI. This part of the core is characterised by a decreasing trend ($271*10^{-6}$ SI at the top).

An increasing trend, with fluctuating values, characterises the water content (w%) (tab. S75, fig. S54) from the bottom to 35 cm (89,2%). Then, w% drops reaching 42,8% at 15 cm. The upper part of the core shows values higher than 70%.

The main sedimentary component (tab. S76, fig. S54) is silt, with an average value of 79,3% (max 87,4%, min 69,8%). With an average value of 14,1%, clay ranges between 24,7% and 6,8%. Sand has an average value of 7,1% (max 14,0%). Sand is almost absent around 55 cm.

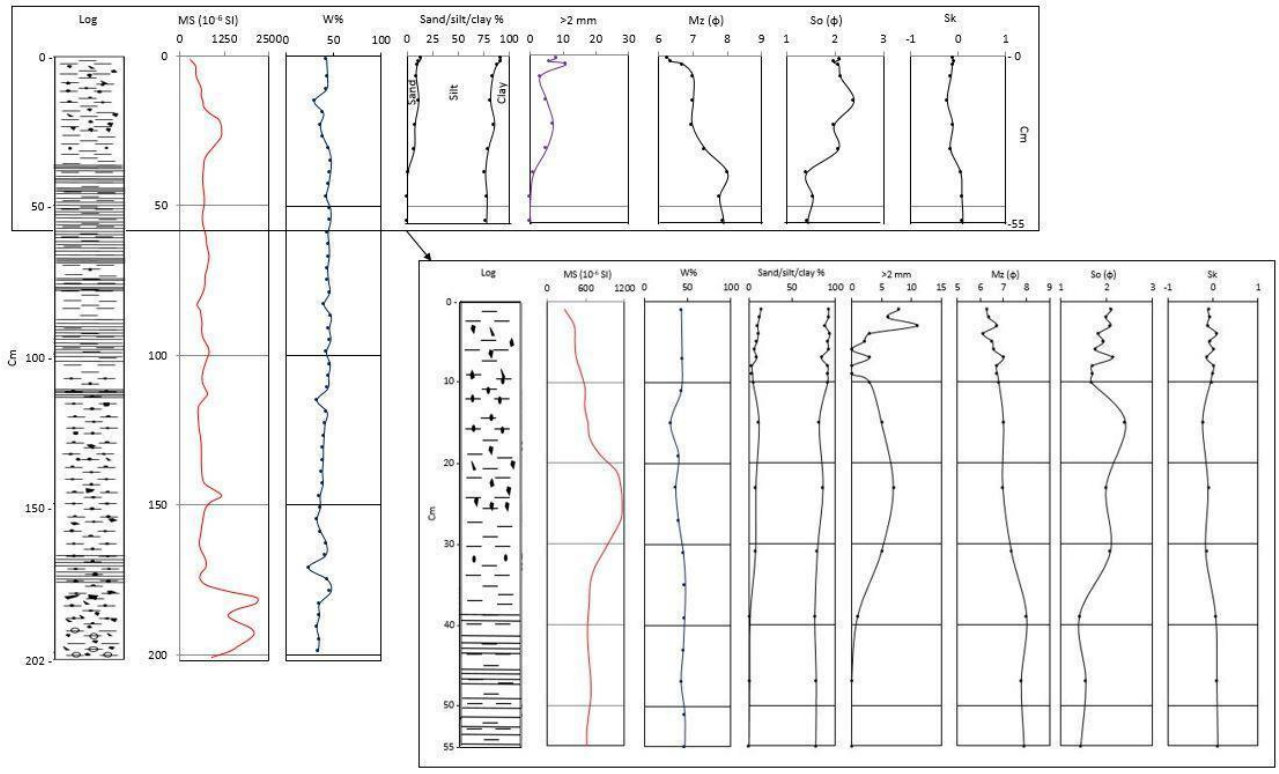

Figure S54 Physical parameters of the core c20. Grain size data have been considered only in the upper 55 cm.

The mean diameter (avg 6,93 ϕ; fine silt) (tab. S77, fig. S54) ranges between 6,13 ϕ (fine silt) and 8,01 ϕ (clay). Sediments are poorly sorted from 55 to 39 cm. Sediments are mainly poorly sorted with few very poorly sorted intervals. The average value of sorting (tab. S77, fig. S54) is 1,86 ϕ. Curves of sediment distribution are mainly symmetric, with few negative asymmetric samples. The average value of Skewness (tab. S77, fig. S54) is -0,05.

Grain size distribution (fig. S55) highlights a primary mode (tab. S68) around 7,50 ϕ with finer intervals (8,00 ϕ) between 55 and 15 cm. Samples are slightly coarser in the upper part of the core with a maximum of 5,00 ϕ at 4 cm. Grain size curves show a unimodal distribution in the deepest samples. In the upper part, curves are characterised by enrichments in the coarser fractions and reach a bimodal distribution in the upper part of the core.

Depth (cm)	MS (10^{-6}SI)
0-1	271
2-3	421
4-5	431
6-7	451
8-9	532
10-11	592
12-13	582
14-15	632
16-17	663
18-19	823
20-21	1073
22-23	1143
24-25	1163
26-27	1144
28-29	1014
30-31	874
32-33	734
34-35	665
36-37	655
38-39	635
40-41	625
42-43	636
44-45	656
46-47	676
48-49	676
50-51	646
52-53	617
54-55	617

Table S74 Magnetic susceptibility of the core ANTA99-c20.

Depth (cm)	W%
0-1	42,5
6-7	43,3
10-11	42,5
14-15	30,0
18-19	39,3
22-23	36,1
26-27	39,0
30-31	44,7
34-35	47,2
38-39	46,2
42-43	44,6
46-47	42,2
50-51	46,5
54-55	46,5

Table S75 Water content of the core ANTA99-c20.

c20	Sand (%)	Silt (%)	Clay (%)	Mz (φ)	So (φ)	Sk	Primary mode (φ)
0-1	14,0	77,9	8,1	6,27	2,11	-0,12	7,50
1-2	12,3	79,4	8,3	6,36	1,98	-0,09	7,00
2-3	10,3	77,9	12,4	6,71	2,09	-0,12	7,00
3-4	11,0	82,2	6,8	6,13	1,82	0,08	5,00
4-5	9,5	81,6	9,0	6,52	1,94	-0,09	7,50
5-6	6,0	85,4	8,6	6,58	1,75	0,00	7,50
6-7	9,3	74,7	16,9	7,01	2,12	-0,15	7,50
7-8	3,4	87,4	9,2	6,71	1,69	0,01	7,50
8-9	4,2	86,6	9,3	6,74	1,69	-0,02	7,50
9-10	4,6	86,4	9,0	6,80	1,67	-0,06	7,50
14-15	11,8	69,8	19,4	7,01	2,40	-0,23	8,00
22-23	8,1	77,6	14,9	6,98	1,98	-0,11	7,50
30-31	7,7	71,8	21,7	7,35	2,07	-0,16	8,00
38-39	1,2	75,3	24,7	8,01	1,41	0,06	8,00
46-47	0,6	77,6	23,2	7,78	1,55	0,08	7,50
54-55	0,0	77,6	23,6	7,90	1,44	0,10	8,00

Table S76 Grain size parameters of the core ANTA99-c20.

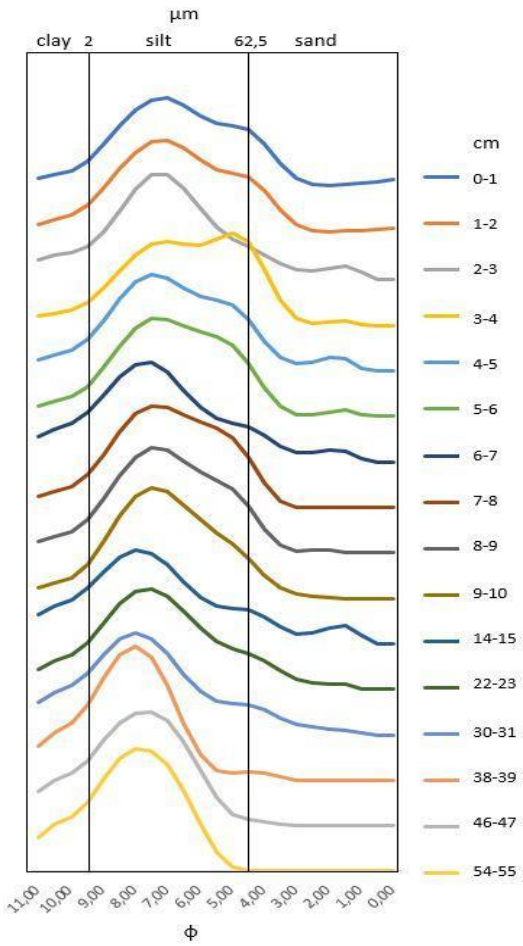

Figure S55 Grain size distribution curves of samples analysed in the upper 55 cm of gravity core c20.

Chemical and Geochemical analyses - Elemental analyses and Organic matter

Elemental analysis was not performed in the upper 10 cm because the core liner was partially empty. Elements (tab. S77) well correlated are Al, Si, K, Fe, Ti and Ca. Rb is correlated with K, Ti and Fe. Sr is highly correlated with Zr, Ca, and also with Si, K, Ti and Ba. Sr is anti-correlated with Br. Br is also anti-correlated with Zr, Sr, Ba and Ca.

c20	Al_cps	Si_cps	K_cps	Ca_cps	Ti_cps	Fe_cps	Br_cps	Rb_cps	Sr_cps	Zr_cps	Ba50_cps
Al_cps		4,97E-15	1,51E-13	7,67E-06	1,32E-14	5,04E-13	0,23451	0,003509	0,020165	0,26814	0,67553
Si_cps	**0,86893**		7,70E-28	1,53E-15	3,12E-21	3,75E-11	0,32022	0,000552	5,59E-06	0,000782	0,13819
K_cps	**0,84513**	**0,96727**		3,82E-13	3,36E-31	1,27E-14	0,62952	4,19E-05	2,73E-05	0,00289	0,034669
Ca_cps	**0,60719**	**0,8762**	**0,83787**		3,04E-11	2,11E-05	0,001494	0,001465	5,84E-15	6,44E-10	0,003821
Ti_cps	**0,86253**	**0,9336**	**0,97708**	**0,79826**		5,50E-19	0,73822	1,52E-05	0,000103	0,013356	0,068681
Fe_cps	**0,83564**	**0,79609**	**0,86279**	*0,58319*	**0,91527**		0,028373	4,70E-05	0,029799	0,36443	0,96693
Br_cps	0,17879	-0,14985	-0,07304	-0,45486	0,050638	0,32337		0,19832	8,48E-05	1,83E-07	0,005511
Rb_cps	0,42175	0,48968	*0,56569*	0,45559	*0,59118*	*0,56265*	0,19319		0,00132	0,008904	0,083373
Sr_cps	0,34157	**0,61432**	*0,57668*	**0,86789**	*0,54116*	0,32067	*-0,54663*	0,4594		8,34E-19	0,000311
Zr_cps	0,16671	0,47791	0,42957	**0,76417**	0,36228	0,13686	**-0,68176**	0,38146	**0,91358**		0,00105
Ba50_cps	-0,0634	0,22196	0,31219	0,41826	0,27083	0,006286	-0,40282	0,25805	*0,50823*	0,46764	

Table S77 Elements correlation of the upper 55 cm of the core c20. Bold and underlined values represent moderate to strong correlation. Underlined values in italics represent low correlation.

Ti (cps) is constant, except between 46 and 31 cm where it shows lower values. Zr/Rb is characterised by values between 1,4 and 1,6 from 55 to 29 cm. The upper part of the core is characterised by values fluctuating between 1,5 and 2,0. Si/Ti shows fluctuating values. Higher values characterise the upper part of the core. Fe/Ti and K/Ti show a constant trend. Br/Ti shows higher values from 55 to 34 cm than in the upper part. Ba/Ti has an increasing trend. Ca/Ti is characterised by a constant trend with slightly higher values between 34 and 10 cm. Mn/Ti is characterised by low and constant values from 55 to 47 cm. The upper part of the core is characterised by higher and fluctuating values. Graphics of elemental ratios are reported in fig. 56 and Ti (cps) is used to represent the lithogenic fraction.

TOC (tab. S78, fig. S57) ranges between 0,16 and 0,42%, with an average value of 0,26%. TOC is constant from 55 to 43 cm. The upper interval between 39 and 15 cm is characterised by lower values. The upper part of the core is characterised by an increasing trend, reaching 0,28% at the top of the core.

C/N (tab. S78, fig. S57) has an average value 9,23. This ratio is characterised by values higher than 10,00 between 55 and 43 cm. The upper 39 cm are characterised by values between 6,05 and 8,36.

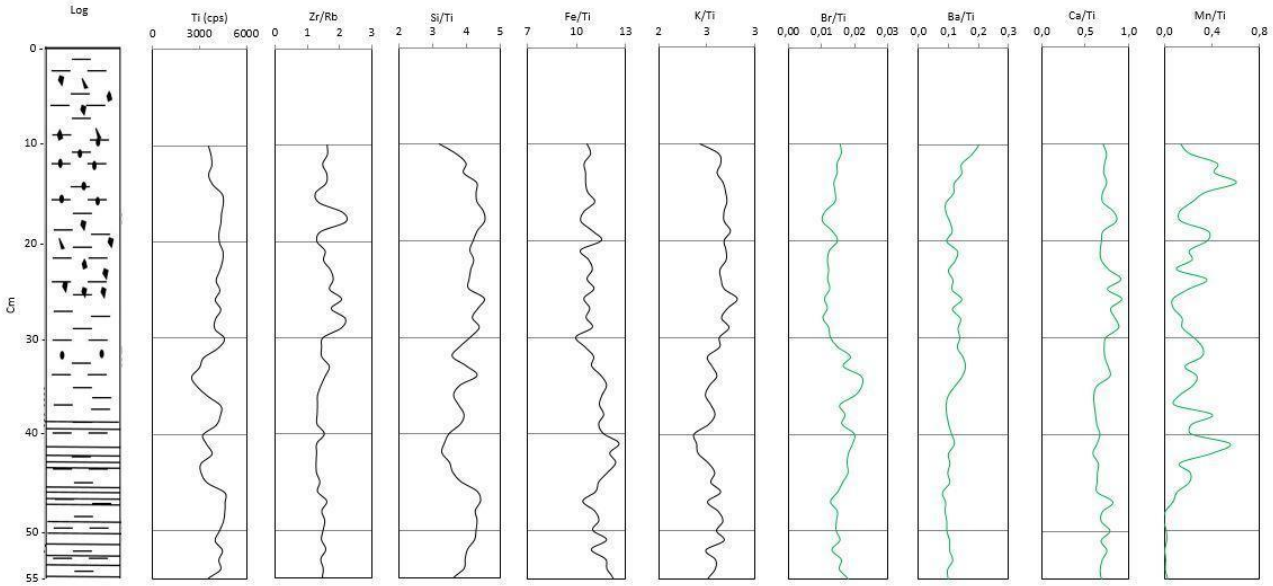

Figure S56 Elemental ratios of the upper 55 cm of the core c20.

$CaCO_3$ (tab. S78, fig. S57) was not measurable in the interval considered. Biogenic silica (tab. S78, fig. S57) is characterised by a slightly increasing trend from 55 to 10 cm. Then, it decreases toward the top of the core.

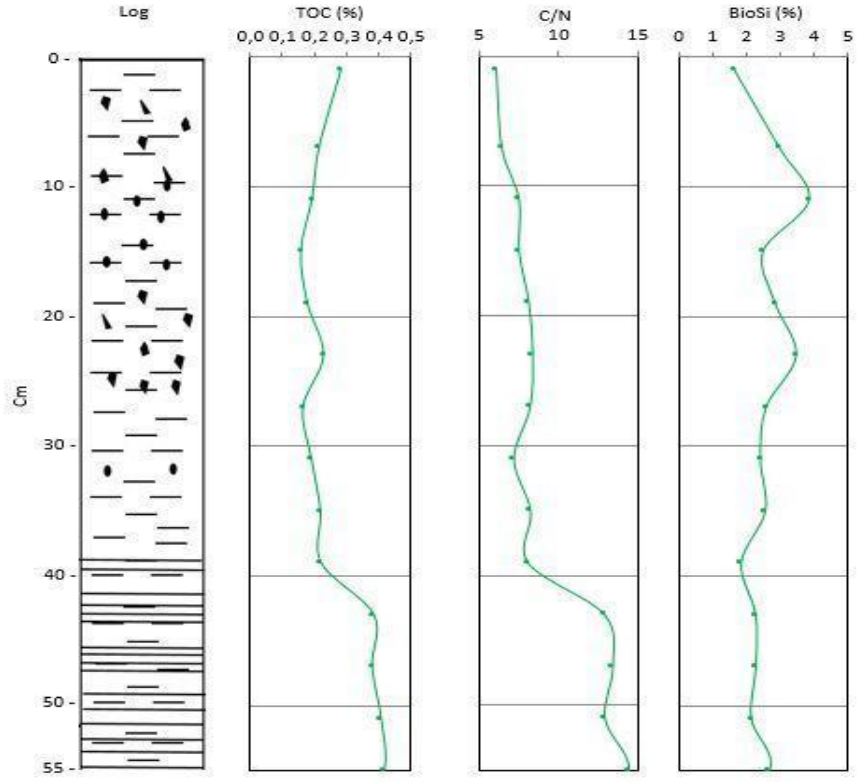

Figure S57 Organic matter and biomarkers parameters of the upper 55 cm of the core c20.

c20	TOC (%)	TN (%)	C/N	BioSi
0-1	0,28	0,05	6,05	1,64
6-7	0,21	0,04	6,40	2,97
10-11	0,19	0,03	7,49	3,85
14-15	0,16	0,02	7,49	2,49
18-19	0,18	0,03	8,12	2,85
22-23	0,23	0,03	8,36	3,47
26-27	0,17	0,02	8,18	2,58
30-31	0,19	0,03	7,17	2,41
34-35	0,22	0,03	8,22	2,56
38-39	0,22	0,03	8,07	1,85
42-43	0,38	0,03	12,90	2,27
46-47	0,38	0,03	13,41	2,28
50-51	0,41	0,04	12,92	2,14
54-55	0,42	0,03	14,43	2,67

Table S78 Organic matter parameters of the core ANTA99-c20.

References

Ackert, R., 2008. Swinging gate or Saloon doors: Do we need a new model of Ross Sea deglaciation? Fifteenth West Antarctic Ice Sheet Meeting, Sterling, Virginia 811;

Ainley D. & Jacobs S.S., 1981. Sea-bird affinities for ocean and ice boundaries in the Antarctic. Deep Sea Research Part A. Oceanographic Research Papers 28, pp. 1173–1185. https://doi.org/10.1016/0198-0149(81) 90054-6;

Alonso B., Anderson J.B., Diaz J.T., Bartek L.R., 1992. Pliocene-Pleistocene seismic stratigraphy of the Ross Sea: evidence for multiple ice sheet grounding episodes D.H. Elliot (Ed.), Contributions to Antarctic Research III, Antarctic Research Series 57, American Geophysical Union, Washington, D.C., pp. 93-103;

Anderson J.B., 1999. Antarctic Marine Geology. Cambridge University Press;

Anderson J.B. & Bartek L.R., 1992. Cenozoic glacial history of the Ross Sea revealed by intermediate resolution seismic reflection data combined with drill site information. In: Kennett J.P. (ed.), The Antarctic Paleoenvironment: A Perspective on Global Change: Part One. American Geophysical Union, Antarctic Research Series 56, pp. 231–263;

Anderson J.B., Kurtz D.D., Domack E.W., Balshaw K.M., 1980. Glacial and glacial marine sediments of the Antarctic continental shelf. The Journal of Geology 88, pp. 399-414;

Anderson J.B., Brake C.F., Myers N.C., 1984. Sedimentation on the Ross Sea continental shelf, Antarctica. Marine Geology 57, pp. 295-333;

Anderson J.B., Kennedy D.S., Smith M.J., Domack E.W., 1991. Sedimentary facies associated with Antarctica's floating ice masses. In: Anderson J.B., Ashley G.M. (Eds.), Glacial Marine Sedimentation; Paleoclimatic Significance 261, Geological Society of America Special Papers, pp. 1–25;

Anderson J.B., Conway H., Bart P.J., Witus A.E., Greenwood S.L., McKay R.M., Hall B.L., Ackert R.P., Licht K., Jakobsson M., Stone J.O., 2014. Ross Sea paleo-ice sheet drainage and deglacial history during and since the LGM. Quaternary Science Review 100, pp. 31-54;

Anderson J.B., Simkins L.M., Bart P.J., De Santis L., Halberstadt A.R.W., Olivo E., Greenwood S.L., 2019. Seismic and geomorphic records of Antarctic Ice Sheet evolution in the Ross Sea and controlling factors in its behaviour. In: Le Heron D.P., Hogan K.A., Phillips E.R., Huuse M., Busfield M.E. & Graham A.G.C. Eds., Glaciated Margins: The Sedimentary and Geophysical Archive. Geological Society, London, Special Publications 475, pp. 223-240;

Andrews J.T., Domack E.W., Cunningham W.L., Leventer A., Licht K.J., Jull A.J.T., De Master D.J., Jennings A.E., 1999. Problems and possible solutions concerning radiocarbon dating of surface marine sediments, Ross Sea, Antarctica. Quaternary Research 52, pp. 206-216;

Antarctic Seismic Data Library System (SDLS; https://sdls.ogs.trieste.it/cache/index.jsp);

Barrett P.J., 1975. Textural characteristics of Cenozoic preglacial and glacial sediments at Site 270, Ross Sea, Antarctica. In: HAYES D.E., FRAKES L.A. ET AL. (eds) Initial Reports of the Deep Sea Drilling Project, 28. US Government Printing Office, Washington, DC, pp.757–767;

Bart P.J., 2003. Were West Antarctic ice sheet grounding events in Ross Sea a consequence of East Antarctic ice sheet expansion during the middle Miocene? Earth and Planetary Science Letters 216, pp. 93–107;

Bart P.J., Anderson J.B., Trincardi F., Shipp S.S., 2000. Seismic data from the Northern basin, Ross Sea, record extreme expansions of the East Antarctic Ice Sheet during the late Neogene. Marine Geology 166, pp. 31–50;

Bart P.J. & Cone A.N., 2012. Early stall of West Antarctic Ice Sheet advance on the eastern Ross Sea middle shelf followed by retreat at 27,500 14 C yr BP. Palaeogeography, Palaeoclimatology, Palaeoecology 335-336, pp. 52-60;

Bart P.J. & Kratochvil M., 2022. A paleo-perspective on West Antarctic Ice Sheet retreat. Scientific Reports 12, 17693;

Bart P.J. & Owolana B., 2012. On the duration of West Antarctic Ice Sheet grounding events in the Ross Sea during the Quaternary. Quaternary Science Review 47, pp. 101-115;

Bart P.J., DeCesare M., Rosenheim B.E., Majewski W., McGlannan A., 2018. A centuries-long delay between a paleo-ice-shelf collapse and grounding-line retreat in the Whales Deep Basin, eastern Ross Sea, Antarctica. Scientific Reports 8, 12392;

Bartek L.R., Vail P.R., Anderson J.B., Emmet P.A., Wu S., 1992. The effect of Cenozoic Ice Sheet fluctuations on the stratigraphic signature of the Neogene. Journal Geophysical Research 96, pp. 6753–6778;

Bartek L.R., Henrys S.A., Anderson J.B., Barrett P.J., 1996. Seismic stratigraphy of McMurdo Sound, Antarctica: implications for glacially influenced early Cenozoic Eustatic Change? Marine Geology 130, pp. 79–98;

Belt S.T., 2018. Source-specific biomarkers as proxies for Arctic and Antarctic sea ice. Organic Geochemistry 125, pp. 277-298;

Belt S.T. & Müller J., 2013. The Arctic sea ice biomarker IP 25?: a review of current understanding , recommendations for future research and applications in palaeo sea ice reconstructions, Quaternary Science Review 79, pp. 9–25. https://doi.org/10.1016/j.quascirev.2012.12.001, 2013;

Belt S.T., Masse G., Rowland S.J., Poulin M., Michel C., Leblanc B., 2007. A novel chemical fossil of palaeo sea ice?: IP 25, Organic Geochemistry 38, pp. 16–27. https://doi.org/10.1016/j.orggeochem.2006.09.013;

Belt S.T., Brown T.A., Rodriguez A.N., Sanz P.C., Tonkin A., Ingle R., 2012. A reproducible method for the extraction, identification and quantification of the Arctic sea ice proxy IP_{25} from marine sediments. Analytical Methods 4, pp. 705-713;

Belt S.T., Smik L., Brown T.A., Kim J.H., Rowland S.J., Allen C.S., Gal J.K., Shin K.H., Lee J.I., Taylor K.W.R., 2016. Source identification and distribution reveals the potential of the geochemical Antarctic sea ice proxy IPSO25. Nature Communication 7, pp. 1–10. https://doi.org/10.1038/ncomms12655;

Belt S.T., Smik L., Köseoğlu D., Knies J., Husum K., 2019. A novel biomarker-based proxy for the spring phytoplankton bloom in Arctic and sub-arctic settings – HBI T_{25}. Earth and Planetary Science Letters 523, p. 115703;

Benn D.I. &Evans D.J.A., 2010. Glaciers and Glaciation. (second) Hodder Education, London, UK;

Bentley M.J., Cofaigh C.Ó., Anderson J.B., Conway H., Davies B., Graham A.G.C., Hillenbrand C.-D., Hodgson D.A., Jamieson S.S.R., Larter R.D, Mackintosh A., Smith J.A., Verleyen E., Ackert R.P., Bart P.J., Berg S., Brunstein D., Canals M., Colhoun E.A., Crosta X., Dickens W.A., Domack E., Dowdeswell J.A., Dunbar R., Ehrmann W., Evans J., Favier V., Fink D., Fogwill C.J., Glasser N.F., Gohl K., Golledge N.R., Goodwin I., Gore D.B., Greenwood S.L., Hall B.L., Hall K., Hedding D.W., Hein A.S., Hocking E.P., Jakobsson M., Johnson J.S., Jomelli V., Jones R.S., Klages J.P., Kristoffersen Y., Kuhn G., Leventer A., Licht K., Lilly K., Lindow J., Livingstone S.J., Massé G., McGlone M. S., McKay R. M., Melles M., Miura H., Mulvaney R., Nel W., Nitsche F.O., O'Brien P.E., Post A.L., Roberts S.J., Saunders K.M., Selkirk P.M., Simms A.R., Spiegel C., Stolldorf T.D., Sugden D.E., van der Putten N., Ommen T., Verfaillie D., Vyverman W., Wagner B., White D.A., Witus A.E., Zwartz D., 2014. A community-based geological reconstruction of Antarctic Ice Sheet deglaciation since the Last Glacial Maximum. Quaternary Science Review 100, pp. 1–9.;

Bertram R.A., Wilson D.J., van de Flierdt T., McKay R.M., Jimenez-Espejo F.J., Escutia C., Duke G., Taylor-Silva B., Riesselman C., 2018. Timescales and event sequences of middle to late Pliocene deglaciations in the Wilkes Subglacial Basin. Earth and Planetary Science Letters 494, pp. 109–116;

Brambati A., Melis R., Quaia T., Salvi G., 2002. Late Quaternary climatic changes in the Ross Sea area, Antarctica. Royal Society of New Zealand Bulletin 35, pp. 359-364;

Brancolini G., Cooper A.K., Coren F., 1995. Seismic facies and glacial history in the Western Ross Sea, Antarctica. In: Cooper A.K., Barker P.F. & Brancolini G. (eds) Geology and Seismic Stratigraphy of the Antarctic Margin. American Geophysical Union, Antarctic Research Series 68, pp. 209–233;

Brown T.A., Belt S.T., Tatarek A., Mundy C.J., 2014. Source identification of the Arctic sea ice proxy IP_{25} . Nature Communication 5, p. 4197;

Budillon G., Castagno P., Aliani S., Spezie G., Padman L., 2011. Thermohaline variability and Antarctic bottom water formation at the Ross Sea shelf break. Deep Sea Research Part I: Oceanographic Research Papers 58, pp. 1002–1018. https://doi.org/10.1016/j.dsr.2011.07.002;

Calligaris M., 2003. Strutture e tessiture di quattro carote prelevate nel Mare di Ross centrale, Antartide. Tesi di laurea, Università degli Studi di Trieste, A.A. 2001/2002;

Canfield D.E., Thamdrup B., Hansen J.W., 1993. The anaerobic degradation of organic matter in Danish coastal sediments: iron reduction, manganese reduction and sulfate reduction. Geochimica et Cosmochimica Acta 57, pp. 3867–3883;

Castagno P., Capozzi V., DiTullio G.R., Falco P., Fusco G., Rintoul S.R., Spezie G., Budillon G., 2019. Rebound of shelf water salinity in the Ross Sea. Nature Communication 10, 5441. https://doi.org/10.1038/s41467-019-13083-8;

Clark P.U., Dyke A.S., Shakum J.D., Carlson A.E., Clark J., Wohlfarth B., Mitrovica J.X., Hostetler S.W., McCabe A.M., 2009. The Last Glacial Maximum. Science 325, pp. 710-714;

Conte R., Rebesco M., De Santis L., Colleoni F., Bensi M., Bergamasco A., Kovacevic V., Gales J., Zgur F., Accettella D., De Steur L., Ursella L., Mckay R., Kim S., Lucchi R.G., IODP Expedition 374 Scientists, 2021. Bottom current control on sediment deposition between the Iselin Bank and the Hillary Canyon (Antarctica) since the late Miocene: an integrated seismic-oceanographic approach Deep Sea Research Part I: Oceanographic Research Papers 176, Article 103606;

Conway H., Hall B.L., Denton G.H., Gades A.M., Waddington E.D., 1999. Past and future grounding-line retreat of the west antarctic ice sheet. Science 286, pp.280-283;

Cooper A.K., Barrett P.J., Hinz K., Traube V., Leitchenkov G., Stagg H.M.J., 1991. Cenozoic prograding sequences of the Antarctic continental margin: a record of glacio-eustatic and tectonic events. Marine Geology 102, pp.175–213;

Danielson M.A. & Bart P.J., 2023. The staggered retreat of grounded ice in Ross Sea, Antarctica, since the LGM. The Cryosphere 18, pp. 1125-1138. https://doi.org/10.5194/tc-18-1125-2024;

Davey F.J., Bennett D.J., Houtz R.E., 1982. Sedimentary basins of the Ross Sea, Antarctica. Journal of Geology and Geophysics 25, pp. 245–255. https://doi.org/10.1080/00288306.1982.10421413;

Davey F.J. & Brancolini G., 1995. The Late Mesozoic and Cenozoic structural setting of the Ross Sea region. In: Cooper A.K., Barker P.F., & Brancolini G. (Eds.), Geology and seismic stratigraphy of the Antarctic margin, Antarctic Research series. Washington, DC: American Geophysical Union, pp. 167-182;

Decesari R.C., Wilson D.S., Luyendyk B.P., Faulkner M., 2007. Cretaceous and tertiary extension throughout the Ross Sea, Antarctica;

De Santis L., Anderson J.B., Brancolini G., Zayatz I., 1995. Seismic record of Late Oligocene through Miocene glaciation on the Central-Eastern Continental Shelf of Ross Sea. In: Cooper A.K., Barker P.F. & Brancolini G. (eds) Geology and Seismic Stratigraphy of the Antarctic Margin. American Geophysical Union, Antarctic Research Series 68, pp. 235–260;

De Santis L., Prato S., Brancolini G., Lovo M., Torelli L., 1999. The Eastern Ross Sea continental shelf during the Cenozoic: implications for the West Antarctic ice sheet development. Global and Planetary Change 2, pp. 173–196;

Dinniman M.S., Klinck J.M., Smith Jr. W.O., 2011. A model study of Circumpolar deep Water on the West Antarctic Peninsula and Ross Sea continental shelves. Deep Sea Research Part II: Topical Studies in Oceanography 58, pp. 1508–1523. https://doi.org/10.1016/j. dsr2.2010.11.013;

Domack E.W., Jacobson E.A., Shipp S., Anderson J.B., 1999. Late Pleistocene–Holocene retreat of the West Antarctic Ice-Sheet system in the Ross Sea: part 2 sedimentologic and stratigraphic signature. Geological Society of America Bulletin 111, pp. 1517-1536;

Dorschel B., Hehemann L., Viquerat S., Warnke F., Dreutter S., Schulze Tenberge Y., Accettella D., An L., Barrios F., Bazhenova E.A., Black J., Bohoyo Fernando., Davey Craig., De Santis L., Escutia Dotti C., Fremand A.C., Fretwell P.T., Gales J.A., Gao J., Gasperini L., Greenbaum J.S., Henderson Jencks J., Hogan K.A., Hong J.K., Jakobsson M., Jensen L., Kool J., Larin S., Larter R.D., Leitchenkov G.L., Loubrieu B., Mackay K., Mayer L., Millan R., Morlighem M., Navidad F., Nitsche F.-O., Nogi Y., Pertuisot C., Post A.L., Pritchard H.D., Purser A., Rebesco M., Rignot E., Roberts J.L., Rovere M., Ryzhov I., Sauli C., Schmitt T., Silvano A., Smith J.E., Snaith H., Tate A.J., Tinto K., Vandenbossche P., Weatherall P., Wintersteller P., Yang C., Zhang T., Arndt J.E., 2022. The International Bathymetric Chart of the Southern Ocean Version 2 (IBCSO v2). PANGAEA. https://doi.org/10.1594/PANGAEA.937574;

Dypvik H. & Harris N.B., 2001. Geochemical facies analysis of fine-grained siliciclastics using Th/U, Zr/Rb and (Zr+Rb)/Sr ratios. Chemical Geology 181, pp. 131–146. http://dx.doi.org/10.1016/s0009-2541(01)00278-9;

Escutia C., DeConto R.M., Dunbar R., De Santis L., Shevenell A., Naish T., 2019. Keeping an eye on Antarctic Ice Sheet stability. Oceanography 32, pp. 32–46. https://doi.org/10.5670/oceanog.2019.117;

Evangelinos D., Escutia C., Etourneau J., Hoem F., Bijl P., Boterblom W., van de Flierdt T., Valero L., Flores J.-A., Rodriguez-Tovar F.J., Jimenez-Espejo F.J., Salabarnada A., Lopez-Quiros A., 2020. Late Oligocene- Miocene proto-Antarctic Circumpolar current dynamics off the Wilkes Land margin, East Antarctica. Global and Planetary Change 191, 103221;

Folk R.L. & Ward W.C., 1957. Brazos River bar: a study in the significance of grain size parameters Journal of Sedimentary Petrology 27, pp. 3-26;

Frank T.D., James N.P., Bone Y., Malcom I., Brenizer L., 2014. Late Quaternary carbonate deposition at the bottom of the world. Sedimentary Geology 305, pp. 1–16. https://doi.org/10.1016/j.sedgeo.2014.02.008;

Fraser A.D., Massom R.A., MIchael K.J., Galton-Fenzi B.K., Lieser J.L., 2012. East Antarctic landfast sea ice distribution and variability, 2000-08. Journal of Climate 25, pp. 1137-1156;

Friedman G.M. & Sanders J.E., 1978. Principles of Sedimentology. John Wiley and Sons, New York;

Galeotti S., DeConto R., Naish T., Stocchi P., Florindo f., Pagani M., Barrett P., Bohaty S.M., Lanci L., Pollard d., Sandroni S., Talarico F.M., Zachos J.C., 2016. Antarctic ice sheet variability across the Eocene-Oligocene boundary climate transition. Science 352, pp. 76-80;

Gales J.A., Larter R.D., Mitchell N.C., Hillenbrand C.-D., Østerhus S., Shoosmith D., 2012. Southern Weddell Sea shelf edge geomorphology: implications for cold, high salinity water overflow as an Antarctic gully-forming mechanism. Journal of Geophysical Research Earth Surface 117, F0421. https://doi.org/10.1029/2012JF002357;

Gales J., Rebesco M., De Santis L., Bergamasco A., Colleoni F., Kim S., Accettella D., Kovacevic V., Liu Y., Olivo E., Colizza E., Florindo-Lopez C., Zgur F., McKay R., 2021. Role of dense shelf water in the development of Antarctic submarine canyon morphology. Geomorphology 372, 107453;

Golledge N.R., Menviel L., Carter L., Fogwill C.J., England M.H., Cortese G., Levy R.H., 2014. Antarctic contribution to meltwater pulse 1A from reduced Southern OCean overturning. Nature communication 5, 5107;

Granot R. & Dyment J., 2018. Late Cenozoic unification of East and West Antarctica. Nature Communication 9, 3189. https://doi.org/10.1038/s41467-018-05270-w;

Greenwood S.L., Gyllencreutz R., Jakobsson M., Anderson J.B., 2012. Ice flow switching and East/ West Antarctic ice sheet roles in glaciation of the western Ross Sea. Geological Society of America Bulletin 124, pp. 1736–1749. https://doi.org/10.1130/B30643.1;

Greenwood S.L., Simkins L.M., Halberstadt A.R.W., Prothro L.O., Anderson J.B., 2018. Holocene reconfiguration and readvance of the east Antarctic ice sheet. Nature Communication 9;

Grobe H., 1987. A simple method for the determination of ice-rafted debris in sediment cores. Polarforschung 57, pp. 123-126. https://doi.org/10013/epic.11658.d001;

Ha S., Colizza E., Torricella F., Langone L., Giglio F., Kuhn G., Macrì P., Khim B.-K., 2022. Glaciomarine sediment deposition on the continental slope and rise of the central Ross Sea since the Last Glacial Maximum. Marine Geology 445, 106752;

Halberstadt A.R.W., Simkins L.M., Greenwood S.L., Anderson J.B. 2016. Past ice-sheet behaviour: retreat scenarios and changing controls in the Ross Sea, Antarctica. The Cryosphere 10, pp. 1003-1020;

Halberstadt A.R.W. , Simkins L.M., Anderson J.B., Prothro L.O., Bart P.J., 2018. Characteristics of the deforming bed: till properties on the deglaciated Antarctic continental shelf Journal of Glaciology 64, pp. 1014-1027;

Hall B.L., Henderson G.M., Baroni C., Kellogg T.B., 2010. Constant Holocene southern-ocean ^{14}C reservoir ages and ice shelf flow rates. Earth and Planetary Science Letters 296, pp. 115-123;

Hall B.L., Denton G.H., Stone J.O., Conway H., 2013. History of the grounded ice sheet in the Ross Sea sector of Antarctica during the Last Glacial Maximum and the last termination. Geological Society, London, 381, pp. 167-181;

Hammer Ø., Harper D.A.T., Ryan P.D., 2001. PAST: Paleontological statistics software package for education and data analysis. Palaeontologia Electronica 4: pp. 9. http://palaeo-electronica.org/2001_1/past/issue1_01.htm;

Harning D.J., Holman B., Woelders L., Jennings A.E., Sepúlveda J., 2023. Biomarker characterization of the North Water Polynya, Baffin Bay: implications for local sea ice and temperature proxies. Biogeosciences 20, pp. 229–249. https://doi.org/10.5194/bg-20-229-2023;

Hayes D.E. & Frakes L.A., 1975. General synthesis: Deep Sea Drilling Project 28. In: Hayes D.E., Frakes L.A. et al. (eds) Initial Reports of the Deep Sea Drilling Project. US Government Printing Office, Washington, DC 28, pp. 919–942;

Heaton T.J., Bard E., Bronk Ramsey C., Butzin M., Hatté C., Hughen K.A., Köhler P., Reimer P.J., 2023. A response to community questions on the Marine20 radiocarbon age calibration curve: marine reservoir ages and the calibration of 14C samples from the ocean. Radiocarbon 65, pp. 247-273;

Hillenbrand C.-D., Smith J.A., Kuhn G., Esper O., Gersonde R., Larter R.D., Maher B., Moreton S.G., Shimmield T.M., Korte M., 2009. Age assignment of a diatomaceous ooze deposited in the western Amundsen Sea Embayment after the Last Glacial Maximum. Journal of Quaternary Science 25, pp. 280-295;

Hillenbrand C.-D., Crowhurst S.J., Williams M., Hodell D.A., McCave I.N., Ehrmann W., Xuan C., Piotrowski A.M., Hernández-Molina F.J., Graham A.G.C., Grobe H., Williams T.J., Horrocks J.R., Allen C.S., Larter R.D., 2021. New insights from multi-proxy data from the West Antarctic continental rise: Implications for dating and interpreting Late Quaternary palaeoenvironmental records. Quaternary Science Reviews 257, 106842. https://doi.org/10.1016/j.quascirev.2021.106842;

Igarashi A., Numanami H., Tsuchiya Y., Fukucki M., 2001. Bathymetric distribution of fossil foraminifera within marine sediment cores from the eastern part of Lutzow Holm Bay, East Antarctica, and its paleoceanographic implications. Marine Micropaleontology 42, pp. 125–162. https://doi.org/10.1016/S0377-8398(01)00004-4;

Jaccard S.L., Galbraith E.D., Martínez-García A., Anderson R.F., 2016. Covariation of deep Southern Ocean oxygenation and atmospheric CO2 through the last ice age. Nature 530, pp. 207-210. https://doi.org/10.1038/nature16514;

Jimenez-Espejo F.J., Presti M., Kuhn G., Mckay R., Crosta X., Escutia C., Lucchic R.G., Tolotti R., Yoshimura Y., Huertas M.O., Macrì P., Caburlotto A., De Santis L., 2020. Late Pleistocene oceanographic and depositional variations along the Wilkes Land margin (East Antarctica)

reconstructed with geochemical proxies in deep-sea sediments. Global and Planetary Change 184, 103045;

King E.C., Hindmarsh R.C., Stokes C.R., 2009. Formation of mega-scale glacial lineations observed beneath a West Antarctic ice stream. Nature Geoscience 2, pp. 585–588;

King M.V., Gales J.A., Laberg J.S., McKay R.M., DeSantis L., Kulhanek D.K., Hosegood P.J., Morris A., I.O.D.P. Expedition, 2022. Pleistocene depositional environments and links to cryosphere-ocean interactions on the eastern Ross Sea continental slope, Antarctica (IODP Hole U1525A) Marine Geology 443, Article 106674;

King J., Anchukaitis K.J., Allen K., Vance T., Hessl A., 2023. Trends and variability in the Southern Annular Mode over the Common Era. Nature Communication 14, 2324. https://doi.org/10.1038/s41467-023-37643-1;

Kulhanek D.K., Levy R.H., Clowes C.D., Prebble J.G., Rodelli D., Jovane L., Morgans H.E.G., Kraus C., Zwingmann H., Griffith E.M., Scher H.D., McKay R.M., Naish T.R., 2019. Revised chronostratigraphy of DSDP Site 270 and late Oligocene to early Miocene paleoecology of the Ross Sea sector of Antarctica. Global and Planetary Change 178, pp. 46-64. https://doi.org/10.1016/j.gloplacha.2019.04.002;

Lamping N., Müller J., Hefter J., Mollenhauer G., Haas C., Shi X., Vorrath M.-E., Lohmann G., Hillenbrand C.-D., 2021. Evaluation of lipid biomarkers as proxies for sea ice and ocean temperatures along the Antarctic continental margin. Climate of the Past 17, pp. 2305–2326. https://doi.org/10.5194/cp-17-2305-2021;

Lawver L.A., Royer J.-Y., Sandwell D.T., Scotse C.R., 1991. Evolution of the Antarctic continental margins. In M.R.A. Thomson, J.A. Crame and J.W. Thomson, eds., Geological Evolution of Antarctica. Cambridge University Press, New York, pp. 533-539;

Lee J.I., McKay R.M., Golledge N.R., Yoon H.I., Yoo K.C., Kim H.J., Hong J.K., 2017. Widespread persistence of expanded East Antarctic glaciers in the southwest Ross Sea during the last deglaciation. Geology 45, pp. 403-406;

Levy R.H., Meyers S.R., Naish T.R., Golledge N.R., McKay R.M., Crampton J.S., DeConto R.M., De Santis L., Florindo F., Gasson E.G.W., Harwood D.M., Luyendyk B.P., Powell R.D., Clowes C., Kulhanek D.K., 2019. Antarctic ice-sheet sensitivity to obliquity forcing enhanced through ocean connections. Nature Geosciences 12, pp. 132–137. https://doi.org/10.1038/s41561-018-0284-4;

Licht K. & Andrews J.T., 2002. A ^{14}C record of late Pleistocene ice advance and retreat in the central Ross Sea, Antarctica. Arctic, Antarctic, and Alpine Research 34, pp. 324-333;

Licht K.J., Jennings A.E., Andrews J.T., Williams K.M., 1996. Chronology of late Wisconsin ice retreat from the western Ross Sea, Antarctica. Geology 24, pp. 223-226;

Licht K.J., Dunbar N.W., Andrews J.T., Jennings A.E., 1999. Distinguishing subglacial till and glacial marine diamictons in the western Ross Sea, Antarctica: implications for a last glacial maximum grounding line. Geological Society of America Bulletin 111, pp. 91-103;

Livingstone S.J., Ó Cofaigh C., Stokes C.R., Hillenbrand C.-D., Vieli A., Jamieson S.S.R., 2012. Antarctic palaeo-ice streams. Earth-science Reviews 111, pp. 90-128;

López-Quirós A., Lobo F.J., Duffy M., Leventer A., Evangelinos D., Escutia C., Bohoyo F., 2021. Late Quaternary high-resolution seismic stratigraphy and core-based paleoenvironmental reconstructions in Ona Basin, southwestern Scotia Sea (Antarctica). Marine Geology 439, 106565. https://doi.org/10.1016/j.margeo.2021.106565;

Lowry D.P., Golledge N.R., Bertler N.A.N., Jones R.S., McKay R., Stutz J., 2020. Geologic controls on ice sheet sensitivity to deglacial climate forcing in the Ross Embayment, Antarctica. Quaternary Science Advances 1, 100002;

Lucchi R.G., Rebesco M., Camerlenghi A., Busetti M., Tomadin L., Villa G., Persico D., Morigi C., Bonci M.C., Giorgetti G., 2002. Mid-late Pleistocene glacimarine sedimentary processes of a high-latitude, deep-sea sediment drift (Antarctic Peninsula Pacific margin). Marine Geology 189, pp. 343-370;

Majewski W., 2005. Benthic foraminiferal communities: distribution and ecology in Admiralty Bay, King George Island, West Antarctica. Polish Polar Research 26, pp. 159-214;

Majewski W., 2013. Benthic foraminifera from Pine Island and Ferrero Bays, Amundsen Sea. Polish Polar research 34, pp. 169-200. doi: 10.2478/popore−2013−0012;

Majewski W., Bart P.J., McGlannan A.J., 2018. Foraminiferal assemblages from ice-proximal paleo-settings in the Whales deep basin, eastern Ross Sea, Antarctica. Palaeogeography, Palaeoclimatology, Palaeoecology 493, pp. 64-81;

Majewski W., Prothro L.O., Simkins L.M., Demianiuk E.J., Anderson J.B., 2020. Foraminiferal patterns in deglacial sediments in the Western Ross Sea, Antarctica: life near grounding lines. Paleoceanography and Paleoclimatology 35, 003716;

Massé G., Belt S.T., Crosta X., Schmidt S., Snape I., Thomas D.N., Rowland S.J., 2011. Highly branched isoprenoids as proxies for variable sea ice conditions in the Southern Ocean. Antarctic Science 23, pp. 487-498;

McGlannan A.J., Bart P.J., Chow J.M., DeCesare M., 2017. On the influence of post-LGM ice shelf loss and grounding zone sedimentation on West Antarctic ice sheet stability. Marine Geology 392, pp. 151-169;

McKay R.M., Dunbar G.B., Naish T.R., Barrett P.J., Carter L., Harper M., 2008. Retreat history of the Ross ice sheet (shelf) since the last glacial maximum from deep-basin sediment cores around Ross Island. Palaeogeography, Palaeoclimatology, Paleoecology 260, pp. 245-261;

McKay R.M., De Santis L., Kulhanek D.K., Ash J.L., Beny F., Browne I.M., Cortese G., Cordeiro de Sousa I.M., Dodd J.P., Esper O.M., Gales J.A., Harwood D.M., Ishino S., Keisling B.A., Kim S., Kim S., Laberg

J.S., Leckie R.M., Müller J., Patterson M.O., Romans B.W., Romero O.E., Sangiorgi F., Seki O., Shevenell A.E., Singh S.M., Sugisaki S.T., van de Flierdt T., van Peer T.E., Xiao W., Xiong Z., Expedition 374 Scientists, 2019. Expedition 374 summary. Proceedings of the International Ocean Discovery Program Volume 374, College Station, TX (International Ocean Discovery Program). https://doi.org/10.14379/iodp.proc.374.101.2019;

McKay R., Albot O., Dunbar G.B., Lee J.I., Lee M.K., Yoo K.-C., Kim S., Turton N., Kulhanek D., Patterson M., Levy R., 2022. A comparison of methods for identifying and quantifying Ice Rafted Debris on the Antarctic margin. Paleoceanography and Paleoclimatology 37, e2021PA004404;

Medlin L., 1990. *Berkeleya* spp. from Antarctic waters, including *Berkeleya adeliensis*, sp. nov., a new tube dwelling diatom from the undersurface of sea-ice. Beiheft zur Nova Hedwigia 100, pp. 77-89;

Melis R. & Salvi G., 2009. Late quaternary foraminiferal assemblages from Western Ross Sea (Antarctica) in relation to the main glacial and marine lithofacies. Marine Micropaleontology 70, pp. 39-53;

Melis R. & Salvi G., 2020. Foraminifer and Ostracod Occurrence in a Cool-Water Carbonate Factory of the Cape Adare (Ross Sea, Antarctica): A Key Lecture for the Climatic and Oceanographic Variations in the Last 30,000 Years. Geosciences 10, 413. https://doi.org/10.3390/geosciences10100413;

Melis R., Capotondi L., Torricella F., Ferretti P., Geniram A., Hong J.K., Kuhn G., Khim B.K., Kim S., Malinverno E., Yoo K.C. , Colizza E., 2021. Last Glacial Maximum to Holocene paleoceanography of the northwestern Ross Sea inferred from sediment core geochemistry and micropaleontology at Hallett Ridge Journal of Micropalaeontology 40, pp. 15-35;

Mezgec K., Stenni B., Crosta X., Masson-Delmotte V., Baroni C., Braida M., Ciardini V., Colizza E., Melis R., Salvatore M.C., Severi M., Scarchilli C., Traversi R., Udisti R., Frezzotti M., 2017. Holocene sea ice variability driven by wind and polynya efficiency in the Ross Sea. Nature COmmunications 8, 1334;

Mosola A.B. & Anderson J.B. 2006. Expansion and rapid retreat of the West Antarctic Ice Sheet in Eastern Ross Sea: possible consequence of over-extended ice stream. Quaternary Science Review 29, pp. 2177-2196;

Müller J., Wagner A., Fahl K., Stein R., Prange M., Lohmann G., 2011. Towards quantitative sea ice reconstructions in the Northern North Atlantic: A combined biomarker and numerical modelling approach. Earth and Planetary Science Letters 306, pp. 137-148;

Murray J.W. & Pudsey C.J., 2004. Living (stained) and dead foraminifera from the newly ice-free Larsen Ice Shelf, Weddell Sea, Antarctica: ecology and taphonomy. Marine Micropaleontology 53, pp. 67–81. https://doi.org/10.1016/j.marmicro.2004.04.001;

Navarro-Rodriguez A., Belt S. T., Knies J., Brown T. A., 2013. Mapping recent sea ice conditions in the Barents Sea using the proxy biomarker IP25: implications for palaeo sea ice reconstructions. Quaternary Science Review 79, pp. 26–39. https://doi.org/10.1016/j.quascirev.2012.11.025;

Nichols P.D., Volkman J.K., Palmisano A.C., Smith G.A., White D.C., 1988. Occurrence of an isoprenoid C_{25} diunsaturated alkene and high neutral lipid content in Antarctic sea-ice diatom communities. Journal of Phycology 24, pp. 90-96;

Nichols P.D., Palmisano A.C., Rayner M.S., Smith G.A., White D.C., 1989. Changes in the lipid composition of Antarctic sea ice diatom communities during a spring bloom: an indication of community physiological status. Antarctic Science 1, pp. 133-140;

Nichols D.S., Nichols P.D., Sullivan C.W., 1993. Fatty acid, sterol and hydrocarbon composition of Antarctic sea ice diatom communities during the spring bloom in McMurdo Sound. Antarctic Science 5, pp. 271-278;

Ó Cofaigh C., Evans J, Dowdeswell J.A., Larter R.D., 2007. Till characteristics, genesis and transport beneath Antarctic paleo-ice streams. Journal of Geophysical Research 112, F03006;

Orsi A.H. & Wiederwohl C.L., 2009. A recount of Ross Sea waters. Deep Sea Research Part II: Topical Studies in Oceanography 56, pp. 778-795;

Pettijohn F.J., 1941. Persistence of heavy minerals and geologic age. The Journal of Geology 49, pp. 610–625. http://dx.doi.org/10.1086/624992;

Pezza A.B., Rashid H.A., Simmonds I., 2012. Climate links and recent extremes in Antarctic sea ice, high-latitude cyclones, Southern Annular Mode and ENSO. Climate Dynamics 38, pp. 57–73. https://doi.org/10.1007/s00382-011-1044-y;

Presti M., Barbara L., Denis D., Schmidt S., De Santis L., Crosta X., 2011. Sediment delivery and depositional patterns off Adélie Land (East Antarctica) in relation to late Quaternary climatic cycles. Marine geology 284, pp. 96-113. https://doi.org/10.1016/j.margeo.2011.03.012;

Prothro L.O., Simkins L.M., Majewski W., Anderson J.B., 2018. Glacial retreat patterns and processes determined from integrated sedimentology and geomorphology records. Marine Geology 395, pp. 104-119;

Prothro L.O., Majewski W., Yokoyama Y., Simkins L.M., Anderson J.B., Yamane M., Miyairi Y., Ohkouchi N., 2020. Timing and pathways of east Antarctic ice sheet retreat. Quaternary Science Review 230, 106166;

Pudsey C.J., 2000. Sedimentation on the continental rise west of the Antarctic Peninsula over the last three glacial cycles. Marine Geology 167, pp. 313-338;

Rignot E., Mouginot J., Scheuchl B., van den Broeke M., van Wessem M.J., Morlighem M., 2019. Four decades of Antarctic Ice Sheet mass balance from 1979–2017. Proceedings of the National Academy of Sciences 116, pp.1095-1103. Doi: 10.1073/pnas.1812883116;

Rodrigo-Gámiz M., Martínez-Ruiz F., Rodríguez-Tovar F.J., Jiménez-Espejo F.J., Pardo-Igúzquiza E., 2014. Millennial- to centennial-scale climate periodicities and forcing mechanisms in the westernmost Mediterranean for the past 20,000 yr. Quaternary Research 81, pp. 78–93;

Rothwell R.G. & Croudace I.W., 2015. Twenty years of XRF core scanning marine sediments: what do geochemical proxies tell us? In: Croudace I.W., Rothwell R.G. (Eds.), Micro-XRF Studies of Sediment Cores. Developments in Paleoenvironmental Research. Springer Science + Business Media, Dordrecht, pp. 25–101;

Rowland S.J. & Robson J.N., 1990. The widespread occurrence of highly branched acyclic C_{20}, C_{25} and C_{30} hydrocarbons in recent sediments and biota-A review. Marine Environmental Research 30, pp. 191-216;

Shipp S. & Anderson J.B., 1997. Grounding zone wedges on the Antarctic continental shelf, Ross Sea. In: Davies T.A., Josenhans H., Polyak L., Solheim A., Stoker M.S., Stravers J.A. (Eds), Glaciated continental margins, An atlas of acoustic images. Chapman & Hall, London, pp. 104-105;

Shipp S., Anderson J.B., Domack E.W., 1999. Late Pleistocene-Holocene retreat of the West Antarctic Ice Sheet system in the Ross Sea: Part 1 - geophysical results. Geological Society of America Bulletin 111, pp. 1486-1516;

Simkins L.M., Anderson J.B., Greenwood S.L., 2016. Glacial landform assemblage reveals complex retreat of grounded ice in the Ross Sea, Antarctica. Geological Society, London, Memoirs 46, pp.353–356;

Simkins L.M., Anderson J.B., Greenwood S.L., Gonnermann H.M., Prothro L.O., Halberstadt A.R.W., Stearns L.A., Pollard D., DeConto R.M., 2017. Anatomy of a meltwater drainage system beneath the ancestral East Antarctic ice sheet. Nature Geosciences 10, pp.691-697. doi: 10.1038/NGEO3012;

Simkins L.M., Greenwood S.L., Anderson J.B., 2018. Diagnosing ice sheet grounding line stability from landform morphology. Cryosphere 12, pp. 2707-2726. https://doi.org/10.5194/tc-12-2707-2018;

Smik L., 2016. Development of biomarker-based proxies for paleo sea-ice reconstructions. PhD Thesis, University of Plymouth,UK;

Smith J.A., Graham A.G., Post A.L., Hillenbrand C.D., Bart P.J., Powell R.D., 2019. The marine geological imprint of Antarctic ice shelves. Nature Communication 10, pp. 1-16;

Smith Jr W.O., Sedwick P.N., Arrigo K.R., Ainley D.G., Orsi A.H., 2012. The Ross Sea in a sea of change. Oceanography 25, special issue on Antarctic Oceanography in a Changing World, pp. 90-103;

Sorlien C.C., Luyendyk B.P., Wilson D.S., Decesari R.C., Bartek L.R., Diebold J.B., 2007. Oligocene development of the West Antarctic Ice Sheet recorded in eastern Ross Sea strata. Geology 35, pp. 467–470;

Stein R., 1991. Accumulation of organic carbon in marine sediments. Results from the Deep Sea Drilling Project/Ocean Drilling Program. In: Bhattacharji S., Friedman G.M., Neugebauer H.J. and Seilacher A., Eds., Lecture Notes in Earth Sciences, Springer, Berlin, pp.217;

Stoner J.S., Channell J.E.T., Hillaire-Marcel C., 1996. The magnetic signature of rapidly deposited detrital layers from the Deep Labrador Sea: Relationship to North Atlantic Heinrich layers. Paleoceanography 11, pp. 309-325. https://doi.org/10.1029/96PA00583;

Stuiver M. & Reimer P.J., 1993. CALIB rev. 8. Radiocarbon 35, pp. 215-230;

Taviani M., Reid D.E., Anderson J.B., 1993. Skeletal and isotopic composition and paleoclimatic significance of late Pleistocene carbonates, Ross Sea, Antarctica. Journal of Sedimentary Research 63, pp. 84–90;

Tesi T., Belt S.T., Gariboldi K., Muschitiello F., Smik L., Finocchiaro F., Giglio F., Colizza E., Gazzurra G., Giordano P., Morigi C., Capotondi L., Nogarotto A., Köseoğlu D., Roberto A.D., Gallerani A., Langone L., 2020. Resolving Sea ice dynamics in the north-western Ross Sea during the last 2.6 ka: from seasonal to millennial timescales. Quaternary Science Review 237, 106299;

Tolotti R., Salvi C., Salvi G., Bonci M.C., 2013. Late Quaternary climate variability as recorded by micropaleontological diatom data and geochemical data in the Western Ross Sea, Antarctica. Antarctic Science 25, pp. 804-820;

Torricella, 2016. Indagini sedimentologiche su una carota prelevata nell'area di scarpata del Mare di Ross (Antartide). Tesi di laurea, Università degli Studi di Trieste, A.A. 2014/2015;

Valle M., 2016. Processi sedimentari sulla scarpata del Mare di Ross orientale (Antartide). Tesi di laurea, Università degli Studi di trieste, A.A. 2015/2016;

Violanti D., 1996. Taxonomy and distribution of recent benthic foraminifers from Terra Nova Bay (Ross Sea, Antarctica), Oceanographic Campaign 1987/1988. Palaeontographia Italica 83, pp. 25-71;

Volkman J.K., 1986. A review of sterol markers for marine and terrigenous organic matter. Organic Geochemistry 9, pp. 83–99. https://doi.org/10.1016/0146-6380(86)90089-6;

Vorrath M.-E., Müller J., Rebolledo L., Cárdenas P., Shi X., Esper O., Opel T., Geibert W., Muñoz P., Haas C., Kuhn G., Lange C.B., Lohmann G., Mollenhauer G., 2020. Sea ice dynamics in the Bransfield Strait, Antarctic Peninsula, during the past 240 years: a multi-proxy intercomparison study. Climate of the Past 16, pp. 2459–2483. https://doi.org/10.5194/cp-16-2459-2020;

Whitworth T., Orsi A.H., Kim S.J., Nowlin Jr. W.D., Locarnini R.A., 1998. Water masses and mixing near the Antarctic slope front. In: Jacobs, S.S., Weiss, R.F. (Eds.), Ocean, Ice, and Atmosphere: Interactions at the Antarctic Continental Margin, pp. 1–27. https://doi.org/10.1029/ar075p0001;

Worthington L.V., 1981. The water masses of the World Ocean: some results from a fine-scale census. B.A. Warren, C. Wunsch (Eds.), Evolution of Physical Oceanography, MIT Press, Cambridge, pp. 44-69;

Wu L., Wang R., Xiao W., Krijgsman W., Li Q., Ge S., Ma T., 2018. Late Quaternary deep stratification-climate coupling in the Southern Ocean: implications for changes in abyssal carbon storage. Geochemistry Geophysics Geosystems 19, pp. 379-395. https://doi.org/10.1002/2017GC007250;

Yang S., Li Z., Yu J.-Y., Hu X., Dong W., He S., 2018. El Niño-Southern Oscillation and its impact in the changing climate. National Science Review 5, pp. 840-857. http://doi.org/10.1093/nsr/nwy046;

Yokoyama Y., Anderson J.B., Yamane M., Simkins L.M., Miyairi Y., Yamazaki T., Koizumi M., Sufa H., Kusahara K., Prothro L., Jasumi H., Southon J.R., Ohkouchi N., 2016. Widespread collapse of the Ross Ice Shelf during the late Holocene. Proceedings of the National Academy of Sciences of the USA 113, pp. 2354–2359;

Ziegler M., Jilbert T., de Lange G.J., Lourens L.J., Reichart G.-J., 2008. Bromine counts from XRF scanning as an estimate of the marine organic carbon content of sediment cores. Geochemistry Geophysics Geosystems 9, Q05009. https://doi.org/10.1029/2007GC001932.

Acknowledgements

I would like to express my gratitude to my supervisor prof. Ester Colizza and my co-supervisor prof. Romana Melis for this thesis, their help and their patience during this PhD and in particular during the writing of this thesis.

I thank Dr. Tommaso Tesi for the period I have spent at the CNR-SIP (Bologna) preparing the samples for biomarker analysis. Thank you to Francesca, Chiara and Alessio for their help and support.

I thank prof. Danilo Morelli and prof. Nicola Corradi for their help and support at the University of Genova during the recovery of geophysical data (SBPs and sparker profile).

I thank Dr. Laura De Santis and Dr. Jenny Gales for allowing me to use the geophysical data (single channel seismic lines) collected in the slope and rise area.

I acknowledge the Norwegian Polar Institute's Quantarctica package, used to create the bathymetric map.

Thank you Fiorenza for the continued support, in particular during the writing of this thesis.

Thank you Alice, amiga y compañera de viaje.

Thank you Rod and Manu, you supported me from the beginning of this geological path we took.

Thank you Alex, Celtico, Lelly and Previ, my best friends. I would have not reached the end of this path without your daily support.

Thank you to the old friends (Kevin, Giulia, Lollo, Luca, Tasso, Fel, Daniele) for your continued support since high school and for all the laughs.

Thank you to the Iceland Group (Fra, Manu, Leo, Fede, Luca, Will, Erica) for all the adventures we had around the world.

Last, but not least, thank you to my family: my mom and dad and my grandmas. You have supported me from the very beginning of this journey. I love you!